DATA READ-OUT AND B_c PRODUCTION IN ATLAS

Publisher: Twente University Press, P.O. Box 217, 7500 AE Enschede, the Netherlands, www.tup.utwente.nl.

Print: Océ Facility Services, Enschede.

ISBN 90-365-1977-2

DATA READ-OUT AND B_c PRODUCTION IN ATLAS

PROEFSCHRIFT

ter verkrijging van
de graad van doctor aan de Universiteit Twente,
op gezag van de rector magnificus,
prof. dr. F.A. van Vught,
volgens besluit van het College voor Promoties
in het openbaar te verdedigen
op woensdag 19 november 2003 om 13.15 uur

door

Reinder Cornelis Scholte

geboren op 9 April 1973

te Groningen

Dit proefschrift is goedgekeurd door:

prof. dr. ing. B. van Eijk (promotor) en
dr. ir. J.C. Vermeulen (assistent-promotor)

Contents

Introduction

The most fundamental understanding of the structure of matter and radiation today is described by the so-called Standard Model. Combining all forces (except for gravity) and being tested to tremendous precision, it is one of the most successful theories of the past decades. All particles predicted by the Standard Model have been detected, except for one: the "Higgs" particle. To find the "Higgs", a new large accelerator is currently being constructed at CERN, near Geneva in Switzerland. The "Large Hadron Collider" or LHC, will collide protons head-on at a centre-of-momentum energy of $\sqrt{s}$=14 TeV. To detect the Higgs particle among many other particles formed in the debris of such a collision, huge detectors are needed. The largest of five experiments which will operate at the LHC is called "A Toroidal Lhc ApparatuS" or ATLAS. The main goal of ATLAS is to find the "Higgs" particle and trace possible physics beyond the Standard Model such as super-symmetry (SUSY). Apart from the Higgs and SUSY, a huge amount of Standard Model particles will be produced, allowing high precision measurements of their properties. A group of Standard Model particles on which ATLAS will focus, are B mesons. These will be produced with very high rates allowing the study of CP violation and rarely formed heavy B mesons, such as the B_c. The B_c meson is the heaviest bound state of two quarks with different flavours and provides an unique testing ground for non-relativistic heavy quark theories. Using various non-relativistic models, the spectroscopy of the (excited states of) the B_c meson can be predicted with high precision. Furthermore, non-relativistic QCD provides a description for the formation of B_c mesons which is rather well quantifiable. In this thesis it is shown that a clear B_c signal can be seen at ATLAS. First the b quark cross section as measured by the CDF and DØ experiments at Fermilab will be extrapolated to LHC energies. A fragmentation approach based on non-relativistic QCD will be used to describe the production of B_c mesons. Predictions for the number of B_c mesons and the number of events observed in the decay channel $B_c \rightarrow J/\psi(l^- l^+)l\nu_l$ with $l = e, \mu$ with the ATLAS detector will be presented.

The outline of this thesis is as follows. First the Standard Model will be briefly described in Chapter 1. Emphasis is placed on B-physics. The theory to describe the production of b quarks is discussed. It demonstrated that the Pythia Monte Carlo program can be made to correctly predict the measured differential and integrated b quark cross sections at $\sqrt{s}$=1.8 TeV. Assuming this to be a robust theoretical basis, the extrapolation is then made to $\sqrt{s}$=14 TeV.

The LHC accelerator and the ATLAS detector are described in chapter 2. Due to the high luminosity foreseen at the LHC collider, a three-stage trigger system is implemented. In section 2.3 the trigger and Data AcQuisition (or DAQ) system of ATLAS is described. Emphasis is placed on the second level trigger (or LVL2 trigger) system, which is connected

to chapters 3, 4 and 5 in this thesis.

In chapter 3, a prototype Read-Out Buffer (called the CRUSH) for ATLAS, is described. The Read-Out Buffers (ROBs) store data from events accepted by the first level trigger until a final decision by the high level triggers is produced. The design and implementation of the CRUSH are discussed and results from test measurements are shown.

The performance of the LVL2 trigger system can be estimated from a discrete event simulation. The simulation uses the distribution of event fragment sizes, as generated by the ROBs, as one of its inputs. In chapter 4 distributions of event fragment sizes for the Inner Detector ROBs are presented.

The LVL2 B-physics trigger may result in a heavy load for the second level trigger system, since in some scenarios the whole TRT detector has to be read out, resulting in large amounts of data. A lossless zero suppression algorithm for the TRT data is investigated in chapter 5. The performance of the algorithm is discussed and timing measurements on the CRUSH and on commercial systems are compared.

The theory on production and decay of the B_c meson in hadronic interactions is reviewed in chapter 6. Starting from the b quark cross section, the fragmentation of b quarks into B_c mesons is described. Non-relativistic QCD is introduced, factorisation and the fragmentation approach is discussed. Subsequently, the spectroscopy of the $b\bar{c}$ bound state is given. It is shown that several excited states (below the BD threshold) decay strongly or electromagnetically to the B_c ground state, contributing to the total B_c cross section. Next, predicted branching ratios of inclusive, semi-inclusive and exclusive decays are given.

Having all the ingredients required to study B_c production at ATLAS, the relevant production mechanisms have been implemented in the ARIADNE Monte Carlo program. The implementation is described in chapter 7. B_c^- production cross sections for Tevatron and LHC energies are derived. Finally an analysis of the decay $B_c \to J/\psi(l^-l^+)l\nu_l$ with $l = e, \mu$ is performed. This is done by using a parametrised simulation of the ATLAS detector response.

Chapter 1

B physics, the Standard Model and beyond

1.1 Standard Model

The Standard Model distinguishes two kinds of particles; fermions and bosons. The former have half-integer spin, while the latter have integer spin. According to quantum mechanics, all fermions obey the Dirac equation, whereas all bosons satisfy the Klein-Gordon equation. In the Standard Model all matter consists of fermions while all the "force-carrying" or mediating particles are bosons. Quarks and leptons are fermions, they are grouped in three families (also known as generations), see table 1.1.

first generation			second generation			third generation		
name	mass [MeV]	Q [e]	name	mass [MeV]	Q [e]	name	mass [MeV]	Q [e]
up	1.5 - 4.5	+2/3	*charm*	1.0 - 1.4 ($\times$ 10^3)	+2/3	*top*	174.3 $\pm$ 5.1 ($\times$ 10^3)	+2/3
down	5 - 8.5	-1/3	*strange*	80 - 155	-1/3	*bottom*	4 - 5 ($\times$ 10^3)	-1/3
e^-	0.511	-1	μ^-	105.6	-1	τ^-	1776.9	-1
ν_e	$< 3 \times 10^{-6}$	0	ν_μ	$< 3 \times 10^{-6}$	0	ν_τ	< 18.2	0

Table 1.1: *Quarks and leptons, their mass and electric charge. Throughout this thesis masses and momenta are expressed in eV, i.e. $\hbar$=c=1. Masses are taken from [1]. The present upper limits for the neutrinos masses are quoted.*

The masses of the quarks are poorly known because they do not exist as free particles, and must be estimated from bound systems such as mesons. Only the top quark mass is measured precisely because it will decay before it can bind into a hadron. Each quark is referred to by its flavour and exists in one of three colour charge states. A colour charge state (or just colour), refers to the internal quantum number of the quarks associated with the strong force. There are three colours (red, green and blue or r, g and b) and three anti-colours ($\bar{r}$, $\bar{g}$, $\bar{b}$). For each quark a corresponding anti-quark exists[1]. Quarks have a positive or negative fractional electric charge. Observed particles always have an integer charge and are colourless, therefore quarks only exist in the combinations qqq ($\bar{q}\bar{q}\bar{q}$) or $q\bar{q}$.

[1] anti-quarks have exactly the same properties as quarks, but their charge and colour are conjugated.

For example, the proton consists of 2 up quarks and one down quark, resulting in a charge of +1. The π^+ consists of one up quark and one anti-down quark. The proton is a baryon, i.e. a particle made from three quarks (or three anti-quarks), the pion is a meson, a combination of a quark and anti-quark. The carriers of the strong interactions are called gluons and they induce changes in the colour of quarks. Gluons are massless, electrically neutral and carry a colour and an anti-colour (e.g. $r\bar{b}$). From three colours, nine gluons can be constructed, of which one is colourless, i.e. it does not mediate colour and does not take part in the strong interaction. The theory describing the interaction of quarks and gluons is called Quantum ChromoDynamics (QCD).

The charge carrying leptons in the Standard Model are the electron and heavier companions, the μ and the τ. Neutral leptons also exist, called neutrinos. Until recently, it was unknown whether the neutrinos were massless or not, however it is now established that neutrinos oscillate between flavours and possess (a very small) mass. In table 1.1 the three lepton families are shown with their respective charges and masses. As in the quark case, they are grouped in generations and for each lepton a corresponding anti-lepton exists.

Electromagnetic interactions are described by QED (Quantum ElectroDynamics). The photon (γ) is the chargeless and massless carrier of the electromagnetic interaction.

The third and last force in the Standard Model is the weak force. The electromagnetic and the weak force are unified in what is called the electroweak theory. The electroweak force couples to all particles in the Standard model, except for the gluons. The carriers of the electroweak force are (apart from the photon) heavy bosons, two of which are charged (W^+, W^-), one is the neutral Z^0. The charged weak interaction can change the flavour of quarks. The strength with which the flavour changing charged current manifests itself is characterised by the Cabibbo-Kobayashi-Maskawa (CKM) matrix. The CKM matrix gives the weak eigenstates of the quarks as linear combinations of quark mass eigenstates. By convention the matrix operates on the charge -$\frac{1}{3}$ quark mass eigenstates down, strange and bottom.

$$\begin{pmatrix} d' \\ s' \\ b' \end{pmatrix} = V \begin{pmatrix} d \\ s \\ b \end{pmatrix} = \begin{pmatrix} V_{ud} & V_{us} & V_{ub} \\ V_{cd} & V_{cs} & V_{cb} \\ V_{td} & V_{ts} & V_{tb} \end{pmatrix} \begin{pmatrix} d \\ s \\ b \end{pmatrix} \tag{1.1}$$

The CKM matrix (V) rotates the mass eigenstates resulting in the weak eigenstates. The first vector represents the weak eigenstates and the last vector the mass eigenstates. In some of the terms in the CKM matrix, complex phase factors enter, introducing CP violation. CP violation occurs if combined application of the Charge (C) and Parity (P) operators give rise to a change in physical observables. The Charge operator changes a particle into an anti-particle, i.e. charge, lepton number, baryon number, flavour and colour are reversed. The Parity operator performs a space inversion on a particle; the space coordinates are mirrored through a point. CP violation was discovered in 1964 [2] in the neutral kaon system and it's origin is still not known. Precision tests have confirmed CP violation in the B meson sector in 2001 [3], [4].

Currently, B physics experiments focus on measuring the CP-violating elements of the

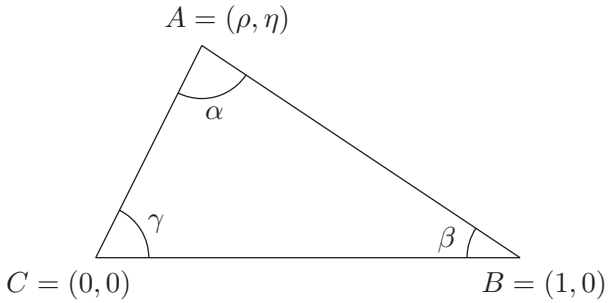

Figure 1.1: *Rescaled unitarity triangle with the vertices A,B and C at* (ρ, η)*, (1,0) and (0,0) respectively.*

CKM matrix. The CKM matrix can be parameterised using four real numbers, of which one is a measure for a complex phase. The complex phase is responsible for CP violation. The parameterisation which is commonly used in the literature is the "Wolfenstein parameterisation". Here, the four mixing parameters are (λ, A, ρ, η) where $\lambda = sin\theta_c = |V_{us}| = 0.22$ (θ_c is the Cabibbo angle) plays the rôle of the expansion parameter and η represents the CP violating phase :

$$V = \begin{pmatrix} 1 - \lambda^2/2 & \lambda & A\lambda^3(\rho - i\eta) \\ -\lambda & 1 - \lambda^2/2 & A\lambda^2 \\ A\lambda^3(1 - \rho - i\eta) & -A\lambda^2 & 1 \end{pmatrix} + \mathcal{O}(\lambda^4) \tag{1.2}$$

The values for the matrix elements are experimentally determined and are given at 90 % confidence level [1]:

$$|V| = \begin{pmatrix} 0.9741 \text{ to } 0.9756 & 0.219 \text{ to } 0.226 & 0.0025 \text{ to } 0.0048 \\ 0.219 \text{ to } 0.226 & 0.9732 \text{ to } 0.9748 & 0.038 \text{ to } 0.044 \\ 0.004 \text{ to } 0.014 & 0.037 \text{ to } 0.044 & 0.9990 \text{ to } 0.9993 \end{pmatrix} \tag{1.3}$$

The large value of the matrix elements on the diagonal and the small value of the off-diagonal matrix elements, show that almost all flavour changing takes place within one generation of quarks. For comparison with high precision measurements usually an extra higher order of λ is included in expression eq. 1.2. By using the unitarity of the matrix, the sum of three complex quantities vanishes. This is expressed in eq. 1.4:

$$V_{ud}V_{ub}^* + V_{cd}V_{cb}^* + V_{td}V_{tb}^* = 0 \tag{1.4}$$

Using eq. 1.4, a rescaled unitarity triangle is constructed in the complex plane by choosing a phase convention such that $(V_{cd}V_{cb}^*)$ is real, thereby aligning this axis with the real axis. Subsequently, the sides are scaled by dividing the lengths of all sides by $|V_{cd}V_{cb}^*|$, making this side unity. Neglecting $\mathcal{O}(\lambda^5)$ terms and higher, the coordinates of the vertices are then (0,0) (1,0) and (ρ, η) (see fig. 1.1).
The three angles in the unitarity triangle are defined as

force	propagator	coupling constant	typical lifetime [s]
electromagnetic	γ	$\alpha \sim \frac{1}{137}$	10^{-19}
strong	g	$\alpha_s \sim \frac{1}{8}$	10^{-23}
weak	W^+, W^-, Z^0	$\alpha_w \sim \frac{1}{29}$	10^{-8}

Table 1.2: *Relative strength of the three forces in the Standard Model. Although the weak force has a stronger coupling than the electromagnetic force, it is weaker at low energies, because the mass of the propagator also enters in the coupling strength. The value for α_s is obtained by evaluating eq. 1.8 at the scale M_Z.*

$$\alpha \equiv arg\left[\frac{V_{td}V_{tb}^*}{V_{ud}V_{ub}^*}\right], \quad \beta \equiv arg\left[\frac{V_{cd}V_{cb}^*}{V_{td}V_{tb}^*}\right], \quad \gamma \equiv arg\left[\frac{V_{ud}V_{ub}^*}{V_{cd}V_{cb}^*}\right] \tag{1.5}$$

The angles are physical quantities that can be measured independently by determining CP asymmetries in for instance B decays. CP violation in B_c decays will be discussed in chapter 6.

Particles that can only decay via the weak interaction, typically have long lifetimes. The masses of the W and Z bosons enter in the denominator of the propagator, thereby reducing the effective coupling at the typical decay energies of for instance B mesons. The reduced strength of the effective coupling leads to longer lifetimes. In the decay to quarks the relevant CKM matrix element also enters quadratically. If the CKM matrix element is small, even longer lifetimes can be expected.

For comparison, the coupling strengths of the electromagnetic, weak and strong force are indicated in table 1.2.

The Standard Model accommodates the massless photon and the three weak gauge bosons. After symmetry breaking, also a massive neutral scalar particle, called the Higgs particle, is predicted. The Higgs field that is introduced in the electroweak symmetry breaking generates the masses of particles in the Standard Model. The mass of the Higgs particle itself is generated by self-interactions of the Higgs field. The strength of the Higgs coupling is proportional to the mass of the particle it couples to. Precision measurements on electroweak couplings in the Standard Model predict a Higgs mass of 81^{+52}_{-33} GeV. LEP searches for the Higgs have resulted in a lower limit of $M_H > 114.3$ GeV, with a 95% confidence level [5].

One of the major goals of the LHC (and specifically ATLAS) is to find the Higgs and to measure its mass and coupling to massive particles, as well as to determine its quantum numbers. Fig. 1.2 shows the statistical significance of a Higgs signal at the ATLAS detector as a function of the mass of the Higgs. The 5σ limit[2] usually is the limit at which a discovery can be claimed. The contributions for the different Higgs decay channels add up to a statistical significance that is well above the 5σ limit. The plot is based on an integrated

[2]this means that the probability of the observed signal being a fluctuation of the background is $\leq 5 \cdot 10^{-5}$ %

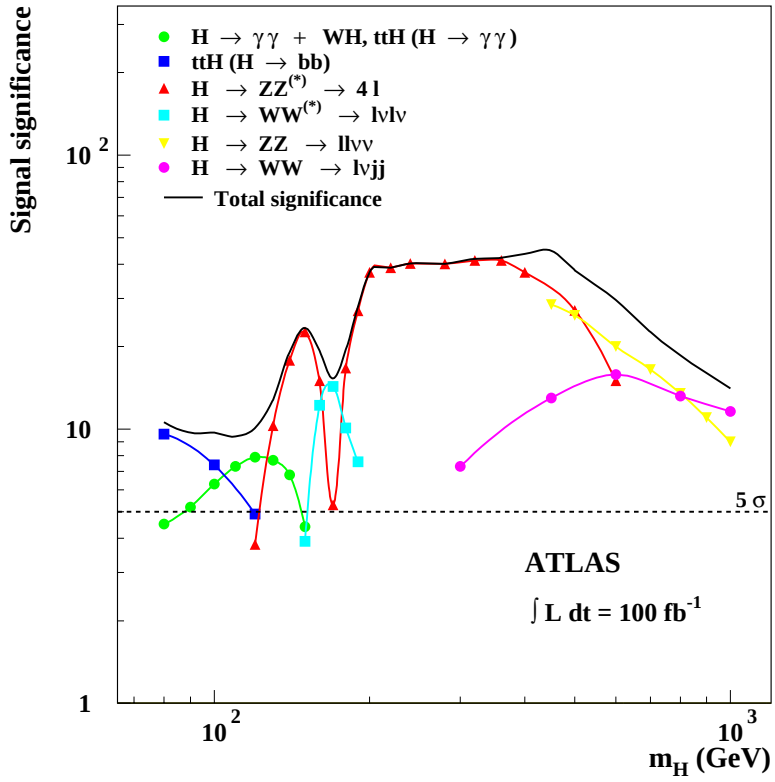

Figure 1.2: *Statistical significance ($S/\sqrt{B}$, with S the signal and B the background) of a Higgs signal at ATLAS as a function of M_H for different Higgs decay channels.*

luminosity of 100 fb^{-1}, equivalent to a one year period of data taking at ATLAS at high luminosity. The ATLAS detector is optimised for the detection of the Higgs particle. For example, in the mass range where the Higgs mass is most difficult to detect ($120 < M_H < 170$ GeV), the dominant decay channels are $H \rightarrow ZZ^{(*)} \rightarrow 4l$ and $H \rightarrow ZZ \rightarrow llνν$ (l=leptons). For $l = \mu$, the typical muon transverse momentum lies in the range of $5 < p_T < 50$ GeV. Since the Higgs width is small in this mass range and a severe background is expected, the Higgs mass resolution must be $\sim 1\%$ [6]. The intrinsic momentum resolution of the muon detector meets this requirement, but due to multiple scattering and energy loss in the calorimeters, an effective lower momentum resolution (of only 2-3 %) is obtained. Therefore, combination with tracks in the inner detector is needed. For Higgs masses of $\sim$ 500-700 GeV, the dominant Higgs decays involve neutrinos and jets ($H \rightarrow ZZ \rightarrow llνν$, $H \rightarrow ZZ \rightarrow lljj$, $H \rightarrow WW \rightarrow lνjj$, with j=jet). To reject the large QCD background in these channels a good E_T^{miss} measurement is required (with a resolution of a few percent), as well as accurate energy measurement of jets. The very large mass Higgs is predominantly produced by quarks which radiate gauge bosons that in turn fuse to form a Higgs. This results in jets at large rapidities that balance the longitudinal momentum of the Higgs. The ATLAS calorimeters must therefore extend up to $|\eta| \sim 5$. [3]

[3] η is the pseudo-rapidity, defined as $-ln(tan(\theta/2))$, where θ represents the angle between the direction of the beam-axis and the direction of the particle considered.

1.2 B production in hadronic collisions

B mesons are copiously produced in so-called "B-factories", i.e. e^+e^- colliders operating at the $\Upsilon(4S)$ resonance. The $\Upsilon(4S)$ resonance is produced by the annihilation of an e^+e^- pair into a photon (or Z^0), which subsequently splits into a $b\bar{b}$ pair and forms the resonance. The $\Upsilon(4S)$ resonance decays predominantly into light B-mesons[4] ($> 96\%$). To study heavier B mesons, $\Upsilon(5S)$ resonances can be produced but the production cross section at e^+e^- colliders is rather small.

At hadron colliders, the dominant contribution to large p_T b quark production stems from gluon-gluon fusion. In this section the production of b quarks in hadronic collisions will be discussed, as well as the theoretical difficulties that are encountered in calculating the b quark cross section.

The inclusive b quark production cross section can be written as :

$$\sigma(pp \to bX) = \int dx_i dx_j f_p(x_i, Q^2) f_p(x_j, Q^2) \hat{\sigma}(ij \to bX) \tag{1.6}$$

x_i and x_j are the longitudinal momentum fractions of the partons in the proton. Their density is given by the parton distribution functions $f_p(x_i, Q^2)$, $f_p(x_j, Q^2)$ of the colliding protons (see section 1.2.1). The partonic cross section $\hat{\sigma}(ij \to bX)$ is evaluated at the typical hard interaction scale Q. The partonic cross section can be written as a power expansion in the strong coupling constant α_s. The dependence of α_s on the scale Q is given by the renormalisation group equation :

$$Q^2 \frac{d\alpha_s(Q)}{dQ^2} = \beta(\alpha_s(Q)) = -b_0 \alpha_s^2(Q) - b_1 \alpha_s^3(Q) + ... \tag{1.7}$$

with $b_0 = (33 - 2N_f)/(12\pi)$, N_f denotes the number of flavours. Only considering the Leading Order (LO) in α_s, eq. 1.7 has the exact analytical solution :

$$\alpha_s(Q) = \frac{1}{b_0 ln(Q^2/\Lambda^2_{QCD})} \tag{1.8}$$

where Λ^2_{QCD} is an integration constant. The measured world average is currently $\alpha_s(M_z)$=0.119 $\pm$ 0.004 [1]. Λ_{QCD} is a fundamental parameter, that must be determined experimentally. By measuring α_s at a fixed scale, Λ_{QCD} can be determined. It is known that eq. 1.8 does not describe the running of α_s properly. If the Next-to-Leading (NLO) term, i.e. the term with b_1 in eq. 1.7, is included no exact analytical solution of eq. 1.7 can be found. In that case, usually an expansion in inverse powers of $ln(Q^2)$ is used [1] :

$$\alpha_s(Q) = \frac{1}{b_0 ln(Q^2/\Lambda^2_{\overline{MS}})} \left[1 - \frac{b_1 ln\left[ln(Q^2/\Lambda^2_{\overline{MS}})\right]}{b_0 ln(Q^2/\Lambda^2_{\overline{MS}})} \right] + \mathcal{O}\left(\frac{ln^2\left[ln(Q^2/\Lambda^2_{\overline{MS}})\right]}{ln(Q^2/\Lambda^2_{\overline{MS}})} \right) \tag{1.9}$$

[4]Only B^0, B^+ and their anti-particles are produced. The mass of the $\Upsilon(4S)$ is below the threshold for B_s ($\bar{B}_s$) production.

where $\overline{MS}$ in the subscript of Λ denotes the "modified minimal subtraction scheme". This scheme is introduced when divergences (in one-loop calculations) are encountered in the integral in the calculation of the matrix element of the form :

$$\int \frac{d^4k}{(2\pi)^4} \frac{k^\alpha k^\beta}{k^4} \tag{1.10}$$

Eq. 1.10 has an ultraviolet (k $\rightarrow \infty$) divergence. The divergence is removed by using "dimensional regularisation", a technical procedure in which the integral is evaluated in 4-ϵ dimensions instead of 4 dimensions. In the course of this procedure an arbitrary scale μ_R is introduced. Due to the introduction of the μ_R the resulting expression has become renormalisation scheme dependent.

In general, an infrared divergence ($k \rightarrow 0$) may also occur in the calculation of a cross section. The expression is then separated (or "factorised") into a part which is perturbatively calculable, and a part which is universal and which can be experimentally determined. This factorisation takes place at a rather arbitrary factorisation scale μ_F. Typically, parton distribution functions and partonic cross sections are μ_F dependent. So taking into account the dependence on μ_R and μ_F, the expression in eq. 1.6 becomes:

$$\sigma(pp \rightarrow bX) = \int dx_i dx_j f_p(x_i, \mu_F^2) f_p(x_j, \mu_F^2) \hat{\sigma}(ij \rightarrow bX) \tag{1.11}$$

where $\hat{\sigma}(ij \rightarrow bX)$ is a function of the introduced scales and α_s : $\hat{\sigma}(\mu_F, \mu_R, \alpha_s(Q, \mu_R))$.

The cross section is a physical observable, so the dependence on μ_R and μ_F should disappear in a calculation where all higher order terms are taken into account. In practice, the partonic cross section and α_s are expanded up to a certain order, thereby omitting higher order corrections. Often a truncated expansion is evaluated at $\mu_F/2$ and $2\mu_F$ to estimate the impact of higher order corrections. The factorisation scale μ_F is usually taken to be equal to the renormalisation scale μ_R.

1.2.1 Parton Distribution Functions

In expression 1.6, the cross section is factorised in a hard partonic cross section convoluted with the Parton Distribution Functions (PDFs) of the protons. PDFs of quarks and gluons in the proton have been measured and parameterised. These parameterised distributions are used by theoretical calculations and event generators (see section 1.2.3). In fig. 1.3 the distributions of valence quarks, sea quarks and gluons in the proton are plotted according to the MRST2001 parametrisation [7]. Sea quarks originate from gluon splitting in the proton. The variable x (see eq. 1.6) is the longitudinal momentum fraction carried by the parton in the proton.
The distributions are given at $\alpha_s(\mu^2)$, with μ^2=10 GeV^2. The PDFs can be evolved to a higher scale using the DGLAP[5] evolution equations [8], which incorporate effects of gluon radiation and gluon splitting as a function of scale and x :

[5]DGLAP: Dokshitzer-Gribov-Lipatov-Altarelli-Parisi

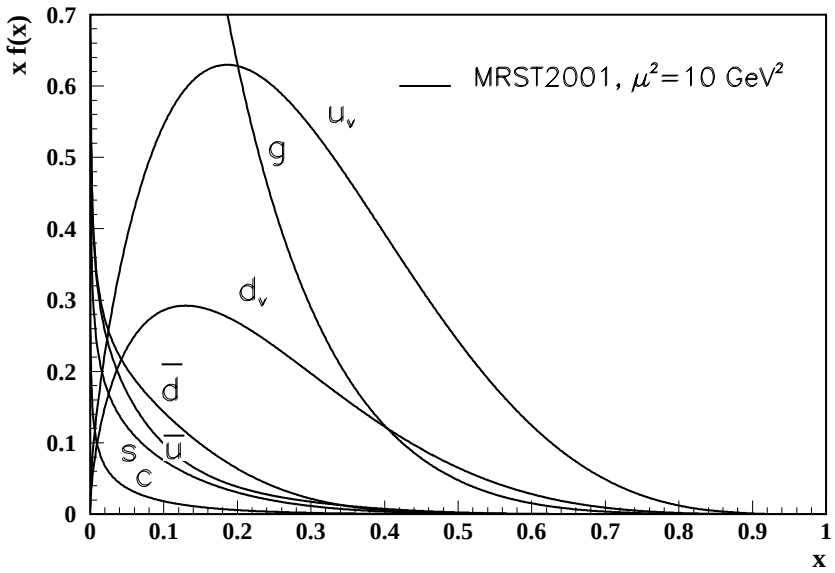

Figure 1.3: *Plot of $x \cdot q_i(x)$, with $q_i(x)$ the unpolarised density distribution, (for $i = u_v, d_v, \bar{u}, \bar{d}, s, c$) according to the MRST2001 [7] parameterisation of partons in the proton at a scale $\mu^2 = 10\ GeV^2$. Valence quarks have a subscript v, sea quarks have no subscript. Also plotted is $x \cdot g(x)$ where $g(x)$ is the gluon distribution function. Figure taken from [1].*

$$\frac{dq_i(x,Q^2)}{dlog(Q^2)} = \frac{\alpha_s}{2\pi}\int_x^1 \left(q_i(z,Q^2)P_{qq}(\left(\frac{x}{z}\right) + g(z,Q^2)P_{qg}\left(\frac{x}{z}\right)\right)\frac{dz}{z} \tag{1.12}$$

$$\frac{dg(x,Q^2)}{dlog(Q^2)} = \frac{\alpha_s}{2\pi}\int_x^1 \left(\sum_i q_i(z,Q^2)P_{gq}(\left(\frac{x}{z}\right) + g(z,Q^2)P_{gg}\left(\frac{x}{z}\right)\right)\frac{dz}{z} \tag{1.13}$$

Eq. 1.12 gives the evolution of the quark distribution function $q_i(x,Q^2)$. Each function $P_{p'p}(x/z)$ represents the probability that a parton of type p radiates a quark or gluon and becomes a parton of type p' carrying fraction (x/z) of the momentum of parton. The functions $P_{p'p}(x/z)$ are referred to as splitting kernels.

1.2.2 LO and NLO b quark production

The term Leading Order (LO) in the context of QCD refers to calculations in which the final state of interest is produced at lowest order in α_s. Next-to-Leading Order (NLO) is commonly used to describe the $\mathcal{O}(\alpha_s)$ corrections to this, comprising real and virtual corrections. Where appropriate in this section, orders of diagrams are designated by powers of α_s. Diagrams for b quark production at $\mathcal{O}(\alpha_s^2)$ are shown in fig. 1.4. In the literature the number of heavy quarks in the final state produced by the hard interaction (no radiation of gluons of photons) determines the nomenclature of the processes. A process with two heavy quarks in the final state is described as pair creation. This involves diagrams 1.4(a) and 1.4(c). The process depicted in diagram 1.4(a) is sometimes called "gluon fusion".

A process with one heavy quark in the final state, as in diagram 1.4(b), is called flavour excitation. It is somewhat ambiguous to classify this diagram as an $\mathcal{O}(\alpha_s^2)$ diagram since the initial b quark has to come from gluon splitting in the proton, which makes it a $\mathcal{O}(\alpha_s^3)$ diagram at lowest order, strictly speaking. However, for the purpose of generating b quarks using a Monte Carlo approach, as described in section 1.2.4, it is classified here as $\mathcal{O}(\alpha_s^2)$ processes. The reason for this will be explained in section 1.2.4. Leading order diagrams including those shown in fig. 1.4 have been calculated already in 1979 [9]. In [9] $2 \rightarrow 2$ diagrams with charm quarks in the final state were studied.

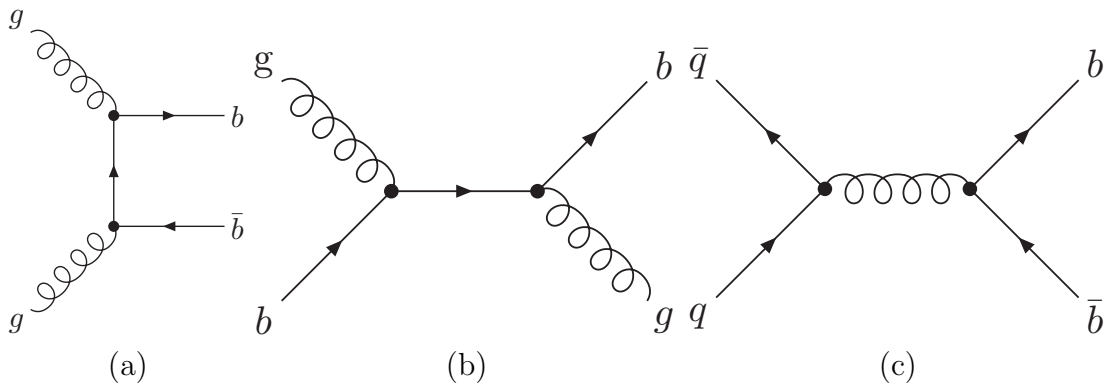

Figure 1.4: *Three of the leading order (α_s^2) diagrams for b quark production. Usually, in the literature, they are referred to as gluon fusion ($gg \rightarrow \bar{b}b$) (a), flavour excitation ($gb \rightarrow gb$) (b) and pair creation with light quarks (u,d possibly s) in the initial state ($qq \rightarrow b\bar{b}$) (c). Obviously, diagram (a) is also a pair creation diagram.*

NLO corrections prove to be as important as LO diagrams. Theoretical calculations for the b quark production cross section have been performed at NLO and appeared in 1989 [10]. Some of the Feynman diagrams that contribute at $\mathcal{O}(\alpha_s^3)$ are given in fig. 1.5. The virtual corrections shown in diagrams 1.5(a) and 1.5(b) interfere with the lowest order diagram 1.4(a) and (c) respectively and contribute at order α_s^2. The process in diagram 1.5(c) is a tree-level diagram which contributes at order α_s^3.

In fig. 1.6 the integrated inclusive b quark cross section measured at DØ [11], [12] and CDF [13], two experiments at the Tevatron, is shown.

The inclusive muon measurement at DØ includes all B meson decays [12]. The b quark cross section was extracted assuming the Peterson fragmentation function [15] with $\epsilon \sim 0.006$ [6]. The Peterson fragmentation function is a simple phenomenological expression which relates the momentum carried by the b quark to the momentum of the resulting B meson :

$$D_{\bar{b}\rightarrow B} \propto \frac{1}{z(1-\frac{1}{z}-\frac{\epsilon}{1-z})^2} \tag{1.14}$$

where z is the longitudinal momentum fraction of the B meson relative to the fragmenting b quark. The DØ di-muon measurement consists of $b\bar{b} \rightarrow \mu^+\mu^-$X, where contributions from

[6] The value of this parameter will be discussed in more detail in chapter 6

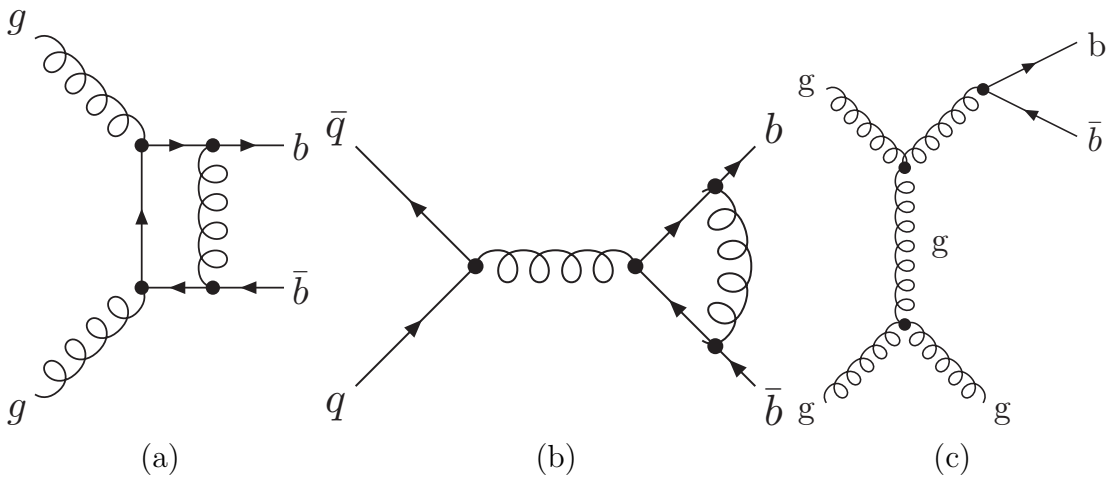

Figure 1.5: *Three diagrams at $\mathcal{O}(\alpha_s^3)$ of b quark production. (a) and (b) are virtual corrections to diagrams 1.4(a) and 1.4(c) respectively. Diagram (c) is a tree-level contribution at $\mathcal{O}(\alpha_s^3)$.*

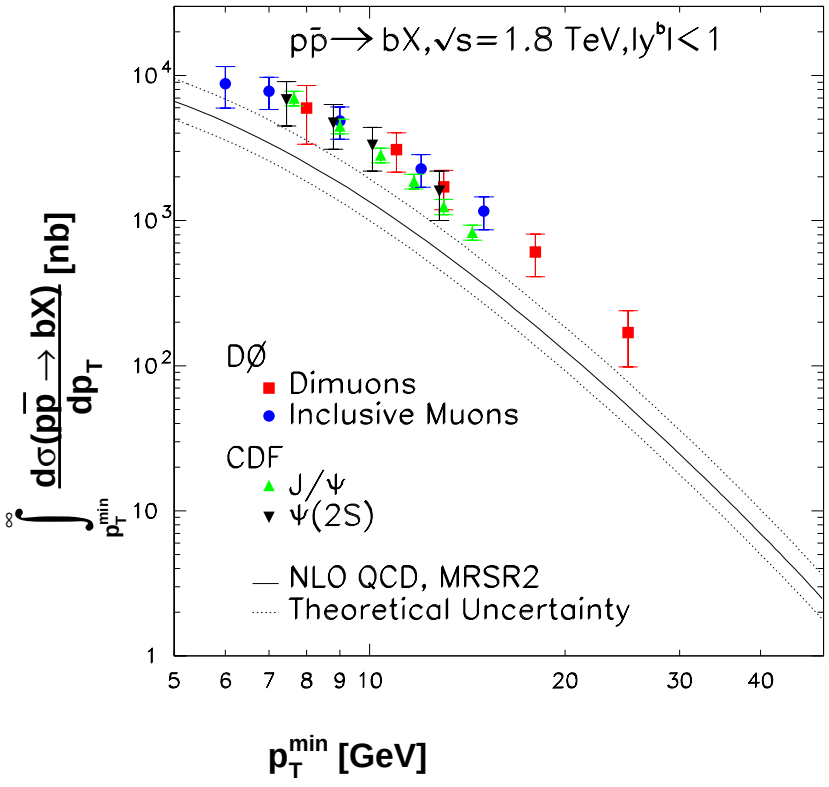

Figure 1.6: *Integrated p_T distribution for inclusive b production measured at the Tevatron and the NLO QCD prediction. Figure taken from [14].*

the background were subtracted using Monte Carlo techniques [12], [11]. CDF determined the b quark cross section from the decays $B^+ \to J/\psi K^+$, $B^0 \to J/\psi K^{*0}(892)$ and $B^+ \to \psi(2S)K^+$, $B^+ \to \psi(2S)K^{*0}(892)$, with J/ψ, $\psi(2S) \to \mu^+\mu^-$ [13]. For the formation of the B mesons the Peterson fragmentation function was used here as well. Background from direct J/ψ production was rejected by imposing a cut on displaced vertices in the transverse plane. For comparison, a NLO QCD calculation using the MRSR2 [16] parametrisation for the parton distribution functions is shown. The theoretical uncertainty is estimated by varying the mass of the b quark (4.5 - 5.0 GeV) and using the scales $\mu_F/2$ and $2\mu_F$, with $\mu_F^2 = m_b^2 + {p_T^b}^2$. The measured cross section is a factor of two to three higher than the NLO calculation. At UA1 [17] a similar discrepancy was found. Various possible sources of the discrepancy have been put forward. The common view is that the NNLO corrections become large, since the NLO corrections also add 100 % or more to the LO terms.

Complete NNLO calculations have not been performed but several effects that lead to divergences in the NLO calculation have been investigated and estimated using so-called "resummation" techniques. Only some of the problems will be illuminated here. Reviews are available elsewhere [18].

- Threshold effects. Coloured particles have a high probability to emit soft gluons. Usually the soft gluons hardly affect the kinematics, but if a high mass object (such as a b quark) is produced, even a small amount of radiated energy by a soft gluon causes the cross section to be suppressed. Since real radiation from the b quark balances the virtual corrections, a suppression of the phase-space for real radiation leads to an incomplete cancellation between the virtual corrections and the radiation. This results in large "left-over" contributions to the cross-section. This is known as the "threshold effect". Various resummation techniques exist to estimate its contribution, see for instance [19] and references therein. The size of the correction of the resummations to NLO is not so clear, but the largest enhancement is of order 15 %.

- High transverse momentum effects. For a high p_T b quark, large higher order corrections occur since the b quark behaves more and more like a massless particle. Therefore, it will radiate a large amount of its energy in the form of hard, collinear gluons. This is mathematically represented by large logarithms of the form $\alpha_s^n \log^n(p_T/m_b)$. This can again be dealt with by using resummation techniques.

- Small-x effects. When the centre-of-momentum energy ($\sqrt{s}$) is much larger than the hard scattering scale Q multiple gluon radiation over a large rapidity range results. Small x ($= \sqrt{(}s)/Q$) values then give rise to large logarithms of the form $\alpha_s^n \ln^n(\sqrt{(}s)/Q)$. Again techniques exist to resum these effects to all orders. For a review see [20].

A resummation generally leads to a reduced dependence on the renormalisation scale, thereby reducing the theoretical error.
Apart from these corrections to the perturbative NLO expression, the hadronisation model used by experiments to extract the b quark cross section from their measurement results of the B meson cross section, is questioned. Recently, a paper [21] was published by the

CDF collaboration on data of Run-I presenting the B^+ meson cross section. In this paper, a Monte Carlo study based on a NLO calculation convoluted with the Peterson fragmentation function with $\epsilon = 0.006$, is presented. The Monte Carlo result was compared with the experimental data. The data resulted in a cross section which was 2.9 times larger than the NLO calculation. However, Nason and Cacciari [22] pointed out that if the Peterson fragmentation (eq. 1.14) is convoluted with a NLO calculation, the value of ϵ should be ≈ 0.002, i.e. the fraction of the longitudinal momentum that the meson receives, should be much less than in a LO calculation. By carefully examining and resumming the fragmentation function eventually a discrepancy with the data with a factor of 1.7 was found. Although this represents an improvement, the data and the calculation still do not agree very well.

A study has also been undertaken [14] starting from the assumption that the incoming partons have a large intrinsic transverse momentum. An unphysically large average value of 4 GeV is taken. The effect on the b quark cross section is large, but the distribution of the azimuthal angle between b and $\bar{b}$ becomes more smeared, which does not comply with the data. Furthermore, if azimuthal correlations among muon pairs, originating from the decay of b quarks, are plotted and compared to models with and without a large intrinsic transverse momentum, the data favour small (or no) intrinsic transverse momentum.

Apart from perturbative QCD calculations, Monte Carlo event generators can be used to model the b quark cross section. These generators are tuned to data of previous experiments and should give the correct b quark cross section. The Monte Carlo approach is briefly discussed in the next section. Subsequently, in section 1.2.4 it is shown that the b quark cross section can be described correctly using the Monte Carlo approach adopted in this thesis.

1.2.3 Monte Carlo approach

Monte Carlo event generators provide a numerical approach to the simulation of multi-particle interactions. They use both theoretical models and experimentally measured quantities to generate multi-particle phase space and phenomenology. Several steps can be distinguished in the simulation procedure. For example, in high-energy proton-proton collisions, the constituents of the proton may undergo an interaction. These constituents (quarks and gluons) carry a certain momentum fraction of the proton and "appear" with a certain relative probability distributed according to experimentally measured densities. The interaction process of the constituents is hard-coded in terms of transition probabilities, the matrix elements; usually at lowest order in the coupling constant. However, as discussed in the previous section, the lowest order approximation may not be sufficient to provide precise results. Higher order corrections may sometimes become very large. The process depicted in 1.5(c) is a good example of a higher order correction with a large contribution to the cross section. Instead of introducing explicit higher order matrix elements, event generators introduce an approximation: the parton shower in which the partons before and after the hard interaction (described by the matrix elements) may radiate gluons and photons or may split into gluon or quark anti-quark pairs. These processes are referred to as initial state radiation (ISR) and final state radiation (FSR). In this way the partons

are "split" into according to well defined rules, mimicking higher order corrections. The radiation process continues until the parton energy has reached the hadronisation scale, typically at $\mathcal{O}(1$ GeV). At this scale, coloured partons combine to form hadrons. In the Monte Carlo event generator PYTHIA [23], splitting kernels (see eqs. 1.12 and 1.13) are introduced for initial and final state radiation. An alternative parton shower approach is provided by ARIADNE [24] in which the parton shower is described by the so-called Colour Dipole Model (see chapter 7, section 7.1). Parton shower and hadronisation models have been extensively compared with experimental data and have been tuned accordingly.

1.2.4 The b quark cross section

The PYTHIA event generator can be made to produce the correct b quark cross section if the correct subprocesses are included, following a prescription outlined in [25]. The hard interactions, $gg \to b\bar{b}$, $qq \to bb$ and $gb \to gb$, $qb \to qb$ are calculated separately. These parton fusion and flavour excitation processes use $\mathcal{O}(\alpha_s^2)$ matrix elements with massive quarks in the propagator, so low p_T interactions do not lead to divergences. The flavour excitation processes $gb \to gb$ and $qb \to qb$ contain a b quark in the initial state. PYTHIA treats this as follows: a b quark is selected according to a parameterisation of the parton distribution functions in the proton, at a scale of the order of the hard interaction. It subsequently evolves the scale downwards using the DGLAP equations, thereby eventually producing the initial b quark from a gluon splitting. Therefore, although the initial b quark comes from gluon splitting, PYTHIA still presents it to the user as a $2 \to 2$ process, which can be selected separately. The process $gg \to gg$ is singular in the limit where the interaction energy goes to zero, therefore a cut on the interaction energy of $\sim m_b$ has been set. The process $gg \to gg$ is generated by switching on all possible QCD processes. Subsequently, to avoid double counting, the events containing b quarks immediately after the hard interaction are *not* taken into account. In all processes initial and final state radiation is switched on.
In fig. 1.7(a) the various contributions to the inclusive differential b quark cross section are given as a funtion of P_T. A rapidity cut $|y^b| < 1$ is imposed to comply with CDF and DØ data. The total integrated b quark cross section as a function of the transverse momentum cut-off P_T^{min} is shown in fig. 1.7(b). The DØ and CDF data is shown as well.The theoretical inclusive b quark cross section is in good agreement with experimental data, therefore this procedure is adopted for further studies presented in chapter 7.

1.3 Beyond the Standard Model

The electroweak sector of the Standard Model has been tested to a high degree of accuray at LEP. The strong interaction, in particular the high energy regime, is also well understood. A recent review on the current experimental status is given in [27]. However, there are a few measurements that may point towards physics beyond the current Standard Model. As mentioned earlier, it has been established that neutrinos have a small mass, whereas in the Standard Model they are assumed massless. This suggests a mixing matrix among leptons similar to the CKM mixing matrix in the quark sector. A mixing matrix among leptons

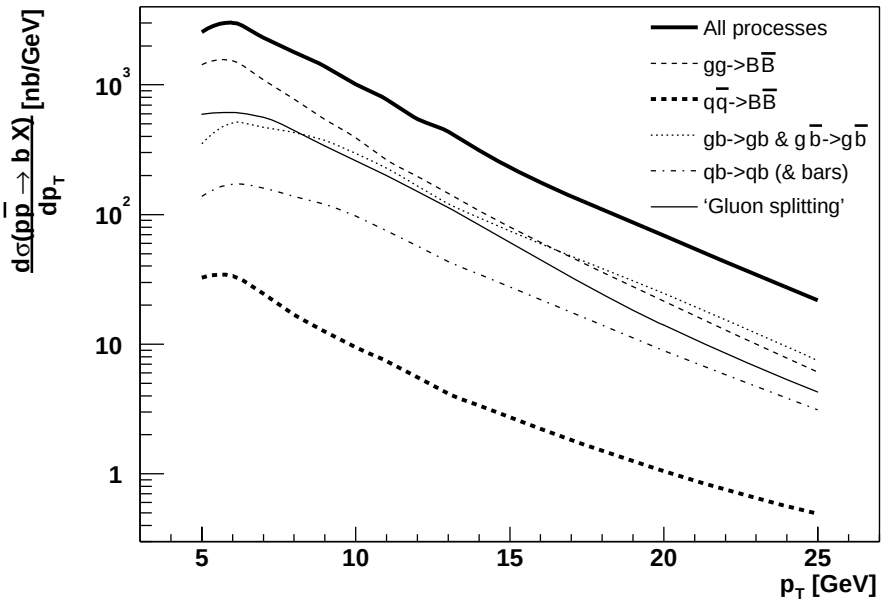

(a)

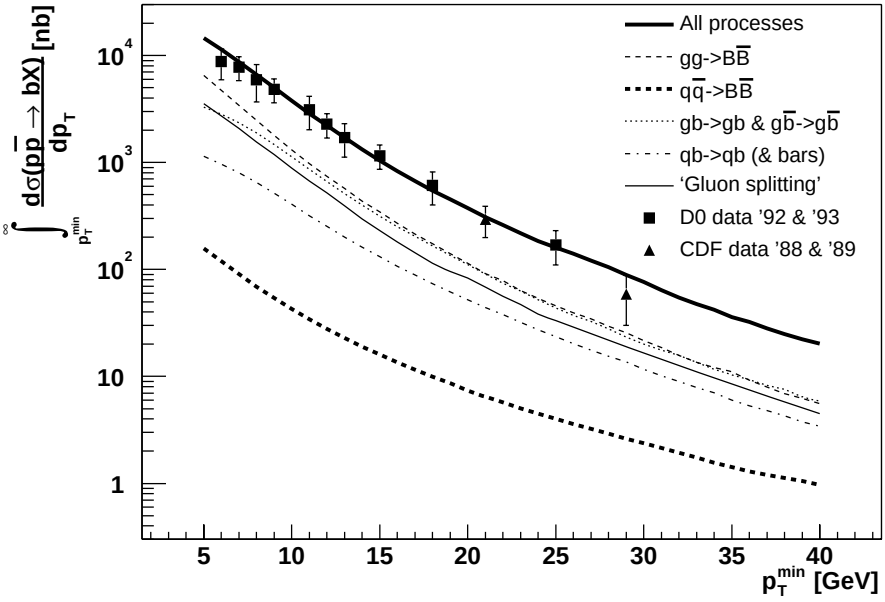

(b)

Figure 1.7: *The differential (a) and integrated (b) b quark cross section as a function of the p_T (p_T^{min}) of the b quark at $\sqrt{s}$=1.8 TeV and $|y^b| < 1$. The fat solid line represents the sum of all contributions. The parametrised parton distribution functions CTEQ3L [26] is used.*

however, can still be accommodated for in the Standard Model. A hint at real new physics beyond the Standard Model is given by the g-2 experiment at the Brookhaven National Laboratory. It is claimed that a deviation of the anomalous magnetic moment of the muon compared to the theoretical prediction [28] is observed. However the deviation is still not significant enough to be conclusive ($\sim 2\ \sigma$).

The Standard Model itself also exhibits several unexplained properties. For instance, consider photon loop corrections to the self energy of electrons, shown in fig. 1.8(a), and a fermion loop correction to the self energy of the Higgs, depicted in fig. 1.8(b).

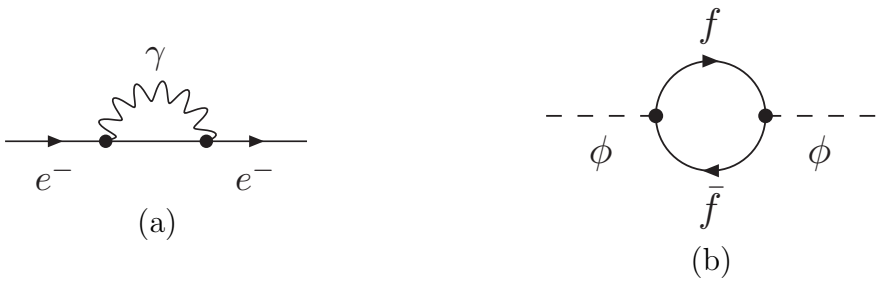

Figure 1.8: *The self energy correction for an electron, via a virtual γ loop (a) and the self energy of the Higgs field via a fermion anti-fermion loop (b).*

The correction from the diagram in fig. 1.8(a) reads

$$-4e^2 m_e \int_0^\infty \frac{d^4k}{(2\pi)^4} \frac{1}{k^2(k^2 - m_e^2)} \tag{1.15}$$

The integral is logarithmically divergent. However, if in the integration of this term "infinity" is replaced by the largest scale in particle physics, the Planck scale, the correction to the electron mass is only ~ 24 %.

The couplings and propagators in the diagram shown in fig. 1.8(b) are quite different, and the correction is given by:

$$-2\lambda_f^2 \int_0^\infty \frac{d^4k}{(2\pi)^4} \left[\frac{1}{k^2 - m_f^2} \frac{2m_f^2}{(k^2 - m_f^2)^2} \right] \tag{1.16}$$

where λ_f is the Higgs to fermion coupling. The expression in eq. 1.16 is quadratically divergent. If the Plank scale is now substituted, a correction of ~ 30 orders of magnitude results ! The introduction of SUSY (SUper SYmmetry) remedies this problem, since the super-symmetric bosonic partners of quarks or leptons will cancel the quadratic divergences in the loop in fig. 1.8(b).

A tantalising hint for a super-symmetric theory is given by Amaldi et. al. [29] who introduced a super-symmetry breaking scale at ~ 1 TeV. Taking into account this scale, the inverse of the coupling constants α_1, α_2 and α_3 are plotted as a function of scale. The coupling constants are defined as $\alpha_1 = (5/3)g'^2/4\pi$, $\alpha_2 = g/4\pi$ and $\alpha_3 = g_s/4\pi$ with g_s the strong coupling constant. g and g' are coupling constants of the electroweak theory: $g/sin\theta_W = g'cos\theta_W$, with θ_W the electroweak mixing angle. Due to the introduction of

the super-symmetric breaking scale, the coupling constants seem to unify at one particular point close to 10^{15} GeV. The SUSY breaking scale is a free parameter, so the fact that the coupling constants converge to a particular value may not seem so spectacular. This model does however predict a lifetime of the proton $\sim 10^{33}$ years which agrees with the present lifetime limit ($> 10^{32}$ years).

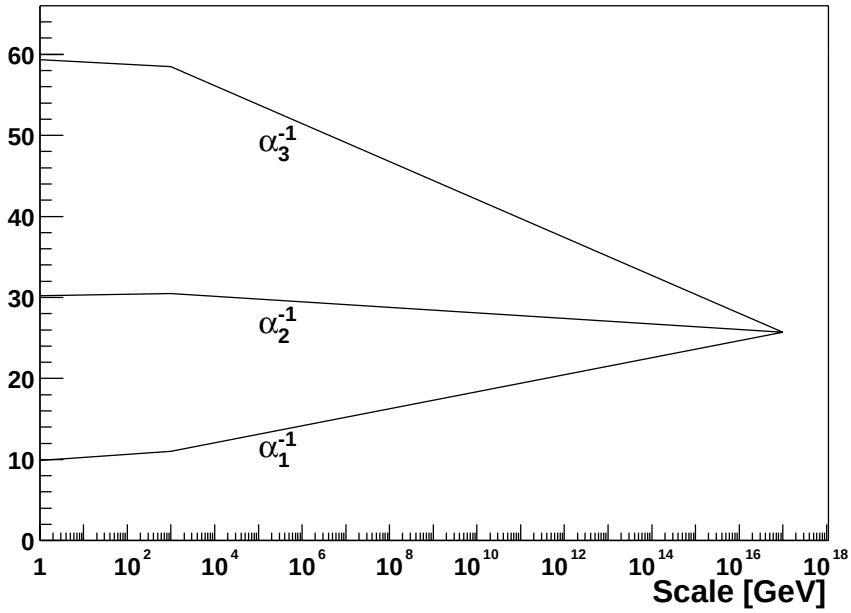

Figure 1.9: *The inverse coupling constants in the MSSM. At the mass scale $\sim$ 1 TeV, the Susy scale is introduced which accounts for the discontinuity in the evolution. The plot is taken from [29].*

Super-symmetric particles have not been discovered yet. If they exist, spectacular signals (multiple jets, missing energy) are predicted and in ATLAS they can be detected within a few days after the start of the experiment.

Several speculations have been presented in the literature in which it is argued that the discrepancy between the measured b quark cross section and NLO calculations stems from the decay of super-symmetric particles. For instance, in [30] a light gluino $\tilde{g}$ (mass $\sim$ 12-16 GeV) is postulated. This gluino decays into a bottom (b) and sbottom ($\tilde{b}$) quark (mass $\sim$ 2-5.5 GeV). Since CLEO results exclude $\tilde{b} \rightarrow cl\tilde{\nu}$ [31] and $\tilde{b} \rightarrow cl$ [32] in the assumed mass range, it is postulated that the sbottom quarks decay only hadronically. Alternatively, the sbottom quark could be long lived, since to date searches at lepton and hadron colliders do not exclude this. The gluino is predominantly produced in $g + g \rightarrow \tilde{g} + \tilde{g}$ at $\sqrt{s} \sim 2$ TeV in this scenario. It is postulated that through $\tilde{g} \rightarrow \tilde{b}b$ an additional contribution to the b quark cross section is generated. The additional SUSY contribution together with the Standard Model QCD contribution is then in agreement with the measured b quark cross section. The sbottom quark in this scenario must be the Lightest Supersymmetric Particle (LSP). With the constraint that the sbottom should only decay hadronically (or live very long), this explanation does not seem very plausible.

Decays in which the process $b \to s\gamma$ occurs, are likely candidates to search for physics beyond the Standard Model. The b quark decays into a strange quark via an intermediate W^- loop, and a γ is radiated from the W^-. In the intermediate quark propagator the Standard Model quarks u, c and t are present. However, also non-Standard Model particles may contribute to this loop. Furthermore, the radiated γ can split into a l^+l^--pair. This interferes with the same final state process $b \to sl^+l^-$ that proceeds via a W^+W^- box diagram. A careful measurement of this final state may enhance the sensitivity to physics beyond the Standard Model.

Chapter 2

LHC, ATLAS Detector and Trigger/DAQ System

A new powerful hadron collider, called the Large Hadron Collider (LHC), is currently being constructed at CERN. It will be housed in the old tunnel in which the Large Electron Positron (LEP) was formerly located. The main goals of the LHC include finding the Higgs particle, studying B-physics and to study possible new physics. The LHC and its specifications will be discussed in section 2.1. Of the five experiments at the LHC, ATLAS (A Toroidal Lhc ApparatuS), will be the largest. The Inner detector of ATLAS will be discussed in section 2.2.1. In sections 2.2.2 and 2.2.3 the calorimeters and muon detectors of ATLAS will be addressed. In section 2.3 the Trigger and Data AcQuisition (DAQ) system of ATLAS will be discussed.

2.1 LHC accelerator

The LHC will be located in the old LEP ring at CERN. LEP was an e^+e^- collider which operated ultimately at a maximum centre-of-momentum energy of 209.2 GeV. The quasi-circular tunnel of LEP has a circumference of approximately 26.7 km. The tunnel is located at the Swiss-French border near Geneva, see fig. 2.1. It is built underground, on an average depth of 100 m. At the LHC, the proton beams are brought into collision at four points at the collider ring. Point 1 and 5 will house the multipurpose LHC experiments ATLAS and CMS. The experiment TOTEM is foreseen to be integrated with the CMS experiment. For ATLAS and CMS, new caverns are being constructed. At Points 2 and 8, which previously housed LEP experiments, the LHC experiments ALICE and LHCb will be constructed. The rest of the points are for beam cleaning, acceleration and extraction.

Protons are generated in the PS, injected in the SPS and then injected in the LHC. The LHC has two separate beam pipes, both accelerating protons, one in the clockwise direction and one in the counter-clockwise direction. 1232 super-conducting dipole magnets are foreseen to bend the orbit of the beam at a peak magnetic field of ~ 8.3 T when 7 TeV protons are produced. A novel feature of the LHC dipole magnets is that the two beam channels and their set of coils are put in one cryostat, the "two-in-one" design. 482 so-called "2-in-1"

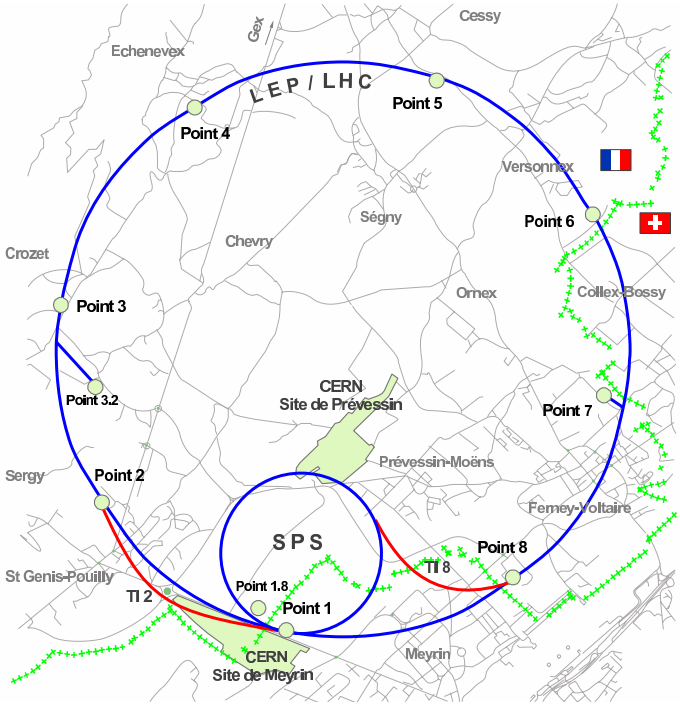

Figure 2.1: *The geographical location of the LHC ring together with the SPS.*

quadrupole magnets will be used for focusing the beam, as well as 24 "1-in-1" quadrupole magnets. The magnets are cooled with 1.9 K superfluid helium. The beam-radius will be 16 μm [1]. The longitudinal spread of a bunch of protons is characterised by a Gaussian, with a standard deviation of 7.5 cm.

Protons will be accelerated to an energy of 7 TeV, resulting in centre-of-momentum energy of 14 TeV. At maximum rate, every 25 ns bunches consisting of $\sim 10^{11}$ protons will collide. There will be 2808 bunches in a ring at any given time. The bunch structure for protons is summarised in fig. 2.2. The PS generates 72 bunches with a spacing of 25 ns. Three or four of these groups of 72 bunches are injected in the LHC with a 334 334 334 333 pattern. The number of missing bunches in the various gaps are given in the figure. Thus approximately 22% of the bunch crossings are empty. The ring will be filled in 4.3 minutes.

The event rate at an accelerator is determined by the interaction cross section and the luminosity :

$$R = \mathcal{L}\sigma_{int} \tag{2.1}$$

The luminosity in turn can be written as

$$\mathcal{L} = \frac{N_1 N_2 f n}{A} \tag{2.2}$$

where N_1 and N_2 are the number of particles per bunch, n is the number of bunches in either beam around the ring, f is the frequency of the bunch crossing, and A (in [cm^2]) is the overlap area of the two bunches. The design luminosity at which ATLAS will run is

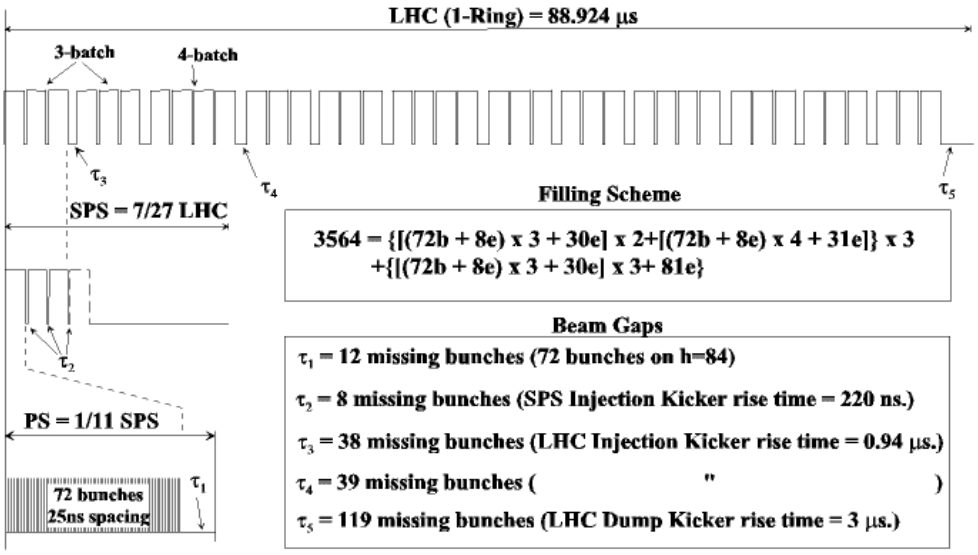

Figure 2.2: *Summary of the LHC bunch structure for protons. Figure taken from [33].*

$1 \cdot 10^{34}$ cm^{-2} s^{-1}. In it's first year of running it is foreseen to run at a luminosity of $1 \cdot 10^{33}$ cm^{-2} s^{-1} to $5 \cdot 10^{33}$ cm^{-2} s^{-1}. The luminosity lifetime is expected to be $\sim$ 15 hours.

The integrated luminosity is a measure for the total amount of data taken by an experiment after a certain time. It is given by

$$L = \int \mathcal{L}(t')dt' \tag{2.3}$$

and is usually expressed[1] in fb^{-1}.

2.1.1 LHC Status

In March 2001 one of the first of the pre-series dipoles was successfully tested, first at 8.3 and then at 9 T. In the following year 5 other pre-series dipole magnets were tested successfully. To keep the magnets cooled, eight cooling plants producing superfluid helium at 1.9 K are needed. Four additional cooling plants were ordered in addition to the four cooling plants already in place for LEP. One of these new plants is starting to operate. The fabrication of 350 dipoles and 185 quadrupoles for the transfer lines from SPS to the LHC has been completed. A prototype section of the LHC has been built in 2001 (String 2). It consisted of one set of three dipole magnets with short sections in between. String 2 was run for 24 hours at nominal current. It performed successfully. The addition of another set of three dipoles in may 2002 completed one full section of the LHC. The LHC is scheduled to be operational in 2007-2008.

[1] b stands for barn. 1 barn = 10^{-28} m^2.

2.2 The ATLAS Detector

The ATLAS detector consists of roughly three components, see fig. 2.3; an Inner Detector, calorimeters and muon detectors. The Inner detector is located close to the interaction point, and is used to precisely determine track parameters of charged particles. The calorimeters are used to give an energy measurement of electrons, photons and hadrons. The muon detectors, located at the outside of ATLAS, are used to measure the transverse momentum of muons.

The Inner detector is enveloped in an axial magnetic field with a nominal value of 2 T, directed along the beam axis. Charged particles are bent into a track in the form of a helix. Using precision detectors at different radii, the transverse momentum of a charged particle and the track it follows can be determined. The muon chambers are located within a toroidal magnetic field with an average field strength of about 0.5 T which provides bending of the muon tracks in the r-z plane of the detector. Since the tubes of the muon chambers are placed orthogonal to the beam-axis, this provides a high resolution of the p_T of the muon. ATLAS is 46 m long, has a height of 22 m and it weighs about 7000 tons.

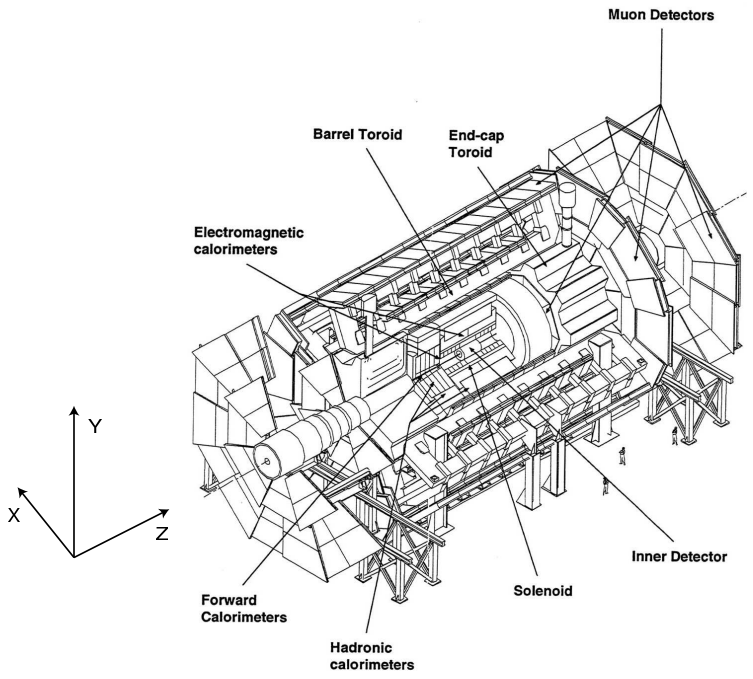

Figure 2.3: *Three-dimensional cut-away overview of the ATLAS detector. The coordinate system used in ATLAS is also indicated.*

Due to the very large interaction rate at the LHC, the various detector parts are subject to a large radiation flux. In particular, the silicon-based tracking detectors (part of the Inner detector) are sensitive to this radiation. The quantity which is relevant for the radiation dose of silicon detectors is expressed in 1 MeV equivalent neutrons (1 $\mathrm{MeV}_{n-equiv}$). This number varies between $1.5 - 50 \cdot 10^{13}$ cm^{-2}/year [34], the highest number being the dose that the inner layer of the pixel detector will receive. The high radiation dose degrades the

sensitive area of the silicon and damages the electronics. The radiation damage is strongly dependent on temperature. Therefore, it is chosen to place the whole silicon detector in a cold envelop. The silicon will operate at a temperature of -5 to -10 ℃. Furthermore, the low temperature reduces the leakage current. All electronics and sensors are built to withstand the radiation doses and the readout chips are bought from recognised manufacturers of radiation-hard chips.

2.2.1 Inner Detector

The Pixel, SCT (SiliCon Tracker) and TRT (Transition Radiation Tracker) detectors are together known as the "Inner detector". An overview of the Inner detector is given in fig. 2.4. Closest to the interaction point, in the lower left corner of fig. 2.4, the three pixel layers can be seen. At a larger radius, the four SCT barrel layers and finally the TRT barrel is depicted. Four pixel disks are shown here, but in the geometry adopted here (the most recent at the time of writing) only three are foreseen.

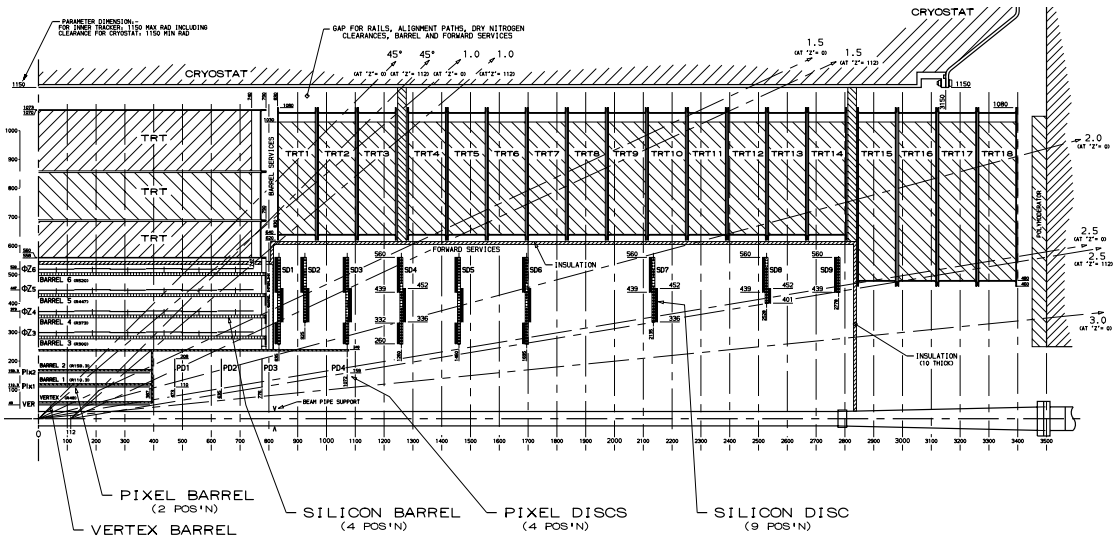

Figure 2.4: *Cross-sectional view of the cylindrical Inner detector. The view is cut along the z axis and shows only the forward part of the Inner detector. The picture shows the geometry which was foreseen in 1997 [35]. In the most recent geometry the pixel detector has three discs instead of the four depicted here.*

Pixel detector

The pixel modules, and in particular the layout of the pixel detector, have evolved significantly since the Inner detector Technical Design Report [35] and the Physics performance Technical Design Report [34]. The latest designs and layouts at the time of writing are given here. The elementary building blocks are pixel modules with a sensitive area of 16.4 mm x 60.8 mm. A pixel module has 16 readout chips (FE chips) which are connected to the

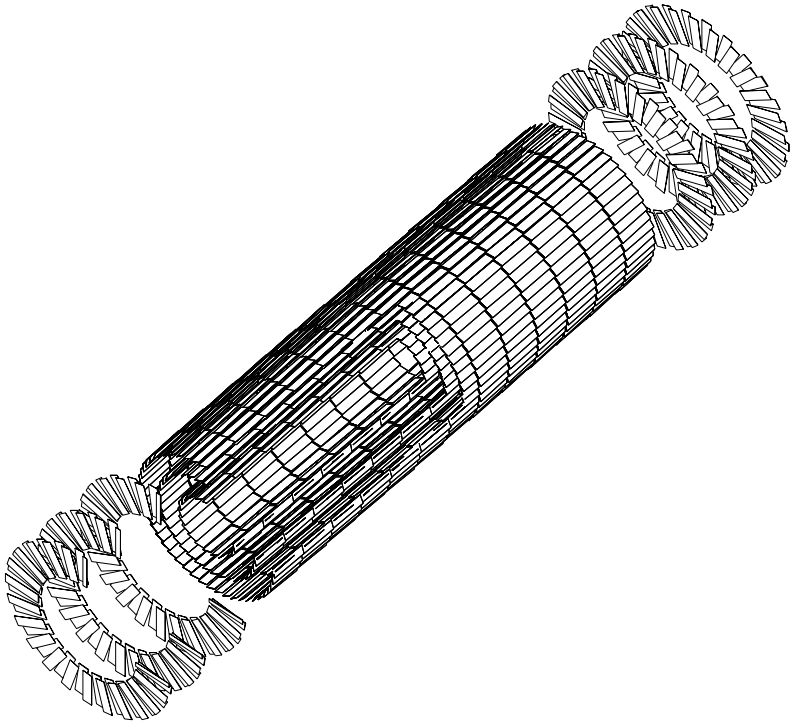

Figure 2.5: *An overview of the pixel detector.*

pixel cells through bump bonds. Each chip serves 18 x 160 pixel cells, totalling 46080 pixels. One pixel cell measures 50 $\times$ 400 μm. The innermost layer has 50 $\times$ 300 μm pixels with (24 $\times$ 160) 61440 pixels. Four integrated circuits (including the FE chips) were initially produced using a radiation hard technology called DMILL. However, it turned out that these chips could not withstand the high radiation dose expected in 10 years of running. The prototypes of the chips are now developed using DSM (Deep SubMicron) techniques. The new prototype chips seem to be able to cope with the radiation. However, the change in technology came rather late in the Pixel project. As a consequence, the Pixel detector has to be installed *after* the SCT. Consequently, the layout of the Pixel detector changed and small changes were made to the layout of the endcap of the SCT.

There are now 3 endcap disks foreseen at each side. The three concentric barrels are located at radii of 5.05, 8.85 and 12.25 cm with 286, 494 and 676 modules, respectively. 13 modules are placed on one stave or ladder, which runs parallel to the beam-axis. Several staves are located around the beam-axis to form a cylinder. The most recent geometry (at the time of writing this chapter) of the pixel detector is shown in fig. 2.5

Test Results In June 2002 the new prototype pre-series sensors have successfully been tested. The yield for the new detectors with the Deep Sub-micron technique was initially low, but is improving now. Prototype DSM pixel detectors have successfully been irradiated up to $1 \cdot 10^{15}$ 1 MeV equivalent neutrons. The noise after irradiation is $\sim$ 340 e^-, with a

threshold of 3200 ± 190 e^-. In fig. 2.6, plots are shown of the efficiency of prototype pixel sensors before (a) and after (b) irradiation.

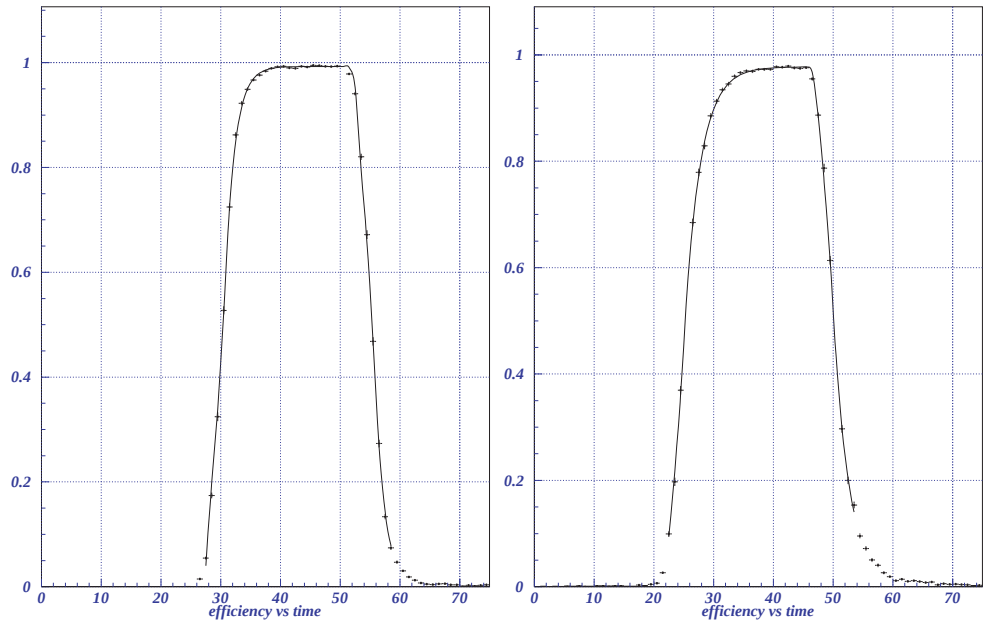

(a) (b)

Figure 2.6: *Full pixel module (sensor + integrated electronics) efficiencies vs. time at ∼ -5 ℃. Unirradiated pixel module, $< \epsilon >$=99.3 % during a time plateau of ∼ 10 ns (a). Irradiated pixel module, i.e. after a dose of 60 MRad or 1 $\times 10^{15}$ 1 $MeV_{n-equiv}$, $< \epsilon >$=97.7 % during a time plateau of 12 ns (b). Figures taken from [36].*

SCT detector

The SCT (SiliCon Tracker) consists of 4 concentric barrels at different radii and two endcaps each comprising eight wheels. The SCT barrels are located just outside the Pixel detector at radii of 300, 373, 447 and 520 mm and they contain 32, 40, 48 and 56 ladders or staves, respectively, each ladder consisting of 12 SCT modules. Alternate modules are staggered ± 1 mm above and below the nominal layer radius for overlap in the active area in the z-direction.

Each of the eight wheels of the SCT consists of 1 to 3 rings. Four types of rings, (designated types 1, 2, 3 and 4) are distinguished. Rings 2-4 all have 40 modules, ring 1 has 52 modules. Modules on a ring have an overlap in ϕ and are therefore separated in z by 0.25 cm. The specification of the rings and their z-positions are shown in table 2.1. See also Appendix A.

One barrel SCT module comprises four sensors. Each sensor is a 63.6 × 64 mm single sided silicon detector with 768 parallel strips with a 80 μm pitch. Two sensors are joined lengthwise to create a 128 mm long detector with 2 mm dead material in the centre. Then two of these joined sensors are glued back-to-back with a 40 mrad stereo angle difference between them. A view of an SCT barrel module is shown in fig. 2.7(a).

wheel number	type of rings	z position [cm]
1	1,2	84.9
2	1,2,4	93.2
3	1,2,4	108.2
4	1,2,4	126.0
5	1,2,4	1375.0
6	1,2,4	1745.0
7	1,2	2070.0
8	1,3	2460.0
9	1	2725.0

Table 2.1: *Specifications of the wheels in a SCT endcap. See also Appendix A.*

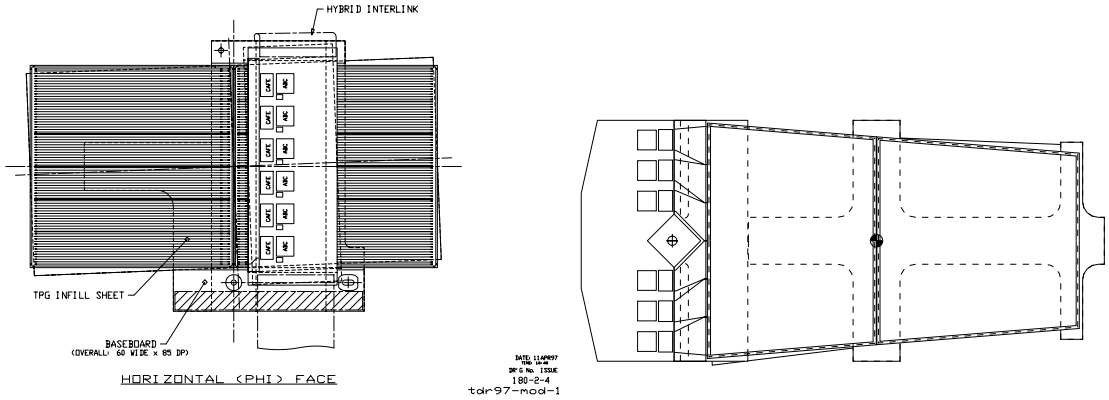

(a) (b)

Figure 2.7: *Configuration of a SCT barrel module (a). Configuration of a SCT endcap module (b).*

Two versions of endcap SCT modules exist. The first consists of two wedge-shaped sensors again joined lengthwise, and subsequently two of these joined sensors are glued back-to-back with a 40 mrad angle between strips on the front and on the back side. For the outer and middle ring the total lengths are about 12 cm. The modules for the inner ring consist of just 2 sensors (instead of four) glued back-to-back with a total length of 71.9 mm. The strips fan out radially, therefore the strip pitch varies from 70.8 - 90.3 μm for modules in the outer ring to 54.4 - 69.5 μm for modules in the inner ring. A schematic drawing of an endcap SCT module is shown in fig. 2.7(b).

Status SCT SCT modules were tested in a test-beam at CERN in 2000. The resolution of a binary readout is simply $\frac{pitch}{\sqrt{12}} \sim 23$ μm. The results of the test-beam show that this resolution is met. Two results from [37] are given in fig. 2.8.

TRT

The TRT (Transition Radiation Tracker) is the outermost detector in the Inner detector of ATLAS. This tracker is designed for high rates with a relatively large number (typically

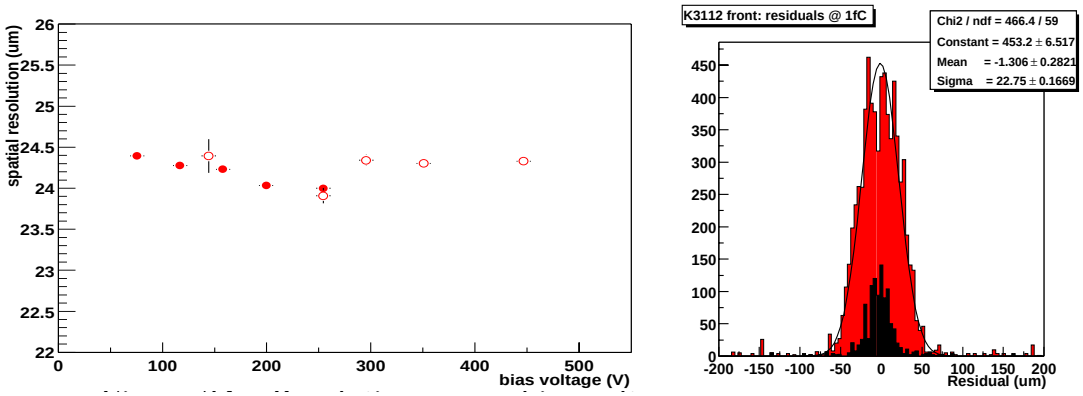

(a) (b)

Figure 2.8: *Resolution of a barrel SCT detector vs. bias voltage (a). The open circles represent modules with irradiated detectors, filled circles the unirradiated modules. In (b) the spatial resolution of strips on the two sides of a barrel silicon detector is shown.*

36) of space point measurements at a low cost.

The TRT can also detect transition radiation occurring when a highly relativistic particle ($\gamma >\sim 1000$) crosses a boundary between two media with different electrical properties.

The resulting radiated photons, as well as charged particles, are detected in "straw tubes" or "straws". These consist of an aluminium cylinder with a diameter of 4 mm filled with xenon gas. In the centre of the 1.5 m long tube a wire of 30 μm diameter is strung, which is held at a positive voltage. To enhance the yield of transition-radiation photons, stacks of polypropylene fibers (the radiators), typically 15 μm thick, are placed between the straws. The radial and azimuthal spacing between straws is 6.8 mm. A schematical picture of a TRT barrel module is shown in fig. 2.9.

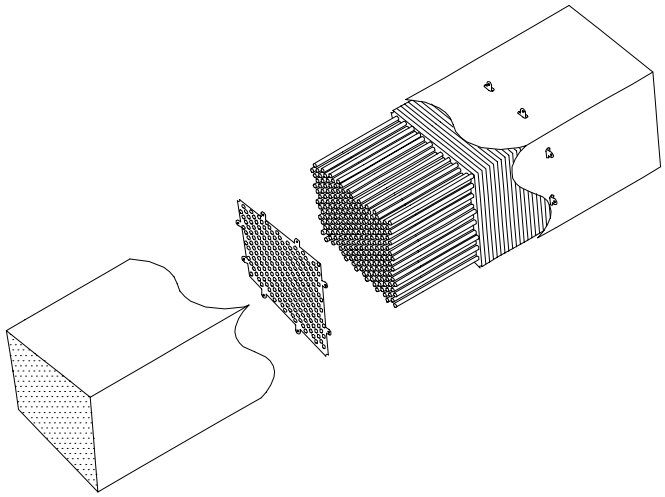

Figure 2.9: *Exploded view of a 1.5 m long TRT barrel module showing the straws, a straw alignment plane, stacks of radiators and enveloping the straws a plastic shell.*

The spatial resolution of a single TRT straw is ~ 170 μm. In the readout a low threshold is used to identify hits for a track, and a high threshold for signalling transition-radiation hits. For more information on the readout of the TRT see chapter 5.

The barrel consists of three concentric rings spanning the radii of 56-69, 69-85 and 85-107 cm. Each ring consists of 32 identical modules arranged in ϕ. The rings have 329, 520 and 793 straws per module in 19, 24 and 30 layers respectively. The first six (innermost) layers are active only over the last 36 cm in z (the central 80 cm is inactive) [35] to reduce their occupancy and maximise the number of crossed straws in the transition region between barrel and endcap. All the straws are embedded in (polypropene) fibers in a foam-like structure, which produce the transition radiation. The straws are split in the middle resulting in a separate readout for each half barrel. With 32 modules in the TRT barrel, this gives 52544 straws or 105088 readout channels. The spacing of the straws in the barrel in azimuthal and radial directions is on average 6.8 mm.

Each of the two endcaps of the TRT detector comprises 18 wheels, divided in three sets of identical wheels. The first set (wheel type A) consists of 6 wheels ($830 < z < 1684$ mm) and contains 12288 radial straws in 16 successive layers spaced by 8 mm in z. Each layer contains 768 straws in r-ϕ. The distance between the straws in the r-ϕ plane varies from about 5.2 mm at the innermost radius to 8.4 mm at the outer radius. The second set (wheel type B) consists of 8 wheels ($1687 < z < 2774$ mm) and contains 6144 radial straws positioned exactly as in the wheel type A, only the spacing between successive layers is now 16 mm. The last set of wheels (wheel type C) comprises 4 wheels ($2818 < z < 3363$ mm) and 9216 radial straws in 16 successive layers spaced by 8 mm along z. Each layer consists of 576 straws in r-ϕ. The distance between the straws in the r-ϕ plane varies from about 5.2 mm at the innermost radius to 11.2 mm at the outer radius.

One of the major functions of the TRT is e/π separation and to a lesser extent K/π separation, which is relevant for B-physics. Detailed simulations were performed in which the TRT detector response was tuned to test-beam results. In fig. 2.10 the separation as a function of momentum is given. The e/π separation is based on the number of transition radiation (TR) hits above threshold. In fig. 2.10(a) the distribution of TR hits for pions and electrons with a p_T=2 GeV is shown, for $0 < |\eta| < 0.8$. The pion rejection is determined by the size of the region of overlap. In fig 2.10(b), the pion efficiency as a function of the electron efficiency is plotted for 2 pseudo-rapidity regions.

2.2.2 Calorimeters

The ATLAS experiment has two types of calorimeters, electromagnetic (EM) and hadronic. Electromagnetic showers are measured in the EM calorimeter, while hadronic showers are mainly detected in the hadronic calorimeter, but can be partially measured in the EM calorimeters. In fig. 2.11 an overview of the various calorimeters in ATLAS is given.
Both type of calorimeters have a barrel and an endcap part. The coverage of the EM calorimeter is $|\eta| < 4.175$ for the barrel and $1.375 < |\eta| < 3.2$ for the endcap. A basic EM calorimeter cell consists of a lead absorber, a liquid argon (LAr) gap, a readout electrode and again a LAr gap. Bremsstrahlung and pair creation processes (both occurring mainly in the absorbers) produce a cascade of electrons, positrons and photons, for incident e's

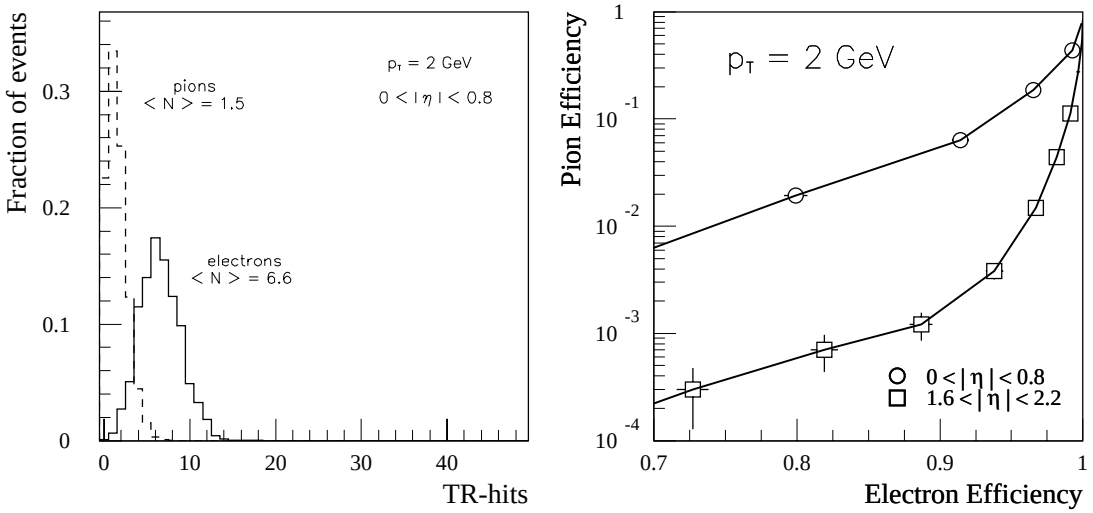

(a) (b)

Figure 2.10: *Plots showing the e/π separation capabilities of the TRT. In (a) the distribution of TR hits above threshold for electrons and pions is plotted for 0 < |η| < 0.8. In (b) the efficiency of pions as a function of the efficiency of electrons is plotted for 2 pseudo-rapidity ranges. For both plots the p_T of pions and electrons is 2 GeV. Figures taken from [34].*

(e^+, e^-) and γ's. The charged particles in the showers ionise the liquid argon (LAr) in between the absorbers, the electrons drift to the readout electrodes and are measured. One of the main physics requirements for the EM calorimeter is to give a good resolution of the γ's and electrons in the decay of a light Higgs (H $\rightarrow \gamma\gamma$ and H $\rightarrow 4e$). The design goal energy resolution of the EM calorimeter is [38]

$$\frac{\sigma_E}{E} = \frac{10\%}{\sqrt{E}} \oplus 1\% \tag{2.4}$$

The endcap EM calorimeter consists of two wheels, the outer wheel covering $1.375 < |\eta| < 2.5$, the inner wheel covers $2.5 < |\eta| < 3.2$. Due to the high level of radiation in the forward region, the forward calorimeters use tungsten rods (clad with copper) for a high density over a relatively small volume. The sensitive medium is again LAr. The forward calorimeters extend the coverage up to $|\eta| = 4.9$. The calorimeters are segmented in cells. The granularity for the EM calorimeters varies from $\Delta\eta \times \Delta\phi = 0.003 \times 0.1$ to $\Delta\eta \times \Delta\phi = 0.025 \times 0.025$.

The barrel part of the hadronic calorimeter ($|\eta| < 1.6$) uses iron plates as the absorber material, and scintillating plastics in between. The scintillating plates are read out by wavelength shifting fibers. In the range $1.5 < |\eta| < 4.9$ LAr is again used for the hadronic calorimetry, because of the higher radiation environment. The resolution of the hadronic calorimeters is worse than the EM calorimeters, caused by the difference in showering mechanisms :

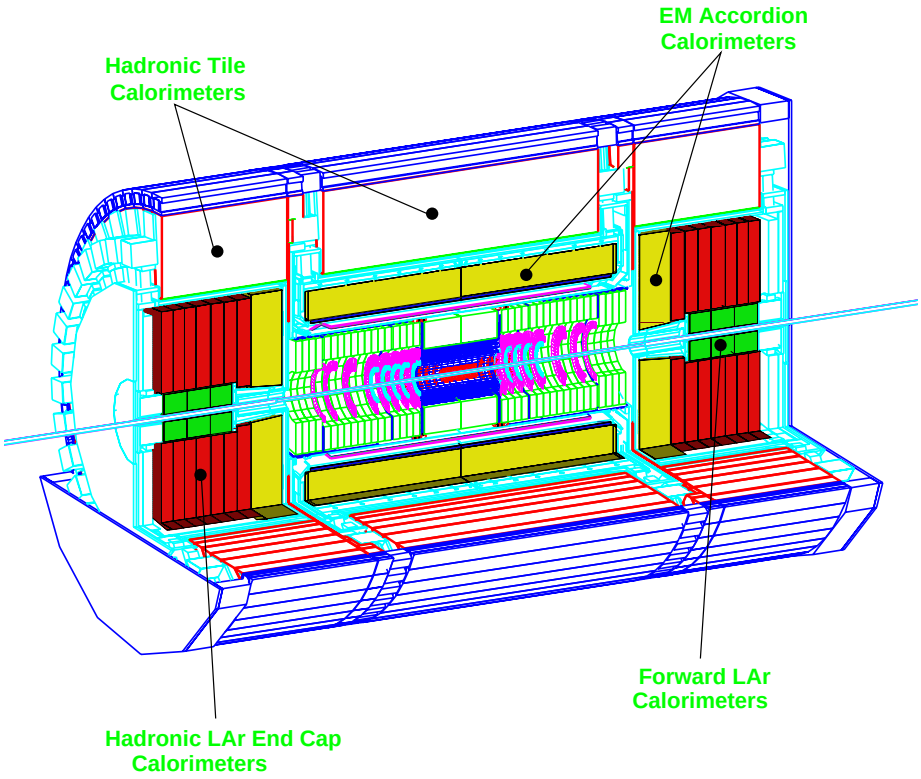

Figure 2.11: *The various calorimeters in the ATLAS experiment.*

$$\frac{\sigma_E}{E} = \frac{50\%}{\sqrt{E}} \oplus 3\% \quad for \;\; |\eta| < 3 \tag{2.5}$$

$$\frac{\sigma_E}{E} = \frac{100\%}{\sqrt{E}} \oplus 10\% \quad for \;\; 3 < |\eta| < 5 \tag{2.6}$$

The requirements for the granularity for the hadronic calorimeter are $\Delta\eta \times \Delta\phi = 0.1 \times 0.1$ for $|\eta| < 3$, and $\Delta\eta \times \Delta\phi = 0.2 \times 0.2$ for larger η.
As an illustration, test-beam results of the hadronic liquid endcap calorimeter ($1.5 < |\eta| < 3.2$) are shown here. Three wedges in ϕ of the hadronic liquid endcap calorimeter were tested in a test-beam in 2000. The measured performances are shown in fig. 2.12.
The average values obtained for the typical energy resolution of pions were:

$$\frac{\sigma_E}{E} = \frac{70.6 \pm 1.5\%}{\sqrt{E}} \oplus (5.8 \pm 0.2)\% \tag{2.7}$$

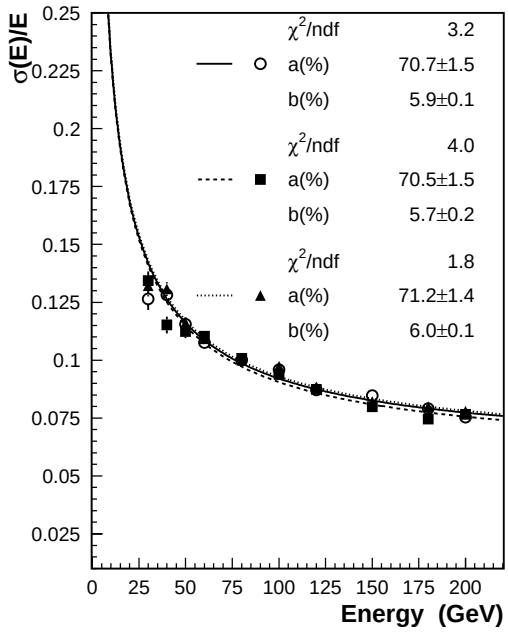

Figure 2.12: *$\sigma(E)/E$ for pions, for three different impact points (a point of impact corresponding to one ϕ wedge). Figure taken from [39].*

Using this result and the resolution of the EM calorimeter in front of the hadronic liquid endcap calorimeter the hadronic resolution for the region ($1.5 < |\eta| < 3.2$) was calculated to be:

$$\frac{\sigma_E}{E} = \frac{54 \pm 2\%}{\sqrt{E}} \oplus (2.6 \pm 0.1)\% \tag{2.8}$$

which is compatible with the resolution in eq. 2.5.

2.2.3 Muon detectors

The muon system of ATLAS plays an important rôle in the discovery of a medium heavy Higgs and super-symmetry. The "gold plated" decay channel for a Higgs is $H \rightarrow ZZ^* \rightarrow 4\mu$. A heavy Higgs can decay via $H \rightarrow ZZ \rightarrow ll\nu\nu$. Moreover, the B-physics program of ATLAS relies heavily on muon identification and measurement. In fact, the trigger for a B-physics event is a muon with a $p_T > 6$ GeV. Very recently, this threshold has been raised to $p_T > 8$ GeV, since the initial foreseen luminosity has been raised to $2 \cdot 10^{33}$ cm^{-2} s^{-1}. However, the results presented in this thesis were obtained using the old threshold, i.e. the $p_T > 6$ GeV trigger will be assumed everywhere in this thesis, unless stated otherwise. The layout of the four different muon systems in the ATLAS detector is shown in fig. 2.13.

In the barrel region ($|\eta| < 1$), the magnetic field is provided by the barrel toroid. For the region $1.4 \leq |\eta| \leq 2.7$, muon tracks are bent by two endcap magnets inserted in both ends of endcap. In the transition region $1.0 \leq |\eta| \leq 1.4$, the tracks are bent by a combination of barrel and endcap magnets.

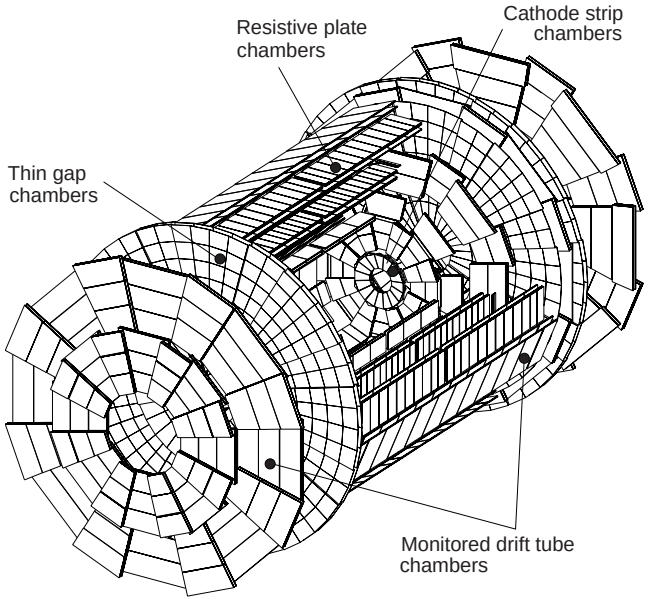

Figure 2.13: *A 3-dimensional overview of the different muon systems in ATLAS.*

Monitored drift tubes

A Monitored Drift Tube (MDT) chamber consists of a number of parallel layers of drift tubes on a support frame, with two closely packed layers on each side. The closely packed layers are referred to as a "multilayer". A drift tube is a cylindrical tube of aluminium with a diameter of 30 mm. In the centre a wire with a diameter of 50 μm is placed [6]. The wire is kept at a nominal voltage of 3270 V. The tube contains a gas which consists of Argon (91%), N_2 (4%) and CH_4 (5%) under a pressure of 3 bar. An average resolution of 80 μm per tube can be obtained. A schematic view of an MDT chamber is given in fig. 2.14.

The MDTs in the barrel are rectangular in shape, while they have a wedge-shape in the endcap. Their lengths vary from 940 mm to 4990 mm. [6].

Cathode Strip Chambers

The Cathode Strip Chambers (CSC) are used in the innermost ring of the inner station of the endcap, where particle fluxes are highest. They cover the range $2.0 < |\eta| < 2.7$. The large counting rates in this region make the MDTs with their large volume and large operating pressure unsuitable. The maximum drift-time of the CSC is about 30 ns, while the maximum drift-time of the MDT is about 480 ns. The CSC are multiwire proportional chambers with wires as anode and segmented strips as cathodes. The distance between the wires is 2.54 mm as is the space between the cathode and the anode. The cathode readout pitch is 5.08 mm.

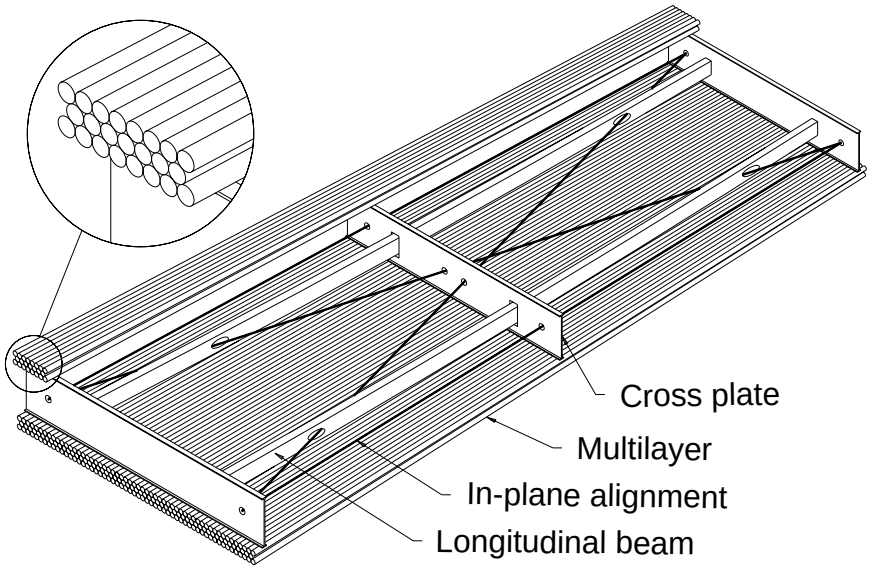

Figure 2.14: *Schematic overview of a MDT chamber with 2 multi-layers, each consisting of 3 rows of staggered tubes.*

Muon trigger system

The B physics program of ATLAS requires a trigger muon with $p_T > 6$ (or 8) GeV. The trigger must be able to distinguish between different bunch-crossings which occur every 25 ns at the LHC. The MDTs and CSCs are not fast enough. Specially developed muon trigger chambers have been constructed; RPCs for the barrel and TGCs for the endcap. A basic RPC (Resistive Plate Chamber) unit consist of two parallel resistive plates, 2 mm apart. The gap is filled with a gas mixture. The signal is read out via capacitive coupling by metal strips on both sides of the detector. One chamber has two orthogonal strips, one for the η direction and one for the ϕ direction. The RPCs have a typical space-time resolution of 1 cm $\times$ 1 ns.

TGCs (Thin Gap Chambers) are constructed in a similar way as the CSCs. However, the distance between the anodes wires (1.8 mm) is larger than the anode-cathode distance (1.4 mm). The combination with a special gas and the short distances results in such a configuration that 99 % of all the signals fall within the 25 ns window. Using the RPCs and TGCs a LVL1 muon trigger signal can be constructed. This will be discussed in section 2.3.1.
The production of the tracking chambers is well underway. The accuracy of the position of the wires is within 5 μm. In fig. 2.15 the dependency of the resolution on the high voltage of the wires is plotted.

A status report given at October 2002 [41] stated that 50 % of the tubes which are needed were produced, and about 14 % of the full MDT chambers (filled with gas) were assembled. It is foreseen that in 2004-2005 the different production sites finish producing their MDT chambers.

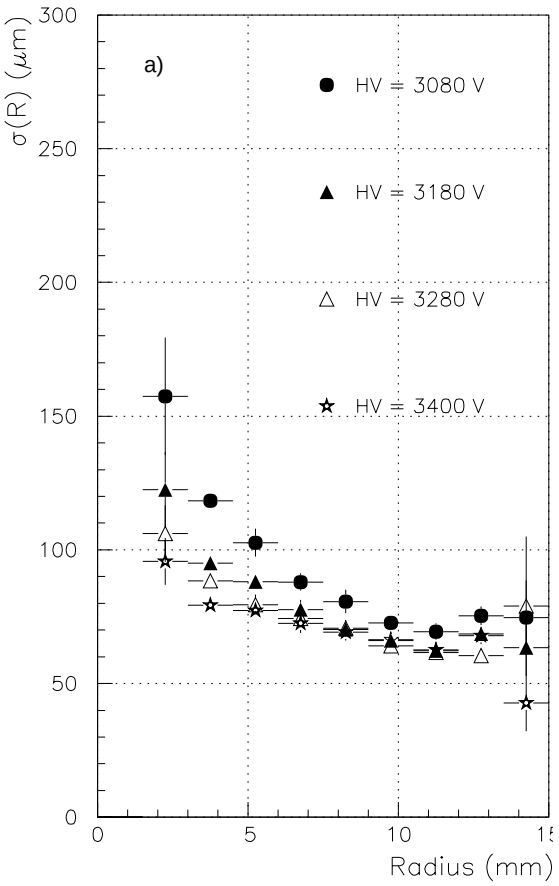

Figure 2.15: *Average resolution as a function of the drift path for several high voltages applied to the tube wires. Figure taken from [40].*

2.3 Trigger/DAQ System of ATLAS

A large number of particles (on the order of a few thousand) is produced in a proton-proton collision at a centre-of-momentum energy of $\sqrt{14}$ TeV. The majority of these particles form a background to the interesting physics. A trigger is needed to distinguish the interesting physics from the minimum bias background. A three-stage trigger was developed for the ATLAS experiment. Each stage refines previous decisions and, when necessary, applies additional criteria. It is paramount that the efficiency for the physics under study remains high. The trigger system is developed with the highest efficiency in mind, while keeping flexibility. An overview of the ATLAS trigger system is given in fig. 2.16.

The first Level trigger (LVL1) reduces the rate of interesting events from the 40 MHz bunch-crossing frequency (interaction rate $\sim 10^9$ Hz) to less than 100 kHz. The first level trigger will be described in section 2.3.1. The second level trigger (LVL2) reduces this rate to less than $\sim$ 3 kHz. More refined algorithms can be applied at LVL2 since more time is available before a decision must be reached. Subsequently, the third stage of the trigger called the Event Filter (EF) reduces the rate from $\sim$ 1 kHz to $\sim$ 200 Hz. The algorithms for

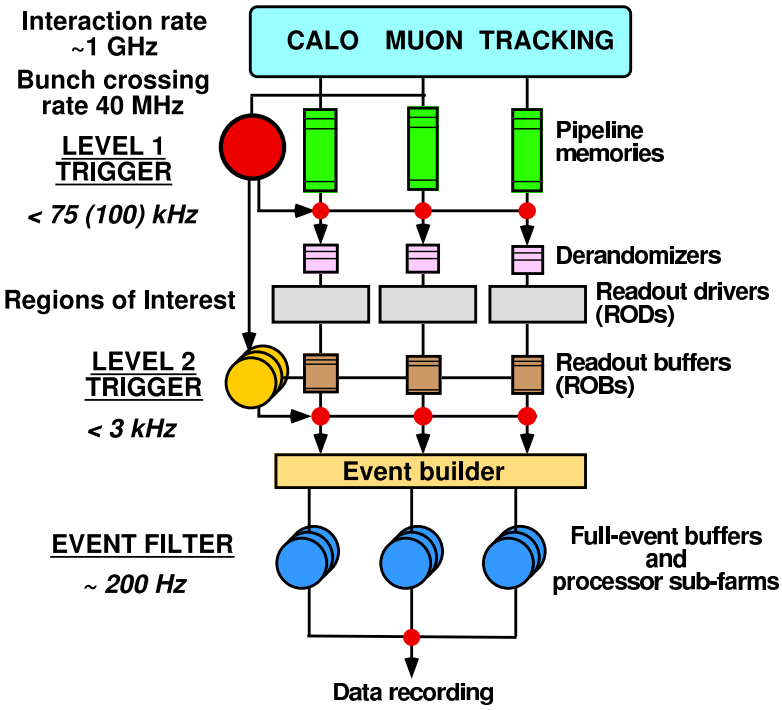

Figure 2.16: *Overview of the ATLAS trigger system.*

the second level trigger and Event Filter are described in section 2.3.2, the implementations are discussed in 2.3.3. Not only the high rates form a challenge to the trigger system, also the amount of data that has to be processed is large. After completion of the last stage 10-100 MB/s will be written to permanent storage.

During the LVL1 trigger decision, all detector data is held in pipeline memories. When the LVL1 accepts an event, digitised data are transferred via derandomizers (necessary to average out peak data volume transfers) and via RODs (ReadOut Drivers) to the ROBs (ReadOut Buffers). The RODs multiplex various signals from the front-end electronics of the detectors, can format the data and add LVL1 ID number and bunch-crossing information. The data is sent from the RODs to the ROBs via high bandwidth links. The ROBs hold the data from an LVL1 accepted event until a LVL2 decision has been reached. In case of a LVL2 reject decision, the appropriate event fragments in the ROBs are deleted. In case of a LVL2 accept decision the event fragments are sent via the event builder to the Event Filter. The processors that have to produce the LVL1 decision have to be fast, the latency of the LVL1 must not exceed 2 μs. The electronics which transfer data to the RODs must also be fast. The electronics in both cases is custom-made and makes use of FGPA-based processors.

Region of Interest (RoI)

An important concept for the LVL1 and LVL2 system of ATLAS is the so-called Region of Interest or "RoI". It is an area in the detector with a certain range in ϕ and η ($\Delta\phi \times$

$\Delta\eta$), where particles from a possible interesting event are detected. Usually, the LVL1 trigger sends RoI information to the LVL2 trigger. The first level trigger optionally can also generate lower threshold RoIs which are not directly used for a trigger decision but can "guide" a specific decision. The LVL2 trigger subsequently uses RoI information by processing data from ROBs that lie within the RoI or RoIs. The LVL2 system can also request data from other parts of the detector than defined in the RoI when it needs to refine its decision. Four types of RoIs are distinguished at LVL1: electromagnetic RoIs, single hadron/tau RoIs, jet RoIs and muon RoIs. The range of RoIs for LVL1 and LVL2 are constrained in η. Muon RoIs have $|\eta| < 2.4$, electromagnetic and single hadron/tau RoIs have $|\eta| < 2.5$ and jet RoIs have $|\eta| < 3.2$. An example of two electromagnetic RoIs and one muon RoI is shown in fig. 2.17.

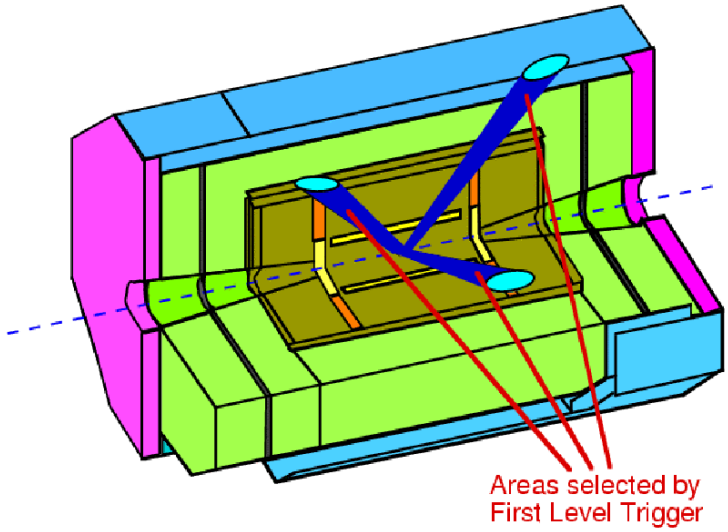

Figure 2.17: *Two electromagnetic RoIs and one muon RoI in the ATLAS detector.*

2.3.1 First level trigger

The LVL1 trigger uses data from the calorimeter (section 2.2.2) and muon detector (section 2.2.3) to make decisions. A functional block diagram of the LVL1 trigger system is shown in fig. 2.18. At the highest level, three main parts can be distinguished: the calorimeter trigger, the muon trigger and the Central Trigger Processor (CTP). Trigger decisions are distributed to the front-end electronics via the Timing, Trigger and Control (TTC) system.

Trigger cell towers with a typical granularity of $\Delta\phi \times \Delta\eta = 0.1 \times 0.1$ provide the input to the calorimeter trigger. The front-end preprocessor block in fig. 2.18 determines the energies deposited in the trigger cells for each bunch-crossing. This information is used as input to the cluster processor and the Jet/energy sum processor. On the former, a high p_T e/γ and a hadron/tau trigger algorithm are implemented. On the latter, a jet trigger algorithm is implemented as well as a missing E_T trigger algorithm. The muon trigger receives data from either the barrel muon trigger or the endcap muon trigger. The

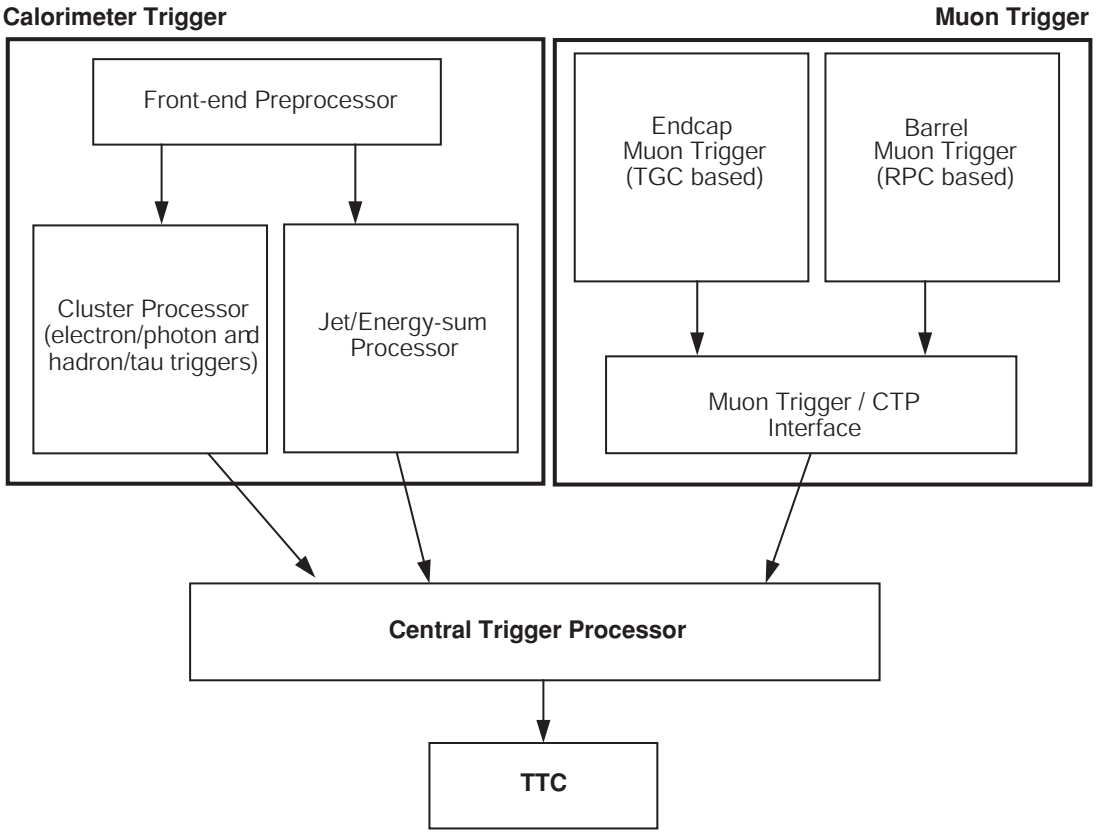

Figure 2.18: *Functional block diagram of the LVL1 trigger system.*

algorithms are described in more detail in [42]. For the LVL1 trigger the following trigger "objects" can be distinguished:

- **electron/photon trigger.** A region of 2 × 2 EM trigger cells is used to identify RoI candidates, see fig. 2.19. The energy in the 2 × 2 cluster is determined by taking the most energetic sum of four possible 2-tower clusters, marked in the figure by "Vertical" and "Horizontal sums". Studies show that a 2-tower cluster (as opposed to 3 or 4 tower clusters) produces the lowest trigger rate, due to the effects of pile-up. A further requirement is that the total energy in the 12 surrounding EM cells should be below a threshold. Furthermore, the total deposited energy in the 4 x 4 hadronic cells behind the RoI region should also be below a threshold.

- **single hadron/tau trigger.** The single hadron tau trigger looks for a localised cluster of high E_T in 2 × 2 trigger cells in the electromagnetic calorimeter and in 2 × 2 trigger cells in the hadronic calorimeter. The sum of these two should be above a given threshold, while the summed energy of all the other possible 2 × 2 configurations in a 4 × 4 space should be less.

- **jet trigger.** A cluster with a size of $\Delta\phi \times \Delta\eta = 0.4 \times 0.4$ is used to identify the candidate jet RoIs. A trigger cluster, which can have sizes of $\Delta\phi \times \Delta\eta = 0.4 \times 0.4$,

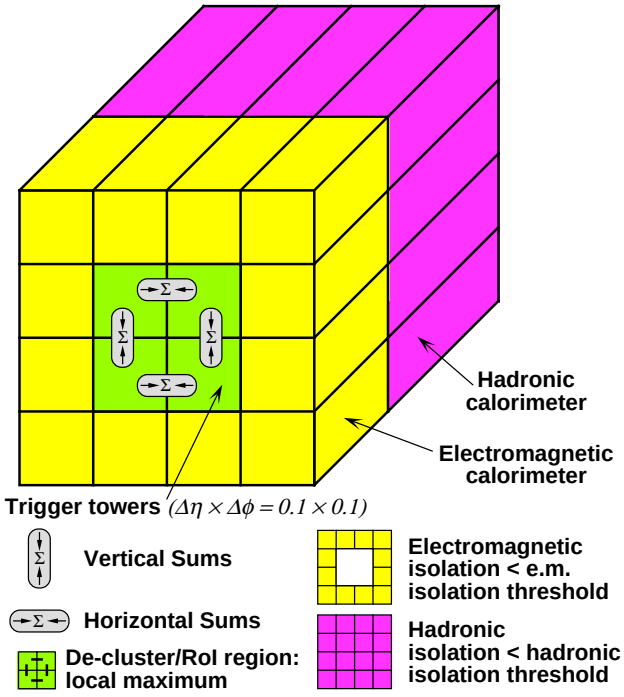

Figure 2.19: *Electron/photon trigger algorithm.*

0.6 × 0.6 or 0.8 × 0.8, is used to determine the jet E_T. The RoI cluster must be a local E_T maximum and it must pass a given E_T threshold in order to pass the jet trigger. For the electromagnetic trigger, the hadron tau trigger and the jet trigger, eight separate thresholds are foreseen.

- **missing E_T trigger.** The total scalar E_T value is calculated by summing the E_T values of all the jet trigger clusters and forward calorimeters. Vector energy components are calculated from the E_T values using look-up tables to multiply by $\sin(\phi)$ or $\cos(\phi)$. After summation of E_x and E_y separately, a look-up table is used to compute the scalar missing E_T value.

- **muon trigger.** The muon trigger scheme is shown in fig. 2.20. The first level trigger for the muon barrel uses three stations of RPCs. The first two are located on both sides of the middle layer of MDT chambers. The third RPC is located at the inside of the outer layer of MDT chambers. One RPC station is made of two doublets, each one in turn consisting of two planes of orthogonal strips.

  The B physics muon trigger (low p_T muon) requires a coincidence in both RPC1 and RPC2 stations [43]. In each station, the coincidence requires hit patterns on both bending (η) and non-bending (ϕ) projections. If a track hit is generated in the RPC2 doublet (or pivot plane), a search for the same track is performed in the RPC1 doublet, within a window with a centre that is defined by the line of conjunction of the hit in the pivot plane with the interaction point. A high p_T trigger ($p_T > 20$ GeV) requires an additional coincidence in RPC3. A similar scheme applies to the TGCs, as illustrated in fig. 2.20. The η and ϕ information is combined to give an RoI of $\sim$ 0.1 × 0.1.

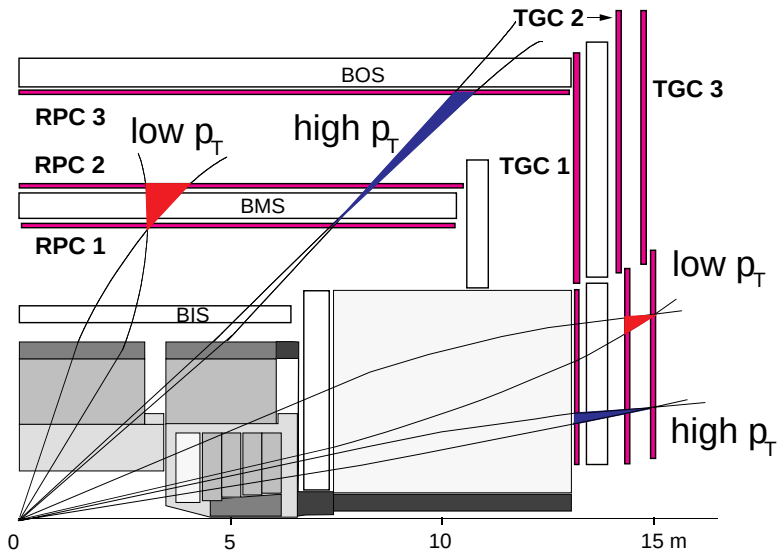

Figure 2.20: *The LVL1 muon trigger scheme.*

- **CTP and TTC.** The rôle of the CTP is to combine the information for the different triggers and their RoI information and form an accept or reject decision. The combination of these triggers is laid down in so-called "trigger menus". These will be discussed in the next section. Furthermore, the CTP can be programmed to downscale certain high-rate trigger menu entries, for instance for collection of data on specific QCD processes or for calibration of the detector. Among other tasks, the TTC is responsible for distributing the LHC clock and the LVL1 trigger decisions to the front-end systems. The TTC receives the LVL1 decisions from the CTP.

Trigger menus

The triggers discussed in the previous section are combined in trigger menus. Each entry in the menu is a combination of trigger objects. A trigger object is one the triggers defined above including the RoI and its threshold. As mentioned before, each trigger object can have several thresholds. The August 2002 LVL1 trigger menus are given in table 2.2.

The structure of the trigger objects is as follows: The (optional) first number is the number of RoIs, the letters signify the nature of the RoI, MU for muon RoI, EM for an electron/photon RoI, J for a jet RoI, TAU for a single hadron tau RoI and XE for a missing energy trigger. After that the threshold (in GeV) is given. In a few cases an "I" follows the threshold number, signalling that an isolation cut is required. For instance, item number 5 in table 2.2(a), requires 2 isolated electromagnetic RoIs of at least 20 GeV. The frequencies add up to a total of about 40 kHz.

2.3.2 High level trigger algorithms

The LVL2 trigger and the Event Filter are collectively known as the High Level Trigger or HLT. As in the LVL1, trigger menus are used to make a decision about an event. In the LVL2 stage of the trigger, first the LVL1 RoIs are confirmed by applying a more refined

trigger	freq [Hz]
MU20	3900
MU20 × 2	300
MU6 × 2	3000
EM30I	24300
EM20I × 2	4900
J290 × (1,2,3)	47, 49, 2
J130 × (3,4,5)	130, 8, 1
J90 × (4,5,6)	141, 15, 5
J290 + J130 × (2,3,4)	52, 8, 1
J290 + J90 × (3,4)	27, 5
J290 × 2 + J90 × (2,3)	9, 1
TAU60 × (1,2,3) + XE60	910, 48, 3
J100 × (1,2,3,4) + XE100	166, 54, 10, 10
J100 × 4 + TAU60 × (1,2,3) + XE60	2, 2, 1.2
J100 × 5 + TAU60 × (1,2,3) + XE60	2.2, 2.2, 1.4
J100 × (1,2,3,4) + TAU60 + XE100	142, 74, 10, 16
J100 × (1,2,3,4) + TAU60 × 2 + XE100	10, 10, 10, 9

(a)

trigger	freq [Hz]
MU6	23000
MU6 × 2	1000
MU6 + EM15I × (1,2)	60, 2.3
MU6 + EM20I	24
MU6 + J180	1.3
MU6 + J75 × 3	2.8
MU6 + J55 × 4	2.8
EM20I	11500
EM15I × 2	1600
EM20I + J55 × 4	68
EM15I × 2 + J55 × 4	180
J180 × (1,2,3)	25, 42, 4
J75 × (3,4,5)	107, 10, 1
J55 × (4,5,6)	131, 17, 3
J180 + J75 × (2,3,4)	63, 15, 7
J180 + J55 × (3,4,5)	28, 7, 2
J180 × 2 + J55 × (2,3)	8, 3
TAU20 × (1,2,3,4,5)	1340, 320, 110, 4, 2
J50 × (1,2,3) + XE50	148, 31, 16
J50 × 4 + TAU20 × (1,2,3) + XE30	16, 7, 7
J50 × 5 + TAU20 × (1,2) + XE30	3, 2
J50 × (1,2,3,4) + TAU20 + XE50	100, 45, 45, 4
J50 × (1,2,3,4) + TAU20 × 2 + XE50	18, 8, 4, 2
J50 × (1,2,3,4,5) + TAU20 × 3 + XE50	2, 1, 2, 2, 1

(b)

Table 2.2: *High (a) and low (b) luminosity LVL1 trigger menu.*

algorithm on the data associated with the RoIs. After the confirmation of a LVL1 RoI, data from the SCT, Pixel detector, TRT or calorimeters (for muon RoIs), associated with the RoI will be requested and analysed. All data from the Inner Detector may be requested by the B-physics trigger. The event is accepted or rejected on the basis of the LVL2 trigger menu.

The LVL2 trigger is foreseen to have an average decision time of $\sim$ 10 ms. The Event Filter has an average decision time of $\sim$ 1 s. The only constraints on the algorithms running at either LVL2 or Event Filter, are formed by the smaller decision time of the LVL2 trigger and the fact that the Event Filter uses the full event information, while the LVL2 trigger uses RoI data. A trigger decision is reached by using sequences of LVL2 or Event Filter algorithms. In this section, various trigger algorithms for the HLT will briefly be outlined.

- **HLT photon/gamma triggers.** For these triggers, first a common e/γ selection is made based on shower shape variables, e.g. fractions of energy within and outside a certain η-ϕ range. The photon trigger is constructed by using the same variables as in the common e/γ selection but with tighter cuts, as well as using additional features,

such as the shower width in η, to reject jets. The efficiency is $\sim$ 97(94) % after the LVL2 and $\sim$ 83(81) % after the Event Filter [44] for high (low) luminosity. For the electron trigger, a search in the TRT and the SCT plus Pixel detector (within the RoI) is performed separately. Using a histogramming method to select the best hits, tracks are fitted to these hits. Furthermore, signals that pass the higher of the two readout thresholds in the TRT detector are likely to be hits from transition radiation caused by an electron. After combining the information from the calorimeters with the Inner Detector, the efficiency is $\sim$ 85(88) % after LVL2 and 78(80) % after the Event Filter for high (low) luminosity.

- **HLT missing E_T, jet and tau triggers.** Missing E_T can be corrected at LVL2 with, for instance, high energetic muons. It is used in conjunction with lepton or jet trigger items. For jets, first at LVL2 all the trigger tower cells in a window of $\Delta\phi \times \Delta\eta = 1.0 \times 1.0$ in the LVL1 RoI direction are summed. A jet with a cone radius of ΔR=0.4 is subsequently reconstructed within the window. In this way, the accuracy of the jets found by the LVL1 trigger is improved. The efficiency after LVL2 is about 90 %. For the Event Filter, the same jet-finding algorithms are used but instead of being guided by an LVL1 RoI, the whole η-ϕ range is searched. The tau trigger is used in conjunction with the other triggers. It requires a narrow isolated jet with 1 to 3 charged tracks. The efficiency after LVL2 is close to 60 %, the possible additional rate reduction by the Event Filter has not been studied.

- **HLT muon triggers.** LVL1 muon triggers are confirmed first using the data from the precision muon chambers and are then combined with information from the SCT, Pixel and TRT detector. The algorithm used in the second level trigger (the μfast algorithm) takes about 0.2 ms [45] on a 1 GHz Linux system for reconstructing tracks in the muon chambers. The track parameters are used to define search areas of $\Delta\eta \times \Delta\phi$=0.2 $\times$ 0.2 in the Inner Detector. Track reconstruction in that area takes about 0.2-0.3 ms. The track with the lowest χ^2 is selected.

B physics selection algorithms

As mentioned before, the threshold for a trigger muon was raised from p_T >6 (MU6) to p_T >8 (MU8), since the initial low luminosity of $1 \cdot 10^{-33}$ cm^{-2} s^{-1} has increased to $2 \cdot 10^{-33}$ cm^{-2} s^{-1}. The baseline B-physics trigger strategy shown in table 2.3 consists of a single or di-muon trigger at LVL1, confirmation at LVL2 and if possible, additional hadron triggers and vertex finding at LVL2 and Event filter. The first item in table 2.3 is a di-muon trigger in which each muon is required to have a $p_T >$ 6 GeV. Recent studies have shown that the minimum p_T with which muons can be triggered in the muon system is $\sim$ 5 GeV for the barrel and $\sim$ 3 GeV for the endcap [47]. For the single muon trigger (the second item in table 2.3) the muon is first confirmed at LVL2. A "full scan" may follow : the TRT detector or the Pixel/SCT detectors are searched for tracks candidates coming from the decay of the other B meson. Subsequently, tracks from the TRT can combined with tracks segments from the Pixel/SCT detectors. Alternatively, tracks from the SCT/Pixel detector from the

LVL1	LVL2	Event Filter
MU6 + MU6	mu6 + mu6	J/ψ(mu6,mu6)vtx B(mu6,mu6)vtx Bd(K*(h1.5,h1.5),mu6,mu6)vtx
MU8[6]	mu8[6] + Bd(pi4,pi4) mu8[6] + Ds(phi(K1.5,K1.5,pi1.5) mu8[6] + J/ψ(e,e)vtx	mu8[6] + Bd(pi4,pi4)vtx Ds(phi(K1.5,K1.5,pi1.5)vtx J/ψ(e,e)vtx
MU8[6] + EM5	mu8[6] + J/ψ(e5,e1.5)vtx	J/ψ(e5,e1.5)vtx

Table 2.3: *Trigger menu for a B-physics trigger. The EM5 trigger item may be a secondary (non-trigger) RoI. J/ψ(mu6,mu6) represents an invariant mass criterion for the J/ψ and "vtx" represents a secondary vertex requirement. Information taken from [46].*

"full scan" can be combined with track segments from the TRT detector. Preliminary [46] studies have been carried out for the case of $B \rightarrow J/\psi(e^+e^+)\mu$. It was shown that electrons with a p_T as low as ~ 1 GeV could be reconstructed efficiently by a TRT track search and subsequent combination with SCT information.

Studies have been performed on guiding the LVL2 decision with the help of a secondary LVL1 trigger item (EM5). This is shown in the third entry in table 2.3.

At the Event Filter or offline, a secondary vertex can be fitted and an invariant mass cut can be placed on the J/ψ. Criteria for the reconstruction of $J/\psi \rightarrow e^+e^-$ [47] which also can serve as a benchmark for $J/\psi \rightarrow \mu^+\mu^-$, include:

- Event Filter: Invariant mass cut in the window 2.62 to 3.34 GeV. Offline: cut around the J/ψ mass of $[-5\sigma, 3\sigma], \sigma = 53$ MeV.
- Event Filter: the vertex fit must satisfy $\chi^2/N_{d.o.f.} < 8.0$. Offline: the vertex fit must satisfy $\chi^2/N_{d.o.f.} < 6.0$.
- Event Filter: Reconstructed transverse decay length $L_{xy}(J/\psi) > 220$ μm. Offline: $L_{xy}(J/\psi) > 250$ μm.

These criteria will be used in a study of the decay $B_c \rightarrow J/\psi(l^+l^-)l\nu_l$ (with $l = e, \mu$) in chapter 7.

2.3.3 HLT/DAQ architectural layout

In this section the architectural layout of the HLT/DAQ system is presented, as well as a description of the hardware components that are foreseen. The HLT/DAQ system is sketched in fig 2.21. The RoI builder (RoIB) combines fragments of RoI information from the LVL1 processor into one event record, which is passed to the supervisor (LVL2S). The supervisor assigns each event to one of the LVL2 processors (in the L2 farm). The LVL2 processor requests the data (via the DF(dataflow) network) from the relevant ROBs and analyses the data. The trigger decision is returned to the supervisor. Decisions are sent

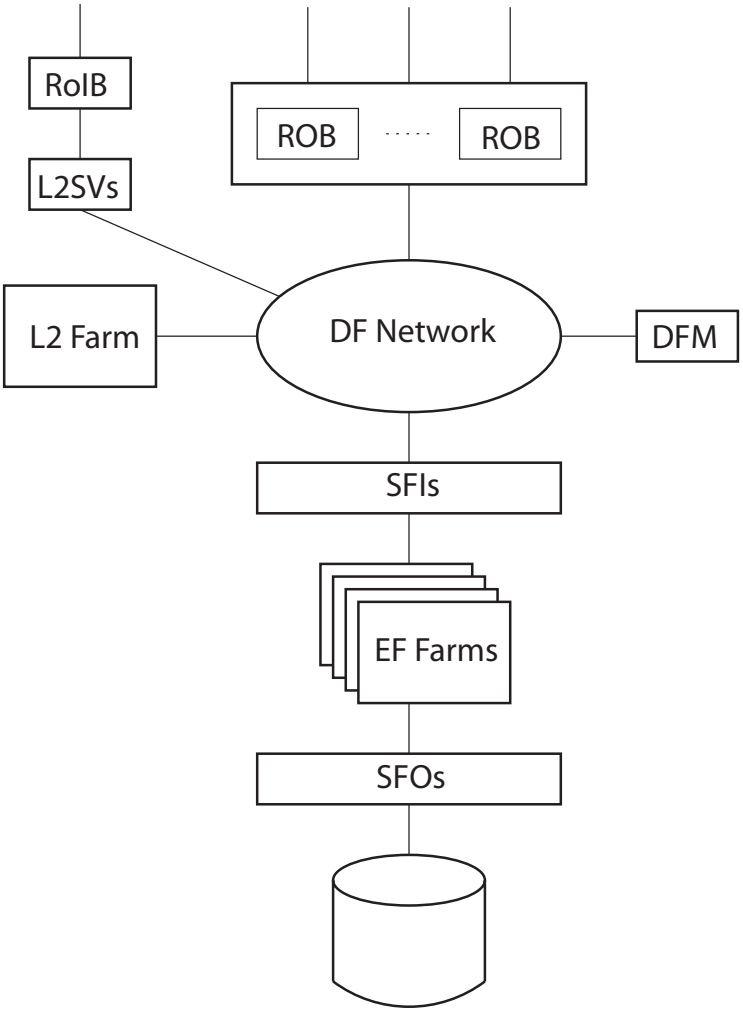

Figure 2.21: *The architecture of the High Level Trigger/Data Acquisition system. Refer to the text for details on the various components.*

to the Data Flow Manager (DFM), rejects give rise to clear commands for the ROBs, accepts give rise to event building requests. The Sub-Farm Interfaces (SFIs) send messages indicating completion of event building to the DFM, these messages also give rise to clear commands. Groups of about 300 clear commands are multi-cast by the DFMs to the ROBs. The SFIs then send the full events to the Event Filter (EF). Events selected by the Event Filter are sent to permanent storage via the Sub-Farm Output (SFO).

The main hardware components that will be used in the HLT/DAQ system will be discussed next.

- **LVL2 Supervisor and RoI Builder.** A RoI builder has been designed to combine the LVL1 RoI information from different data streams and forward the data to a RoI processor. The prototype handles 12 input data streams. It can service 2 RoI processors and is data-driven and scalable. A small test system comprising an RoI builder and a small supervisor farm showed that the requirements for the LVL2 trigger,

i.e. up to a trigger rate of 100 kHz, can be met.

- **Switches and Links.** In order to study different network implementations, several test-beds were used. The test-beds varied in size from a few to $\sim$ 100 nodes. Ethernet (Fast and Gigabit), ATM and SCI technologies were tested. Since Gigabit ethernet offers adequate performance and is already available at reasonable prices, this technology is currently foreseen as the final choice. Concentrator switches will be introduced at various places in the HLT/DAQ system, in order to reduce the number of ports on central switches.

- **LVL2 Farm.** Commercially available rack-mounted Dual CPU systems running Linux will be used for the LVL2 farm. The current clock speed of processors ($\sim$ 2.5 GHz) is well suited for the required performance. If Moore's law holds, processors running at a clock speed of 8 GHz or more can be expected in 2007. The processors have two major tasks: retrieving data and analysing events. The former task has been tested on a small-scale test-bed, the latter task is being studied by timing LVL2 algorithms.

- **ROBs.** ROBs (Read-Out-Buffers) are functional units, which hold the data from the LVL1 trigger until a LVL2 accept or reject has been received. On an accept decision, the data is sent on to the Event Filter, otherwise the data is deleted. Thus the input side of the ROBs must cope with the input rate and data volume of the events accepted by the LVL1 trigger. Furthermore, the ROB must handle and process requests for data coming from the LVL2 processors. This "bookkeeping" of requests, incoming events and deleted/sent events is done with a microprocessor. In the implementation of the ROBs, the output part, i.e. the component that sends data to the LVL2 network or the EF, may be separated from the input part. The former is then referred to as a ROBOut and the latter as a ROBIn. This separation has the advantage that multiple ROBIns can connect to one ROBOut, the latter forming a concentrator, so that the amount of links to the central switch is reduced. For more details on a test implementation of a ROB, i.e a system with both ROBIns and a ROBOut, see chapter 3.

- **Data flow Manager.** The DFM is implemented using rack mounted systems running Linux as well. Multiple DFMs may be required if the HLT/DAQ system is partitioned in several sub-systems. DFMs receive input from the LVL2 supervisor and communicate with the SFIs and ROBs.

- **Sub-Farm Interface.** THE SFIs are rack-mounted (Dual CPU) systems running Linux, which have a second Gigabit ethernet interface that connects them to the Event Filter network.

- **EF Farms.** An Event Filter farm is a small network of Event Filter nodes, a small set of SFIs (possibly one), and SFOs. Such a modular setup allows maximum flexibility in choosing the number of Event Filter nodes for each farm. Due to the large computing performance required (and the relatively small I/O demand), servers which house a

few hundred processors combined with local switches may provide a better alternative than the baseline rack-mounted systems.

- **Sub-Farm Output and Mass storage.** The SFOs take accepted events from the Event Filter and pass them to mass storage. Currently it is foreseen that the SFOs will be normal PCs which write the accepted events to disk. A different process is assumed to fetch these events and pass them to the mass storage. The SFOs also provide buffering if the network connection to the mass storage is not available.

Chapter 3

A prototype ROBIn for ATLAS

In this chapter the design and implementation of a prototype ROBIn as well as results of test measurements are discussed. This chapter is based on an ATLAS note [48], co-authored by the author of this thesis. As explained in section 2.3.3, the ROB functionality comprises buffers that hold the data from the LVL1 trigger until an accept or reject decision from the LVL2 trigger has been received. An accept decision results in data being sent to the Event Filter, while a reject decision causes the event data to be deleted. Thus the key requirement for the ROBIn is to be able to cope with the data input rate of the LVL1, while at the same time handling requests for data and decisions from the LVL2 trigger. The maximum LVL1 trigger rate is foreseen to be 100 kHz, at an average event fragment size of $\sim$ 1 kByte. The CRUSH (Compact ROBIn Using a SHARC) is a test implementation of the ROBIn, developed at NIKHEF. In section 3.1 the CRUSH is described, both in terms of functionality and implementation. The software used for the performance measurements is discussed in section 3.1.1. Subsequently, in section 3.2.1 the test setup for stand-alone measurements is described and in section 3.2.2 results in terms of rates and data volumes of the CRUSH are given. In section 3.3.1 the setup of a CRUSH placed in a ROB complex, i.e in a small system of ROBIns and a ROBOut, is described. Measurement results for the ROB complex are given in section 3.3.2. Finally, conclusions are drawn in section 3.4

3.1 Design and implementation

The CRUSH module is a test implementation of the ATLAS ROBIn. It provides automatic hardware controlled storage of event fragments, entering from an ROL (Read-Out Link) in a buffer, while some relevant event information (" summary information") is copied to a so-called Paged FIFO. The summary information consists of a few words per event fragment, e. g. Begin-Of-Fragment, Event-ID, End-Of-Fragment. Also the start position of the event fragment in the buffer is written to the Paged FIFO, from where the on-board processor can read it. The event fragments are written sequentially into the buffer memory. Event fragments are written to the start of the buffer memory once the end is reached. The on-board processor is responsible for preventing overwriting of data by moving data out of the buffer memory if necessary. A block scheme of the CRUSH is presented in fig. 3.1, the card itself is shown in fig. 3.2.
The on-board processor is an ADSP 21060L (SHARC) processor from Analog Devices [49]

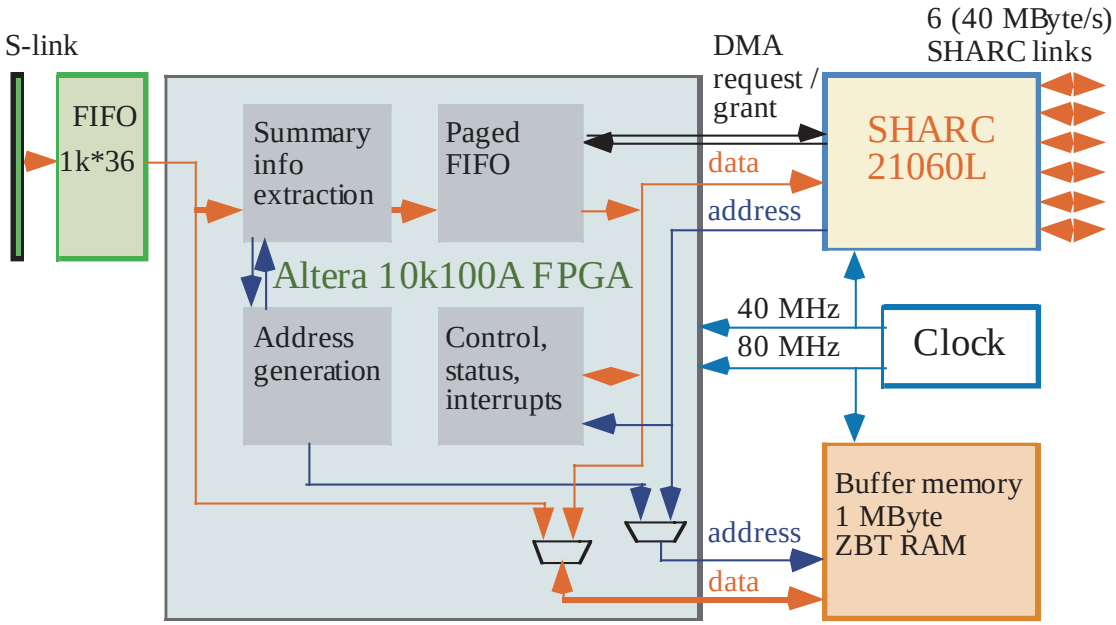

Figure 3.1: *Block diagram of the CRUSH module. Please refer to the text for details*

with a clock frequency of 40 MHz. Its main features are its on-chip memory (512 kBytes), 6 independently operating communication links (40 MByte/s each) with hardware handshaking and 10 on-chip DMA controllers for transferring data via the links as well as between the external memory bus of the SHARC and its internal memory. Its DMA capabilities make the SHARC well suited for handling the data and message streams present in a ROB, as multi-channel communication can take place in parallel with buffer management and data processing operations.

Input data from the S-link (coming from the RODs) is inspected in an FPGA (Field Programmable Gate Array). The FPGA [1] is an Altera 10k100A [50] clocked with the same clock as the SHARC processor. The data is transferred from the S-link interface into the FPGA via an intermediate FIFO. This decoupling is needed, since the clocks of the S-link interface and the FPGA are not synchronised. The FPGA compares pre-programmed 'Begin-Of-Fragment' and 'End-Of-Fragment' masks with the input data stream. If a double 'Begin-Of-Fragment' or 'End-Of-Fragment' is found an error is generated, otherwise the data in between is transferred into the buffer memory. The event summary information (including the LVL1 ID) as well as the address in the buffer memory where the data can be found is transferred to the SHARC processor.

The buffer memory is implemented with 1 MByte of ZBT ('Zero-Bus-Turnaround') RAM. This type of memory has the advantage that it can operate without wait cycles, also when a read cycle is immediately followed by a write cycle or vice versa. The buffer memory is clocked at 80 MHz, allowing an access from the SHARC and an access from the S-link FIFO every 25 ns. Interfacing to (the buffer memory) in the FPGA is strongly pipelined. This is not a problem for the S-link, from which up to 160 MByte/s can be transferred into the memory. However due to the pipe-lining, the SHARC requires four system clock cycles

[1] A Field Programmable Gate Array is a programmable integrated circuit, which is well suited (fast) to perform bitwise operations such as bit-masking and bit-shifting.

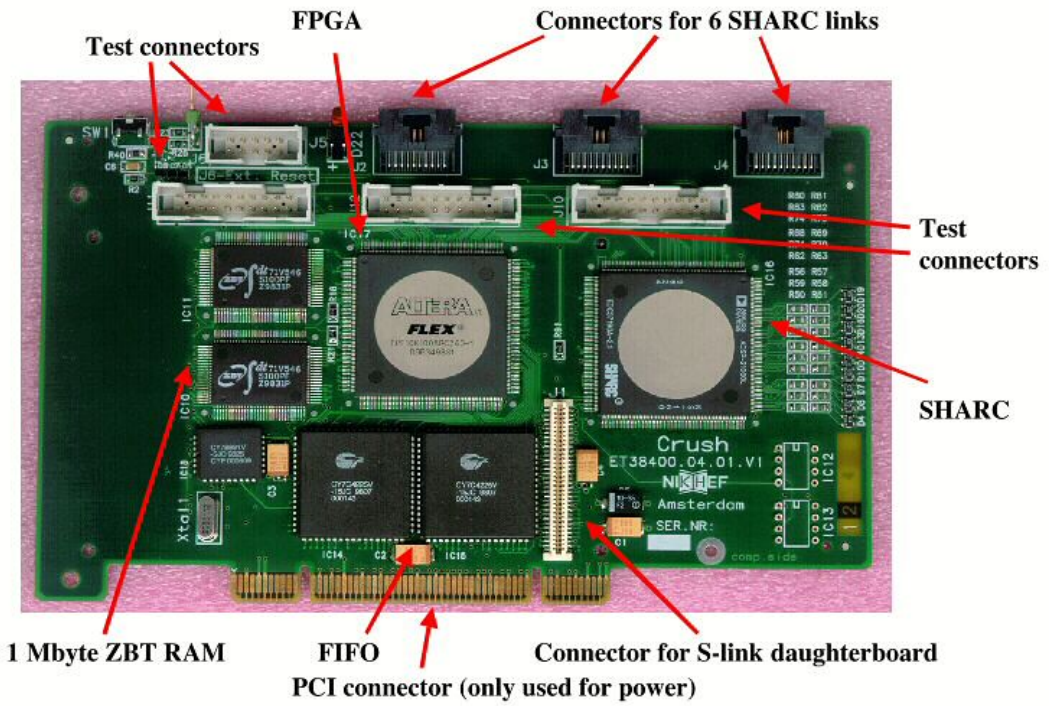

Figure 3.2: *The CRUSH board*

to write or read data in or out of the buffer memory, so the transfer speed from buffer memory to SHARC is at maximum 40 MByte/s. This is equal to the bandwidth of one of the SHARC links.
Several functions of the FPGA are controlled by the on-board processor. By means of registers in the FPGA, the bit patterns used for recognising 'Begin-Of-Fragment' and 'End-Of-Fragment'-words and the amount of words that have to be copied from the event buffer memory to the Paged FIFO, can be set.

The CRUSH board has a PCI board form factor but the CRUSH only takes its power from the PCI-bus. Most components are 3.3 V components, the power dissipation of the complete board (without S-link daughter board[2]) is about 2-3 W. The on-board SHARC processor is booted via its Link Port 4; all 6 SHARC Link Ports are available on connectors on the board's edge. A more detailed description of the design of the CRUSH module can be found in [51].

3.1.1 Software

All actions are triggered by I/O polling in one big loop, introducing potentially some latency in the actions, but avoiding any interrupt routine overhead. All input and output by the SHARC is performed under DMA control. All input and output streams are buffered in SHARC on-chip memory.

Fig. 3.3 shows a schematic view of the software used for the performance measurements

[2]this is a small piggy back card plugged onto the S-link connector handling the S-link protocol.

of the CRUSH. The polling loop is indicated by the arrows connecting the various blocks. Arrows entering from the left or pointing to the left indicate data flowing into or out of the SHARC. Blocks labelled with ".... input " indicate places in the code where the status of DMA transfers for input of data from either the paged FIFO of the FPGA (holding the summary information or"Event Info data") or from a SHARC link is examined and where new DMA transfers for input of data are initiated. Event fragment data (" RoID" data for requested RoI data or "EBD" data for accepted event data to be sent to the Event Builder) is transferred with two DMA transfers: first the data is transferred from the ZBT RAM to a buffer in the internal memory of the SHARC (the bandwidth for these transfers is 40 MByte/s), in the second step the data is transferred via one of the SHARC links.
The following types of processing can be distinguished:

- 1. "Event Info input" processing consists of copying event summary information to a list ordered according to event ID, after checking whether the location in the list has not already been taken, followed by checking whether the buffer memory is (almost) full. Errors lead to a halt in the programs as they should not occur during testing.

- 2. RoI request and LVL2 decision block input handling ("RoIR / T2DR input handling") consists of checking whether a RoI request or a decision record is arriving, starting a DMA for transfer of the remaining information into the "RoIR" buffer or the "T2DR" buffer and detection of the end of transfers and updating of the appropriate buffer pointers.

- 3. RoI Request processing ("RoIR processing / RoID building") consists of finding the event summary information for the event ID specified in the RoI request message, creation of a header (7 words) in the "RoID/ EBD buffer" and of starting a DMA transfer from the event buffer memory to the "RoID/ EBD buffer" in the SHARC internal memory. This is done only if there is an empty slot in the "RoID/ EBD buffer" and if a DMA transfer is possible.

- 4. LVL2 Decision Record processing ("T2DR processing / EBD building"). For each decision in the decision record, the event summary information with the corresponding event ID is looked up. For a reject, the occupied event fragment buffer space and the entry in the event summary list for the corresponding event ID is marked as being free. For an accept, a header (7 words) is created in the "RoID/ EBD buffer", a DMA transfer is started from the event buffer memory to the "RoID/ EBD buffer" in the SHARC internal memory and the entry in the event summary list for the corresponding event ID is marked as being free. This is done only if there is an empty slot in the "RoID/ EBD buffer" and if a DMA transfer is possible. After handling up to 10 decisions "T2DR processing / EBD building" stops, unless all decisions in the record have been processed. In that case a contiguous block of buffer memory, up to the first event fragment not marked as being free, is added to the free buffer memory space.

- 5. "EBD output handling" checks for the end of a DMA transfer of a fragment of an accepted event from the buffer memory to the "RoID/ EBD buffer": if the transfer is finished the buffer space used is marked as being free.

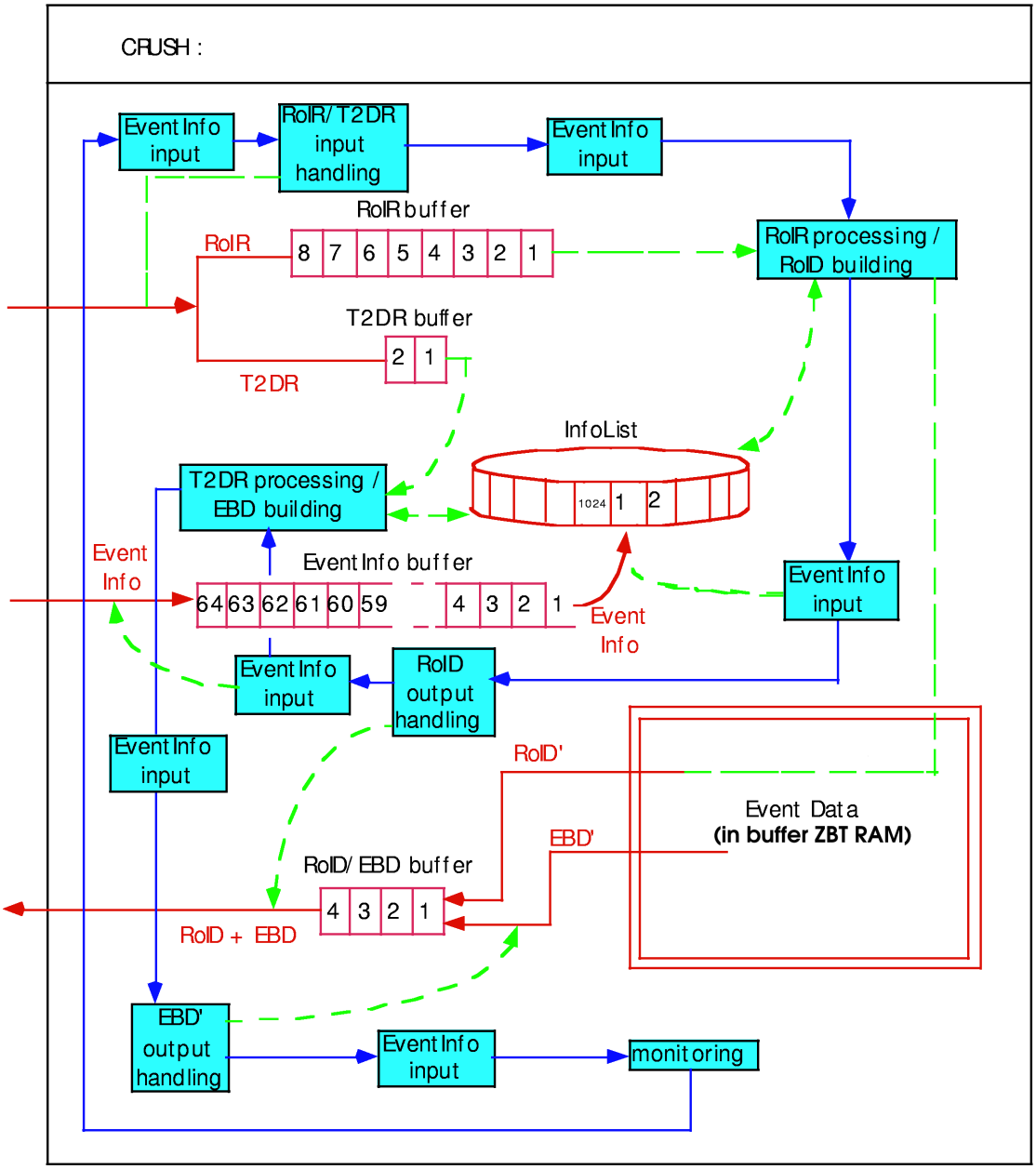

Figure 3.3: *Schematic view of the software used in the performance measurement of the CRUSH module. See the text for details. Figure taken from [48].*

- 6. "RoID output handling" initiates DMA transfers for output across one of the SHARC links if there is data in the "RoID/ EBD buffer" and the output SHARC link is free. Keeping track of which parts of the buffer memory are used for storing event fragment data is done as part of the "Event Info input" processing. This includes checking whether there is enough contiguous space left (including a safety margin) in the buffer memory for storing new event data arriving via the ROL. If there is not enough space left the oldest fragment(s) need to be moved from the buffer memory to the internal memory of the SHARC. The occupied space in the buffer can then be used for storing new event fragments. Checking whether there is enough space left is implemented, but the software used for the performance tests can not move event fragments if necessary. With a large enough buffer memory however, this should be necessary only for a small fraction of the events. For more details on the buffer management of the CRUSH see [48].

The buffer memory is mapped twice in the memory map of the SHARC. This simplifies the handling of buffer wrap-around situations: it enables transfer of an event fragment by a single DMA operation even when it is "wrapped-around" the end of the buffer.

The software used for the performance tests was written by H. Boterenbrood and uses less than 10 k words for code (consisting of 48-bit words) and about 17 k words for data (32-bit), leaving close to 100 k words (32-bit) available for additional dynamically allocated event summary and data storage. The software is written in C using the Analog Devices Development Tools version 3.3 for the SHARC processor.

3.2 Stand-alone measurements

Two different test setups with a single CRUSH module have been used. The first setup is shown in fig. 3.4. The second setup is identical to the first, but now the virtual S-link input is replaced by a real S-link input. In the following sections the test setup will be described and measurement results are presented.

3.2.1 Description of the setup

The setup contained a mix of CRUSH and PCISHARC modules. The PCISHARC module is a board developed at NIKHEF with a SHARC processor and an AMCC PCI interface chip [52]. One PCISHARC provides a path for booting and interaction with the CRUSH module. Another PCISHARC module provides the source and destination of the data streams required to run the simulation.
In the setup in fig. 3.4 an S-Link input stream is simulated by externally providing a stream of event summaries on one of the SHARC Link Ports ("virtual S-link"). The CRUSH reads the summaries from the Link Port in the same way as if it would read them from its Paged FIFO. To the SHARC processor there is no difference in handling event summaries entering through the Paged FIFO or through a Link Port. There is no need to provide real S-Link input to test the software because the actual event data flow into the CRUSH's ring buffer is completely handled by hardware and does not affect the SHARC's processing performance in any way. The advantage of such a simulated or "virtual S-Link" input is that the

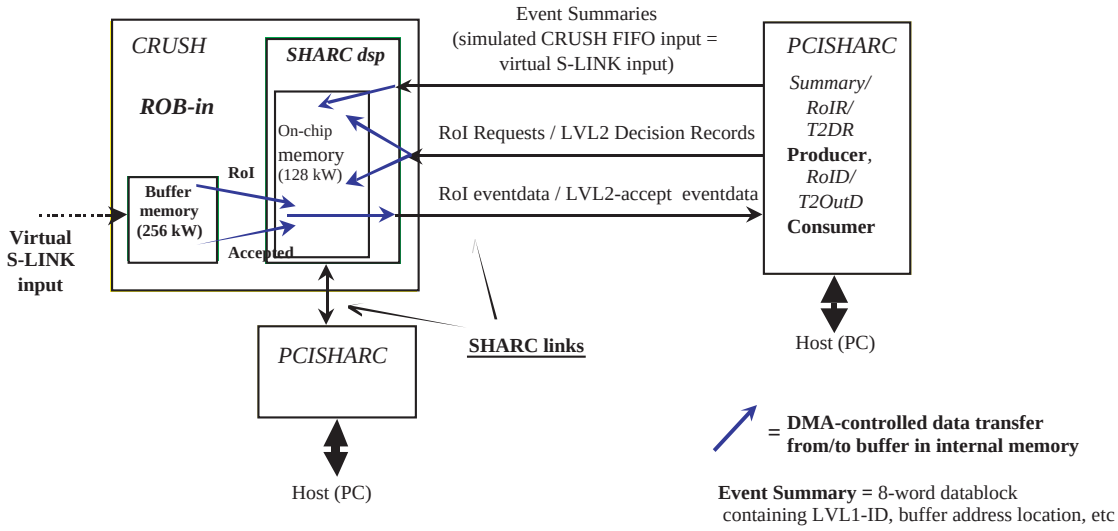

Figure 3.4: *Measurement setup for a single CRUSH, using a virtual S-link input.*

"virtual S-Link" input rate automatically is limited by either the maximum performance of the ROBIn software (running on the SHARC), the maximum transfer speed out of the buffer memory or the maximum throughput of the SHARC links. This maximum performance is measured as a function of, among other parameters, event fragment size; in different words: the maximum S-Link input rate for a particular event fragment size that can be handled, is measured.

The setup with a real S-link used an external module (MicroEnable [53] or SLIDAS [54]) to function as an event fragment S-link input source. Measurements showed that the "virtual S-link" setup results in a roughly 10 % lower maximum event fragment rate due to necessary simulation related overhead compared to the equivalent measurement with real S-link input. Therefore, the measurement results for the maximum event fragment rate presented here-after (obtained with the virtual S-link setup) are lower than would be obtained with real S-link input.

3.2.2 Measurement results for a single CRUSH

Measurements were performed for event sizes of 256, 512, 768, 1024, 1280, 1536, 2048, 3072 and 4096 Bytes, RoI request fractions of 5, 10, 14, 20, 25, 33, 50 and 100 % and accept fractions of 0, 1, 3, 5 and 10 %. The RoI request fractions and accept fractions are the fractions at which RoI requests and accept decisions are received with respect to the rate of events received via the virtual S-link. The size of the decision record was kept constant at 100 decisions.

For each combination the maximum event fragment rate which the CRUSH module can handle was determined. The maximum event fragment rates as a function of the event size for the different accept fractions and for RoI request fractions of 10% and 50% are shown in fig. 3.5.

As is shown in figs. 3.5(c) and (d), for small event fragment sizes the maximum event rate is independent of the size, for larger event fragments the inverse rate is seen to be

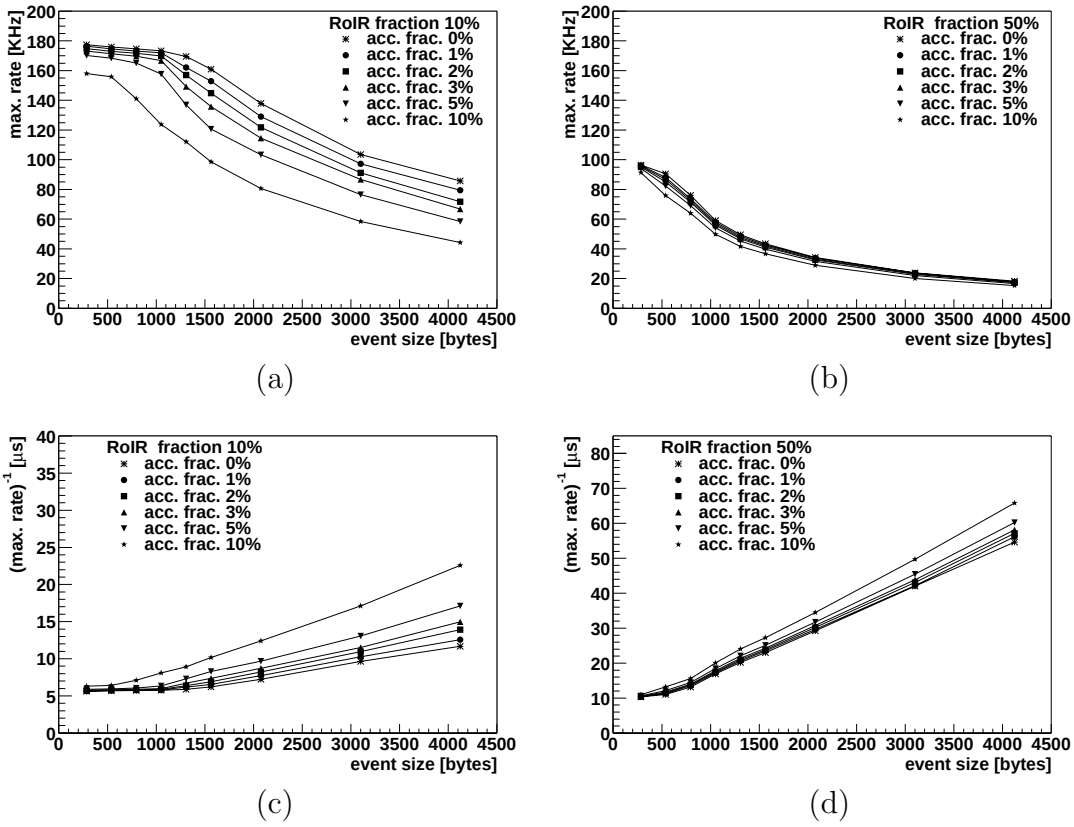

Figure 3.5: *Maximum event fragment rate as a function of event fragment size for Region of Interest Request fraction (RoIR) 10% (a), and 50%(b). The inverse rate in µs as a function of event fragment size is shown in (c) and (d) for RoIR fractions of 10 % and 50% respectively. The lines are for guiding the eye.*

approximately linear dependent on the size. The inverse rate $1/f$ can be expressed as:

$$\begin{aligned} \frac{1}{f} &= max(\frac{1}{f_a}, \frac{1}{f_b}) \\ \frac{1}{f_a} &= c_1 + c_2 \cdot R + c_3 \cdot A \qquad (3.1) \\ \frac{1}{f_b} &= c_4 + c_5 \cdot R + c_6 \cdot A + c_7 \cdot E \cdot (R + A) \qquad (3.2) \end{aligned}$$

with R: RoI request fraction, A: accept fraction and E: event fragment size and f = rate in kHz. For small event fragments, processing in the SHARC limits the maximum rate (eq. 3.1), while for larger fragment sizes the bandwidth of the output link (40 MByte/s) is the limiting factor (eq. 3.2) The results were fitted with a ROOT macro using TMinuit, a class interfacing to the FORTRAN minimising program Minuit. Two fits were made, one with c_7 fixed to 25 ns per byte (corresponding to the 40 MByte/s bandwidth of the output link) and one with c_7 free. The latter fit resulted in a value of 24.9 ns for this

type of fit	c_1	c_2	c_3	c_4	c_5	c_6	c_7
1 fit, c_7 free	4.70	11.29	6.69	1.35	4.62	4.83	0.0249
1 fit, c_7 fixed	4.69	11.34	6.94	1.34	4.46	4.63	0.0250
2 fits, c_7 free	4.54	11.53	7.51	1.31	5.18	4.84	0.0249

Table 3.1: *Fitted values of parameters from eqs. 3.1 and 3.2. The last row in the table contains results for $1/f_a$ and $1/f_b$ fitted separately, using selected sets of data points. The first and the second row correspond to fits where $max(1/f_a,1/f_b)$ is taken, and the parameter c_7 is left free and fixed at 0.0250, respectively.*

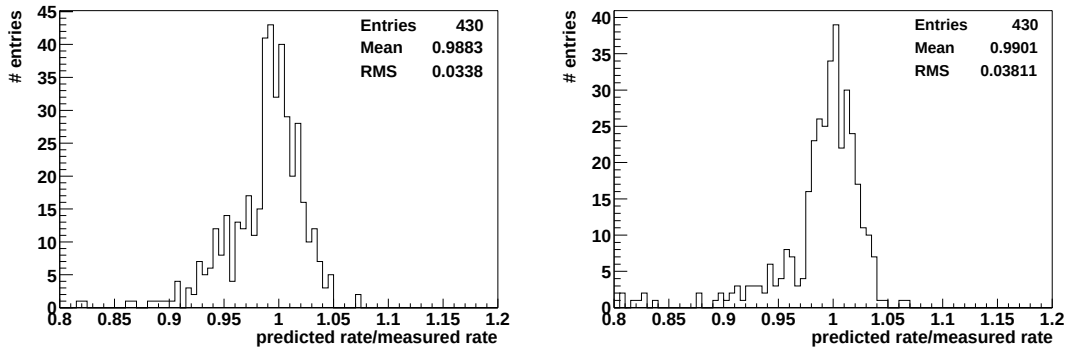

(a) (b)

Figure 3.6: *Ratio of predicted over measured rate corresponding to the values from fits in the first (a) and third (b) entry in table 3.1.*

parameter. The results for the parameters (all values have the dimension μs, except for c_7 which has the dimension μs/byte) are presented in table 3.1. It was also attempted to make separate fits of the equations for $(1/f_a)$ and $(1/f_b)$, for each fit using a different set of selected data points. The resulting parameters are all presented in table 3.1. Fig. 3.6 shows the distribution of the ratio of predicted and measured rate for all measurements (430 in total). A similar distribution for the overall fit with c_7 fixed looks almost the same. In fig. 3.6(b) the distribution of the ratio of predicted and measured rates for a selected set of measurements using the parameters obtained with the two separate fits is shown. A somewhat narrower peak is observed. The distributions are asymmetrical with a tail for values lower than 1, i.e. the largest deviations between measured and predicted rates occur for predicted rates which are too low.

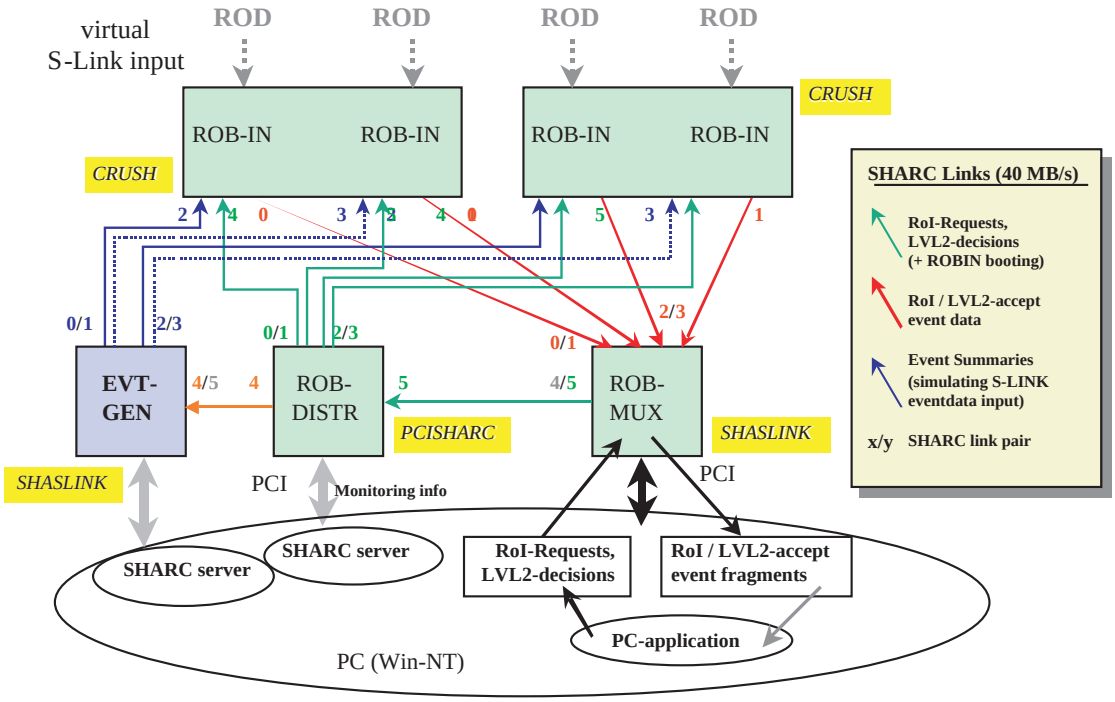

Figure 3.7: *Configuration of the ROB complex setup.*

3.3 System measurements: the CRUSH in a ROB complex

The CRUSH was planned to operate together with other ROBIns, in the context of a ROB complex[3]. To study the performance of the CRUSH in a network, a ROB Complex has been built from two CRUSH modules, a ShaSLINK module and a PC. In the following section, the measurement setup is described. In the subsequent section, measurement results are presented.

3.3.1 Description of the setup

The ShaSLINK (Sharc + S-link source) module is a PCI card with a SHARC processor, a PCI interface and an S-link source interface. A detailed description of the module can be found in [55]. The two CRUSH modules and the ShaSLINK module were connected via SHARC links. Output can go either via PCI bus or S-link. In this test output via S-link is not considered. In fig. 3.7 the layout of the ROB Complex test setup built with two CRUSH modules, two ShaSLINK modules, a PCISHARC module and two PCs is shown. Since a single PC of the type used only has 3 empty slots available, it was necessary to use a second PC. Short flat cables were used for interconnecting the SHARCs.
The PCISHARC module is used for distributing RoI requests and LVL2 decisions to the ROBIns. For the test measurements again "virtual S-link input" has been used: the event

[3]Recently, the name "ROB complex" has changed into Read-Out System or "ROS". However, the old terminology will continued to be used here.

summary information (during normal operation read from the Paged FIFO in the FPGA), is sent to each CRUSH module via a SHARC link. One of the ShaSLINK modules (the "EVT-GEN" block in fig. 3.7) generates the event summary information, while the other functions as ROBout, but is here referred to as ROB-"multiplexer" (the "ROB-MUX"). It combines event fragments that it receives into larger fragments. Each CRUSH module functions as a single ROBIn, but data transferred via one of its links can also be transferred simultaneously via a second link. In this way from the point of view of the "ROB-MUX" 2 ROBIns are sending their data in stead of a single ROBIn. The setup therefore allows to obtain information on the behaviour of a ROB complex with up to 4 ROBIns.

One of the PCs, a 200 MHz Pentium Pro machine, with Windows NT as operating system, generates RoI requests and LVL2 accepts/rejects and waits for event fragments to arrive. The RoI request rate and the accept rate relative to the LVL1 rate can again be specified. Again the maximum event rate given the number of requests and accepts is measured. The "ROB-MUX" passes RoI requests and decision blocks to the "ROB-DISTR" and it receives event fragments from the CRUSH modules and combines these into larger fragments which are stored via DMA controlled block transfers via the PCI bus in the memory of the PC. The "EVT-GEN" generates summary information independently and sends this information to each CRUSH individually. The event generation process is throttled by the "ROB-DISTR", which sends signals to the "EVT-GEN" indicating how far it can advance with the generation of new events. RoI requests and LVL2 accepts/rejects are passed by the "ROB-DISTR" to the CRUSH modules. The PCI interfaces of the cards implementing the "ROB-DISTR" and "EVT-GEN" functions are only used for monitoring purposes.

3.3.2 Measurement results for a ROB complex

For RoIR fractions of 5%, 10%, 14.3%, 20%, 25%, 33.3%, 50% and 100%, eventsizes of 256, 512, 1024, 2048, 3072 and 4096 bytes and accept fractions of 1%, 3% and 5% the maximum LVL1 rate for the setup described in section 3.3.1 was measured. The decision record was kept constant at 100 decisions.

In addition the test setup was configured in 4 different ways:

- "1" : 1 CRUSH module used, data is transferred to the "ROB-MUX" via 1 SHARC link,
- "1 + 1" : 2 CRUSH modules used, each transfers event data to the "ROB-MUX" via one SHARC link, the "ROB-MUX" builds events from the fragments from both input data streams,
- "2 + 1" : 2 CRUSH modules used, one transfers event data via a SHARC link and in parallel the same event data via a second SHARC link to the "ROB-MUX", the other transfers event data to the "ROB-MUX" via one SHARC link, the "ROB-MUX" builds events from the fragments from the three input data streams,
- "2 + 2" : 2 CRUSH modules used, both transfer event fragment data via a SHARC link and in parallel the same data via a second SHARC link to the "ROB-MUX", the "ROB-MUX" builds events from the fragments from the four input data streams.

In fig. 3.8 results for the inverse rate for 1% accept fraction as a function of the event fragment size are presented. The same behaviour as for a single CRUSH module is observed: for small fragments the rate is independent of the fragment size, for larger fragments the inverse rate increases linearly with the fragment size, indicating that there is a bandwidth limitation. For the "1" and "1 + 1" configurations the limitation stems from the SHARC link(s). The maximum internal bandwidth of the SHARC processor of the ShaSLINK for simultaneous input via its links and output via its external bus interface is 80 MByte/s. This limits the output bandwidth for the other configurations (and for the "1 + 1" configuration as well, but in this case the limit is the same as the maximum throughput via two SHARC links). The measurement results from table 3.2 were fitted with almost the same formulae as earlier:

$$\begin{aligned} \frac{1}{f} &= max(\frac{1}{f_a}, \frac{1}{f_b}, \frac{1}{f_c}) \\ \frac{1}{f_a} &= c_1 + c_2 \cdot R + c_3 \cdot A \\ \frac{1}{f_b} &= c_4 + c_5 \cdot R + c_6 \cdot A + c_7 \cdot E \cdot (R + A) \\ \frac{1}{f_c} &= \frac{1}{165} \text{ (“1” configuration) } \frac{1}{f_c} = \frac{1}{120} \text{ (other configurations)} \end{aligned} \tag{3.3}$$

The maximum event rate for small RoI request and accept fractions and small event fragments is about 165 kHz for the "1" configuration and about 120 kHz for the "1 + 1", "2 + 1" and "2 + 2" configurations. These numbers are the same for different RoI request fractions, accept fractions and event fragment sizes. This shows that the measurement procedure rather than the performance of the CRUSH modules and "ROB-MUX" determines these maximum rates. The reduction of the maximum event rate for the "1 + 1", "2 + 1" and "2 + 2" configurations can be attributed to he "EVT-GEN", which has to generate and send event summary information at twice the full event rate for these configurations. For higher RoI request fractions and still for small event fragments a maximum rate is found which depends on the RoI request and accept fractions, but not on the event fragment size. This is the behaviour described by the equation for $(1/f_a)$. Only measured rates lower than 165 (" 1" configuration) or 120 kHz (" 1 + 1", "2 + 1" and "2 + 2" configurations) have been used in fitting it. For the larger event fragments the equation for $(1/f_b)$ was fitted to the measured rates. In view of the limited number of accept fractions it was not attempted to do a combined fit. The measurement results used for each fit were selected with the help of plots similar to those shown in fig. 3.8.

The complete measurement data set is given in [48].
The results of the fits are presented in table 3.2 (all values have the dimension μs, except for c_7 which has the dimension μs/byte). The distribution of the ratio of predicted and measured maximum rate for all 570 measurements is presented in fig. 3.9. For the "2 + 2" configuration, the dependence on A was not taken into account for $(1/f_b)$ as a negative value was found for the c_6 parameter if A was used in the fit. For the "1 + 1" configuration c1 and c4 were found to have small negative values. The parameters in table 3.2 result from a fit with c_1 and c_4 set to 0.

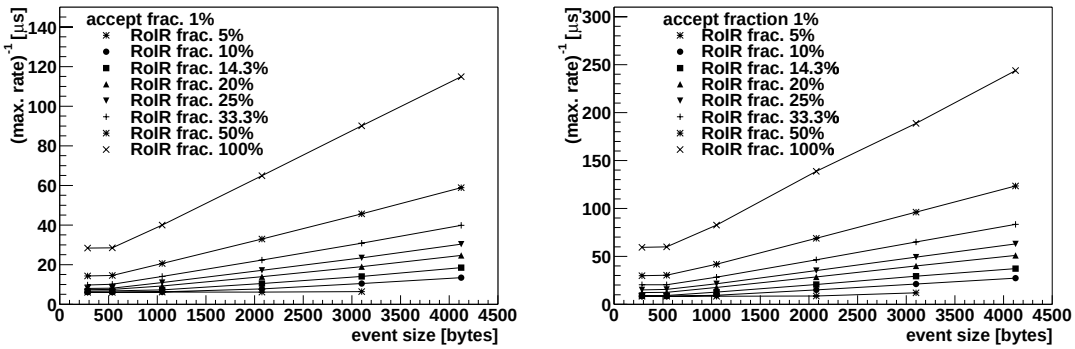

(a) (b)

Figure 3.8: *The inverse of the maximum rate as a function of the event size for different RoI request fractions and an accept fraction of 1%. Results for the "1" configuration are given in (a), for the "2+2" configuration in (b).*

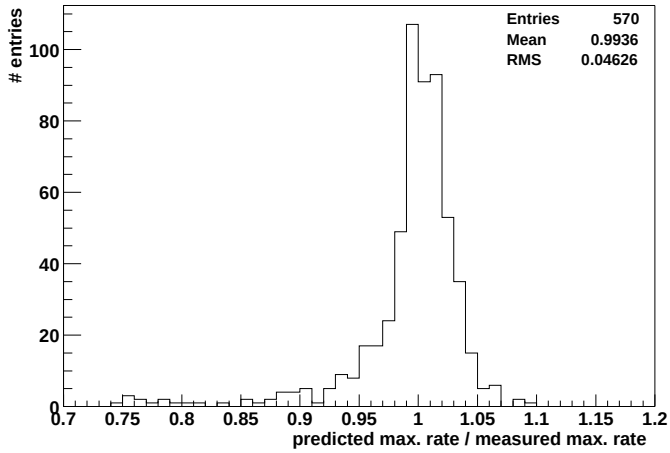

Figure 3.9: *Ratio of predicted over measured rate corresponding to the values from fits in table 3.2.*

The maximum bandwidth available for output of data can be inferred from the value found for c_7: it is the 40 MByte/s of a single SHARC link for the "1" configuration. For the other configurations the merging of the fragments in the "ROB-MUX" has to be taken into account, so the maximum bandwidth is either $2/0.0250 = 80$ MByte/s, $3/0.0403 = 74$ MByte/s or $4/0.0512 = 78$ MByte/s. These results confirm the expectation that the maximum throughput of the "ROB-MUX" is limited to 80 MByte/s by the internal bandwidth of the SHARC for simultaneous data input via the links and output via the external bus interface. The traffic on the PCI bus was also studied with a PCI bus analyser. Within bursts the data was flowing at the maximum rate. However, the bursts were interrupted regularly, which is probably due to the throughput of the "ROB-MUX" being smaller than the 132 MByte/s bandwidth of the PCI bus.
The parameters depend more strongly on the RoI request fraction than found for a single

configuration	c_1	c_2	c_3	c_4	c_5	c_6	c_7
1	0.68	27.4	23.8	0.78	13.7	9.57	0.0244
1 + 1	-	38.8	36.8	-	20.4	55.8	0.0250
2 + 1	0.38	46.1	51.2	0.69	17.7	5.49	0.0403
2 + 2	0.36	58.3	51.6	1.32	28.8	-	0.0512

Table 3.2: *Fitted values of parameters from equation 3.3. For every configuration separately the data was fitted.*

ROBIn. This results in a faster decrease of the maximum event rate for increasing RoI request fraction, which can be attributed to the action of the "ROB-MUX" and to the generation of event summary information and of RoI request and accept messages. The measured maximum rates hence provide lower bounds to the rates that could be obtained in the real application.

3.4 Conclusions and discussion

The measurement results show good performance of the hardware and software, satisfying the requirements obtained from modelling [56], [57]. The measurement procedure may be limiting the maximum rates, in particular for the ROB Complex measurements. The maximum rates observed can be estimated with simple equations, based on parameters obtained from fitting the measurement results.

The point-to-point SHARC links are well suited for the internal (probably on-board) connections inside a ROB Complex. The automatic handshaking per 32-bits word transferred across a link is very useful and makes it straightforward to avoid overflows of buffers for requests and decisions inside the ROB Complex. As the "ROB-MUX" takes care of fragment building and fanning out RoI requests and decisions the message rate across the PCI bus is smaller than for ROB Complexes using the PCI bus for connecting ROBIns to a CPU of a PC or Single Board Computer. Also the load of the CPU of the PC or Single Board Computer may be smaller.

The compact design and the low power dissipation of the CRUSH would allow to build a ROB complex with about 6 ROBIns on a single 6U Eurocard, if a good way is found to connect 6 S-links to a 6U board.

The ADSP-21160 processor is the successor of the ADSP-21060. It is 2.5 times as fast, has 6 100 MByte/s links, also 512 kByte of internal memory, a smaller footprint than the ADSP-21060 and also a low power dissipation. A new design based on it (possibly in combination with a new generation of FPGAs) would not suffer from the bandwidth limitation of 80 MByte/s in the "ROB-MUX", whereas the performance of this processor could be high enough to allow servicing of two S-links. An even more compact design could be possible at a lower price due to a reduction in the number of processors needed.

The S-link output of the ShaSLINK could be used as an alternative to output via PCI bus. This allows to study a scenario in which groups of ROBs are outputting event data via dedicated links (S-links in this case) connecting to processors of the LVL2 farm. These processors would then provide the required network interfacing together with processing

capacity for the LVL2 trigger. RoI requests and decisions would reach the ROB complex either via PCI bus or via a SHARC link interfaced to a PC or Single Board Computer servicing many ROB complexes. This and other scenarios are discussed in [57] and [58].

Chapter 4

Event fragment size distributions

The architectural layout of the LVL2 system with its hardware components as described in section 2.3.3 can be simulated to verify the assumptions made on link speeds, processor times, switching times, etc. The LVL2 system is modelled using a static model, the Papermodel, and dynamic models, referred to as computer models. The Papermodel (initially a spreadsheet, hence the name) is a simple C++ program which uses as input averages of event fragment sizes, processing times, switching times, accept fractions, trigger menus and link speeds. It then returns the required CPU power, required bandwidth, number of links and in general allows to judge whether the number and specifications of the various components are up to the task. The computer model is a dynamic model, it outputs distributions for e.g. the LVL2 decision times and queue sizes. One of the computer models used is called SIMDAQ. Distributions for SIMDAQ for event fragment sizes coming out of the ROBs and going into the LVL2 system were not available. A study, detailed in this chapter, was undertaken to generate these distributions. More details on this study can be found in [59].

4.1 Simulation of event fragment sizes: method and samples

Distributions have been obtained for sizes of event fragments stored in the Read Out Buffers (ROBs) of the Pixel, SCT and TRT detectors, for low luminosity ($1 \cdot 10^{33}$ cm^{-2} s^{-1}), intermediate luminosity ($2 \cdot 10^{33}$ cm^{-2} s^{-1}) and high luminosity ($1 \cdot 10^{34}$ cm^{-2} s^{-1}) running of the ATLAS detector at the LHC.

Events that contain only information at the particle level have been passed through a full GEANT3 detector simulation (DICE) [60]. For each module of the sub-detectors of the Inner Detector, the digitisation information has been extracted. The modules are grouped into “Minimum Units of Readout” (MURs). One MUR usually consists of six modules. The event fragment size distributions are generated for different mappings of modules to MURs, MURs into RODs, and a 1 to 1 correspondence of ROD to ROB. In this chapter the phrase ”event fragment size distribution of a ROB” refers to the distribution of sizes of the event fragments output by a ROBIn. After the submission of the Physics TDR [34], the geometry of the Pixel detector has changed. The new Pixel detector layout is commonly

referred to as the "Insertable Pixel layout". Small changes in the endcap SCT detector geometry have also been made. Throughout this chapter, the new geometry is referred to as "fall 2001 geometry" and the old geometry as "TDR geometry". Only distributions for the fall 2001 geometry will be shown, since the TDR geometry is obsolete.

4.1.1 Data samples

The data samples for the distributions are generated using the computer program DICE [60], version June 28, 1999. The signal sample consists of $b\bar{b}$ pairs where one of the b's is forced to decay into a muon with $p_T \geq 6$ GeV, and the other b can decay into anything (this is commonly written as $b\bar{b} \rightarrow \mu 6\text{X}$).

The background consists of QCD minimum bias events. For low, intermediate and high luminosity, 2.4, 4.8 and 24 QCD minimum bias events respectively, were added to the trigger bunch-crossing (BX) and subsequently digitised. The QCD minimum bias background was generated using the MSEL=1 switch of PYTHIA 6.1 [61]. The same procedure is used by the ATLAS B-physics simulation group to generate minimum bias events [62]. The standard low luminosity LVL1 trigger cut (an event should contain one μ with a $p_T \geq 6$ GeV) was used for both low and intermediate luminosity data samples. For high luminosity a μ with a $p_T \geq 20$ GeV was used, therefore in this data sample electromagnetic RoIs dominate.

For the event fragment size distributions for the TRT detector, again a $b\bar{b} \rightarrow \mu 6\text{X}$ sample with minimum bias added but now four BXs before and two BXs after the trigger BX were taken together and subsequently digitised. Compared to the Pixel detector and endcap SCT detector data sample, this a different procedure, since the digitisation routine of the TRT takes into account the longer drift times of the ionisation electron clusters in the TRT straw tubes. These drift times typically span a few BXs (see also chapter 5).

For the event fragment size distributions for the SCT detector for electron Regions of Interest (RoI), a data sample [63] was used which was passed through the trigger simulation program ATRIG [64].

4.1.2 Implementation

The digitisation information was extracted from the data samples and was written to plain ASCII text files. The text files produced, contained geometry information, local coordinates of the pixel, strip or straw hit and the digitised output of the respective sensitive volumes. C++ classes for barrel modules and endcap modules have been defined for the different detectors. A program using the ROOT [65] package reads in the text files and stores the information from the files per event into a list of endcap and barrel module objects. The module objects are subsequently ordered in a list of MURs by module-to-MUR maps detailed in Appendix A. A MUR usually consists of 6 modules (for the SCT barrel for instance one half ladder). For every object representing a module its position in (η, ϕ, $z(r)$) space is stored as well as a (unique) MUR number that is assigned to it. A general ROB class is also defined.

For the Pixel detector and SCT detector various mappings from MURs to ROBs are used to generate the event fragment size distributions per ROB, by adding module objects with the appropriate MUR numbers to a ROB object. The range covered in (η, ϕ, r(z)) space by a ROB object is defined by the coordinates of the module objects going into that ROB object. The size of the event fragments received by the ROB is equal to the sum of the sizes of the event fragments produced by the modules (including headers). Finally, to get the total event fragment size produced by a ROB, a ROB header is added.

4.2 Distributions for the SCT detector

The configuration of the SCT detector is given in section 2.2.1. The configuration of layers, modules and ladders of the SCT barrel has not changed due to the Insertable Pixel layout. The geometry of the endcap SCT detector has changed with respect to the positioning of the endcap wheels in z. The length of the inner modules has shrunk, increasing the inner radius of the endcap wheels. Also, the first wheel in the fall 2001 geometry has two rings and the second wheel has three rings of modules (counting the wheels from the barrel), as opposed to the TDR geometry where it was the other way around. The following information is used for obtaining the event fragment sizes:

- each strip hit gives 2 bytes
- each module sends headers with a size of 2 bytes
- each ROB sends headers with a size of 8 bytes

4.2.1 SCT barrel

On average 3% of the strips are considered to be inefficient, as assumed in the Inner Detector TDR [35], and are not taken into account. Three different MUR to ROB SCT barrel maps have been used and two MUR to ROB SCT endcap maps. The maps are specified in Appendix A.

Results for SCT barrel tower mapping A, the mapping used in the paper model [66], are displayed in fig. 4.1. In fig. 4.1(a), the distributions of the barrel ROBs for low, intermediate and high luminosity are plotted on a log scale to show the tails of the distribution. In fig. 4.1(b), the average event fragment size per individual ROB is shown for the three different luminosities. Fig. 4.1(b) (high luminosity graph) shows that 12 of the 44 ROBs give a smaller event fragment size than the other ROBs. This is caused by the fact that these ROBs do not receive data from modules in the inner barrel layer. The occupancy of the SCT layers differ significantly, as can be seen in fig. 4.2. The average event fragment size per ROB for SCT barrel tower mapping B, shown in fig. 4.3(b), has a more homogeneous distribution. The ROBs with the larger event fragment sizes contain 2 instead of 1 MUR in the inner barrel layer. A note of caution is appropriate here: in the figures presented in this chapter the ROB numbers are counted starting from the first ROB in one of the endcaps, then the ROBs in the barrel are counted up to the last ROB in the other endcap. In Appendix A, however, the ROB numbers start counting with each half barrel or half

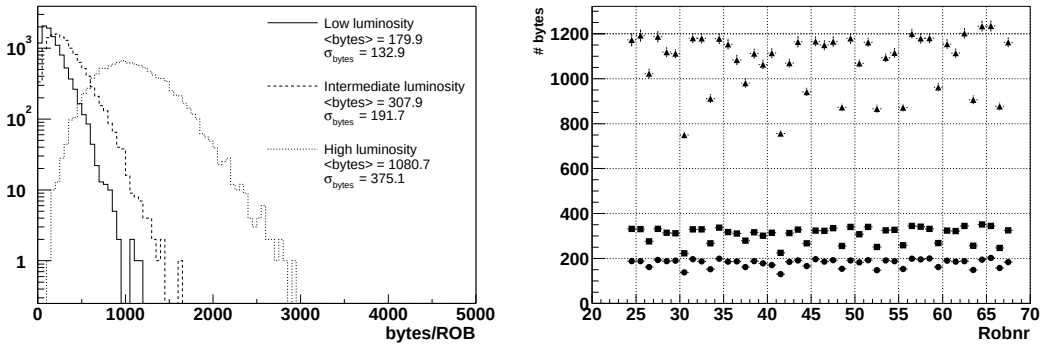

(a) (b)

Figure 4.1: *Event fragment size distribution (a) and average event fragment sizes per ROB (b) for barrel SCT ROBs using SCT barrel tower mapping A. Low, intermediate and high luminosity are indicated by triangles, squares, and circles in (b), respectively. The error on the average event fragment size is given by the (hardly noticeable) vertical error bars.*

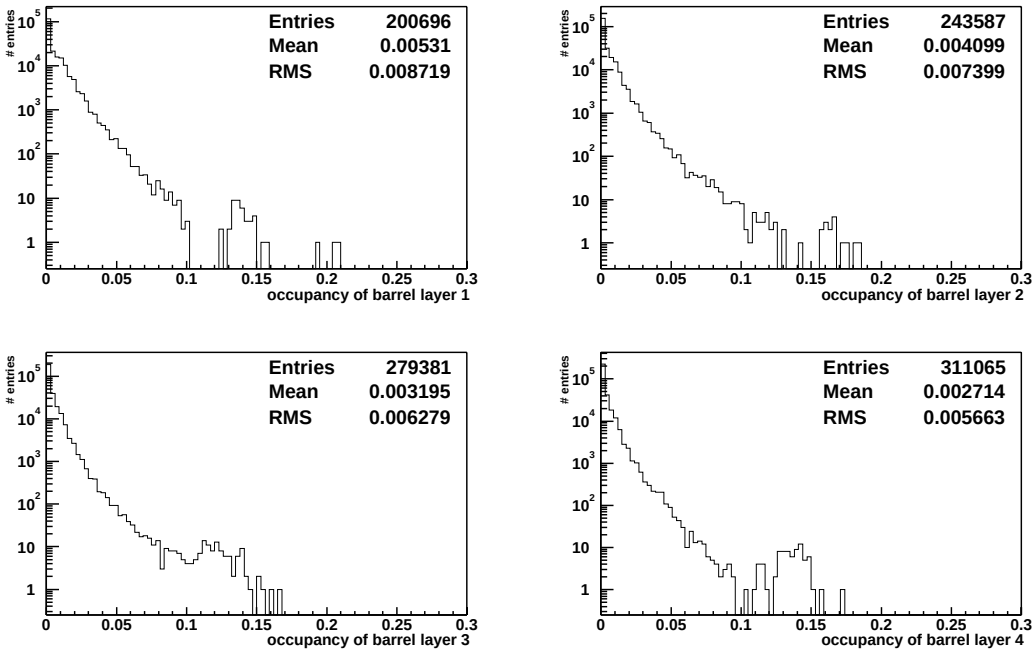

Figure 4.2: *Fractions of strips hit per SCT barrel module for the four different layers of the SCT barrel. These distributions are for high luminosity, SCT barrel tower mapping A.*

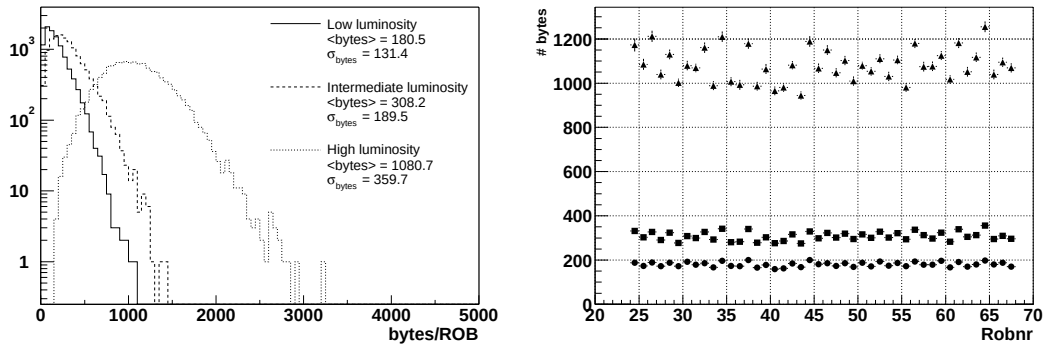

(a) (b)

Figure 4.3: *Event fragment size distribution (a) and average event fragment sizes per ROB (b) for barrel SCT ROBs using SCT barrel tower mapping B.*

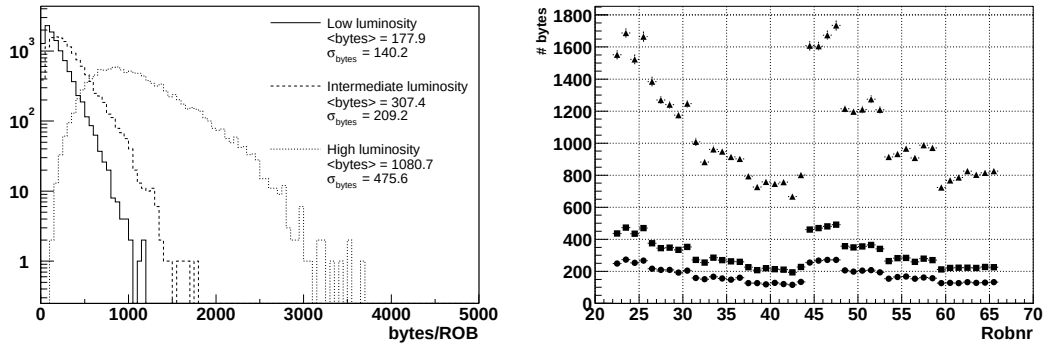

(a) (b)

Figure 4.4: *Event fragment size distribution (a) and average event fragment sizes per ROB (b) for barrel SCT ROBs using the SCT barrel layer mapping.*

endcap. Because of the symmetry of the detectors, comparison between the figures and Appendix A should be straightforward.

The event fragment size distribution using the SCT barrel layer mapping is shown in fig. 4.4. It clearly shows the effect of using ROBs per barrel layer as opposed to an (approximate) projective mapping. The ROBs which receive data from the inner barrel modules only, i.e. the ROBs which have the largest average event fragment size, are clearly visible. The mean from the event fragment size distribution where SCT barrel tower mapping A is used is 1081 bytes, for high luminosity. In the results presented here, the event fragment size is determined mainly by minimum bias background with an underlying B-physics event.

4.2.2 SCT endcap

The event fragment size distributions for the two MUR to ROB maps for the SCT endcap are given in Fig. 4.5 and fig. 4.6. In the fall 2001 geometry the inner radius of the endcap disks went from 25 cm to 26.7 with the inner endcap modules becoming accordingly shorter [67]. The average event fragment size per ROB presented in fig. 4.5(b) shows considerable

differences between individual ROBs. This is due to the fact that a layer mapping is used instead of a projective mapping. The last few ROBs in the endcap tower mapping of fig. 4.6 show a smaller average event fragment size. These ROBs are mapped to the last three endcap wheels, which have 3, 2.5 and 1 ring, respectively. The 2.5 means that smaller modules are used in the inner ring of the 8th wheel.

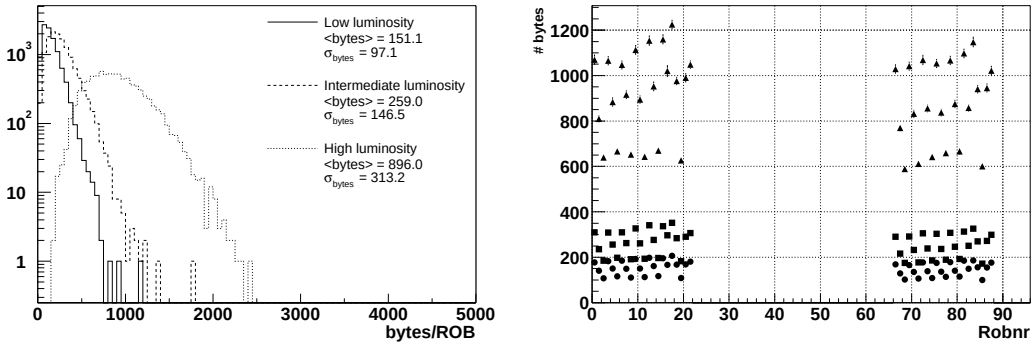

(a) (b)

Figure 4.5: *Event fragment size distribution (a) and average event fragment sizes per ROB (b) for endcap SCT ROBs using the SCT endcap layer mapping.*

The SCT endcap layer mapping gives event fragment size distributions which have means of 151, 259 and 896 bytes for low, intermediate and high luminosity, respectively. The event fragment size distributions according to the SCT endcap tower mapping, have means of 141, 239 and 822 bytes for low, intermediate and high luminosity.

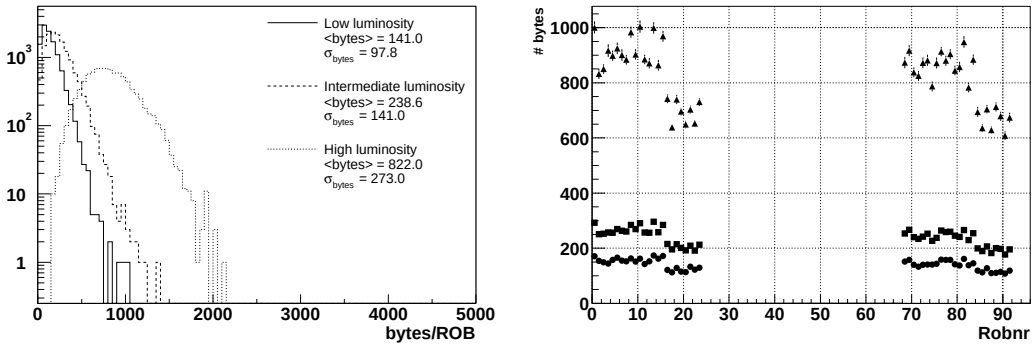

(a) (b)

Figure 4.6: *Event fragment size distribution (a) and average event fragment sizes per ROB (b) for endcap SCT ROBs using the SCT endcap tower mapping.*

4.2.3 Distributions for barrel SCT ROBs in an electron RoI

All event fragment size distributions previously presented in this chapter have been obtained by taking all ROBs in a sub-detector into account. Thus the distributions are strictly speaking only applicable when a B-physics trigger occurs at low or intermediate luminosity which initiates a scan of the whole Inner Detector. Therefore it has to be verified, whether the event fragment size distributions obtained for high luminosity, taking all ROBs into account, can also be used for a ROB receiving data from modules located within an electron RoI. For the results presented in fig. 4.7, only ROBs that are located within an electron RoI have been taken into account. For the data sample used here an electron RoI is defined such that the summed E_T off all particles in the electromagnetic calorimeter in a square grid of size 0.12×0.12 ($\Delta\phi \times \Delta\eta$) is $\geq$ 17 GeV, excluding muons and neutrinos [68]. Furthermore, the isolation cut in the electromagnetic calorimeter is set to 6 GeV, while the cut on energy in hadron calorimeter is 3 GeV, see [68] and [42]. The datasample was taken from [63].

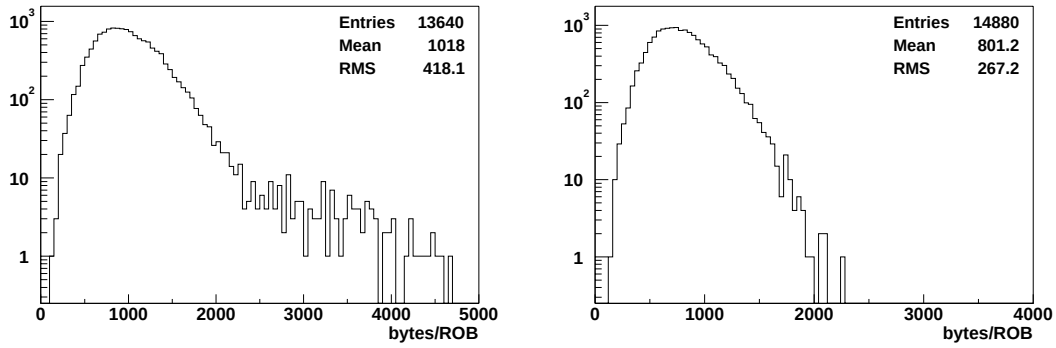

(a) (b)

Figure 4.7: *Event fragment size distribution for barrel SCT ROBs receiving data from modules located within an electron RoI, using the SCT barrel tower mapping A, high luminosity (a). Event fragment size distribution for endcap SCT ROBs receiving data from modules located within an electron RoI, using the SCT endcap tower mapping, high luminosity (b).*

The means of these distributions differ only slightly from the means in fig. 4.1 and fig. 4.6, i.e. 1081 vs. 1018 bytes for the barrel and 822 vs. 801 bytes for the endcap. The RMS of both distributions is also of comparable size, 375 vs. 418 for the barrel and 273 vs. 267 for the endcap. The reason that these numbers are comparable is that at high luminosity the average event fragment size of a ROB is dominated by the minimum bias background. Consequently, it is assumed that the high luminosity event fragment size distributions given in this chapter can be used when a ROB is receiving data from modules located within an electron RoI.

4.3 Distributions for the Pixels

The Pixel barrel detector consists of three concentric cylinders. Each cylinder is assembled from a number of ladders. Each ladder contains 13 modules. In this chapter it is chosen to have 6 modules in a MUR in one half barrel and 7 modules in a MUR in the other half barrel. Results are given for the fall 2001 geometry [69]. The following information is used for obtaining the event fragment sizes:

- each strip hit gives 2 bytes
- each module sends headers with a size of 4 bytes
- each ROB sends a header with a size of 8 bytes

4.3.1 Pixel barrel and endcap

The Pixel barrel geometry has changed with respect to the Pixel TDR-layout [70]: the B-layer is at a larger radius of 5.05 cm (instead of 4.15 cm), the two outer cylindrical layers have new radii of 8.85 cm and 12.25 cm (instead of 10.1 cm and 13.2 cm). The radii of the disks in the fall 2001 layout (R=8.877-15.957 cm) are smaller than quoted in the Pixel TDR [71] where they were 12.63-18.67 cm. The number of endcap disks was reduced from 5 to 3, and the new z-positions of the three disks range from 49.5-65.0 cm instead of 49.5-92.6 cm. Since the three barrel layers are shifted with respect to the TDR geometry, the number of ladders per barrel layer has also changed. From [72] it is known that the B-layer RODs are designed for 6-7 modules, the first layer RODs are designed for 13 modules and the second layer RODs are designed for 26 modules. The mapping here is done such that 1 B-layer ROD receives data from all the modules on one B-layer half ladder, one first layer ROD receives data from two adjacent first layer half ladders and one second layer ROD receives data from 4 adjacent second layer half ladders. Since there are 13 modules on one ladder, one half of the barrel contains 6 modules/MUR, while the other half contains 7 modules/MUR. See also Appendix A for the mapping. The event fragment size distributions are shown in fig. 4.8. The average event fragment size per ROB is presented in fig. 4.9.

Since the endcap of the Pixel detector now contains three endcap disks instead of five, a new mapping is proposed here. With the information from [72] it seems reasonable to use 8 modules/MUR, with 3 MURs in a ROD, so that one ROD receives data from 24 modules. Then, the number of MURs/ROD (MURs/ROB) is the same as in the old endcap Pixel tower map assumed in the Inner Detector TDR, and there are now 6 ROBs per Pixel endcap. The resulting values of the event fragment sizes are shown in fig. 4.10.

4.4 Distributions for the TRT detector

For the TRT barrel and endcap, a true projective mapping [69] is assumed. The division in ROBs is fixed, 32 ROBS in one half barrel, 96 per TRT endcap. The data is processed in the RODs according to the scheme detailed in section 5.1. Furthermore, it is foreseen that a zero-suppression algorithm reduces the data further.

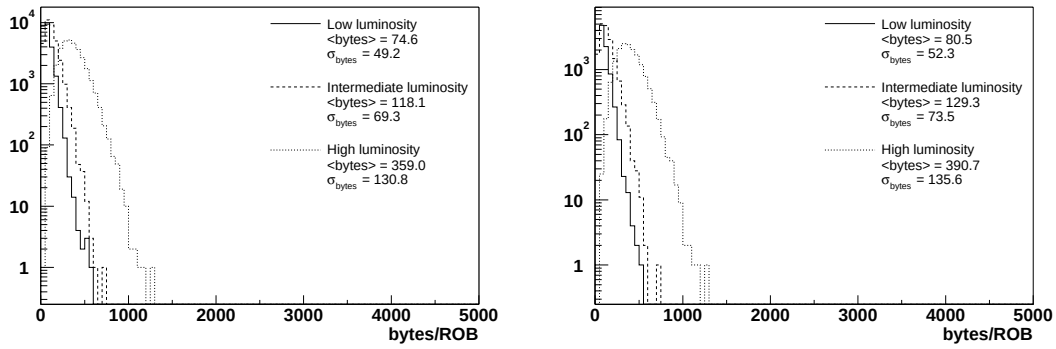

(a) (b)

Figure 4.8: *Event fragment size distribution for barrel Pixel ROBs using the Pixel barrel layer mapping, for MURs with 6 modules (a) and for MURs with 7 modules (b).*

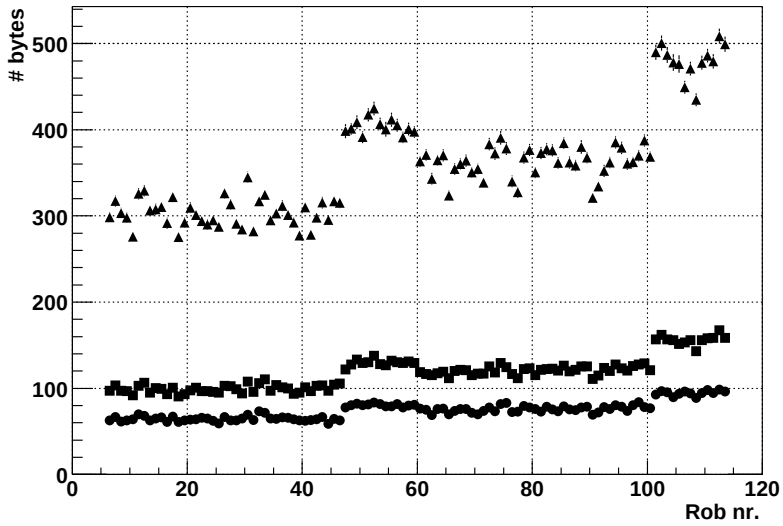

Figure 4.9: *Average event fragment sizes per barrel Pixel ROB using the Pixel barrel layer mapping.*

4.4.1 TRT barrel

In the high luminosity case an eleven bit header is used to give each straw an unique address, and this header plus the drift time data is sent from the ROBs to the LVL2 processors. For the low and intermediate luminosity a zero suppression scheme is assumed, see also chapter 5. It is assumed here that this zero-suppression will be done in the RODs [73] to reduce the data-volume across the links and switches going to the LVL2 processors. This zero suppression scheme does not give each straw an unique header but a header indicating the number of straws (*offset*) to the previous straw that has been hit. This header can be much smaller than eleven bits. The optimum header size N depends on the percentage of

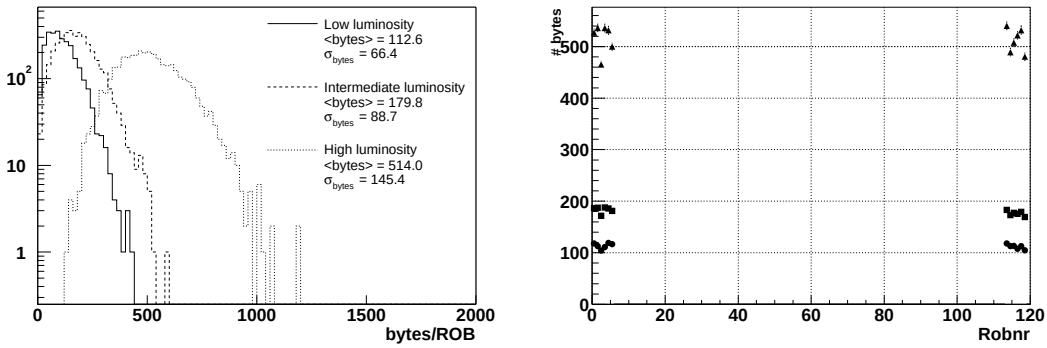

(a) (b)

Figure 4.10: *Distribution of event fragment sizes of all endcap Pixel ROBs with 8 modules/MUR (3 MURs in one ROB) (a). Average event fragment sizes per endcap Pixel ROB using 8 modules/MUR (b).*

straws hit and the spread of the hit straws in a readout segment. The results in this chapter are for 5 bit headers in the case of low and intermediate luminosity. In fig. 4.11 the event fragment size distributions for low, intermediate and high luminosity is presented.
The mean of the event fragment size distribution is 199 bytes for low and 325 bytes for intermediate luminosity. These numbers are in agreement with the results presented in [73] where a digitisation procedure for the TRT is described, which is used here for generating the data sample. In [73] a simple Monte Carlo procedure is used to generate the number of VALID straws. In contrast, in this thesis, fully simulated events are used. The average event fragment size for the high luminosity case is 1106 bytes.

4.4.2 TRT endcap

One TRT endcap consists of 18 wheels. One ROB reads out a projective wedge in ϕ of $1/96 \times 2\pi$ of all wheels. Fig. 4.12 shows the event fragment size distributions for the TRT endcap detector. The mean value of the distributions of barrel event fragment sizes and endcap event fragment sizes for the different luminosities are very similar, as a consequence of the similar sizes of eta-phi space covered by one ROB. $\Delta\eta \times \Delta\phi$ is 0.7×0.2 for the barrel (0.14) and 1.8×0.07 for the endcap (0.13).

4.5 Probability density functions in SIMDAQ

SIMDAQ is an object oriented discrete event simulation package for the DAQ/LVL2 system of ATLAS written in C++. Interacting objects are defined such that they can be conglomerations of multiple objects, e.g. the object "PC" can consists of the objects "network interface" and an object "processor". The objects can represent hardware or software components. Interactions between objects may cause state changes. Each object has an event-handler through which the state of the object can change.The simulation is based on an event list, which is ordered by the simulation time at which events should occur. New events are inserted in this list by the actions of simulated objects.

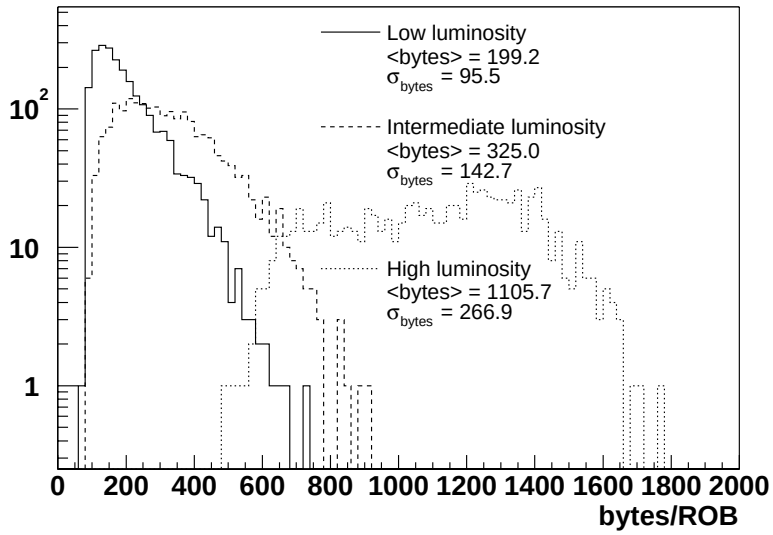

Figure 4.11: *Distribution of event fragment sizes of all barrel TRT ROBs. One ROB covers a wedge of 1/32 × 2π of one half barrel. The distributions are given for low, intermediate and high luminosity.*

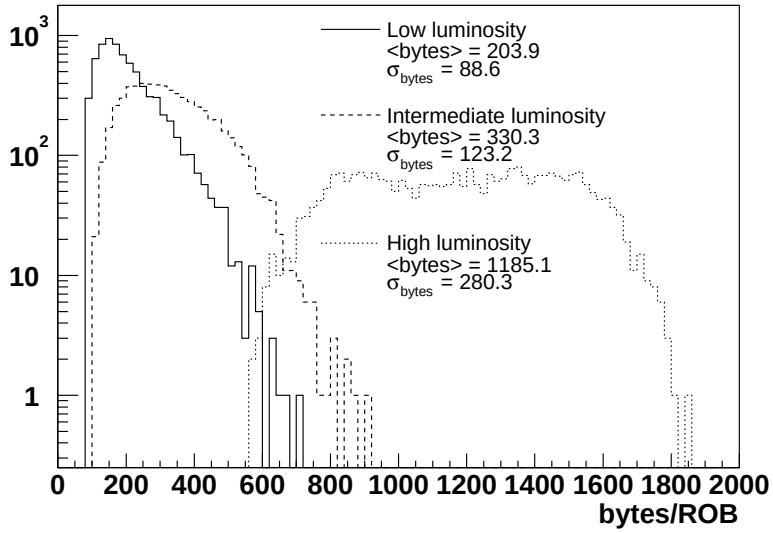

Figure 4.12: *Distribution of event fragment sizes of all endcap TRT ROBs. One ROB receives data from modules located in a wedge of 1/96 × 2π of one endcap barrel. The distributions are given for low, intermediate and high luminosity. The former two use a zero suppression scheme, while the latter does not (see text).*

	paper model	new mean fixed	distribution
SCT ROB proc. utilisation (%)	87.77	87.79	87.64
TRT ROB proc. utilisation (%)	85.91	85.93	85.78
PIXSCT FEX queue (nr. of fragments)	55.55	54.92	54.66
TRT FEX queue (nr. of fragments)	25.74	25.66	25.63
SCT volume out (Mbytes/s)	3.43	2.82	2.82
TRT volume out (Mbytes/s)	4.69	3.12	3.13

Table 4.1: *Selected average values obtained from SIMDAQ. Results from runs with average fixed event fragment sizes as used in the paper model, with the average fixed event fragment sized obtained using the obsolete TDR geometries and with event fragment size distributions with the same mean values as the former, are compared.*

One of the inputs that SIMDAQ uses is a configuration file, detailing for how many system parts the simulation will be performed and how they will be interconnected. For each system part, the appropriate objects are instantiated. Furthermore, the configuration file includes the LVL1 trigger menus as well as distributions of processing times. Another configuration file includes a look-up table which maps ROBs to RoIs.

Separate distributions for endcap and barrel ROBs can be used, since it is possible to define an event fragment size distribution for individual ROBs and groups of ROBs.

Event fragment size distributions for the old obsolete TDR geometries (not shown in this chapter) were also generated to compare with earlier results from SIMDAQ and the Papermodel. SIMDAQ was run in three ways. First, with mean values used in the 2001 paper model [66]. Second, with only the mean values of the distributions for the obsolete TDR geometries. The third run was performed using the full distributions for the TDR geometries.

4.5.1 SIMDAQ results

Hardly any difference can be seen between using mean values and distributions with the same mean values. Quantities like the LVL2 decision time and CPU utilisation of the LVL2 processors are almost the same.

In table 4.1 selected average values obtained from SIMDAQ are presented for the three runs at intermediate luminosity. The difference between using fixed mean values and using distributions for the event fragment size are hardly noticeable and can be accounted for by statistics.

4.6 Summary

In table 4.6 an overview of average event fragment sizes is presented for the mappings that seem appropriate to be used. The numbers are given for low, intermediate and high

detector part	map name	low lumi	int. lumi	high lumi
SCT barrel	tower mapping A	180	308	1081
SCT endcap	tower mapping	141	239	822
Pixel barrel	layer mapping (fall 2001 geometry)	75	118	359
Pixel endcap	tower mapping (fall 2001 geometry) [a]	113	180	514
TRT barrel	barrel mapping	199	325	1106
TRT endcap	endcap mapping	204	330	1185

[a]The map chosen here has 8 modules/MUR, 3 MURs/ROB.

Table 4.2: *Average event fragment sizes for the preferred mappings. The name of the maps refer to the names used in Appendix A.*

luminosity. These numbers are realistic averages dominated by minimum bias background.

4.7 Conclusions and possible future work

In this chapter event fragment size distributions are presented for Pixel, SCT and TRT ROBs and for low, intermediate and high luminosity. Distinction is made between endcap and barrel ROBs. Distributions for fall 2001 geometries arising from the use of a new insertable Pixel layout, are given. Conclusions that can be drawn are:

- The average event fragment sizes of endcap ROBs and barrel ROBs differ significantly in some cases. This is not taken into account in previous versions of the paper model or computer models.
- A new mapping is introduced for the insertable layout geometry of the Pixel detector. The mapping is chosen such that the mean of the event fragment size distributions for ROBs of the Pixel detector is roughly the same as in the TDR geometry. The new Pixel detector endcap mapping is dictated by the fact that the number of MURs/ROB is the same as in the TDR mapping.
- The difference between using fixed event fragment sizes or event fragment sizes chosen from a distribution has a negligible effect on the results obtained with SIMDAQ.

Regarding possible future work with this software one can think of the following:

- The software written to extract the event fragment size distributions from data samples, can also be used for other detectors, such as the electromagnetic calorimeter or the muon precision tracker.
- Instead of making a distinction between barrel and endcap ROBs, one can extract for each ROB an individual distribution, which subsequently can be used in SIMDAQ.
- In the software used in this study, each object representing a ROB has associated with it an η - ϕ range. It is therefore possible to combine this information with for instance ATRIG to identify RoIs. Distributions for different classes of RoIs, such a jet-RoIs or isolated muon RoIs can subsequently be generated.

The first two suggestions may not be that worthwhile to pursue in view of the negligible effect of replacing fixed event fragment sizes by event fragment sizes according to a distribution. However, for the sake of completeness, these studies can be performed relatively easy using the software presented in this chapter. The study suggested in the last item may be beneficial to pursue, since the results in this chapter take into account all ROBs in a specific sub-detector, i.e. the distributions are dominated by background. Future work should establish whether the distributions presented here can also be used for data requested by the LVL2 trigger, i.e. for "RoI data".

Chapter 5

TRT zero suppression algorithm

In section 2.3.2 it was explained that some of the scenario's for the ATLAS B-physics trigger involve a full scan of the TRT detector, after a muon with $p_T > 6$ GeV accepted by the LVL1 trigger is confirmed by the LVL2 trigger using data from the muon spectrometer and Inner Detector. Subsequently, an unguided track search is performed in which all TRT ROBs (256) have to be read out [44]. Using the ROD data format [69], the total data volume produced by the scan in the output of the ROBs is typically 256 $\times$ 400 bytes = 100 kBytes. The LVL2 rate at which the muons are confirmed is $\sim$ 5 KHz, resulting in a required bandwidth of 500 MBytes/s. This high bandwidth makes the use of a zero suppression algorithm, optimised for a relatively high percentage of non-hit straws (which is the case at low luminosity running, where B-physics in ATLAS will be performed) of interest. In this chapter, a possible zero suppression algorithm is studied. It has been investigated whether it is feasible to run the algorithm in the ROBs. An implementation on the SHARC processor (see chapter 3) has been tested as well as an implementation on an Intel platform. The estimated LVL2 muon confirmation rate of 5 KHz restricts the algorithm to run within 0.2 ms. More details on the study presented in this chapter can be found in [74].

5.1 Data volumes and format

The layout of the TRT detector is described in section 2.2.1. The reader is reminded that the readout of the TRT barrel is segmented in 32 projective wedges in ϕ per half barrel. Data from one segment is read out into a single ROD. The 18 wheels of an endcap are divided into 96 readout segments. Each segment receives data from all 18 rings and covers 0.065 rad. in ϕ.

The data going into the RODs has a size of 27 bits per channel. It contains information from three consecutive bunch-crossing intervals (BXs). Per BX, one bit indicates the state of the high threshold discriminator. A signal exceeding the high threshold (5 keV) indicates a 'transition radiation candidate' (electron). The low threshold (0.2 keV) is used to identify *all* minimum ionising particles. The state of the low threshold is given by 8 bits per BX, each bit indicating the state in a 3.125 (=25/8) ns time window. The total input data volume per ROD including headers, trailers and byte alignment is about 50 kbits/event.

The data is transferred from the RODs to the ROBs. It is envisaged that there will be

a 1:1 correspondence between ROBs and RODs for the TRT. Before transmission to the ROB the data is compressed. Only data of validated straws is sent (see table 5.1). Straw data is declared 'VALID' when the low threshold is exceeded between 42.0 ns and 54.5 ns after the bunch crossing. The reason for this is as follows: each particle crossing the straw usually causes ionisation near the straw wall. The maximum drift time to the wire is 42.0 ns. The signal from the wire is delayed by the electronics by about 7-8 ns. Applying a narrow window between 42 ns and 54.5 ns allows efficient identification of the hits from the bunch crossing under investigation, while the number of accepted hits from neighbouring bunch crossings is minimised [35].

For straw data to be declared 'VALID', any of the last two low threshold bits of the second BX and the first two of the third BX have to be set. All other cases are defined as 'NOT VALID'. For 'VALID' straw data the number of leading edges (transitions from 0 to 1) in the low threshold bits for the first two BXs are determined. Depending on the number of leading edges the following data is transferred:

<11><ttt><ttt><H><T>	for two leading edges
<10><tttt><H><T>	for one leading edge
<01><1><L&H><T>	for zero leading edges

where:

<tttt> or <ttt>	are a 4-bit or 3-bit encoding of the location of the transition (from 0 to 1) bit.
<H> / <L>	are one bit ORs of all of the high / low threshold bits.
<L&H>	is a one bit encoding of all low and high threshold bits.
<T>	is one bit to indicate that a trailing edge occurred in the third BX.

If two leading edges are encountered in the same time-slice (BX) the first will be dropped and only the second edge will be encoded. In reference [73] it is shown that having a maximum of one edge per time-slice results in a negligible difference compared to the situation where all edges within one time-slice are counted. For 'NOT VALID' straws two bits are transferred if no low threshold bit is set, else four bits are transferred:

<00>	if no bit is set
<01><0><L&H>	if at least one bit is set

In table 5.1 an overview of the five possible formats of the TRT data sent to the ROBs is given. The ROB adds to each event fragment a header and trailer. The header is 32 bytes long, the trailer 12 bytes.

In [73] a slightly different scenario for data compression in the ROD (the "Istanbul" scenario) was described. An estimate of the difference between the "Istanbul" scenario and the scenario described here was made. For the mean values of percentage of straws with 0, 1 and 2 leading edges and the percentage of non-hit straws, it was found that the differences are small: the '"Istanbul" scenario results in about 5% smaller event fragment sizes. For the remainder of this chapter only the scenario outlined above has been used.

data type	<00>	<01><0>	<01><1>	<10>	<11>
validation	NOT VALID	NOT VALID	VALID	VALID	VALID
size (bits)	2	2 + 2	2 + 3	2 + 6	2 + 8

Table 5.1: *Different types of encoded straw data sent to the TRT ROBs.*

5.2 Zero suppression algorithm

In [69] an algorithm for data reduction in the ROB is presented. In this algorithm, only data for hit straws is sent to the LVL2 trigger. Each data item has an address header indicating the straw position. For both the barrel and endcap modules, eleven address header bits are needed to give each straw a specific header (2^{10} <1664< 2^{11}).
When this zero suppression algorithm is used, the data sent to the LVL2 trigger consists mainly of address header bits. An alternative algorithm, first suggested by N. Ellis [75], consists of replacing the address header by an offset header indicating the number of straws (*offset*) to the previous straw that has been hit. This offset header can be much smaller than eleven bits. The optimum offset header size N depends on the percentage of straws hit and the spread of the hit straws in a readout segment. If the offset between two hit straws is larger than 2^N straws, it is not possible to encode it in N bits. In that case, an extra data item has to be added to specify the offset to the header of the next hit straw.
In general, the zero suppression algorithm with offset produces a smaller output volume than the algorithm without offset. The former has the disadvantage that a larger number of processing steps per event is needed: for each non-hit straw the value of the offset counter has to be checked, and extra data items have to be copied to the output.

5.3 Generation of input data

The digitised output of the straws, i.e. the input for the RODs, has been simulated by feeding data generated by an event generator into the simulation of the electronics of the TRT readout. To create a realistic event data sample, two effects must be taken into account: multiple interactions in 1 bunch crossing and the fact that the readout time of the TRT is longer than the 25 ns gap between bunch crossings. Since the drift-time of the ions in the straw tubes spans several bunch-crossings, 4 bunch crossings before and 2 bunch crossings after the trigger bunch crossing are added to the event data. In each bunch crossing on average 2.3, 4.6 and 23 (Poisson distributed) hard interactions take place for low, intermediate and high luminosity, respectively. These possible extra interactions are also added to the event data. The samples used here are the same as in [73]. On the basis of the resulting events, digitised data was produced with the help of the digitisation routine for the TRT [73]. This routine has been modified to output x, y and z coordinates of the centre of hit straws as well as the ϕ segment (a number from 1-192) and the layer (a number from 1-300 for the barrel and 1-220 for the endcap) in which the hit straw is located.

To generate the input for the ROBs, the data must be compressed in the RODs according to method outlined previously. This has been done in two steps. First a database of straw positions, phi segments and layer numbers was created. In the second step the digitised

	barrel			endcap		
luminosity:	low	int	high	low	int	high
%<00>:	92.68	85.11	61.51	92.65	85.25	62.40
%<01><0>:	4.73	9.71	19.70	4.75	9.47	18.44
%<01><1>:	0.04	0.15	1.68	0.07	0.24	2.09
%<10>:	2.34	4.50	14.35	2.42	4.76	15.31
%<11>:	0.30	0.49	2.76	0.11	0.29	1.75

Table 5.2: *The different possibilities of ROD output data used as input for the zero suppression algorithm. The numbers are percentages. Due to rounding errors they do not exactly sum up to 100 %.*

data sample has been read in per event per ROD. A ROD spans 6 ϕ segments in the barrel and 2 in the endcap. The straws in the data sample have been compared with the straws in the database. If a straw was missing in the data sample (it was not hit) <00> is written, if a straw was present the correct ROD output was written. The output stream thus created is ordered in a layer-by-layer fashion. Average percentages of different possibilities of ROD output data (shown in table 5.2) agree nicely with the numbers found in [73], where a subset was used of the same data sample that is used here. The output data obtained in the way described has been used as input for the zero-suppression algorithm.

5.4 Implementation

The zero suppression algorithm has been implemented in C. The basic operations per event consist of copying the ROD header and trailer to the output, checking for each straw the type of data and copying data and header for hit straws to the output. If a straw has not been hit, a counter indicating the offset to the previous hit is incremented. The header for hit straws is formed by the N bit encoding of this offset counter. In addition, a check is made to see if the offset counter equals 2^N. If this is the case a N bit header with all bits set to 1 followed by two zero's is copied to the output. Time measurements have been made per event. A time stamp was set when the copying of the event header started, another one when the copying of the event trailer was done. So only the time spent in the algorithm was measured, no file operations or printout statements were included in the time measurement. In the implementation for the Pentium platform, the time stamps were obtained from assembler code with which the number of clock cycles since the computer booted was read out. Information on the CPU speed was then used to convert this number into ms. The difference in time, together with the event size, was copied to the event header to be read out later.
In addition, an implementation for the SHARC processor [48] (see also chapter 3) has been written. A SHARC processor on a SHaSLink [55] board was used. Also here the number of clock cycles was counted and later converted into ms. In the tests, only the data compression program was running on the SHARC. Assembler code specific to the SHARC has been used to execute operations such as bit-shifts and logical comparisons of bytes (the most time consuming parts of the algorithm). The rest of the code was identical to the

standard C implementation. For both implementations compiler optimisation options have been used.

5.5 Results

Distributions were made of the ratio of output and input size on an event-by-event basis. This was done for different header sizes N. The input sizes are standard ROD output format including headers and trailers. Distributions of the ratio of output and input size for the barrel, for low and intermediate luminosity are shown in fig. 5.1(a) and (b), respectively. The header sizes used were 5 and 4 bits for fig. 5.1(a) and (b), respectively. Due to the spread of hit straws in the input data stream, large tails are observed in the ratio distribution.

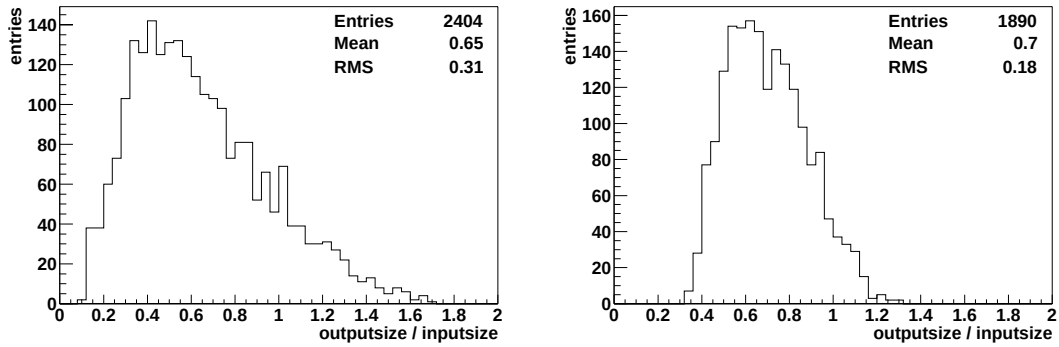

(a) (b)

Figure 5.1: *Ratio of output and input size per barrel ROB for low (a) and intermediate (b) luminosity running. 5 header bits are used were used for (a), 4 header bits were used for (b).*

The ratio per header bit for low luminosity running is shown in fig. 5.2(a) for the barrel and in fig. 5.2(b) for the endcap. The plots for intermediate luminosity running are presented in fig. 5.3. The horizontal line (in all four plots) gives the results in case of zero suppression *without* offset, i.e using an eleven bit address header for all hit straws.

The error bars in figs. 5.2 and 5.3 represent the RMS of the ratio distributions. For header sizes smaller than the optimal header size, the ratio is larger due to an increase in the number of extra data items (<11..1><00>). This results in a larger output. Above the optimal header size, the extra header bits that have to be sent for each hit straw result in a larger output. For the barrel the optimal header size for low luminosity is 5 bits, which gives a ratio of output/input size of 49.29%. The ratio with a 6 bit header size is almost the same (50.09%). For intermediate luminosity, the minimum ratio for the barrel (70.1%) is observed when a 4 bit header size is used. This ratio is larger than the typical ratios in the low luminosity case, since relatively more straws are hit, and thus the average number of sequential non hits is smaller. For the endcap, the optimal header sizes are 5 bits for low luminosity (ratio of 51.64%) and 4 bits for intermediate luminosity (ratio of 73.44%).

In fig. 5.4 the ROB input data size distributions are shown, for low and intermediate luminosity. The distributions for the input sizes are relatively narrow, the distributions for

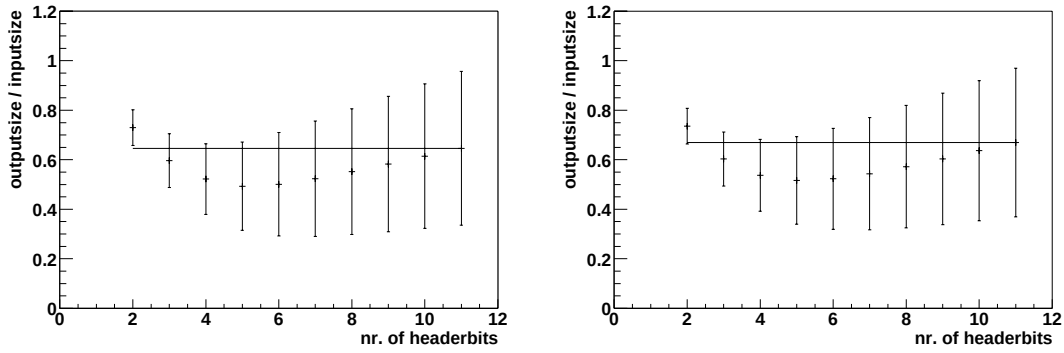

(a) (b)

Figure 5.2: *Ratio of output and input size per barrel (a) and endcap (b) ROB for low luminosity running, as a function of the number of header bits used in the zero suppression algorithm with offset. The error bars represent the RMS (root-mean-square) of the distributions.*

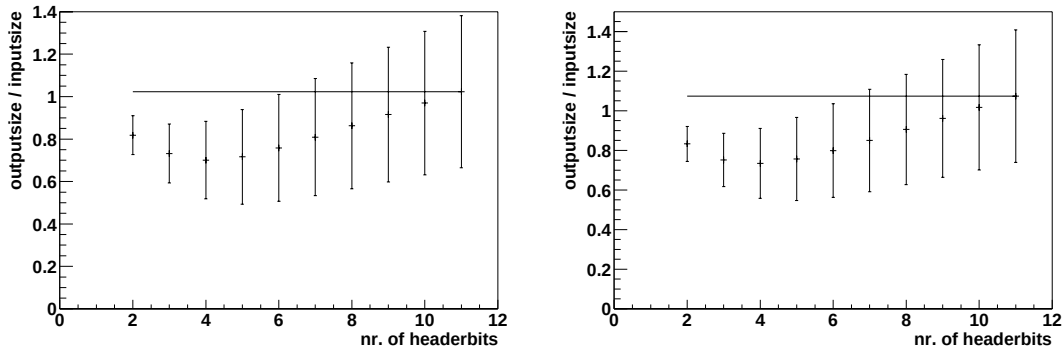

(a) (b)

Figure 5.3: *Ratio of output and input size per barrel (a) and endcap (b) ROB for intermediate luminosity running, as a function of the number of header bits used in the zero suppression algorithm with offset.*

the output sizes have a considerably larger width, see fig. 5.5. In fig. 5.5(a) the barrel ROB output data size distribution is shown for the optimal header size (N=5) for low luminosity and for intermediate luminosity (N=4). In fig. 5.5(b) the output size distribution is shown for endcap ROBs for low (N=5) and intermediate luminosity (N=4). The long tail in the output size distribution is a result of the large spread in percentages of hit straws. Large output sizes stem from relatively large numbers of non-empty straws.

5.5.1 Processing times

The processing time of the algorithm was measured on the SHARC processor (clock frequency 40 MHz) and on various Pentium based Linux systems. For the optimal header sizes for barrel and endcap data, the distribution of processing time on a 1 GHz machine is shown in fig. 5.6. The distributions of processing times for the optimal header sizes,

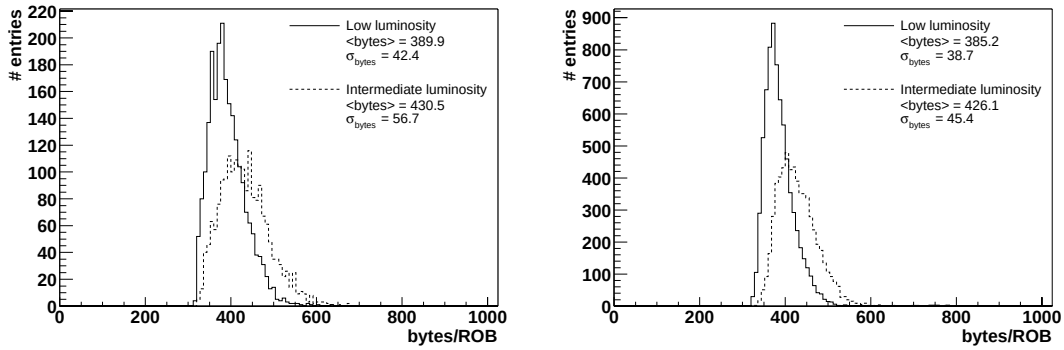

(a) (b)

Figure 5.4: *Distribution of input event fragment sizes per barrel ROB (a) and per endcap ROB (b). The distribution was made by looping over all appropriate ROBs. The solid line gives the distribution for low luminosity, the dashed line for intermediate luminosity.*

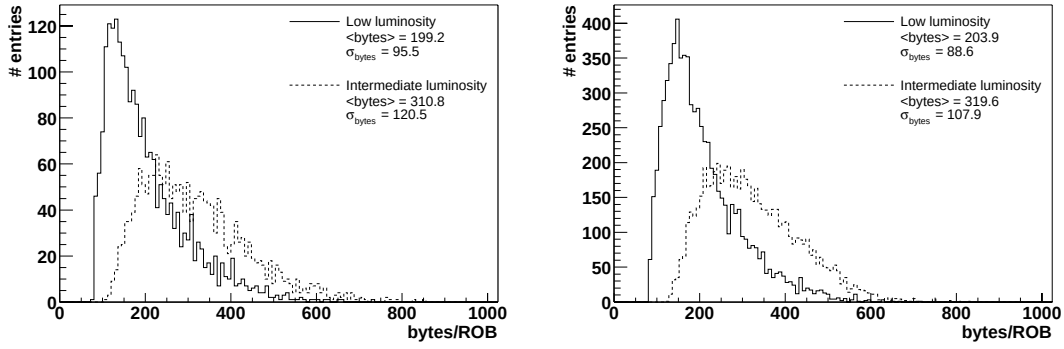

(a) (b)

Figure 5.5: *Distribution of output event fragment sizes per barrel ROB (a) and endcap ROB (b) where the zero suppression algorithm with offset has been used. For the barrel ROBs, the optimal number of 5 header bits for low luminosity (solid line) and 4 header bits for intermediate luminosity (dashed line) was used. For endcap ROBs, the optimal number of 5 header bits for low luminosity and 4 header bits for intermediate luminosity was used.*

running on a SHARC processor are shown in fig. 5.7.

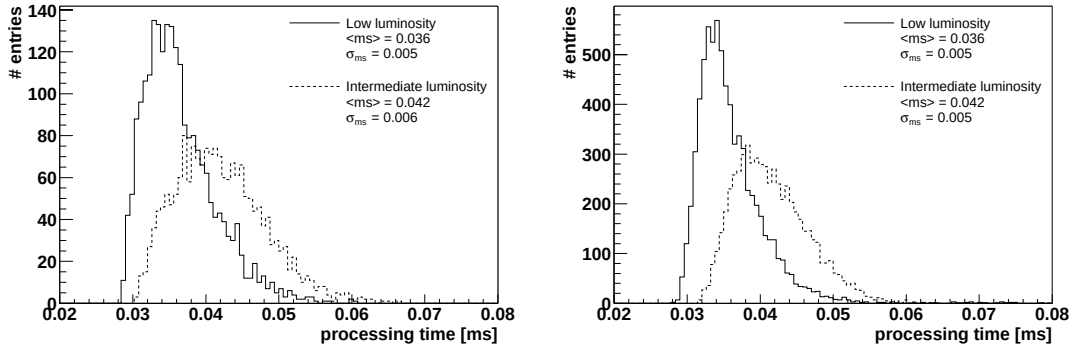

(a) (b)

Figure 5.6: *Distribution of processing times on a 1 GHz Pentium III system, for the optimal header size of 5 bits for low luminosity (solid line) and 4 bits for intermediate luminosity (dashed line), for barrel data (a). The same plot for endcap data, for a header size of 5 bits for low luminosity and 4 bits for intermediate luminosity (b).*

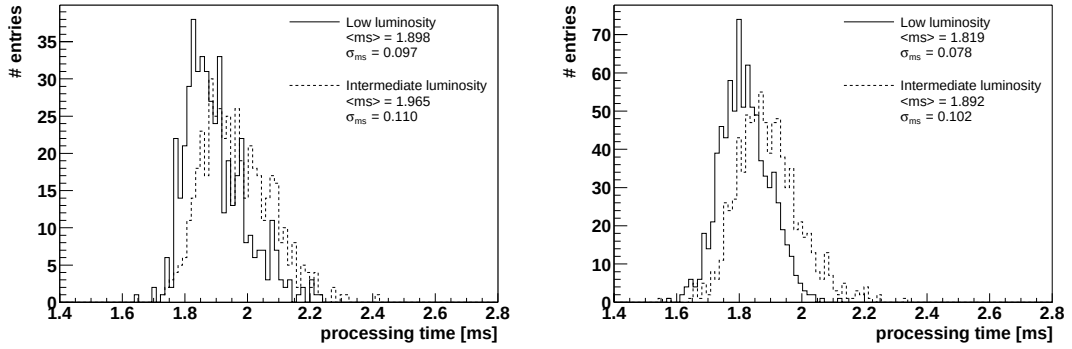

(a) (b)

Figure 5.7: *Distribution of processing times on the SHARC processor, for the optimal header size of 5 bits for low luminosity (solid line) and 4 bits for intermediate luminosity (dashed line), for barrel ROB data (a). The same plot for endcap ROB data, for a header size of 5 bits for low luminosity and 4 bits for intermediate luminosity (b).*

The distributions in fig. 5.7 look more Gaussian than the distributions in fig. 5.6. This can be attributed to two possible effects. First, no other processes were running on the SHARC processor, while the algorithm running on Pentium platforms had to share it's time with other processes of the operating system. Second, the architecture of Pentium processors differs significantly from that of the SHARC processor. The Pentium processor has a much longer instruction pipeline compared to the SHARC. If a jump in the code occurs, this long pipeline must be flushed, which can take a relatively long time.

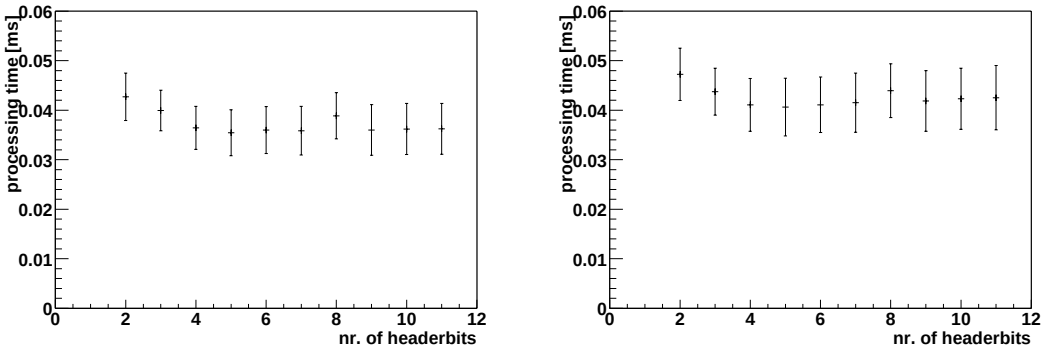

(a) (b)

Figure 5.8: *Mean and standard deviation of the processing time, measured on a 1 GHz Pentium III system, as a function of the number of header bits, for endcap data at low luminosity (a) and at intermediate luminosity (b).*

It was found that there is no significant dependence of the processing time on the number of header bits. This is shown in fig. 5.8 for the measurement performed on a 1 GHz Pentium III system for endcap data. The same plot for measurements performed on the SHARC processor looks similar, with processing times scaled accordingly.

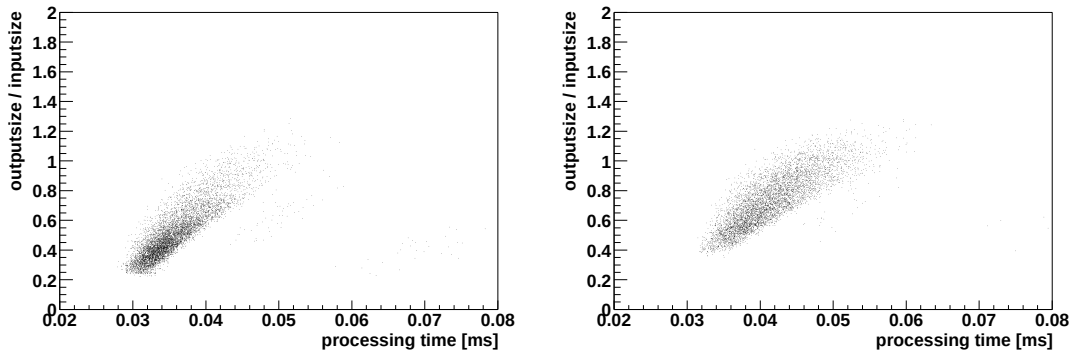

(a) (b)

Figure 5.9: *Scatter plot of the processing time on a 1 GHz Pentium III system as a function of the ratio of output and input size. The data used was for the endcap ROBs, at low luminosity running, with an optimal header size of 5 bits (a). The same plot for intermediate luminosity, with an optimal header size of 4 bits (b).*

For the measurements performed on a 1 GHz Pentium platform, the ratio of input size and output size versus the processing time, for the endcap ROBs, is shown in fig. 5.9 for low and intermediate luminosity. The plots show a weak dependence of the ratio of input and output size on the processing time. The average processing times on the different platforms are shown in table 5.3. A scatter plot was also made of the number of straws hit vs. the processing time. A clear linear dependence can be seen. A straight line fit through the data

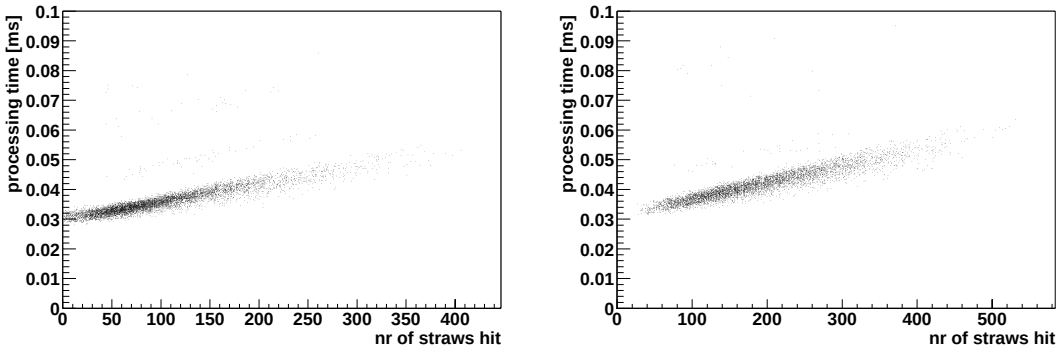

(a) (b)

Figure 5.10: *Scatter plot of the processing time on a 1 GHz Pentium III system as a function of the number of straws hit (seen by one ROB). The data used was for endcap ROBs, low luminosity, optimal header size of 5 bits (a). The same plot for intermediate luminosity, with an optimal header size of 4 bits (b).*

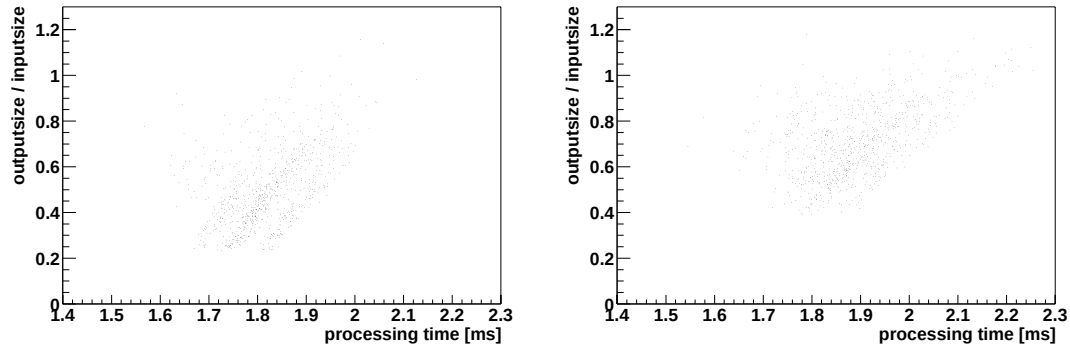

(a) (b)

Figure 5.11: *Scatter plot of the processing time on SHARC processor vs. the number of straws hit (seen by one ROB). The data used was for endcap ROBs, low luminosity, optimal header size of 5 bits (a). The same plot for intermediate luminosity, with an optimal header size of 4 bits (b).*

shows that of $\sim$ 50-60 ns is spent per straw, i.e. on the 1 GHz Pentium III system about 50-60 cycles per straw hit. The same data for the SHARC (fig. 5.11) shows that approximately 20-25 cycles are needed per straw. The difference is due to different architecture for the processors as well as different instruction sets and different speeds for transferring data to and from the memory. Differences in system and processor architecture cause the number of clock cycles for the various Pentium platforms to differ from each other (see table 5.3). For the processing time measurements performed on the SHARC processor, a subset of the total data sample was used. As a result of this lower statistics, the scatter plots in fig. 5.11 seem to have a somewhat larger spread. The "parallel lines' which can be observed in figs. 5.10 and 5.11 are probably due to effects of different execution paths in the algorithm.

processor	frequency [MHz]	processing time [ms]	# clock cycles
SHARC	40.0	1.82	6.69×10^4
PentiumII	450	0.082	3.62×10^4
PentiumIII	733	0.051	3.56×10^4
PentiumIII	1000	0.038	3.62×10^4
PentiumIV	1400	0.038	5.01×10^4
PentiumIV	1700	0.031	4.95×10^4

Table 5.3: *Average processing time per event for zero suppression with offset (using 5 header bits) for endcap ROBs for low luminosity, on different processors. In the last column the number average of clock cycles per event is given.*

5.6 Summary and conclusions

Results from the study presented in this chapter are summarised in table 5.4. Also included is the reduction factor obtained when the output size for the zero suppression algorithm is compared with the output size for an 11 bit address header. Note that although the clock on the Pentium system runs a factor of ~ 25 times faster than the clock of the SHARC processor, the processing time is a factor ~ 50 smaller. The difference is caused by the different architectures of the two systems.

	barrel		endcap	
luminosity	low	int	low	int
header size [bits]	5	4	5	4
output size [bytes]	199	311	204	320
ratio (output size/input size) [%]	49.3	70.1	51.7	73.4
reduction* [%]	23.7	31.5	23.0	31.6
Proc. time (SHARC) [ms]	1.90	1.97	1.82	1.89
Proc. time (1 GHz Pentium III) [ms]	0.036	0.042	0.038	0.042

Table 5.4: *Summary of the average of the most relevant parameters for the zero suppression algorithm for barrel and endcap, for low and intermediate luminosity (* w.r.t. 11 bit header, no offset).*

Several measurements with zero suppression algorithms for TRT data were conducted with and without offset on data sizes and processing times. The measurements were performed using the SHARC processor as well as on Pentium-based systems. The following conclusions can be drawn:

- With the data-sets used in this study, zero suppression with a 5-bit offset header for both endcap ROBs and barrel ROBs, gives a maximum reduction in data size for the full TRT scan for low luminosity. For intermediate luminosity, the optimal header size is 4 bits for both barrel and endcap ROBs. The zero-suppression processing time hardly varies with the header size.

- Zero suppression using the SHARC processor is too slow. On average, the processing time needs to be smaller than 0.2 ms. The processing times measured are 1.82 ms for endcap ROBs and 1.90 ms for barrel ROBs while running at low luminosity. In addition, also other tasks besides the zero suppression algorithm have to be executed on a ROB, such as handling incoming RoI requests and deleting events, thereby increasing the total processing time even more.
- Zero suppression on Pentium-processors can be done easily. Less than 50 μsecond per event, can already be achieved by a 1 GHz processor.
- Since the algorithm consists mainly of evaluating simple if-then-else statements and case statements, an implementation of the algorithm in FPGAs could be advantageous.

It is probably advantageous to move the zero suppression up to the RODs. At ROD-level the data is already compressed into the 'ROB format' (see section 5.1). Performing the zero suppression algorithm at this level can be done fast if it is possible to implement it in FPGAs. An additional advantage is the size reduction of all event fragments sent from ROD to ROB. The results of the study presented here depend on the order of reading out the straws. A layer-by-layer order (within one phi-segment) has been assumed. When this study was performed it was not clear whether this reflected the real read-out sequence. Recently however, an internal ATLAS note [76] has appeared which confirms that this is indeed the read out sequence foreseen for the TRT detector.

Chapter 6

B_C Production and decay

The B_c meson was discovered by the CDF collaboration at Fermilab in 1998 [77]. In the decay channel $B_c \to J/\psi + l + \nu_l$ (with $l = e, \mu$) $20.4^{+6.2}_{-5.5}$ events above background were found with a statistical significance of 4.8 standard deviations. The mass was determined to be 6.40 $\pm$ 0.39 (stat.) $\pm$ 0.13 (syst.) GeV and it's lifetime $0.46^{+0.18}_{-0.16}$(stat.) $\pm$ 0.03 (syst.) ps. Due to its composition (the heavy b and c quark), the B_c offers a unique testing ground for non-relativistic QCD (NRQCD). It is expected that the B_c will be copiously produced at the LHC; $\sim 10^8$-10^9 B_c's at an integrated luminosity of 10 fb^{-1}, which corresponds to one year of data taking at low luminosity.

In this chapter the production and decay of the B_c is discussed[1]. Emphasis is placed on the production of the B_c bound state through the fragmentation mechanism. First a general introduction to hadronic production of heavy quark mesons using the fragmentation approach is given in section 6.1. The parton fragmentation mechanism is described using NRQCD. This framework is discussed in sections 6.1.1 and 6.1.2. Subsequently, it is shown in section 6.1.3 that NRQCD correctly predicts the production rate of ψ' in hadronic interactions. Having established the validity of NRQCD with respect to heavy meson production, it is applied to $b \to B_c$ and $g \to B_c$ fragmentation in sections 6.1.5 and 6.1.6, respectively. Next, a comparison between the fragmentation approach and an $\mathcal{O}(\alpha_s^4)$ calculation is presented in section 6.1.7.
The spectroscopy of the B_c is described in section 6.2. The model for calculating the inclusive decay width and lifetime of B_c is discussed in section 6.3. The leptonic, semi-leptonic and non-leptonic decay of the B_c are considered in section 6.4. Branching ratios for the various decay modes are given. Finally, some possible CP violating modes are discussed in section 6.5. The fragmentation functions presented in this chapter, as well the modelling of the spectroscopy and decay channels, will be used in a Monte Carlo analysis in chapter 7. The analysis estimates the integrated and differential production cross sections of the B_c for both the Tevatron and LHC.

[1]Throughout this chapter, when a statement is made about a $\bar{b}$ quark or a bound $b\bar{c}$ state, implicitly the same statement applies to the charged conjugate state, unless stated otherwise.

6.1 Hadronic production of heavy mesons

A schematic overview for the production of mesons and baryons at hadron colliders is depicted in fig. 6.1. Partons from the proton are selected according to parton distribution functions (I) (PDFs), see 1.2.1. Subsequently, the partons undergo a hard interaction, denoted by $\otimes$. The hard interaction in case of b quark production has been discussed in chapter 1 (sections 1.2.2 and 1.2.4). Gluons (and photons) radiate from the partons that undergo the hard interaction (ISR) as well as from partons that emerge from the hard interaction (FSR). The radiated gluons can split into quarks which may radiate again. This is called the "parton shower" (II). In the parton shower, the partons loose energy. Subsequently, the partons hadronise into mesons and baryons, at an energy scale typically of the order of the mass of the hadrons formed (III). Finally, the hadrons decay into lighter hadrons, leptons or photons (IV).

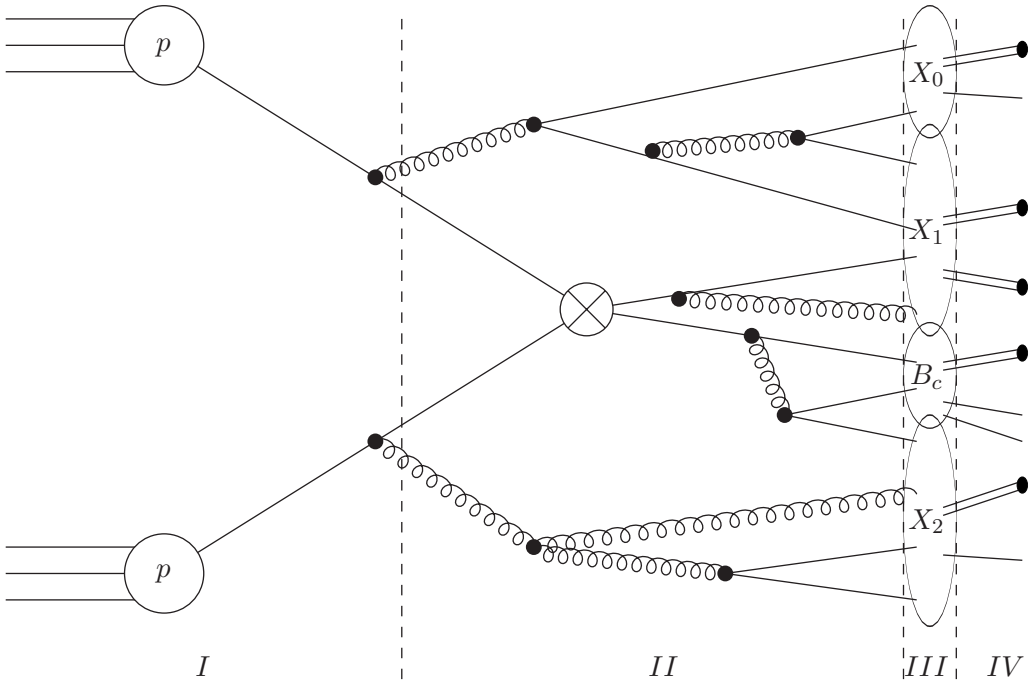

Figure 6.1: *Scheme for hadronic production of mesons and baryons. Four energy (distance) scales may be distinguished separated by dashed vertical lines. Partons from the incoming protons (I) undergo a hard interaction (denoted by $\otimes$). Before and after the hard interaction the partons may radiate gluons (and photons) which in turn can split into quarks (the parton shower) (II). Next, partons hadronise into baryons and mesons (III). Finally, the hadrons decay into leptons, photons or lighter hadrons (IV).*

The separation into several regions in fig. 6.1 relies on the principle of factorisation, which has been discussed in chapter 1 in section 1.2.

The formation of hadrons (III) from partons (II) is a process which is not well understood. The most widely adopted model is the Lund string fragmentation, in which colour strings between partons are assumed, which "snap" if the distance between the partons becomes too large. Depending on the energy of the resulting partons they can fragment again or form hadrons. The probability to form hadrons in this model is governed by a fragmentation function dependent on z which is "symmetric" in the sense that starting from one end of the string yields the same results as starting from the other end. An alternative model ("Independent fragmentation") assumes that the partons after the hard interaction, are disconnected (no colour string between them) and consequently the partons are hadronised separately. However, in the case of B meson production at e^+e^- colliders, is was found that the Peterson fragmentation function (see eq. 1.14), provides a better description. The parameter ϵ has to be fitted from the data. In the case of $c\bar{c}$, $b\bar{b}$ or $b\bar{c}$, the hadronisation process can be further factorised into two steps.

Starting with a heavy anti-quark $\bar{Q}^*$ from the hard interaction, a gluon is radiated which subsequently splits into a $Q\bar{Q}$ pair, see fig. 6.2(a) (also part(II) of fig. 6.1).

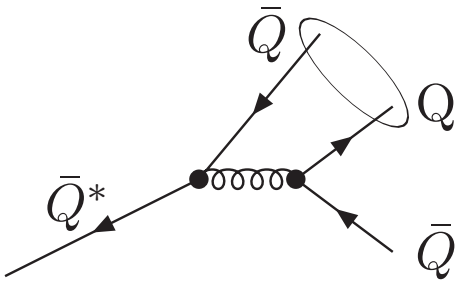

Figure 6.2: *Feynman diagram representing a heavy anti-quark $\bar{Q}^*$ fragmenting into a $Q\bar{Q}$ bound state at lowest order in α_s.*

The total momentum transferred in the gluon splitting is $q^2 \geq 4m_Q^2$ which is, in the case of $Q = c, b$, much larger than ${\Lambda^2}_{QCD}$, so perturbative calculations can be performed reliably. In contrast, the second step, the binding of the heavy quarks into a bound state (part (III) in fig. 6.1) is a non-perturbative process which is universal and is largely independent of q^2. The universal parameters governing this non-perturbative process can be inferred from measurements of the decay of the formed mesons.

The factorisation into perturbative and non-perturbative processes in the context of the $c\bar{c}$ bound state was already applied to describe the production of these mesons in 1993 [78]. The fragmentation functions that are derived in this way are a function of the variable z, where z denotes the fraction of longitudinal momentum of the bound state with respect to that of the fragmenting parton. The fragmentation functions also have a dependence on the factorisation scale μ_F and the renormalisation scale μ_R (see section 1.2). Fragmentation functions for heavy quark mesons can be derived using Non-Relativistic QuantumChromoDynamics (NRQCD). Sections 6.1.1 and 6.1.2 will discuss the NRQCD framework. Subsequently, it is shown in section 6.1.3 that fragmentation functions derived using NRQCD, correctly predict the production cross section for ψ'.

6.1.1 NRQCD framework

The production of heavy bound states can be described by the formalism of separating short distance and long distance scales. The short distance part represents a process which can be calculated perturbatively, while the long distance part represents the non-perturbative formation of a bound state. A model based on the separation formalism is the so-called "colour singlet model". Since a meson is a colour-less particle, the colour singlet model assumes that the quarks bind into a colour singlet state, as depicted in fig. 6.2. In the colour singlet model the production cross section for a ψ' is given by

$$d\sigma(c\bar{c} \rightarrow \psi' + X) = d\widehat{\sigma}(c\bar{c}(\underline{1}, {}^3S_1) + X)\ |R_{\psi'}(0)|^2 \tag{6.1}$$

where $d\widehat{\sigma}$ is the short distance cross section describing the creation of a $c\bar{c}$ pair in a colour singlet state (indicated by $\underline{1}$). The usual spectroscopic notation is adopted to indicate specific spin states: a state will be denoted by $n^{2S+1}L_J$, where S is the intrinsic spin and L is the orbital momentum. The total spin J ranges from $L+S, L+S-1, .., |L-S|$ and n is the principal quantum number giving the radial excitation. The L=0, L=1 and L=2 states are indicated by S, P and D, respectively. In eq. 6.1 $|R_{\psi'}(0)|^2$ is the square of the radial wave function at the origin which gives the probability that the colour singlet $c\bar{c}$ will form a ψ' bound state at the long distance scale.

The colour singlet model has large predictive power: the production cross section of quarkonium is predicted in terms of a single non-perturbative parameter, the radial wave function at the origin, for every orbital-angular-momentum multiplet. In general for a quarkonium H the matrix element reads:

$$< O_1^H >= \frac{9}{2\pi}|\frac{d^l}{dr^l}R_l(0)|^2 \tag{6.2}$$

where l denotes the orbital momentum. From eq. 6.2 it follows that a L=1 (or P-wave) state is proportional to the first derivative of the radial wave function at the origin, $|R(0)'|^2$. Furthermore, $|R(0)^2|$ can be determined from measurements, for instance the width for the decay of ψ' into e^+e^- can be written as:

$$\Gamma(\psi' \rightarrow e^+e^-) \approx \frac{4\alpha_s^2}{9m_c^2}|R_{\psi'}(0)|^2; \tag{6.3}$$

The colour singlet model however, does not give a complete description of the production or decay of a quarkonium state. It was already pointed out in 1976 [79] that the perturbative calculation of decays of P-wave state quarkonium gives rise to logarithmic divergences. For instance, in the decay of $\chi_{cJ} \rightarrow q\bar{q}g$, a divergence occurs when the energy of the radiated gluon goes to zero. After taking into account all possible diagrams, and after integration over phase space a logarithmic divergence remains. This divergence can not be factored into the long distance factor $|R'(0)|$ [80].

The solution to the problem of logarithmic divergences was given by Bodwin, Braaten and Lepage [80]. They proposed that after radiating the soft gluon from either the c or $\bar{c}$ in

the ^3P_J bound state, the $c\bar{c}$ pair is in a colour octet $^3S_1$ state. It then annihilates through the process $c\bar{c} \to q\bar{q}$. The annihilation of the $c\bar{c}$ pair in the colour octet state $^3S_1$ is thus the short distance (perturbatively calculable) part of the decay amplitude. Therefore, for the total χ_J decay amplitude a colour octet term is needed, in addition to the conventional colour singlet term. The colour octet term is factorised in the short distance annihilation process $c\bar{c} \to q\bar{q}$ and a long distance factor $|R(0)'|^2$ which gives the probability for the χ_{cJ} to contain a point-like $c\bar{c}$ pair in a colour octet state.

For the *production* of a P-wave charmonium state a similar argument holds. The factorised expression for P-wave state charmonium production can be written as:

$$\begin{aligned} d\sigma(c\bar{c} \to \chi_{cJ} + X) &= d\widehat{\sigma}(c\bar{c}(\underline{1}, {}^3P_J) + X)\ |R'_{\chi_c}(0)|^2 \\ &\quad + (2J+1)\ d\widehat{\sigma}(c\bar{c}(\underline{8}, {}^3S_1) + X)\ \langle O_8^{\chi_c} \rangle. \end{aligned} \tag{6.4}$$

The first term stems from the colour singlet model, where the short distance factor is the cross section for producing a $c\bar{c}$ pair in a colour singlet ^3P_J state while the long distance factor is proportional to $|R'(0)|^2$. The second term is the colour octet contribution. The short distance factor in this term is the cross section for producing a $c\bar{c}$ pair in a colour octet $^3S_1$ state. The long distance non-perturbative factor $< O_8^{\chi_c} >$ is proportional to the probability for a a $c\bar{c}$ pair in a colour octet $^3S_1$ state to form a χ_c. Eq. 6.4 holds to all orders in perturbation theory in the non-relativistic limit. This is the limit in which the typical relative velocity of the quarks in the meson with respect to the common centre of mass, $v(c \equiv 1)$, goes to zero.

In the following, the role of the velocity v as an "ordering" parameter in NRQCD will be explained. It will be made plausible that relativistic corrections can be added systematically by expanding the long distance matrix elements in powers of v.

6.1.2 Scaling in NRQCD

In NRQCD three energy scales play an important role: the mass of the heavy quark m_Q $(Q = c, b)$, the three-momentum $m_Q v$ in the meson rest-frame and the kinetic energy $m_Q v^2$. Lattice QCD calculations as well as quark potential models estimate $v^2 \sim \frac{1}{3}$ for charmonium and $v^2 \sim \frac{1}{10}$ for bottomonium. NRQCD assumes that these three energy scales are well separated: $(m_Q v^2)^2 << (m_Q v)^2 << m_Q^2$. The inverse of the scales gives the hierarchy in distances (with $\bar{h}$=c=1). $1/m_Q$ gives the short distance scale at which annihilation or production of the partons takes place. Perturbative QCD can be used here, because, for instance, $\alpha_s(m_Q) \sim 0.18$ for bottomonium. The inverse of the lower momentum scale $m_Q v$ is identified with the size of the bound state. The scale $m_Q v^2$ is typically of the order of the transition energy between radial excitations and between orbital-angular momentum excitations.

NRQCD is an effective field theory in which the heavy quark fields are decoupled from the light quark fields. The decoupling is necessarily an approximation which can be made more accurate by including more terms in the NRQCD Lagrangian. The expectation values of operators in the NRQCD Lagrangian can be estimated with the so-called "velocity scaling

rules". The expectation value of the heavy quark field ψ for example, can be estimated by $m_Q v^{\frac{3}{2}}$ while the expectation value of a covariant derivative can be estimated by $m_Q v^2$ [80]. The number of terms in a NRQCD calculation is determined by the desired accuracy. Usually only the leading order terms will be used in the calculation of a fragmentation function.

The emerging picture is then that a fragmentation function for a general quarkonium H is factorised into two parts:

$$D_{"parton"\to H}(z,\mu) = \sum_n d_n(z,\mu) < 0|O_n^H|0 > \tag{6.5}$$

where $d_n(z,\mu)$ describes the short distance terms which can be expanded in α_s. The long distance parts are represented by $< 0|O_n^H|0 >$ and can be expanded in v^2. Again z is the longitudinal momentum fraction of the bound state relative to the fragmenting parton while μ is the factorisation scale. The configuration of colour and angular momentum states is labelled by n.

Eq. 6.5 is an expansion in v^2 ($< \mathcal{O}_n^H >$) and α_s ($d_n(z,\mu)$). Thus, it may happen that a process A with order α_s^3 and v^2 can contribute at the same order as process B which is of lower order α_s^2, but is suppressed by a higher order v^4.

6.1.3 ψ' production

In chapter 7 the B_c production cross section will be predicted using fragmentation functions based on the NRQCD framework. Since v and α_s for B_c are smaller than in the case of ψ', NRQCD should assure more accurate predictions for the heavier meson. In this section it is shown that the measured ψ' cross section at the Tevatron is correctly predicted by NRQCD. This gives confidence that the predictions for the LHC presented in chapter 7 are sensible.

At first sight, it would be more natural to look for possible evidence of an octet mechanism in the production of J/ψ since the cross section is larger than that of ψ'. However, ψ' is a better choice since its cross section does not have contributions from decays of higher excited $\bar{c}c$ states. From fig. 6.3, where the hierarchy of $\bar{c}c$ states is shown, it is obvious that the mass of the ψ''s is larger than that of any of the χ_{cJ} states. Contributions from the decay of even heavier $\bar{c}c$ states can be excluded since their mass is above the threshold for the decay into two D mesons. Furthermore, only prompt production has to be considered, i.e. ψ''s originating from the decay of B mesons can be excluded by removing events with a displaced vertex. Finally, the narrow ψ' and J/ψ resonances have different invariant masses.

When the production cross section of ψ' calculated by the colour singlet model was compared to measurements, the measurements showed a result which was ~ 30 higher than that predicted by the color singlet model [81], [82]. This can be understood by analysing the gluon fragmentation function. In analogy with eq. 6.5 the $g \to \psi'$ fragmentation function can be written as:

$$D_{g\to\psi'(z,\mu)} = \sum_n d_n(z,\mu) < 0|O_n^{\psi'}|0 > \tag{6.6}$$

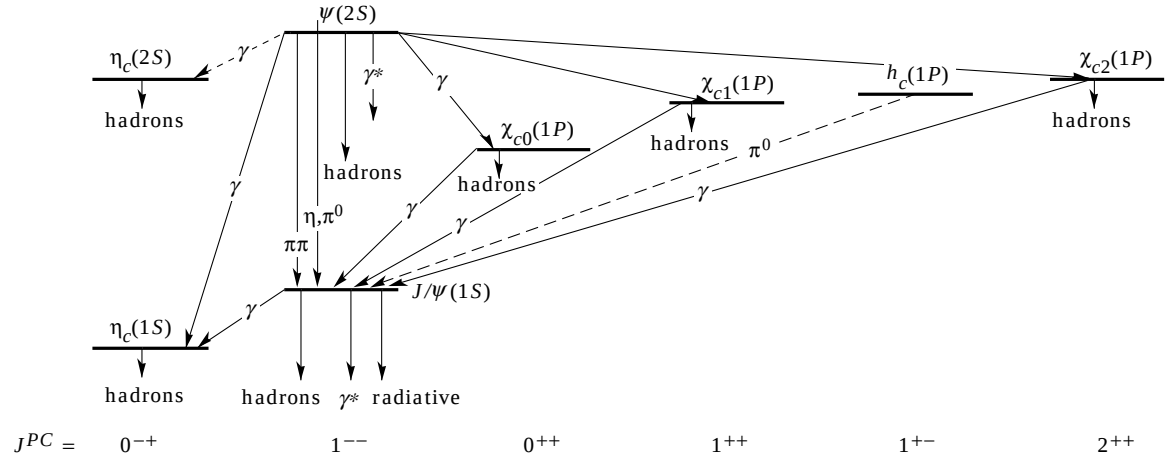

Figure 6.3: *The spectrum of charmonium states with possible radiative transitions. The measured cross section from J/ψ has contributions from the decay of χ_{cJ} states and other heavier states. For the ψ' $(= \psi(2S))$ state, these contributions are absent. Figure taken from [1].*

where $d_n(z,\mu)$ and $< 0|O_n^{\psi'}|0 >$ have the same meaning as in eq. 6.5. The short-distance factor $d_n(z,\mu)$ associated with the long distance matrix element $<O_1^{\psi'}(^3S_1)>$ is of order α_s^3, since evolving from the point-like colour singlet state to the final colour singlet S-wave state requires emitting two gluons to correctly conserve spin and colour quantum numbers, as is illustrated in fig. 6.4(a).

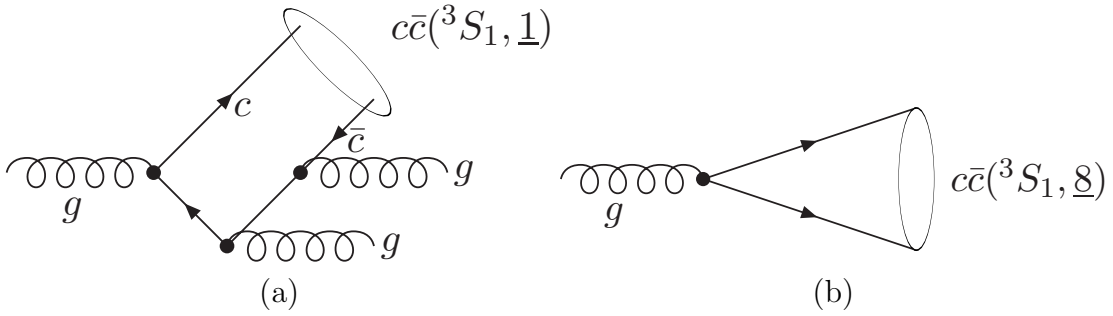

Figure 6.4: *Gluon fragmentation into S-wave point-like $\bar{c}c$ singlet state (a). To match spin and colour in the point-like and final state, two gluons must be radiated. The point-like state will evolve to the ψ' state with a probability $<O_1^{\psi'}(^3S_1)>$. Gluon fragmentation resulting in a point-like S-wave colour octet state (b). The evolution to the colour singlet state involves radiating or absorbing soft gluons. The probability of forming ψ' from this state is given by $<O_8^{\psi'}(^3S_1)>$*

The leading matrix element $<O_1^{\psi'}(^3S_1)>$ is of order $m_c^3 v^3$ [80], thus the total fragmentation function scales as $\alpha_s^3 v^3$. All other matrix elements are suppressed by additional powers of v. If the virtual gluon splits into a point-like colour octet state, $g \to c\bar{c}$, see fig. 6.4(b), the short distance part is of order α_s, two orders of α_s less than in the point-like colour

singlet case. The leading long distance matrix element for the octet case is $<O_8^{\psi'}(^3S_1)>$ which scales like $m_c^3 v^7$ [80]. The enhancement by two powers of α_s can be sufficient to counter the decreasing effect of the additional v^4 from the long distance matrix elements.

The ψ' differential production cross section measured by CDF was fitted using the theoretical expression for the singlet and octet contributions. The non-perturbative parameter of the latter was adjusted so that the theoretical prediction agreed to the data [83], resulting in $<O_8^{\psi'}(^3S_1)> = 0.0042\ GeV^3$. This value conforms to what is predicted by NRQCD: the $<O_8^{\psi'}(^3S_1)>$ is suppressed by v^4 with respect to $<O_1^{\psi'}(^3S_1)>$.

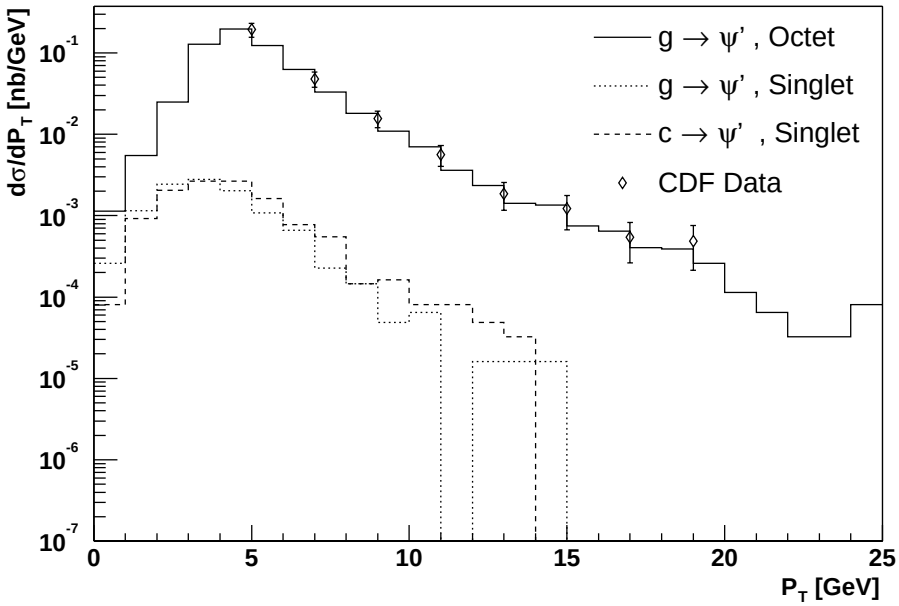

Figure 6.5: *Contribution of gluon octet (solid line), c quark (dashed line) and gluon singlet (dotted line) fragmentation functions to the differential production cross section of prompt ψ'. The gluon octet fragmentation contribution dominates the differential cross section. The data points are measurements from CDF. See also [84].*

As is illustrated in fig. 6.5 the gluon octet component in the gluon fragmentation function completely dominates the ψ' differential production cross section. The histogram with the solid line represents the contribution from the octet gluon fragmentation function only. The contributions from c quark fragmentation and gluon fragmentation to a point-like colour singlet state are the histograms with the dashed and dotted line respectively. The histograms are generated using the Monte Carlo event generator ARIADNE [24] with the appropriate parameters for the ψ' fragmentation functions. The data points are measurements from CDF [85]. Only prompt ψ' production was considered, contributions from B decays were excluded by removing events where the ψ' was associated with a secondary vertex. A rapidity cut of $|y^{\psi'}| < 0.6$ was imposed as well as a cut on the transverse momentum of the ψ', $p_T > 5$ GeV.

NRQCD provides an excellent explanation for the experimentally observed ψ' cross

section.

6.1.4 B_c formation

In this section the production of the B_c in terms of fragmentation functions derived with the framework of NRQCD is discussed. Since NRQCD correctly predicts the ψ' production cross section, it also should lead to a valid prediction for the B_c production cross section. Even more so, since the perturbative parameters involved, α_s and v, have smaller values for B_c ($\frac{1}{10} < v^2 < \frac{1}{3}$) than in the case of ψ' ($v^2 \sim \frac{1}{3}$) production. The b quark and gluon fragmentation processes into B_c at lowest order in α_s are shown in fig. 6.6(a) and 6.6(b), respectively.

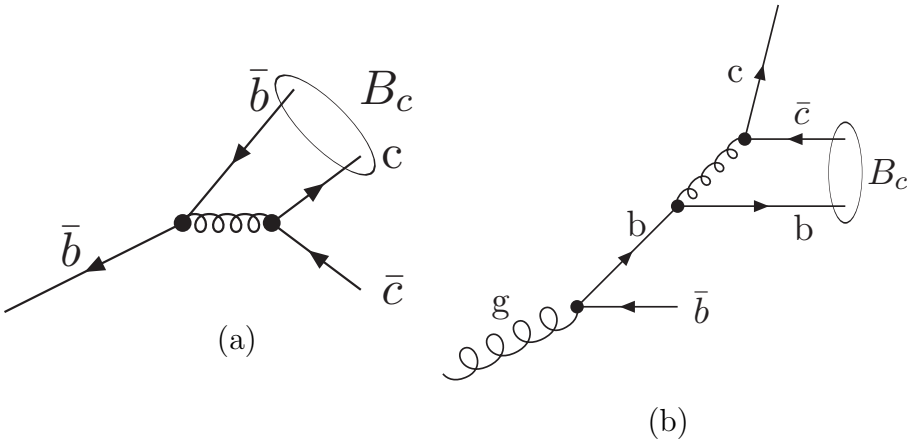

Figure 6.6: *Fragmentation of a b quark (a) and gluon (b) into B_c at lowest order in α_s.*

The main difference with respect to ψ' production is that no $\mathcal{O}(\alpha_s)$ gluon fragmentation can take place. Instead, the lowest order gluon fragmentation contribution to B_c production is at the level of α_s^3. Therefore, a very large α_s colour octet component, as encountered in the production of ψ', will be absent. A colour octet contribution is however present in the production of P-wave B_c states. In this case a $c\bar{c}$ pair is produced in a colour octet $^3S_1$ state at the short distance scale. Subsequently, a gluon is radiated at the long distance scale and a colour singlet ^3P_J state is formed. The n=1 and n=2 sets of S and P-wave B_c states have masses lower than the combined invariant mass of a B and a D meson. They decay strongly or electromagnetically to the $^1S_0$ ground state since decay into a B and D is forbidden. Therefore all these contributions should be taken into account when comparing with measurements of the B_c production cross section. S and P-wave fragmentation functions for $b \to B_c$ will be discussed in 6.1.5. Although the gluon fragmentation contribution is of $\mathcal{O}(\alpha_s^3)$, the large $gg \to gg$ cross section expected at the LHC can still lead to a sizeable $g \to B_c$ contribution. This is discussed in section 6.1.6.

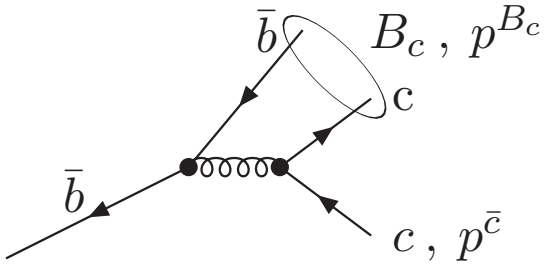

Figure 6.7: *Kinematical variables used in the derivation of* $b \to B_c(^1S_0)$.

6.1.5 $b \to B_c$ Fragmentation

In this section the derivation of the fragmentation function for $b \to B_c$, with B_c in the ground state, is outlined. Details of the derivation can be found in [86] and [87].
The diagram of fig. 6.7 is used to calculate the b quark fragmentation function. The four momentum of the B_c is p^{B_c} while the total four momentum for the production of a B_c and $\bar{c}$ is defined by $p^{tot} = p^{\bar{c}} + p^{B_c}$. To isolate the fragmentation function, the total production rate of a virtual $\bar{b}$ and the subsequent fragmentation into B_c (denoted by the matrix element squared $\mathcal{M}^2$) is divided by the production rate of a virtual $\bar{b}$ (denoted by the matrix element squared $\mathcal{M}_0^2$).

$$D_{\bar{b}\to B_c}(z,\mu_0) = \frac{1}{16\pi}\int ds\ \theta_{step}(s,z) \times \lim_{p^{tot}\to\infty}\frac{|\mathcal{M}|^2}{|\mathcal{M}_0|^2} \tag{6.7}$$

with the step-function:

$$\theta_{step}(s,z) = \theta\left(s - \frac{(m_b+m_c)^2}{z} - \frac{m_c^2}{1-z}\right) \tag{6.8}$$

When the momentum of the B_c is $p^{B_c} = (p_0^{B_c}, p_1^{B_c}, p_2^{B_c}, p_3^{B_c})$ in a frame where $p^{tot} = (p_0^{tot}, 0, 0, p_3^{tot})$, the longitudinal momentum fraction z is defined as $z = (p_0^{B_c} + p_3^{B_c})/(p_0^{tot} + p_3^{tot})$. If the limit $p^{tot} \to \infty$ is chosen in the Lorentz frame where only fig. 6.7 contributes, then $p^{tot}/p^{B_c} \to 1$. The lower bound on $s = (p^{tot})^2$ follows from

$$s = \frac{(m_b+m_c)^2 + p_T^2}{z} + \frac{m_c^2 + p_T^2}{1-z} \tag{6.9}$$

where $p_T = \sqrt{(p_1^{B_c})^2 + (p_2^{B_c})^2}$ and is implemented through the step function $\theta_{step}(s,z)$. The matrix element squared can be compactly written as [86]:

$$|\mathcal{M}|^2 = \frac{64\pi\alpha_s(\mu)|R(0)|^2}{27M}\frac{1}{r^2(s-m_b^2)^4} tr\left(\Gamma\bar{\Gamma}\Delta\right) \tag{6.10}$$

where $M = m_b + m_c$ and $r = m_c/(m_b+m_c)$. The amplitude for the production of $\bar{b}$ and c is projected onto the amplitude for a $^1S_0$ B_c state. The latter amplitude depends on the spin,

orbital momentum and radial excitation of the bound state. It is proportional to the radial wave function at the origin $|R(0)|$. The dependencies on the four vectors p^{tot} and p^{B_c} are contained in the Dirac matrix Δ. The production of a virtual $\bar{b}$ quark is given by the Dirac spinor $\bar{\Gamma}$. Its explicit form is not needed for the calculation, since it will cancel. The Dirac matrix is simplified by dropping higher order terms and by the substitution $p^{B_c} = zp^{tot}$.The square of the matrix element $\mathcal{M}_0$ is given by

$$|\mathcal{M}_0|^2 = tr[\Gamma\bar{\Gamma}(\not{p}^{tot} - m_b)] \tag{6.11}$$

In the fragmentation limit, $\not{p}^{tot} >> m_b$, so the mass m_b in eq. 6.11 can be ignored. The resulting expressions for $|\mathcal{M}|^2$ and $|\mathcal{M}_0|^2$ are subsequently inserted into eq. 6.7:

$$D_{\bar{b}\to B_c}(z,\mu) = \frac{4(\alpha_s(\mu))^2|R(0)|^2}{27\pi m_c^3}\int ds\theta_{step}\left(s - \frac{(m_b+m_c)^2}{z} - \frac{m_c^2}{1-z}\right)P(s,z) \tag{6.12}$$

with :

$$\begin{aligned} P(s,z) \;=& \frac{(1-z)(1+rz)^2 rM^2}{[1-(1-r)z]^2(s-m_b^2)^2} \\ &- \frac{[2(1-2r)-(3-4r+4r^2)z+(1-r)(1-2r)z^2]rM^4}{[1-(1-r)z](s-m_b^2)^3} \\ &- \frac{4r^2(1-r)M^6}{(s-m_b^2)^4} \end{aligned} \tag{6.13}$$

Finally the integral over s is evaluated:

$$D_{\bar{b}\to B_c}(z,\mu) = \frac{2(\alpha_s(2m_c))^2|R(0)|^2}{81\pi m_c^3}\frac{rz(1-z)^2}{(1-\bar{r}z)^6}\,Q(z,r) \tag{6.14}$$

with :

$$\begin{aligned} Q(z,r) \;=& 6 - 18(1-2r)z + (21-74r+68r^2)z^2 \\ &- 2\bar{r}(6-19r+18r^2)z^3 + 3\bar{r}^2(1-2r+2r^2)z^4 \end{aligned} \tag{6.15}$$

where $\bar{r} = 1-r$. The scale of α_s is set at the minimal virtual gluon mass for creating a $c\bar{c}$ pair, $2m_c$. A similar equation holds for the spin triplet S-wave state B_c^* and is given in appendix B.

The contribution of P-wave B_c states to the total B_c production cross section has been calculated to be $\sim$ 20 % [88],[89]. The P-wave state receives contributions from the production of the point-like P-wave colour singlet state and the S-wave colour octet state. From eq. 6.2 it follows that the long distance colour-singlet matrix element is proportional to $|R(0)'|^2$, which is in turn proportional to v^2. The evolution of the S-wave colour octet

state into the P-wave colour singlet bound state involves radiating or combining the octet state with a gluon, which has a probability proportional to v^2. Thus the singlet and octet contribution in the P-wave state are of the same order and must both be taken into account. To leading order in v^2 and all orders in α_s, this can be written as:

$$\begin{aligned} D_{\bar{b}\to\bar{b}c(n^1P_1)}(z,\mu) =& \frac{H_{1(\bar{b}c)}(n)}{m} D^{(1)}_{\bar{b}\to\bar{b}c(^1P_1)}(z,\mu) + \\ & 3\frac{H'_{8(\bar{b}c)}(\mu)}{m} D^{(8)}_{\bar{b}\to\bar{b}c(^1S_0)}(z) \end{aligned} \tag{6.16}$$

for the spin singlet (S=0) state, while for the spin triplet (S=1):

$$\begin{aligned} D_{\bar{b}\to\bar{b}c(n^3P_J)}(z,\mu) =& \frac{H_{1(\bar{b}c)}(n)}{m} D^{(1)}_{\bar{b}\to\bar{b}c(^3P_J)}(z,\mu) + \\ & (2J+1)\frac{H'_{8(\bar{b}c)}(\mu)}{m} D^{(8)}_{\bar{b}\to\bar{b}c(^3S_1)}(z) \end{aligned} \tag{6.17}$$

The factorisation scale μ is introduced to separate the short distance processes from the long distance matrix elements. H_1 and H'_8 are the non-perturbative long distance factors for the colour singlet and colour octet state, respectively and $m = (m_c m_b)/(m_c + m_b)$ is the reduced mass. The short distance factors $D^{(1)}(z,\mu)$ and $D^{(8)}(z)$ can again be calculated perturbatively. The scale dependence resides in $D^{(1)}$ and H'_8, and the factorisation scale μ is usually taken to be of the order of the reduced mass m. H_1 is invariant for variations in the scale μ (to order α_s). The fragmentation functions for the singlet and octet P-wave contributions are given in appendix B.

From eq. 6.2 it follows that H_1 is proportional to the derivative of the radial wave function at the origin:

$$H_{1(\bar{b}c)} \approx \frac{9}{2\pi}\frac{|R'_{nP}(0)|^2}{2m^4}[1+\mathcal{O}(v^2)] \tag{6.18}$$

$H'_{8(\bar{b}c)}$ satisfies the renormalisation group equation [80]:

$$\Lambda\frac{d}{d\mu}H'_{8(\bar{b}c)}(\mu) = \frac{16}{27\pi}\alpha_s(\mu)H_{1(\bar{b}c)} \tag{6.19}$$

which has a logarithmic solution:

$$H'_{8(\bar{b}c)}(\mu) = H'_{8(\bar{b}c)}(\mu_0) + \frac{16}{27\beta_0} ln\left(\frac{\alpha_s(\mu_0)}{\alpha_s(\mu)}\right) H_{1(\bar{b}c)} \tag{6.20}$$

with $\beta_0 = 2\pi b_0 = 9/2$ (with b_0 as in eq. 1.7) the first coefficient in the β function of QCD with three flavours of light quarks. A constant value is usually taken for $H'_{8(\bar{b}c)}(\mu)$ since the dependence on μ is very weak due to the logarithmic term (eq. 6.20).

For a given principal quantum number n, the $^1P_1$ state and $^3P_1$ states mix to form physical states, $|1^{+'}>$ and $|1^+>$:

$$|1^{+'}> = \cos\theta|^1P_1> - \sin\theta|^3P_1> \quad (6.21)$$
$$|1^+> = \sin\theta|^1P_1> + \cos\theta|^3P_1> \quad (6.22)$$

So in general the fragmentation functions for a $\bar{b}$ to the physical states $|1^{+'}>$ and $|1^+>$ B_c states are given by:

$$D^{(1)}_{\bar{b}\to\bar{b}c(1+')} = \cos^2\theta D^{(1)}_{\bar{b}\to\bar{b}c(^1P_1)}(z) + \sin^2\theta D^{(1)}_{\bar{b}\to\bar{b}c(^3P_1)}(z) - \sin\theta\cos\theta D^{(1)}_{mix}(z) \quad (6.23)$$
$$D^{(1)}_{\bar{b}\to\bar{b}c(1+)} = \sin^2\theta\ D^{(1)}_{\bar{b}\to\bar{b}c(^1P_1)}z) + \cos^2\theta D^{(1)}_{\bar{b}\to\bar{b}c(^3P_1)}z) + \sin\theta\cos\theta D^{(1)}_{mix}(z) \quad (6.24)$$

The mixing is small, for the first set of P-wave states, $\cos\theta_{mix} = 0.999$ and for the second set of P-wave states, $\theta_{mix} = 0.957$. The explicit expression for $D^{(1)}_{mix}(z)$ is given in appendix B.

Fragmentation functions for $\bar{b}$ to D-wave $\bar{b}c$ states have been derived in [90]. Again two D-wave states ($^1D_2$ and $^3D_2$) with the same quantum numbers mix to give two physical states. However, the mixing is very small and can be ignored. The D-wave states are suppressed by an additional factor v^2 originating from the second derivative squared of the radial wave function in the origin, $|R(0)''|^2$. The D-wave states contribute roughly 1-2 % to the total B_c cross section. These will be ignored in the remainder of this thesis.

The fragmentation functions of n=1 states are identical to n=2 states, except for the non-perturbative parameter, $|R_n(0)|^2$. For the S-wave states for instance:

$$\frac{|R_{2S}(0)|^2}{|R_{1S}(0)|^2} = \left(\frac{0.99}{1.28}\right)^2 \sim 0.6 \quad (6.25)$$

The probability of a c quark fragmenting into a B_c is suppressed and two orders of magnitude smaller than the probability of a b quark to fragment into a B_c since the fragmentation function in the latter case is $\propto 1/m_c^3$ instead of $1/m_b^3$. The fragmentation probabilities are summarised in table 6.1.
The fragmentation functions 1^1S_0, 1^3S_1, 1^1P_1 and 1^3P_0 are plotted in fig. 6.8(a) with the scale μ_R of α_s set to $2m_c$. The functions in fig. 6.8(a) are normalised to the total $b \to B_c$ probability $P_{tot} = 1.9 \cdot 10^{-3}$ from table 6.1. Clearly the 1^3S_1 state has the largest contribution and the P-wave states contribute little compared to the S-wave states. However, the distributions of the former are more peaked towards z=1.

For comparison the 1^3S_1 B_c^* fragmentation function is shown in fig. 6.8(b) together with the Peterson fragmentation function [15], already introduced in chapter 1:

$$D_{\bar{b}\to B}(z) \propto \frac{1}{z(1-\frac{1}{z}-\frac{\epsilon}{1-z})^2} \quad (6.26)$$

wave	state	probability	reference
S	1^1S_0	3.8×10^{-4}	[86]
	1^3S_1	5.4×10^{-4}	
	2^1S_0	2.3×10^{-4}	
	2^3S_1	3.2×10^{-4}	
P	1^3P_0	2.3×10^{-5}	[87]
	1 1+'	4.4×10^{-5}	
	1 1+	4.8×10^{-5}	
	1^3P_2	5.6×10^{-5}	
	2^3P_0	3.0×10^{-5}	
	2 1+'	8.1×10^{-5}	
	2 1+	4.0×10^{-5}	
	2^3P_2	7.5×10^{-5}	
D	1^1D_2	6.7×10^{-6}	[90]
	1^3D_1	1.7×10^{-6}	
	1^3D_2	6.5×10^{-6}	
	1^3D_3	8.5×10^{-6}	
Total sum	P_{tot}	1.9×10^{-3}	

Table 6.1: *Overview of estimated fragmentation probabilities for $\bar{b}$ to split into S, P and D-wave $\bar{b}c$ states. $|1+'>$ and $|1+>$ are mixed P-wave states and represent the actual physical states. Mixed D-wave states are not given here, since the mixing can be ignored. The total probability of $b \to B_c$ is $P_{tot} = 1.9 \times 10^{-3}$.*

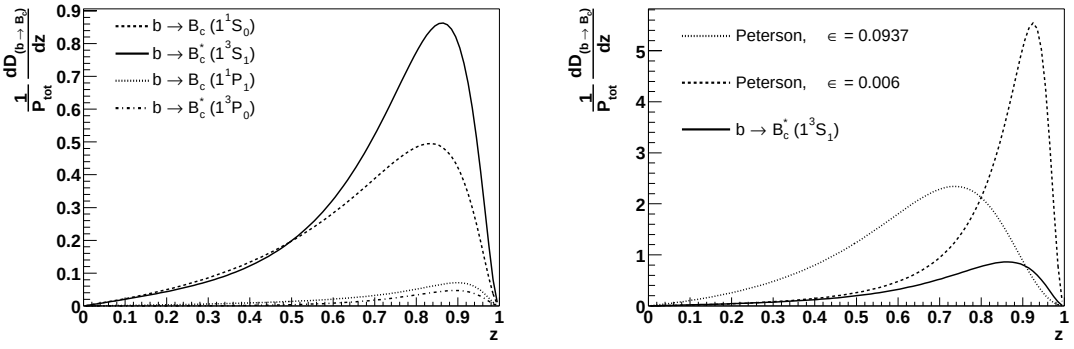

Figure 6.8: *Overview of the $b \to B_c$ fragmentation functions. In (a) the 4 functions $D_{\bar{b} \to \bar{b}c(1^1S_0)}(z)$, $D_{\bar{b} \to \bar{b}c(1^3S_1)}(z)$, $D_{\bar{b} \to \bar{b}c(1^1P_1)}(z)$ and $D_{\bar{b} \to \bar{b}c(1^3P_0)}(z)$ are drawn normalised to P_{tot}. For comparison the Peterson fragmentation function with two different values of ϵ is also plotted in (b), together with $D_{\bar{b} \to \bar{b}c(1^3S_1)}(z)$. The value ϵ=0.006 is commonly used to describe $b \to B_u, B_d, B_s$ fragmentation, while $\epsilon = m_c^2/m_b^2 \sim 0.0937$ would have to be used for B_c.*

The values for ϵ used for the Peterson fragmentation function in fig. 6.8(b) are $m_c^2/m_b^2 \sim 0.0937$ and ϵ=0.006. The latter is commonly used to describe $b \to B_u, B_d, B_s$ fragmentation. The Peterson fragmentation functions in fig. 6.8(b) are normalised in such a way that their total fragmentation probability is $1.9 \cdot 10^{-3}$.

6.1.6 $g \to B_c$ Fragmentation

The fragmentation functions $D_{b\to B_c}$ are derived at an initial scale μ_0, with μ_0 of the order of the heavy quark mass. At LHC (and Tevatron) the scale μ at which fragmentation production will be analysed is often higher than the initial scale μ_0, due to experimental event selection criteria. The evolution of the initial scale μ_0 to the higher scale μ is described by the DGLAP equations. These equations were already introduced in chapter 1, (eqs. 1.12, 1.13) in the context of the evolution of parton distribution functions. The same equations apply for the evolution of fragmentation functions. At leading order, the splitting kernels are also the same as in the case of parton distribution functions evolution:

$$\mu\frac{\partial}{\partial\mu}D_{\bar{b}\to B_c}(z,\mu) = \int_z^1 \frac{dy}{y}P_{\bar{b}\to\bar{b}}(z/y,\mu)\; D_{\bar{b}\to B_c}(y,\mu) + \int_z^1 \frac{dy}{y}P_{\bar{b}\to g}(z/y,\mu)\; D_{g\to B_c}(y,\mu) \tag{6.27}$$

$$\mu\frac{\partial}{\partial\mu}D_{g\to B_c}(z,\mu) = \int_z^1 \frac{dy}{y}P_{g\to\bar{b}}(z/y,\mu)\; D_{\bar{b}\to B_c}(y,\mu) + \int_z^1 \frac{dy}{y}P_{g\to g}(z/y,\mu)\; D_{g\to B_c}(y,\mu) \tag{6.28}$$

A gluon fragmenting into a b quark, in turn fragmenting into a B_c, represents an α_s^3 process, while direct $b \to B_c$ fragmentation is of $\mathcal{O}(\alpha_s^2)$, see fig. 6.6. Therefore, the fragmentation function $D_g \to B_c$ is set to zero at the initial scale μ_0. When eq. 6.28 is evolved, the induced gluon fragmentation functions $D_{g\to B_c,B_c^*}(z,\mu)$ become of order $\alpha_s^3\log(\mu/\mu_0)$ at a higher scale μ. At large enough scale μ, the logarithmic factor $\log(\mu/\mu_0)$ may compensate the extra power in α_s. The induced gluon contribution becomes effectively of order α_s^2, i.e. the same order as the direct b quark fragmentation functions. However, in [91] it is shown that the induced gluon fragmentation contribution increases slowly with the scale μ, and only at the very large scale of 0.8 TeV the contribution becomes $\sim 10\%$.

Since the $gg \to gg$ cross section is roughly 2 orders of magnitude larger than the $gg \to b\bar{b}$ cross section at LHC energies, the total $g \to B_c$ contribution is still sizeable (order of 30 %) compared to the $b \to B_c$ contribution.

In fig. 6.9 the probability of gluons fragmenting into the spin singlet 1^1S_0 and spin triplet 1^3S_1 $\bar{b}c$ states is shown as a function of scale μ (see also [91]). At a scale of $\mathcal{O}(M_{B_c})$ the probability of $g \to B_c$ is of $\mathcal{O}(10^{-6})$.

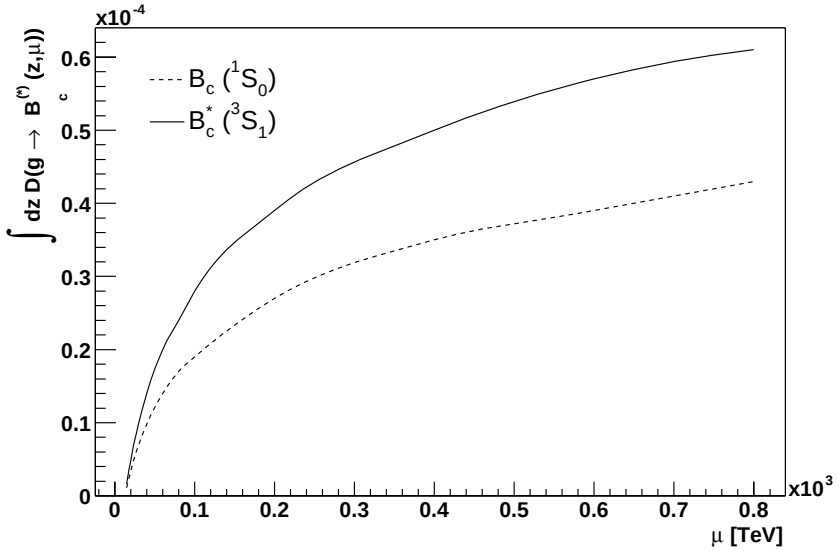

Figure 6.9: *Probability of $g \to B_c$ and $g \to B_c^*$ as a function of the evolution scale μ.*

6.1.7 Fragmentation approach and $\mathcal{O}(\alpha_s^4)$ calculations

$\mathcal{O}(\alpha_s^4)$ tree-level calculations for $g \to B_c c\bar{c}$ have also been performed. However, these calculations do not take into account divergences arising from soft non-perturbative physics or collinear divergences. The fragmentation approach does take into account these effects by absorbing the divergences into universal parameters. Furthermore, due to the factorisation inherent to the fragmentation approach, fragmentation functions can be implemented rather easily in Monte Carlo event generators. The latter is important for the study presented in chapter 7. The $\mathcal{O}(\alpha_s^4)$ calculation and the fragmentation approach should yield similar results when production at large p_T is considered.

The validity of the fragmentation approach has been questioned in several publications. $\mathcal{O}(\alpha_s^4)$ calculations in which 36 diagrams were taken into account, gave results which differ from the fragmentation approach. Several studies indicate, that recombination of the b and c quark is the main source for B_c production and that fragmentation only can be applied at a transverse momentum $p_T(B_c) \geq 6M_{B_c} \sim 40$ GeV (see [92] and references therein). Several perturbative calculations (refs 2,3,4,6 in [93]) gave inconclusive results.

However, in a paper by Kolodziej et al. [93] it was clearly shown that the fragmentation description provides a good approximation for $p_T \geq 10$ GeV. The deviation from the $\mathcal{O}(\alpha_s^4)$ results is much smaller than the uncertainties due to the choice of scale Q^2, the decay constant $f_{B_c^{(*)}}$ and the effective values of m_b and m_c.

In fig. 6.10(a) the differential production cross section of the ground state B_c is given as a function of $p_T(B_c)$, calculated following the fragmentation approach and the $\mathcal{O}(\alpha_s^4)$ calculation (solid lines) for both Tevatron and LHC energies, for a $p_T \geq 5$ GeV. In fig. 6.10(b) the integrated cross section is shown as a function of a p_T cut-off. Good agreement is observed.

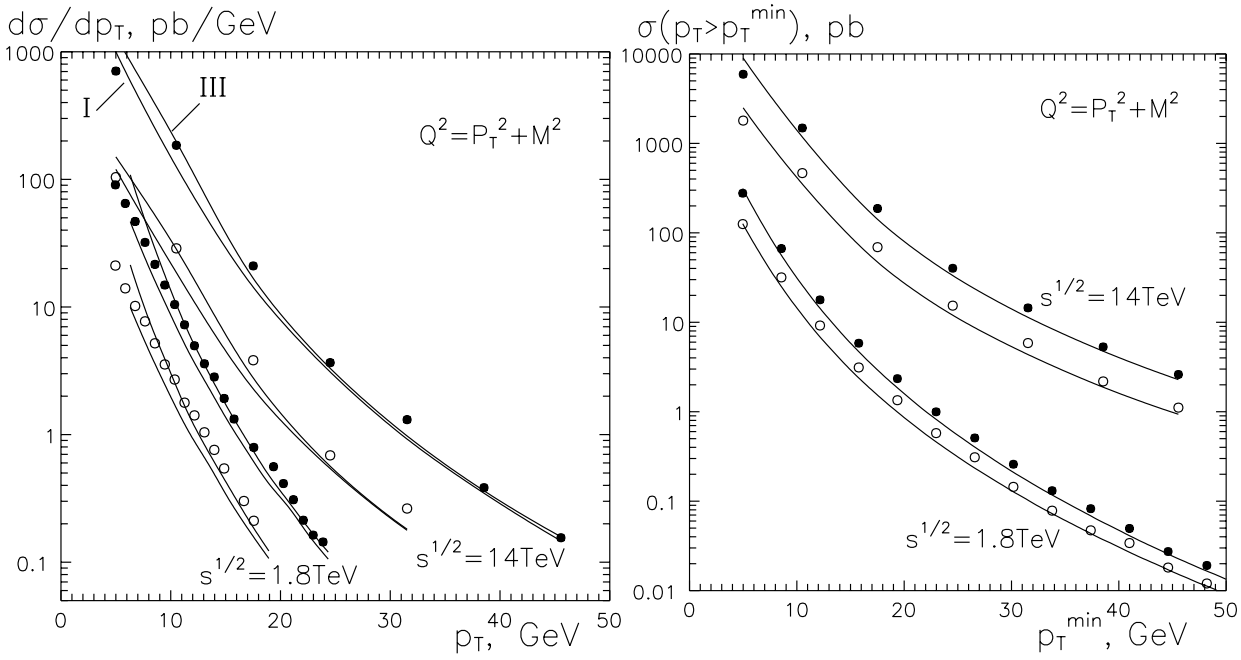

Figure 6.10: *Transverse momentum distribution of the ground state B_c at Tevatron and LHC energies (a): $\mathcal{O}(\alpha_s^4)$ tree level calculation (circles) and fragmentation approximation (solid curves). The labels I and III refer to a scale μ of order M and 0 respectively. At each energy, results are shown without a rapidity cut (full circles) and for $|y| \leq 0.5$ (empty circles). Integrated production cross sections for the B_c as functions of the minimum p_T cut (b): $\mathcal{O}(\alpha_s^4)$ tree level calculation (circles) and fragmentation approximation using μ of order m_b. For each energy, results are shown without a rapidity cut (full circles) and for $|y| \leq 1$ (empty circles) (Figures taken from [93]).*

6.2 B_c spectroscopy

The total cross section for B_c production is the sum of the direct production cross section and the cross section for production of excited states below the BD threshold. The excited states decay via electromagnetic or strong (emission of pions) interactions to the ground state.

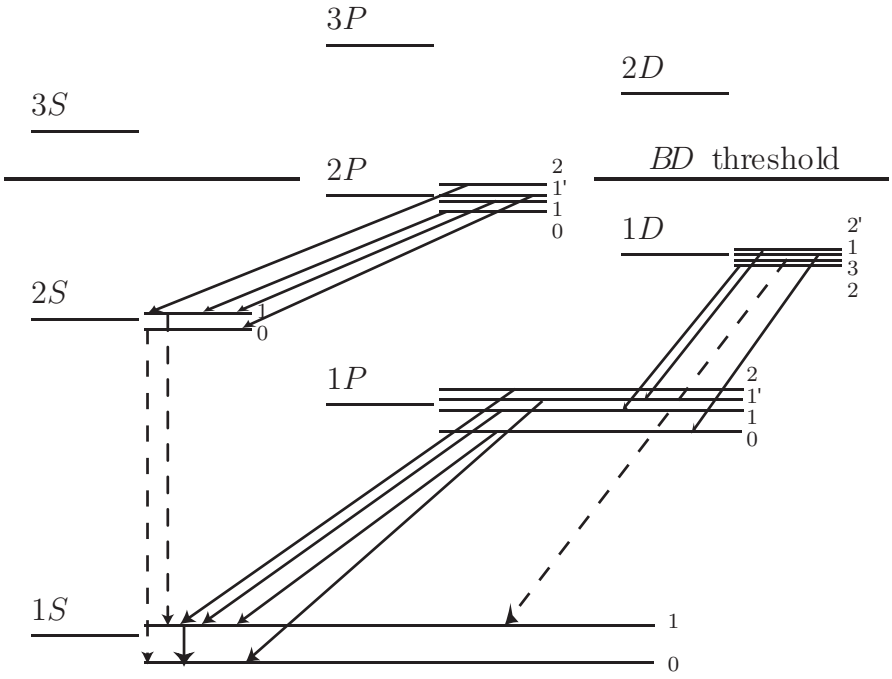

Figure 6.11: *The spectrum of $(\bar{b}c)$ states with the dominant transitions to lower lying states (see table 6.3). Solid arrows indicate radiative decay modes, dashed arrows indicate hadronic decay modes. The mass hierarchy corresponds to the entries in table 6.2.*

The masses of the various spin states have been calculated in the literature by several authors using quark potential models [94], [95], [96] and are shown in table 6.2.

As can be seen, the different approaches give consistent results. The hierarchy of the bound states in terms of their mass is shown in fig. 6.11.

The dominant decay modes of the 15 $\bar{b}c$ states that are predicted to lie below the production threshold of a B and D meson and above the ground state are given in table 6.3, together with their branching ratios [96]. Note that in some of the radiative decays, e.g. from $2^1S_0 \rightarrow 1^1S_0$ the mass difference between the two states is large enough to allow a hadronic decay including two pions.

6.3 Inclusive decays, B_c lifetime

This section gives a brief overview of the theoretical tools which are used to estimate the lifetime of the B_c meson. The total decay width of a B_c can be written as:

state	[94]	[95]	[96]
1^1S_0	6.253	6.264	6.270
1^3S_1	6.317	6.337	6.332
1^3P_0	6.683	6.700	6.699
$1P1$	6.717	6.730	6.734
$1P1'$	6.729	6.736	6.749
1^3P_2	6.743	6.747	6.762
2^1S_0	6.867	6.856	6.835
2^3S_1	6.902	6.899	6.881
1^3D_1	7.008	7.012	7.072
$1D2$	7.001	7.009	7.077
$1D2'$	7.016	7.012	7.079
1^3D_3	7.007	7.005	7.081
2^3P_0	7.088	7.108	7.091
$2P1$	7.113	7.135	7.126
$2P1'$	7.124	7.142	7.145
2^3P_2	7.134	7.153	7.156

Table 6.2: *Masses (in GeV) of bound $(\bar{b}c)$-states below the threshold for decay into a pair of heavy B, D mesons, calculated for models with different interquark potentials. The masses in the last column will be adopted for the analysis presented in chapter 7.*

state	dominant decay mode	BR (%)
1^3S_1 (B_c^*)	$1^1S_0+\gamma$	100
1^3P_0	$1^3S_1+\gamma$	100
$1P1$	$1^3S_1+\gamma$	81
$1P1'$	$1^1S_0+\gamma$	91
1^3P_2	$1^3S_1+\gamma$	100
2^1S_0	$1^1S_0+\pi\pi$	92
2^3S_1	$1^3S_1+\pi\pi$	77
1^3D_1	$1^3P_0+\gamma$	54
$1D2$	$1P1+\gamma$	65
$1D2'$	$1P1'+\gamma$	69
1^3D_3	$1^3S_1+\pi\pi$	76
2^3P_0	$2^3S_1+\gamma$	67
$2P1$	$2^3S_1+\gamma$	75
$2P1'$	$2^1S_0+\gamma$	74
2^3P_2	$2^3S_1+\gamma$	78

Table 6.3: *The fifteen $\bar{b}c$ states above the ground state, below the BD threshold and their dominant decay modes and branching ratios. $\pi\pi$ in a decay mode includes both $\pi^+\pi^-$ and $\pi^0\pi^0$ decays.*

$$\Gamma_{B_c} = \frac{1}{2M_{B_c}} \langle B_c | \mathcal{T} | B_c \rangle \equiv < \mathcal{T} > \tag{6.29}$$

where the transition operator $< \mathcal{T} >$ is related to an effective Hamiltonian describing the low energy weak decays of b and c quarks [97].
In the case of a heavy quark decay (for instance the b-quark) an Operator Product Expansion (OPE) can be performed on $\mathcal{T}$ in $1/m_b$, since the momentum of the internal propagators is large $\mathcal{O}(m_W)$. The OPE is then of the form [97]:

$$\mathcal{T} = \Gamma_b \bar{b} b + \frac{z_G}{m_b^2} \bar{b} g \sigma \cdot G b + \sum \frac{z_{qi}}{m_b^3} \bar{b} \Gamma_i q \; \bar{q} \Gamma_i b + ... \tag{6.30}$$

The first few operators include Γ_b and z_k, so-called Wilson coefficients, which contain perturbative QCD contributions. The other operators contain the non-perturbative part. From eq. 6.30 it can be seen that higher dimensional operators are suppressed by powers of $1/m_b^4$, therefore these can be ignored. The three terms are sketched in diagram form in fig. 6.12. The fat black dots in the diagrams correspond to effective low energy four-fermion operators. Basically the expansion in eq. 6.30 factorises the transition operator into a low energy weak four-fermion coupling multiplied by the Wilson coefficients in which the latter can be calculated perturbatively. The calculation of the Wilson coefficients is usually performed by matching a full perturbative calculation to the operator product expansion. The total transition operator of a B_c consists of a term from the b quark, see fig. 6.12(a), and an equivalent term from the c quark (not shown) as well as annihilation contributions. These last two involve what is called a W-annihilation (WA) and a Pauli Interference term. The latter processes are depicted in fig. 6.12 (c) and (d).

The first term in eq. 6.30, the matrix element $\bar{b}b$, can be expanded using HQET[2] [97]. Eventually this leads to [97]:

$$\Gamma_{B_c} = \Gamma_b \left(1 - \frac{v_b^2}{2}\right) + \Gamma_c \left(1 - \frac{v_c^2}{2}\right) + \Delta\Gamma_{PI} + \Delta\Gamma_{WA} + \mathcal{O}(v^4) \tag{6.31}$$

where, v (=v/c) is the velocity of the heavy quark with respect to the common centre of mass of the B_c. Thus to lowest order the sum of the two (weak) quark decays determines the total width, $\Gamma_{B_c} = \Gamma_b + \Gamma_c$. The first bound state corrections are of order v^2 : (1 - $v^2/2$), where $v_c^2 \sim 0.38$ and $v_b^2 \sim 0.035$ [98]. The corrections are interpreted as time-dilatation, i.e. the effect of binding compels the quarks to move around each other, thus retarding their decay. At $\mathcal{O}(v^3)$ the Pauli Interference and W-annihilation terms arise. The numerical evaluation of eq. 6.31 gives [98]:

$$\tau_{B_c} = \frac{1}{\Gamma_{B_c}} = 0.55 \pm 0.15 \; ps \tag{6.32}$$

[2]HQET stands for Heavy Quark Effective Theory, in which heavy quark and light quark fields and gluon fields are decoupled from each other

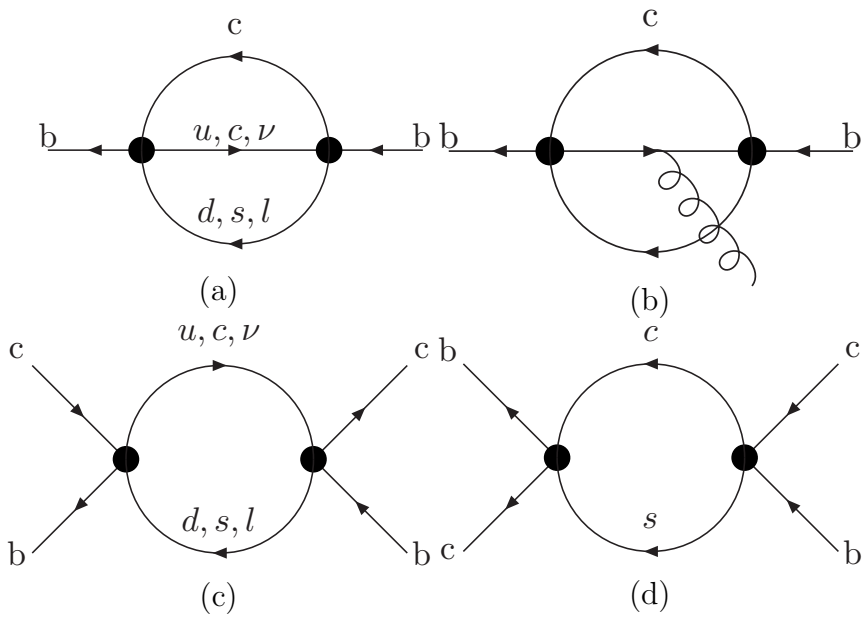

Figure 6.12: *Graphical representation of the Operator Product Expansion in eq. 6.30. (a) and (b) represent the first and second term of the expansion. Figures (c) and (d) both represent the third term in the expansion, W-annihilation and Pauli Interference, respectively. The fat black dots represent low energy four-fermion weak effective couplings.*

with the large uncertainty coming from the mass m_c. The calculated value agrees with the CDF measurement [77]:

$$\tau_{B_c}^{meas.} = 0.46^{+0.18}_{-0.16} \pm 0.03\ ps. \tag{6.33}$$

where the asymmetric errors are statistical and 0.03 ps is a systematic error[3]. With the method described above, inclusive decay rates can then be calculated. The charm quark decay width dominates over the b quark decay width largely due to the CKM matrix element $|V_{cs}|^2$, which is ~ 0.94 and is large compared to $|V_{bc}|^2$ (~ 0.002). Table 6.4 (taken from [99]) gives an overview of the inclusive decay rates. Apart from the branching ratios calculated with HQET, also the sum of exclusive decay rates in potential model calculations (PM) and derived from QCD sum rules (SR) is given.

6.4 Exclusive decays

As mentioned earlier, the excited $\bar{b}c$ states with masses below the threshold for decay into a B and D meson, decay via electromagnetic or strong interactions to the ground state.

[3]The asymmetry of the statistical error originates from the simulated contribution of the background to the measured parameter $c\tau$. Since only $B_c \to J/\psi + l + \nu_l$ decays were used in the measurement, different background process for two distance ranges were considered (-100 $< c\tau <$ 60 μm and $c\tau >$ 60μm). The former range also has contributions from "prompt" charmonium decays.

B_c decay mode	OPE, [%]	PM, [%]	SR, [%]
$\bar{b} \to \bar{c} l^+ \nu_l$	3.9 ± 1.0	3.7 ± 0.9	2.9 ± 0.3
$\bar{b} \to \bar{c} u d$	16.2 ± 4.1	16.7 ± 4.2	13.1 ± 1.3
$\sum b \to \bar{c}$	25.0 ± 6.2	25.0 ± 6.2	19.6 ± 1.9
$c \to s l^+ \nu_l$	8.5 ± 2.1	10.1 ± 2.5	9.0 ± 0.9
$c \to s u d$	47.3 ± 11.8	45.4 ± 11.4	54.0 ± 5.4
$\sum c \to s$	64.3 ± 16.1	65.6 ± 16.4	72.0 ± 7.2
$B_c^+ \to \tau^+ \nu_\tau$	2.9 ± 0.7	2.0 ± 0.5	1.8 ± 0.2
$B_c^+ \to c \bar{s}$	7.2 ± 1.8	7.2 ± 1.8	6.6 ± 0.7

Table 6.4: *Branching ratios of B_c decay modes calculated using the operator product expansion (OPE) approach, by summing the contributions from the exclusive modes from potential models (PM) [100], and by applying QCD sum rules (SR) and NRQCD [101].*

The ground state then decays weakly. In this section, theoretical models describing various exclusive decay modes are discussed and predictions for branching ratios are given. Since a large number of different theories are being used to calculate the decays of the B_c the following sections only outline the mainstream models, they do not contain a comprehensive overview. If not explicitly stated, results from other theories or models for the same quantities are in agreement with the results given here.

6.4.1 Pure leptonic decays

In fig. 6.13 the Feynman diagram for pure leptonic decay for the B_c is depicted. The lepton and anti-neutrino must have the same helicity in the rest frame of the ground state B_c (spin 0). Since the anti-neutrino always is right-handed, i.e. has positive helicity, the lepton also must have positive helicity. Now, a very light lepton behaves almost like a neutrino in terms of helicity, i.e. in the limit of a massless lepton, the weak current only couples to leptons with negative helicity. Thus a positive helicity state is hard to attain for a light lepton. When the mass of the lepton increases, the decay becomes less suppressed. This is called helicity suppression. Thus the leptonic annihilation decay width is proportional to the masses of the leptons in the final state. The process is analogue to the pion decay.

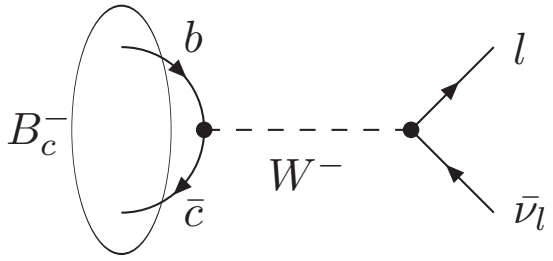

Figure 6.13: *Annihilation diagram of a $b\bar{c}$ bound state into a lepton and an anti-neutrino.*

In eq. 6.34 the width for the leptonic mode is given [102]:

$$\Gamma_{lep.ann.} = \sum_{i=e,\mu,\tau} \frac{G_F^2}{8\pi} |V_{bc}|^2 f_{B_c}^2 M_{B_c} m_i^2 (1 - \frac{m_i^2}{M_{B_c}^2})^2 \tag{6.34}$$

where $|V_{bc}|$ is the CKM matrix element. The form-factor f_{Bc} is (in non-relativistic approximation) proportional to the radial wave function at the origin. Usually f_{Bc} is taken to be in the range 300-500 MeV.

Helicity suppression does not occur for the channel $B_c \to l\nu_l\gamma$. In [103] this decay mode is discussed as well as one loop QED corrections. The results for these radiative corrections are compared to the $B_c \to l\nu_l$ decay in table 6.5. The mode $B_c \to \mu\nu_\mu$ has approximately the same width (in order of magnitude) as $B_c \to \mu\nu_\mu\gamma$. The effect of radiative corrections in the case of $B_c \to \tau\nu_\tau$ is small. The electronic decay is completely dominated by the radiative mode. If the photon can be detected, predictions for the radiative modes can be verified and the form factor f_{B_c} can be fitted from the data.

decay with lepton	Γ pure [GeV]	Γ pure + rad [GeV]	BR pure	BR pure + rad.
e	$1.73 \cdot 10^{-21}$	$6.09 \cdot 10^{-17}$	$1.36 \cdot 10^{-9}$	$5.45 \cdot 10^{-5}$
μ	$0.74 \cdot 10^{-16}$	$1.39 \cdot 10^{-16}$	$0.59 \cdot 10^{-4}$	$10.98 \cdot 10^{-5}$
τ	$1.77 \cdot 10^{-14}$	$1.78 \cdot 10^{-14}$	$1.40 \cdot 10^{-2}$	$1.41 \cdot 10^{-2}$

Table 6.5: *Leptonic decay widths and branching fractions (τ_{B_c} = 0.46 ps) for the "pure" mode $B_c \to l\nu_l$ and the "radiative" (rad) mode $B_c \to l\nu_l\gamma$.*

Recently, new theoretical results [104] on leptonic decay with gluon-bremsstrahlung have been reported. The claim is that the leptonic modes $B_c \to l + \nu_l$ with radiation of one or two gluon(s), can be used to experimentally verify the contribution of singlet or octet components in the decay of the B_c state. The energy spectrum of the charged lepton should be dominated at large energy by the contribution from the octet mode, since only one gluon has to radiate as opposed to the singlet state in which 2 gluons must be radiated.

6.4.2 Semi-leptonic decays

In the calculation of semi-leptonic (and non-leptonic) B_c decays, form factors are used to determine the decay widths. The form factors are usually calculated in the framework of "QCD sum rules". The theory of QCD sum rules is rather complicated and will not be discussed here. Reviews are available elsewhere [105].

Exhaustive treatments of semi-leptonic B_c decays in the framework of QCD sum rules are given in [106], [101], [107]. Gluon corrections of $\mathcal{O}(\alpha_s/v)$ are included and give an enhancement of the form factors ($\sim$ factor 2) over the diagram in which the quarks are treated as free partons. These corrections make the QCD sum rule approach consistent with results from quark potential model calculations. Semi-leptonic branching ratios from these calculations as well as estimates from quark potential models [108] and a relativistic constituent quark model [109] are summarised in table 6.6. The range of the values obtained from the three references are presented.

channel	$\Gamma(10^{-15}$ [GeV])	BR
$B_c^+ \to B_s e^+ \nu$	11 - 61	[8 - 42] $\times 10^{-3}$
$B_c^+ \to B_s^* e^+ \nu$	30 - 79	[21 - 55] $\times 10^{-3}$
$B_c^+ \to B_d e^+ \nu$	1 - 4	[7 - 28] $\times 10^{-4}$
$B_c^+ \to B_d^* e^+ \nu$	2 - 6	[14 - 42] $\times 10^{-4}$
$B_c^+ \to \eta_c e^+ \nu$	2 - 14	[14 - 98] $\times 10^{-4}$
$B_c^+ \to J/\psi e^+ \nu$	22 - 35	[15 - 24] $\times 10^{-3}$
$B_c^+ \to \eta_c' e^+ \nu$	0.3 - 0.7	[2 - 5] $\times 10^{-4}$
$B_c^+ \to \psi_c' e^+ \nu$	0.3 - 0.7	[7 - 14] $\times 10^{-4}$
$B_c^+ \to D^0 e^+ \nu$	0.01 - 0.09	[7 - 63] $\times 10^{-6}$
$B_c^+ \to D^{*0} e^+ \nu$	0.1 - 0.3	[7 - 21] $\times 10^{-5}$

Table 6.6: *Semi-leptonic B_c^+ decay widths and branching fractions.*

6.4.3 Non-leptonic decays

The description of non-leptonic decay modes is based on factorisation of the weak transition and the hadronisation of quarks into mesons.

In the usual potential model approaches the overlap of the wave functions of the two constituent quarks forming a resonance (a bound state) is taken to be large. If the overlap is large, the recoil is small. In the potential model the relative motion of the two heavy quarks is treated in the centre of mass system of the meson. Consequently, the wave function of the meson is also defined in this centre of mass system. However, for the decays of B_c into a $\bar{c}c$ state a common centre of mass system between the initial B_c and the J/ψ can not be found (a system in which both the initial meson and the produced meson are at rest at the same time), since the recoil in this decay is large ($m_{B_c} \sim 6.4$ GeV, $m_{J/\psi} \sim 3.1$ GeV). In [110] NRQCD is again employed to correct for the large recoil. For $\mu^2 < (m_Q \cdot v)^2$ non-relativistic wave functions are used, while for $\mu^2 > (m_Q \cdot v)^2$, thus $\mu^2 > \Lambda^2_{QCD}$, the exchange of hard gluons between the constituent quarks in the B_c meson is introduced, accommodating the effect of the large recoil. In fig. 6.14 diagrams for the non-leptonic $B_c^+ \to J/\psi\pi^+(\rho^+)$ decays are shown.

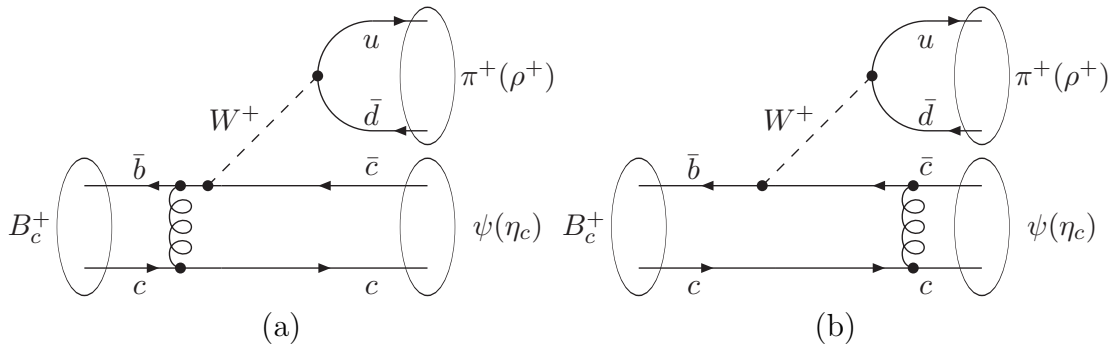

Figure 6.14: *Diagrams of $B_c \to \psi(\eta_c)\pi^+(\rho^+)$ with hard gluon exchange between the heavy quarks.*

decay mode	$\Gamma(10^{-15}$ [GeV])
$B_c^+ \to J/\psi + \pi^+$	2.93 [108], 10.32 [111]
$B_c^+ \to \eta_c + \pi^+$	3.29 [108], 13.33 [111]
$B_c^+ \to J/\psi + \rho^+$	9.45 [108], 41.28 [111]
$B_c^+ \to \eta_c + \rho^+$	8.70 [108],42.87
$B_c^+ \to \eta_c + K^+$	0.256 [108]
$B_c^+ \to J/\psi + K^+$	0.242 [108]
$B_c^+ \to \eta_c + D^+$	3.4×10^{-4} [108]
$B_c^+ \to J/\psi + D^+$	0.382×10^{-6} [108]
$B_c^+ \to \eta_c + D_s$	0.173 [108]
$B_c^+ \to J/\psi + D_s$	0.085 [108]

Table 6.7: *Widths of non-leptonic $B_c \to c\bar{c} + X$ decays. The $B_c \to J/\psi(\eta_c) + \pi^+(\rho^+)$ decays have two entries in the table, i.e values from [108] and [111]. The former does not take into account hard gluon exchange, while the latter does.*

In the two particle hadronic decay of $B_c \to c\bar{c} + \pi(\rho)$ the B_c can decay into S, P and D-wave charmonium states. A number of these excited charmonium states can subsequently decay electromagnetically into J/ψ. The extra yield resulting from P-wave charmonium states is estimated to be 20-25 % of the total S-wave charmonium contribution [111].

In table 6.7 widths of non-leptonic B_c decays are presented. Most widths are taken from [108] where the hard gluon correction is absent. For $B_c \to J/\psi(\eta_c) + \pi^+(\rho^+)$ also widths are given that do take into account the exchange of a hard gluon [111]. The large recoil enhances these widths considerably.

6.5 CP violation

Possible CP violating decay modes of the B_c have been studied. The CP violation in B_c decays is "direct", i.e. the ratio of decay amplitudes $|B_c^+ \to f^+|/|B_c^- \to f^-| \neq 1$. The weak phase difference which causes the asymmetry originates from CP violation in the weak interaction as described in chapter 1, section 1.1. In [112] CP violation is discussed in two-body hadronic decays. A next-to-leading order effective Hamiltonian is used, in which the CKM matrix elements are incorporated. Both tree level diagrams (fig. 6.15(a)) and penguin diagrams (6.15(b)) and their interference terms have been considered.

These decays of the B_c provide a measurement of the angle γ in the CKM unitarity triangle. Using both the asymmetry and the expected branching ratio as requirements to observe CP violation in B_c decays, ref. [112] concludes that the $B_c \to DK$ modes are the most promising. The asymmetry is defined as:

$$\mathcal{A}_{cp}(f) \equiv \frac{|A(f)|^2 - |\bar{A}(\bar{f})|^2}{|A(f)|^2 + |\bar{A}(\bar{f})|^2} \tag{6.35}$$

where f denotes the final state and $A(f)$ the amplitude of the corresponding decay. Table 6.8 gives a summary of the expected branching ratios and asymmetries.

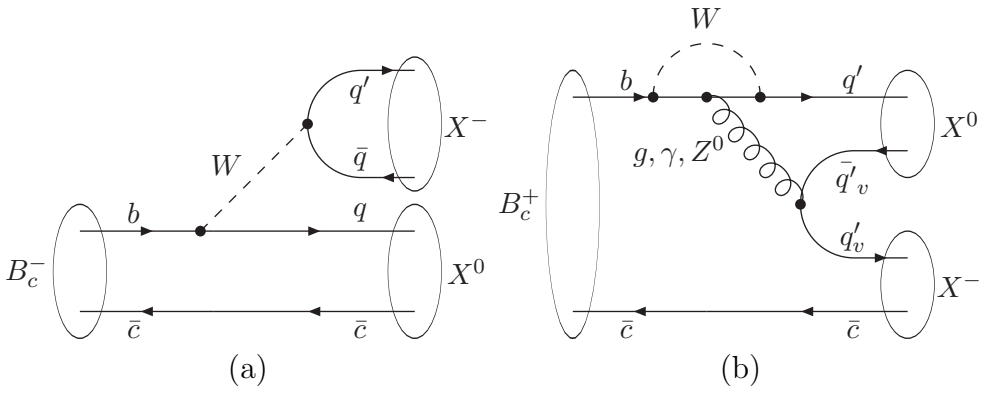

Figure 6.15: *Two possible diagrams of B_c decays, one at tree level (a) and one so-called "penguin" decay (b). Both diagrams can go to the same CP eigenstate, and they interfere with each other.*

mode	$\mathcal{A}_{cp}$	BR
$K^{*0}D_s^{*-}$	6.14×10^{-2}	2.85×10^{-7}
D^0K^-	-9.51×10^{-2}	4.67×10^{-6}
$\bar{D}^{*0}K^-$	-3.31×10^{-1}	4.89×10^{-7}
D^0K^{*-}	-1.94×10^{-2}	3.58×10^{-6}
$D^{*0}K^{*-}$	-1.94×10^{-2}	3.87×10^{-6}

Table 6.8: *CP violating decay modes with relatively large expected asymmetries and their branching ratio's.*

Although the asymmetries are relatively large, the branching ratio's are rather small and no studies from an experimental point of view have been performed for these decay modes.

Another study focuses on $B_c^+ \to D_s^+\bar{D}^0$ [113]. The four Feynman diagrams for this process are shown in fig. 6.16. Diagrams with the small CKM matrix element V_{ub} are not colour suppressed, while diagrams with the larger matrix element V_{cb} do have a colour suppression. Due to the colour-suppression and the ratios of the various CKM matrix elements involved, the ratio of $|B_c^+ \to D_s^+D^0|$ and $|B_c^+ \to D_s^+\bar{D}^0|$ is of $\mathcal{O}(1)$. Thus the amplitudes of these processes are of similar size, which is convenient for extracting the CKM angle γ. Due to the quark structure of the final state mesons, penguin contributions as in fig. 6.15(b) are absent. Therefore, the decay is theoretically rather clean. Furthermore, in figs. 6.16(a) and (b) only the $\bar{b} \to \bar{u}$ transition contains a weak phase. So the relations:

$$A(B_c^+ \to D_s^+\bar{D}^0) = A(B_c^- \to D_s^-D^0) \quad (6.36)$$

$$A(B_c^+ \to D_s^+D^0) = e^{i2\gamma}A(B_c^- \to D_s^-\bar{D}^0) \quad (6.37)$$

are exact in the Standard Model. However, the branching ratios for these decays are small $\mathcal{O}(10^{-5} - 10^{-6})$ and require D reconstruction, which can be rather complicated. Therefore, only about 20 events per year at the LHC are expected [113].

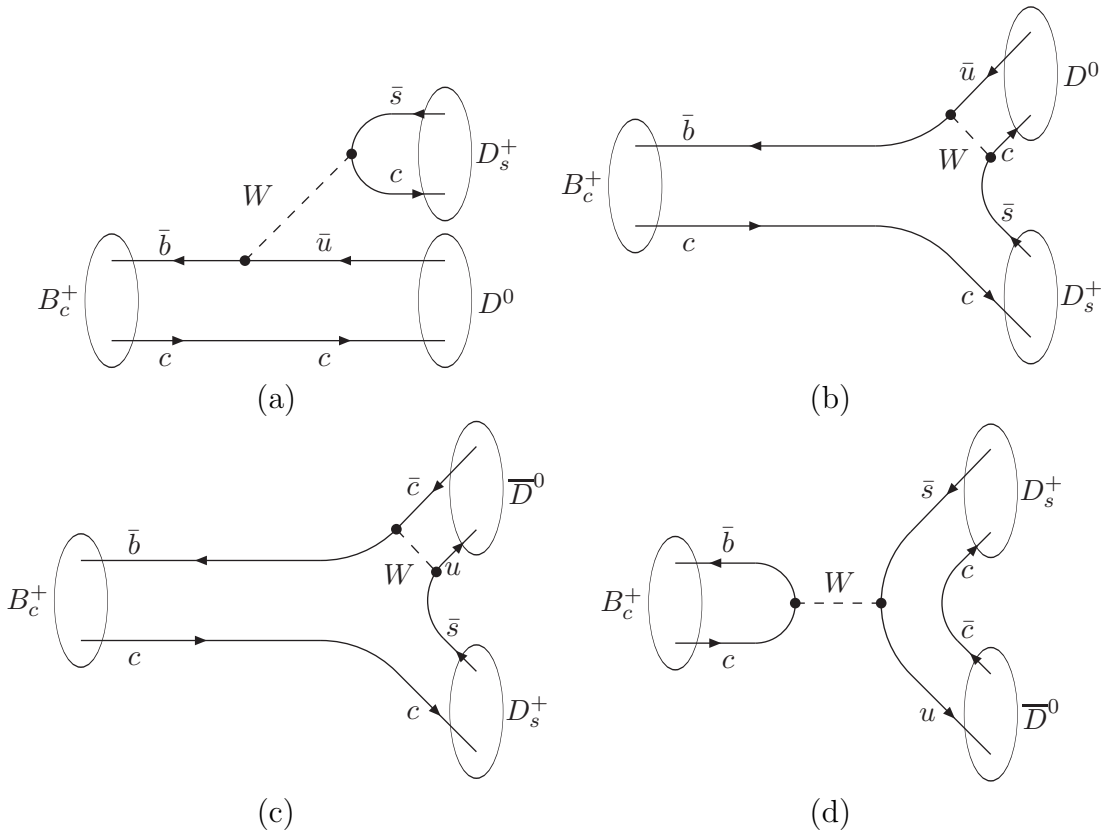

Figure 6.16: *The four possible Feynman diagrams for $B_c^+ \to D_s^+ D^0$. The amplitude of the diagrams in figs. (a) and (b) are proportional to the CKM matrix element $|V_{ub}|$, while (c) and (d) are proportional to $|V_{bc}|$. The diagrams with the larger $|V_{bc}|$ matrix element are colour suppressed with respect to the diagrams with the the smaller $|V_{ub}|$ matrix element.*

Chapter 7

The B_C meson; from Tevatron to LHC

In this chapter, the implementation of the fragmentation approach for producing a B_c meson is described. By comparing numerical results on the B_c^- production cross section and z distributions to analytical results, the validity of the implementation is verified. Next, using the scheme for b quark production introduced in chapter 1, the B_c^- production cross section for $p\bar{p}$ collisions at $\sqrt{s}$=1.8 TeV is calculated. In section 7.2, it is demonstrated that this cross section is compatible with experimental results from CDF. Subsequently, in section 7.3, an extrapolation is made to pp collisions at $\sqrt{s}$=14 TeV resulting in a prediction for the B_c^- production cross section at LHC. In section 7.4 an analysis of the decay $B_c \rightarrow J/\psi(l^+l^-)l\nu_l$ is presented. This channel provides a clean signal due to its displaced tri-lepton vertex. ATLAS trigger criteria for the selection of J/ψ originating from B decays are given in section 7.4.1. Backgrounds are discussed in 7.4.2. In sections 7.4.3 and 7.4.4 an analysis of signal and backgrounds is presented. Finally, the expected number of signal and background events is given in section 7.5 and an outlook is given on possible further studies.

7.1 B_c formation with ARIADNE in PYTHIA

The Monte Carlo program ARIADNE [24] uses PYTHIA [23] to perform the calculations concerning hard scattering and hadronisation processes. The QCD cascade is handled by ARIADNE and is based on the Color Dipole Model (CDM). In the CDM, gluons emitted from a $q\bar{q}$ pair produced in for instance an e^+e^- collision, are treated as radiation from the color dipole formed by the q and $\bar{q}$. This is schematically depicted in fig. 7.1(a). To a good approximation, the radiation of a softer gluon can be described as dipole radiation from the resulting gq and $g\bar{q}$ dipoles, as schematically shown in fig. 7.1(b) and (c). A subsequent emission of a third, still softer gluon is then given by three dipoles, etc.

The emission of gluons in ARIADNE is strongly ordered, i.e. an emission at scale p_{T1}^2 will occur "before" an emission at a lower scale p_{T2}^2, $p_{T2}^2 < p_{T1}^2$. This is implemented by introducing a Sudakov form factor which gives the probability of emitting a gluon at some specific scale determined by p_T^2. The form factor also depends on the rapidity y. The formation of quarkonium (and B_c) within ARIADNE is performed using the variables

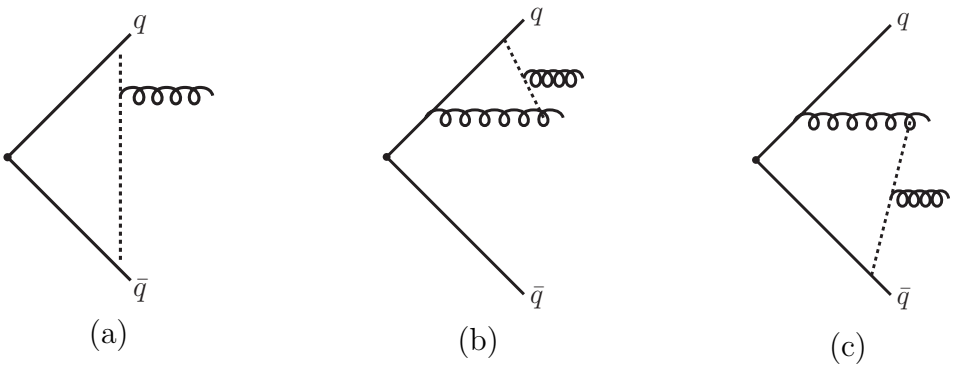

Figure 7.1: *A gluon is emitted from the color dipole between the q and $\bar{q}$ (a). Subsequently, the emission of a softer gluon is described by dipole radiation from the resulting gq and $g\bar{q}$ dipoles (b) and (c). Although the dashed line suggests only a contribution from one of the gq dipoles, the other $g\bar{q}$ dipole contributes as well.*

$$m_T^2 \equiv m_{\mathcal{O}}^2 + p_T^2 = zs \tag{7.1}$$

and

$$y = ln\frac{zW^2}{s} \tag{7.2}$$

where $m_{\mathcal{O}}$ is the mass of the heavy bound state. m_T and y are the transverse mass and the rapidity of the heavy bound state produced in the centre of mass of the dipole. The scale of the running coupling constant α_s is taken to be m_T^2. Heavy bound state $(Q\bar{Q})$ production is treated as in the process $qg\bar{q} \rightarrow Q\bar{Q}q\bar{q}$, see fig. 7.2. The probability of a $qg\bar{q}$ producing a gluon (the qg and $g\bar{q}$ dipole each have an equal probability for radiating a gluon), competes with the probability that the $qg\bar{q}$ fragments into a $Q\bar{Q}$ pair. This probability is given by the appropriate fragmentation function. In the case of fragmentation of a quark into quarkonium, the splitting kernel is connected to the dipole that is connected to the quark. Charmonium production using fragmentation functions was already implemented in ARIADNE [114]. This implementation has been extended to the production of B_c^- mesons [115], [116]. For B_c^- fragmentation, as discussed in the chapter 6, only the b quark will be allowed to fragment into B_c^-, since the probability for a c quark to fragment into a B_c^- is ~ 2 orders of magnitudes smaller.

The b quark fragmentation to the S-wave states $B_c^-(^1S_0)$ and $B_c^-(^3S_1)$ are implemented, as well as the fragmentation to the P-wave states $B_c^-(^1P_1)$, $B_c^-(^3P_0)$, $B_c^-(^3P_1)$ and $B_c^-(^3P_2)$. Furthermore, the mixed P-wave states P1' and P1 are also implemented, their mixing angle can be adjusted. The n=1 and n=2 states (S and P) are included. The production of the various states can be enabled individually.

To verify the implementation, the generated differential B_c^- production cross section $d\sigma(p\bar{p} \rightarrow B_c^- X)/dp_T$ is compared to analytical results published in [89]. In this publication, fragmentation functions are used to predict the production cross section for B_c^- at Tevatron

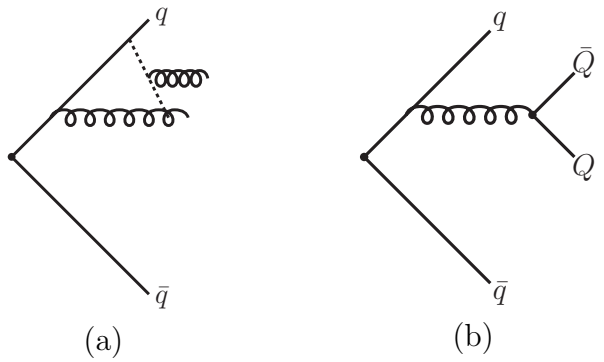

Figure 7.2: *The radiated gluon has two competing probabilities. (a): The dipole between qg (or $g\bar{q}$) can radiate another gluon. (b): The gluon fragments into a $Q\bar{Q}$ pair.*

energies. The centre-of-momentum energy is set to $\sqrt{s}$=1.8 TeV and the parton distribution functions CTEQ2M [26] are used. The quark masses are fixed at m_c=1.5 GeV and m_b=4.9 GeV. The non-perturbative parameters $R(0)$, H_1, H_8' and the mixing angle θ_{mix} (see chapter 6) are set to the values given in table 7.1.

	n=1	*n=2*
m_b	4.9 GeV	4.9 GeV
m_c	1.5 GeV	1.5 GeV
$R_{nS}(0)$	1.28 GeV$^{\frac{3}{2}}$	0.99 GeV$^{\frac{3}{2}}$
H_1	10 MeV	14 MeV
$H_8'(m)$	1.3 MeV	1.8 MeV
$cos(\theta_{mix})$	0.999	0.957

Table 7.1: *Parameters used to obtain the numerical and analytical results presented in fig. 7.3 and used in the further analysis.*

PYTHIA version 6.203 has been used and all QCD hard processes are generated assuming massless partons in the hard QCD $2 \to 2$ processes[1], in order to compare with the analytical results published in [89]. In fig. 7.3 the differential production cross section of n=1 S-wave and P-wave B_c^- states as a function of p_T are depicted. Furthermore, the analytical curves for the $B_c^-(1^1S_0)$, $B_c^-(1^3S_1)$, $B_c^-(1^3P_0)$ and $B_c^-(1^3P_2)$ states [89] are drawn. For $p_T >$ 10 GeV, the numerical calculations and analytical results agree fairly well. The evolution equations used in ARIADNE differ somewhat from the DGLAP equations which were used in [89]. It was pointed out in [81] that the DGLAP evolution equations do not correctly respect the phase space constraints. In particular, the constraint $D_{g\to B_c} \neq 0$ for z $< M_{B_c}^2/\mu^2$ is not obeyed. An alternative non-homogeneous evolution equation was suggested [81]:

$$\mu^2 \frac{\partial}{\partial \mu^2} D_i(z,\mu^2) = d(z,\mu^2) + \frac{\alpha_s(\mu^2)}{2\pi} \sum_j \int_z^1 \frac{dy}{y} P_{ij}(y) D_j(z/y, y\mu^2) \tag{7.3}$$

[1]In PYTHIA this is accomplished by selecting MSEL=1.

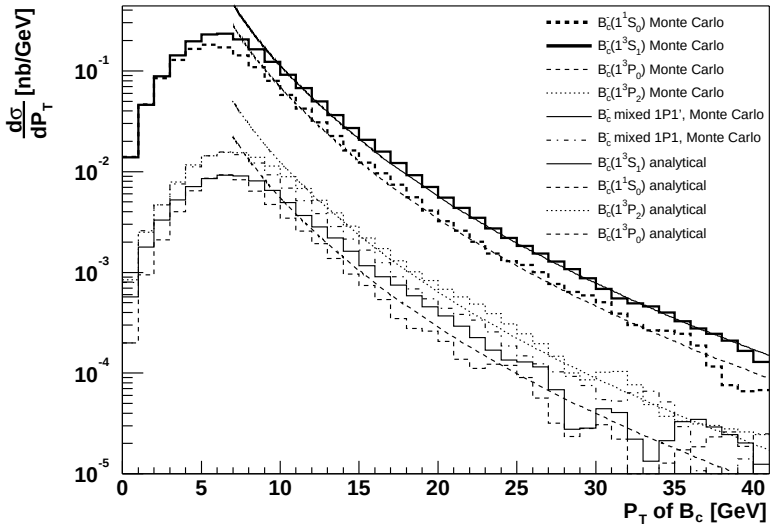

Figure 7.3: *Differential cross section $d\sigma/dp_T$ as a function of p_T of the B_c^- meson in various spin-orbital states with n=1 at $\sqrt{s}$=1.8 TeV, derived with PYTHIA and ARIADNE (histograms). Also drawn are analytical (smooth) curves from [89]. A rapidity cut of $|y(B_c^-)| < 1$ is imposed. The CTEQ2M parton distribution functions are used.*

This equation, implemented in the Monte Carlo program ARIADNE, does correctly take into account phase space suppression at threshold, i.e. the fragmentation probability is zero when phase space constraints apply. The generated differential cross section in this region becomes smaller than the analytical cross section. Above $p_T > 10$ GeV, the analytical curve exhibits the same behaviour as the $\mathcal{O}(\alpha_s^4)$ calculation discussed in section 6.1.7.

In the meantime, the CTEQ2M parton distribution functions have been retracted by the authors. However, using more recent PDFs does not change the differential cross section appreciably, as shown in fig. 7.4. Here, the CTEQ5L [117] parton distribution functions have been used, the default distribution functions in version 6.203 of PYTHIA.
Near threshold, the same behaviour is observed as depicted in fig 7.3. The differential cross section becomes somewhat smaller at larger values of p_T.

The gluon-induced fragmentation probability, i.e. the probability that a b quark originating from gluon-splitting in the QCD cascade subsequently fragments into B_c^-, has a large impact on the differential production cross section. In the DGLAP evolution equations, the gluon-induced contributions are directly related to the splitting kernels of $g \to b$ and $g \to g$. When forcing only one gluon emission from a dipole, these contributions effectively disappear as becomes apparent in fig. 7.5 where the simulation result is compared with previous analytical curves. The differential cross section is smaller by about a factor of 2 at low p_T and becomes even smaller at higher p_T.

The conclusion can be drawn that the QCD cascade implementation of the fragmentation functions behaves as expected.

The Monte Carlo implementation is also tested by comparing the generated z distributions

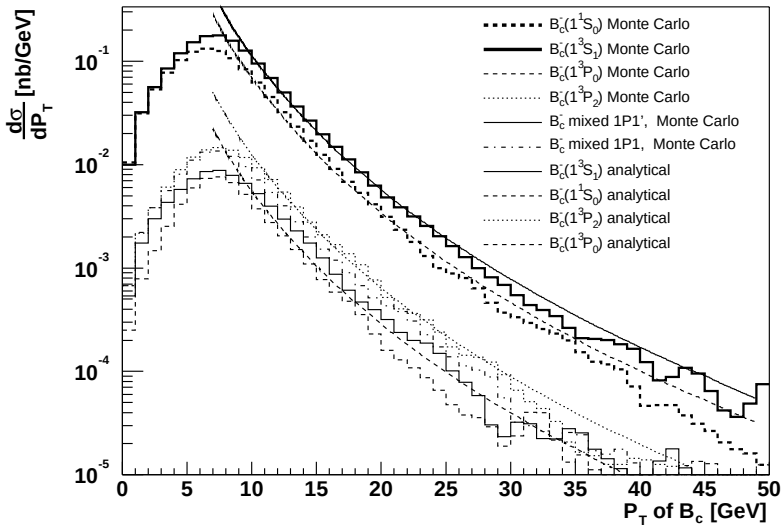

Figure 7.4: *Differential cross section $d\sigma/dp_T$ as a function of p_T of the B_c^- meson in various spin-orbital states at $\sqrt{s} = 1.8$ TeV, with $|y(B_c^-)|$ <1. The same cuts apply as in fig. 7.3, however, the CTEQ5L parton distribution functions are applied.*

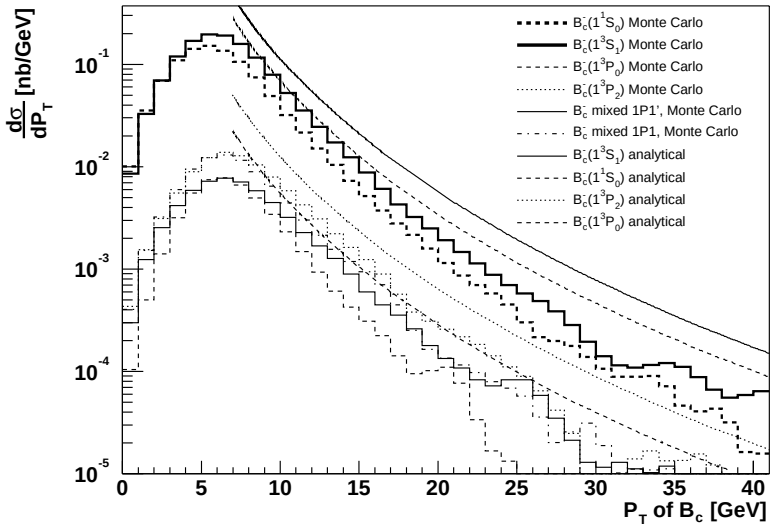

Figure 7.5: *Differential cross section $d\sigma/dp_T$ as a function of p_T of the B_c^- meson in various spin-orbital states at $\sqrt{s}$=1.8 TeV and $|y(B_c^-)|$ <1. Radiation of only one gluon is forced, i.e. the QCD cascade is truncated.*

with the analytical functions. The latter are calculated by integrating the fragmentation functions given in appendix B from $s = 0$ to $s = \infty$. Polynomial expressions in z result. In fig. 7.6 the analytical and numerical z distributions for the $B_c^-(^1S_0)$ and $B_c^-(1^3S_1)$ states are depicted. Both the analytical functions and the Monte Carlo distributions are normalised to unity.

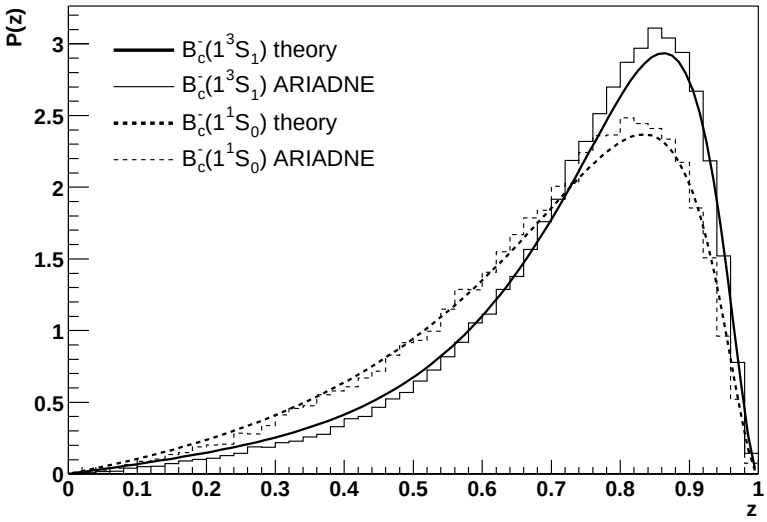

Figure 7.6: *Comparison of the z distributions from analytical calculations and Monte Carlo (single gluon emission), n=1 S-wave B_c^- states.*

The Monte Carlo was applied allowing the emission of only one single gluon, i.e. the full cascade was truncated. In this way, the true $b \to B_c^-$ fragmentation function is reproduced. The analytical and Monte Carlo generated distributions agree fairly well. The maximum of the latter distribution is somewhat larger, and seems slightly shifted towards smaller z. This is most likely due to the different evolution equations. The z distributions generated with Monte Carlo with the full cascade switched on become somewhat more peaked towards higher z values, see fig. 7.7.

Instead of using the assumption of massless partons in the $2 \to 2$ hard scattering process, the b quark production cross section will now be generated as outlined in chapter 1, section 1.2.4. In chapter 1 it was shown that by summing the contributions of five different hard sub-processes, the experimentally derived b production cross section can be reproduced. The assumption of massless partons is referred to as the "default" option, while the method outlined in chapter 1 will be referred to as the "baseline" option. Using the "baseline" option, the differential production cross sections $d\sigma(p\bar{p} \to B_c^- X)/dp_T$ for n=1 and n=2 (S and P-waves) are shown in figs. 7.8(a) and (b), respectively. For comparison, the analytical curves are also drawn. The differential cross sections are smaller than those presented in [89]. This is expected since the b quark cross section generated with the "default" option, results in a cross section that is too large by about a factor of ~ 2 [118].

The decays of excited spin-orbital $b\bar{c}$ states to the B_c^- ground state have been implemented in the Monte Carlo as well. Branching ratios are taken from [96] and [94]. Recent results on the masses and widths of the excited states are taken from [96]. In [89] the

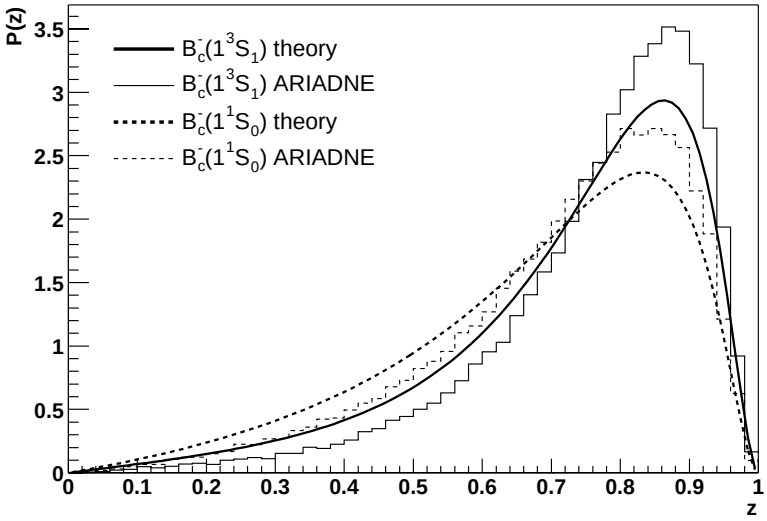

Figure 7.7: *Comparison of the z distributions from analytical calculations and generated by Monte Carlo (full cascade), for the n=1 S-wave B_c^- states. The same analytical curves apply as in fig. 7.6.*

transverse momentum distribution of the B_c^- ground state ($B_c^-(1^1S_0)$) is approximated by summing the individual transverse momentum distributions of the excited states. Cascade decays are not explicitly included. In fig. 7.9, $d\sigma(p\bar{p} \to B_c^- X)/dp_T$ is shown for this approximation (solid line) and the full implementation of cascade decays (dashed line). Due to the small mass difference between the excited states and ground state, the difference is indeed very small.

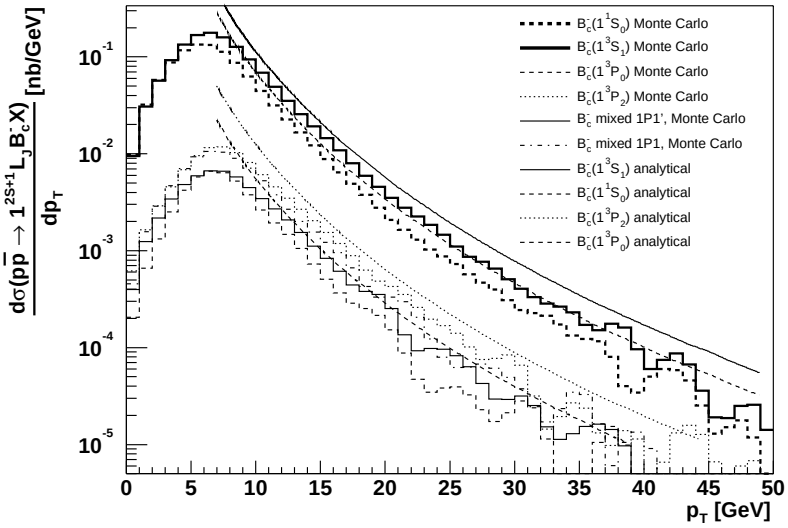

(a)

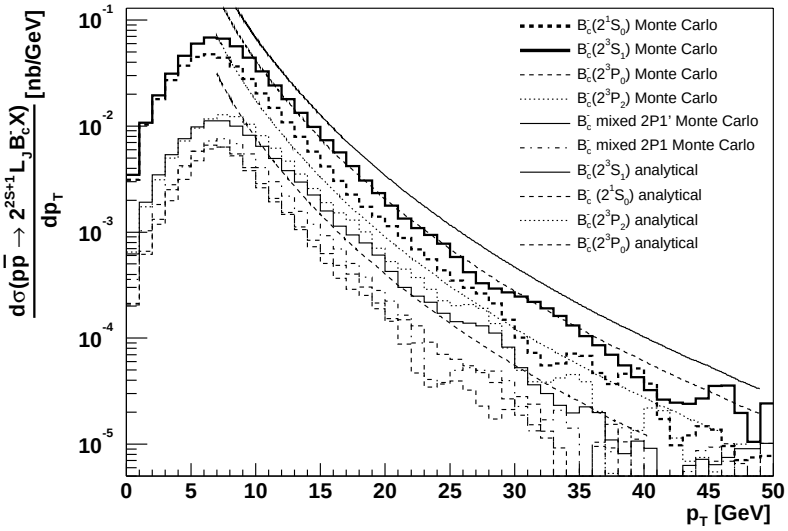

(b)

Figure 7.8: *Differential cross section $d\sigma(p\bar{p} \to B_c^- X)/dp_T$ as a function of p_T of the B_c^- meson in various spin-orbital states with n=1 (a) and n=2 (b) at $\sqrt{s}$=1.8 TeV and $|y(B_c^-)| < 1$. The "baseline" option was used (see text) as well as the CTEQ5L parton distribution functions.*

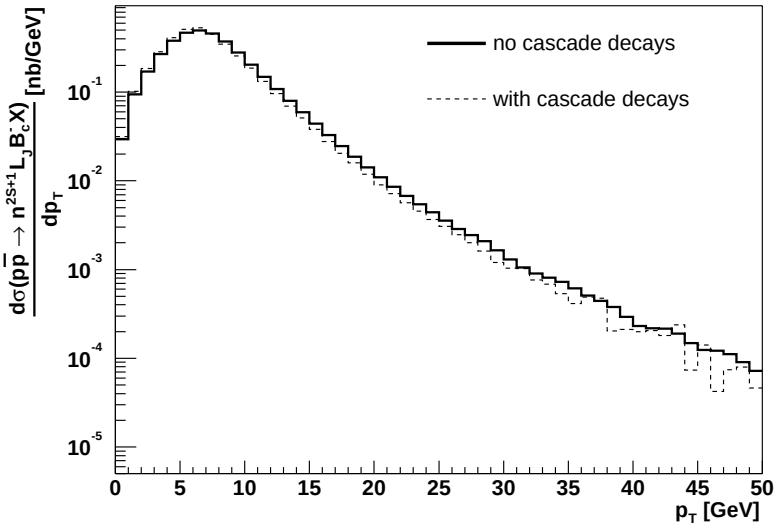

Figure 7.9: *Inclusive differential cross section $d\sigma(p\bar{p} \to B_c^- X)/dp_T$ as a function of p_T of the B_c^- meson at $\sqrt{s}$=1.8 TeV and $|y(B_c^-)| < 1$. The solid line represents the sum of transverse momentum distributions of all excited states (no cascade decays). The dashed line gives the transverse momentum distribution of the ground state $B_c^-(1^1S_0)$ including the decay of the excited states. The "baseline" option was used as well as the CTEQ5L parton distribution functions.*

The integrated cross sections $\sigma(p\bar{p} \to B_c^- X, p_T > p_T^{min})$ as a function of the minimum transverse momentum cut-off p_T^{min} for the n=1 and n=2 (S and P) B_c^- states at $\sqrt{s}$=1.8 TeV are shown in fig. 7.10(a) and (b), respectively. Finally, the total integrated cross section $\sigma(p\bar{p} \to B_c^- X, p_T > p_T^{min})$ of the $B_c^-(1^1S_0)$ ground state after the cascade decays of the excited states is shown in fig. 7.11.

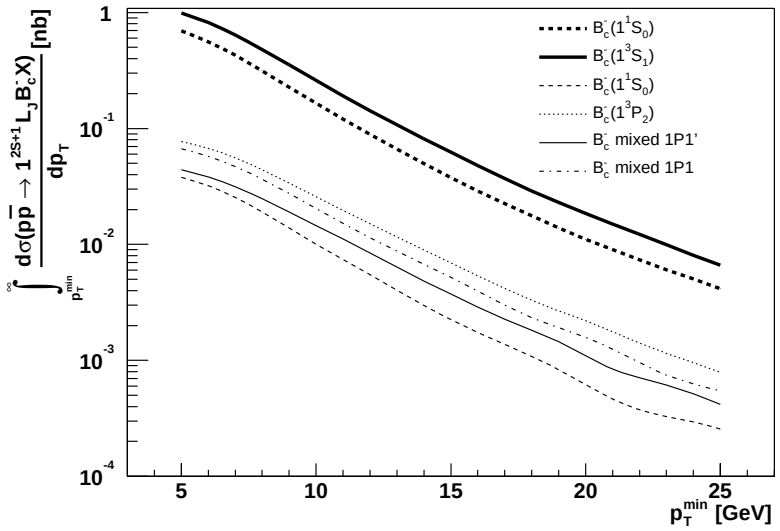

(a)

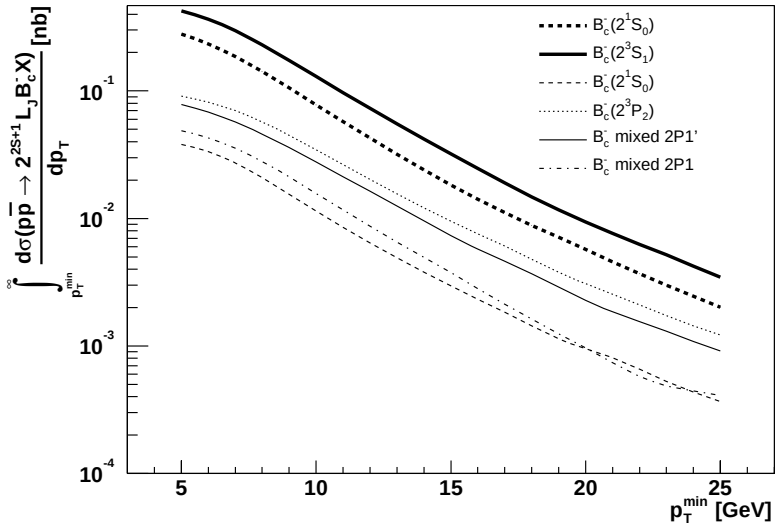

(b)

Figure 7.10: *Integrated cross section $\sigma(p\bar{p} \to B_c^- X, p_T > p_T^{min})$ as a function of p_T^{min} of the B_c^- meson in various spin-orbital states with n=1 (a) and n=2 (b) at $\sqrt{s}$=1.8 TeV and $|y(B_c^-| < 1$, using the "baseline" option and the CTEQ5L parton distribution functions.*

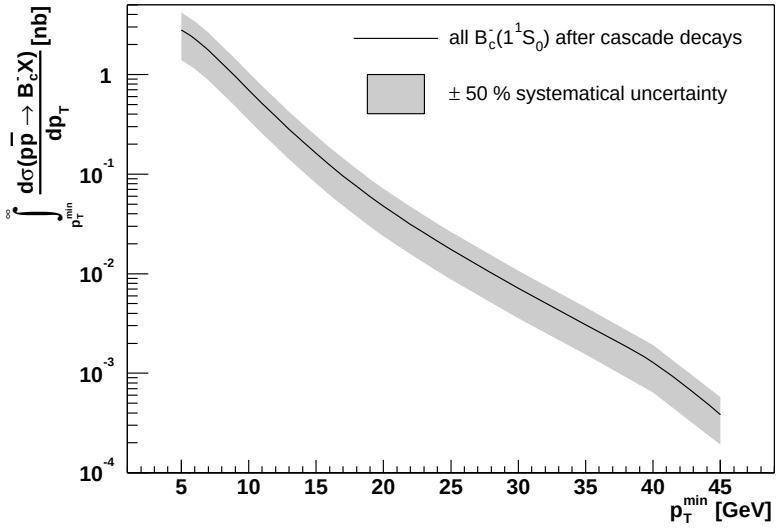

Figure 7.11: *Integrated cross section $\sigma(p\bar{p} \to B_c^-(1^1S_0)X, p_T > p_T^{min})$ as a function of p_T^{min} of the B_c^- meson at $\sqrt{s}$=1.8 TeV and $|y(B_c^-| < 1$, using the "baseline" option. The cross section includes all directly produced $B_c^-(1^1S_0)$ ground states as well as the ground states originating from the decay of excited S and P wave states. The systematical uncertainty is also depicted.*

The expected inclusive cross sections as well as the estimated uncertainties are listed in table 7.2. The main contribution to the uncertainty stems from the not well determined mass of the c quark, which appears with a third power in the denominator of the dominant S-wave fragmentation functions (eq. 6.14).

p_T^{min}	$\sigma(p\bar{p} \to B_c^-(1^1S_0)X)$ [nb] $p_T > p_T^{min}$ from [89]	$\sigma(p\bar{p} \to B_c^-(1^1S_0)X)$ [nb] $p_T > p_T^{min}$, this thesis
6	5.43	2.28 ± 1.14
10	1.16	0.68 ± 0.34
15	0.29	0.16 ± 0.08
20	0.097	0.047 ± 0.0235
25	0.038	0.017 ± 0.0085
30	0.018	0.015 ± 0.0075
35	0.0087	0.0029 ± 0.0015
40	0.0046	0.0013 ± 0.00065

Table 7.2: *Comparison of the predictions for the inclusive B_c^- production cross sections at the Tevatron from [89] and this thesis. The uncertainties are estimated to be ∼ 50 %.*

By varying m_c (1.5 ± 0.2 GeV) the uncertainty becomes ∼ 50 %. The uncertainty on the b quark cross section obtained by CDF and DØ is claimed to be much smaller (see chapter

1, fig. 1.7). One possible source of errors mentioned in [89] is the use of homogeneous DGLAP equations. However, in ARIADNE non-homogeneous evolution equations are implemented, as explained above. The non-perturbative parameters which are present in the fragmentation functions can (as yet) not be derived from existing measurements and must be derived from theory. The mass and width, as well as decay modes and branching ratio's of the B_c^- ground state and higher B_c^- states can be calculated from theory rather precisely. In particular the electromagnetic transitions of excited B_c^- states to the ground state are rather well estimated. In any case, from fig. 7.9 one may conclude that uncertainties due to cascade decays are of minor importance.

7.2 Comparison with CDF measurements

The integrated cross section from fig. 7.11 is compared to measurements by the CDF [77] collaboration. CDF searched for a B_c signal in the decay mode $B_c \rightarrow J/\psi l \nu_l$, since the displaced tri-lepton vertex of this decay channel provides a clean signal. B_c candidates were selected using the following criteria [77]:

- Only decay channels $B_c \rightarrow J/\psi + l\nu_l$ are considered, with l=e, μ and $J/\psi \rightarrow \mu^+\mu^-$.
- The lepton l in the direct decay of B_c is referred to as the "third lepton" and must have $p_T > 3$ GeV and $|\eta| < 1$.
- The muons from the J/ψ decay have to satisfy $p_T > 2$ GeV and $|\eta| < 1$.
- A cut is placed on the displaced vertex using variables related to the transverse plane, since the longitudinal (z) coordinate is badly measured. A measure of the time between production and decay of a B_c candidate is the pseudo-proper decay length ct^*:

$$ct^* = \frac{M(J/\psi l) \cdot L_{xy}(J/\psi l)}{|p_T(J/\psi l)|} \tag{7.4}$$

  with the L_{xy} the decay length projected on the plane perpendicular to the beams:

$$L_{xy}(J/\psi l) = \frac{\vec{X} \cdot \vec{p_T^{J/\psi l}}}{|p_T^{J/\psi l}|} \tag{7.5}$$

  where the vector $\vec{X}$ points from the primary to the secondary vertex in the transverse plane, and $p_T(J/\psi l)$ and $M(J/\psi l)$ are the transverse momentum and the invariant mass of the $J/\psi + l$ system, respectively. The requirement on the pseudo-proper decay length of the $J/\psi + l$ system is $ct^* > 60\ \mu m$. The transverse decay length introduced in eq. 7.5 will also be used in the analysis presented in section 7.4

In [88], CDF results on the ratio $\frac{\sigma(B_c^+)}{\sigma(b)}$ are compared with the fragmentation approach. Here it is assumed that the $\frac{\sigma(B_c^-)}{\sigma(b)}$ yields the same result. The induced gluon contribution and the P-wave contribution are taken into account as well as the 2 S states below the production threshold for a B and a D meson. The result reads:

$$\frac{\sigma(B_c^-)}{\sigma(b)} = \frac{BR(B^- \to J/\psi K^-)}{BR(B_c^- \to J/\psi l^- \bar{\nu}_l)} \frac{\sigma(B^-)}{\sigma(b)} \times \mathcal{R} = \left(2.08^{+1.06}_{-0.95}\right) \times 10^{-3} \tag{7.6}$$

where R is the experimentally obtained ratio [77]:

$$\mathcal{R} = \frac{\sigma(B_c^-) BR(B_c^- \to J/\psi l^- \bar{\nu}_l)}{\sigma(B^-) BR(B^- \to J/\psi K^-)} = 0.132^{+0.041}_{-0.037}(stat.) \pm 0.031(syst.)^{+0.032}_{-0.020} \tag{7.7}$$

The last error originates from the error on the life time measurement. The theoretical estimate BR($B_c^- \to J/\psi l^- \bar{\nu}_l$) = 2.5 ± 0.5 % [101], while [119]

$$B^- \to J/\psi K^- = (9.9 \pm 1.0) \times 10^{-4} \tag{7.8}$$

and [1]:

$$\frac{\sigma(B^-)}{\sigma(b)} = 0.397^{+0.018}_{-0.022} \tag{7.9}$$

The result in eq. 7.6 is consistent with the models considered. Probably due to the low statistics collected by CDF (about 20 events), a (differential) cross section is not published. As discussed before, the largest theoretical uncertainty in using the fragmentation approach originates from the poorly known mass of the c quark. The ratio $\frac{\sigma(B_c^-)}{\sigma(b)}$ can also be estimated with the model presented in this thesis. The ratio measured by CDF is for B_c^- and B^- with $p_T > 6.0$ GeV and $|y| < 1$ [77]. In table 7.2 the integrated B_c^- cross section is given for $p_T^{min} > 6$ GeV. With an average z-value in the b quark fragmentation of ~ 0.7 (fig 7.6), this corresponds to a p_T cut on the b quark of ~ 8.5 GeV. From fig. 1.7 the integrated b quark cross section can then be obtained resulting in:

$$\frac{\sigma(B_c^-)}{\sigma(b)} = (0.91 \pm 0.45) \times 10^{-3} \tag{7.10}$$

The ratio is consistent with the CDF result (eq. 7.6).

CDF's fit to the $J/\psi l$ mass distribution yields $20.4^{+6.2}_{-5.5}$ B_c events [77]. The largest background is attributed to the decays in flight of pions and kaons. This background, estimated from a full detector simulation, has already been subtracted. The kinematical and geometrical cuts described above are applied to the data sample from fig. 7.11. Detector smearing is not taken into account; relevant efficiencies are shown in table 7.3. The right-most column

criterion	reduction factor	cross section [nb]	# B_c^-
-	-	2.282	2.51 $\times 10^5$
BR($B_c^- \to J/\psi l^- \nu_l, l = e, \mu$	25	9.13 $\times 10^{-2}$	1.004 $\times 10^4$
cut due to spread interaction point	1.67	5.48 $\times 10^{-2}$	6.024 $\times 10^3$
J/ψ LVL2 trigger eff.	2.0	2.74 $\times 10^{-2}$	3.012 $\times 10^3$
$p_T(l) > 3$ GeV, $\lvert\eta(l)\rvert < 1$	2.22	1.23 $\times 10^{-2}$	1.355 $\times 10^3$
BR($J/\psi \to \mu^+\mu^-$)	17.00	7.25 $\times 10^{-4}$	79.7
$p_T(\mu) > 2$ GeV, $\lvert\eta(\mu)\rvert < 1$	5.26	1.38 $\times 10^{-4}$	15.1
vertex requirement, $ct^* > 60\ \mu m$	1.54	8.95 $\times 10^{-5}$	9.84

Table 7.3: *Impact of geometrical acceptance, kinematical cuts and trigger efficiencies [77] on the simulated B_c^- data sample. The reduction factors are cumulative, each row in the table forms a subset of the previous row. The initial cross section is taken from table 7.2. The number of events is calculated for an integrated luminosity of 110 pb^{-1}.*

shows the number of expected events assuming a total integrated luminosity of 110 pb^{-1}. Due to the large spread in the primary interaction point, only ~ 60 % of all $J/\psi \to \mu^+ u^-$ could be reconstructed [120]. The J/ψ LVL2 trigger efficiency is somewhat unclear, but is estimated to be close to $\sim 50\%$ [120].
After cuts, ~ 9.84 simulated events pass, thus ~ 19.7 B_c^- and B_c^+ events, in excellent agreement with the ~ 20 events extracted from the CDF data sample. Obviously, table 7.3 is a rather rough approximation, nevertheless, the Monte Carlo prediction is surprisingly well confirmed. Run IIb at the Tevatron will be completed in 2008. A total integrated luminosity of 15 fb^{-1} will then be collected, corresponding to $\sim 10^7$ B_c's with $p_T > 10$ GeV.

7.3 B_c production; Extrapolation to the LHC

In this section predictions are presented for the differential and integrated cross sections $\sigma(pp \to B_c^- X)$ at a centre-of-momentum energy of $\sqrt{s}$=14 TeV. The pseudo-rapidity range is limited to $|\eta(B_c)| < 2.5$, matching the pseudo-rapidity range of the ATLAS Inner Detector. As in the previous section, the b quark cross section is obtained using the "baseline" option" and the CTEQ5L parton distribution functions are selected. The differential cross sections $d\sigma(pp \to B_c^- X)/dp_T$ for n=1 and n=2 (S and P-waves) are shown in figs. 7.12(a) and (b), respectively. The integrated cross sections $\sigma(pp \to B_c^- X, p_T > p_T^{min})$ as a function of the minimum transverse momentum cut-off p_T^{min} for the n=1 and n=2 (S and P) B_c^- states at $\sqrt{s}$=14 TeV are shown in fig. 7.13(a) and (b), respectively. The contribution of the P-wave states to the inclusive B_c^- cross section is 20-30 %, in accordance to table 6.1. In fig. 7.14 the $d\sigma(pp \to B_c^- X)/dp_T$ of the sum of transverse momentum distributions of all excited states (no cascade decays) is shown as well as the $d\sigma(pp \to B_c^- X)/dp_T$ of ground state $B_c^-(1^1S_0)$ after the decay cascade. The difference between the two p_T distributions is again very small. Finally, in fig. 7.15, the integrated cross section $\sigma(pp \to B_c^-(1^1S_0)X, p_T > p_T^{min})$ as a function of p_T^{min} is depicted.

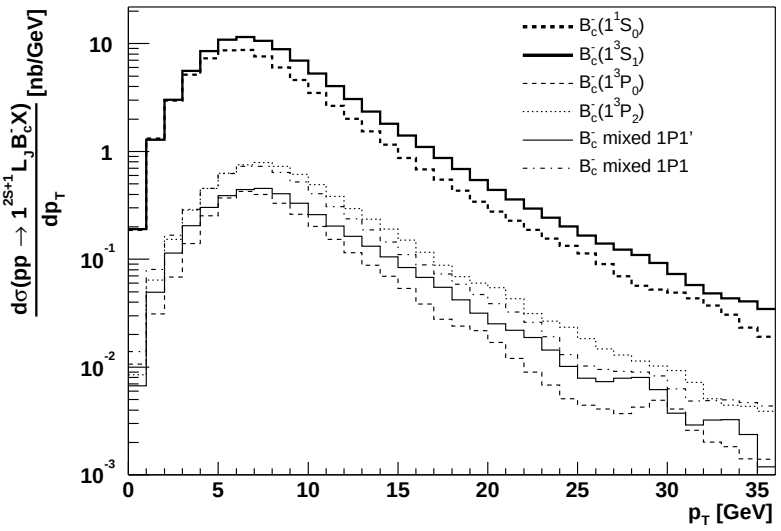

(a)

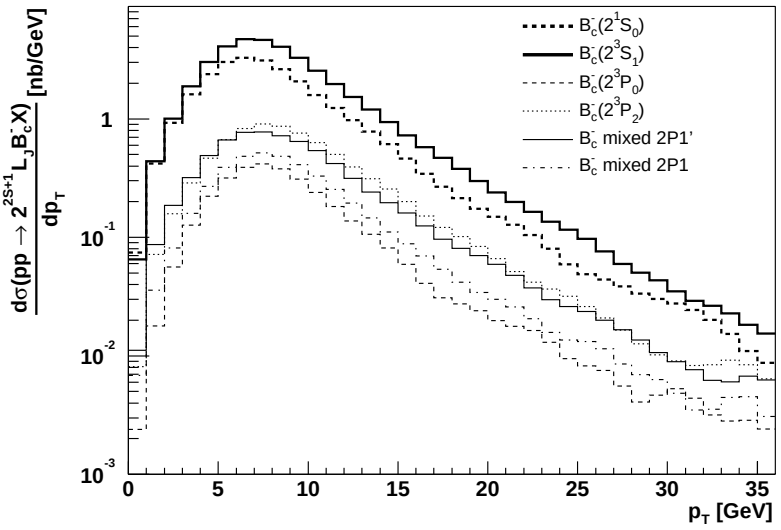

(b)

Figure 7.12: *Differential cross section $d\sigma(pp \to B_c^- X)/dp_T$ as a function of p_T of the B_c^- meson for various spin-orbital states for n=1 (a) and n=2 (b) at $\sqrt{s}$=14 TeV for $|\eta(B_c^-)| < 2.5$.*

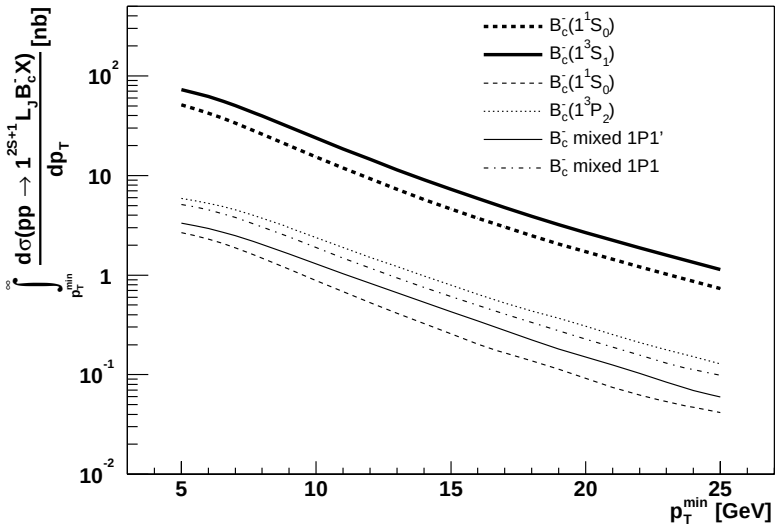

(a)

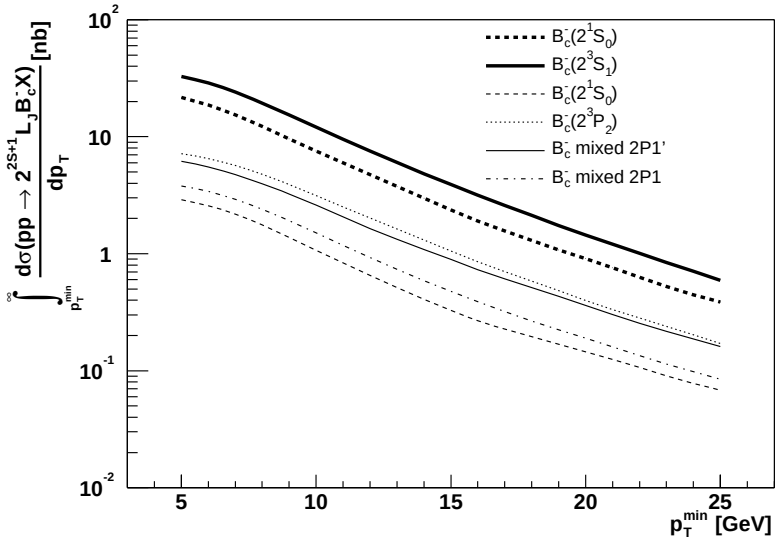

(b)

Figure 7.13: *Integrated cross sections $\sigma(pp \to B_c^- X, p_T > p_T^{min})$ as a function of p_T^{min} of the B_c^- meson for various spin-orbital states with n=1 (a) and n=2 (b) at $\sqrt{s}$=14 TeV for $|\eta(B_c^-)| < 2.5$.*

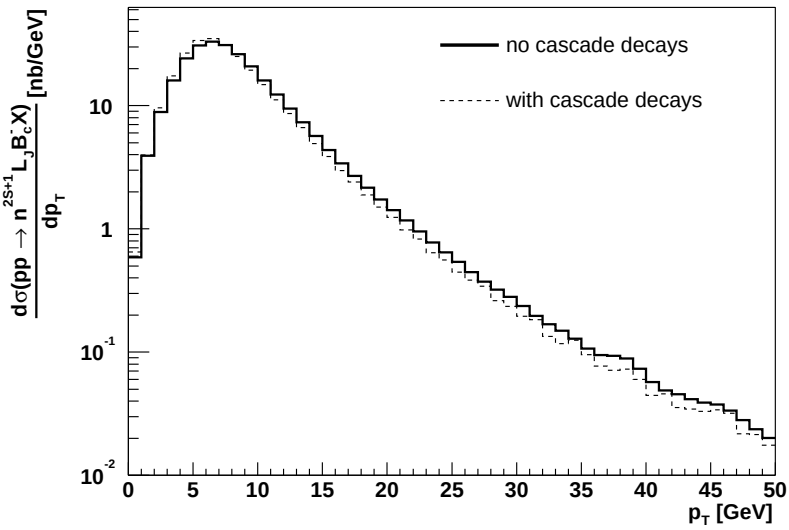

Figure 7.14: *Inclusive differential cross section $d\sigma(pp \to B_c^- X)/dp_T$ as a function of p_T of the B_c^- meson at $\sqrt{s}$=14 TeV and $|\eta(B_c^-)| < 2.5$. The solid line represents the sum of transverse momentum distributions of all excited states (no cascade decays). The dashed line gives the transverse momentum distribution of the $B_c^-(1^1S_0)$ ground state including cascade decays.*

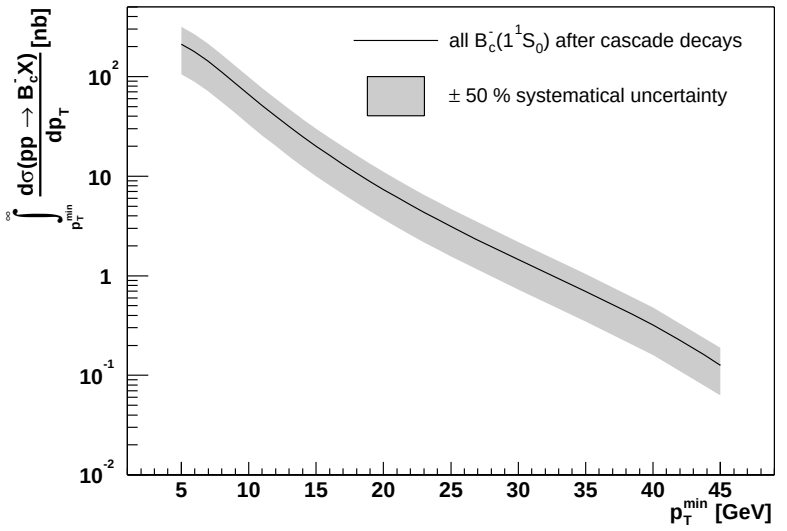

Figure 7.15: *Integrated cross section $\sigma(pp \to B_c^-(1^1S_0)X, p_T > p_T^{min})$ as a function of p_T^{min} of the B_c^- meson at $\sqrt{s}$=14 TeV and $|\eta(B_c^-)| < 2.5$. This cross section includes all directly produced $B_c^-(1^1S_0)$ ground states as well as the ground states originating from the decay of excited S and P wave states.*

In table 7.4 the value of the cross section for $|\eta(B_c^-)| < 2.5$ is given at selected bins of p_T^{min}. Since the cross section again heavily depends on the value of the charm mass, the same systematical uncertainty is assumed as for the Tevatron data sample. With an integrated luminosity of 10 fb^{-1} (assuming low luminosity, $1{\times}10^{-33}$ cm^{-2} s^{-1}, and one year of operation), ATLAS will obtain $\sim 7 \times 10^8$ events (with $p_T > 10$ GeV) per year. Due to trigger cuts and by only selecting particular final states, a fraction of these mesons will be reconstructed.

p_T^{min}	$\sigma(pp \to B_c^-(1^1S_0)X)$ [nb]
	$p_T > p_T^{min}$, $\|\eta(B_c^-)\| < 2.5$
10	66.10 ± 33.05
15	20.00 ± 10.00
20	7.36 ± 3.68
25	3.12 ± 1.56
30	1.45 ± 0.73
35	0.70 ± 0.35
40	0.32 ± 0.16

Table 7.4: *Integrated cross section $\sigma(pp \to B_c^-(1^1S_0)X, p_T > p_T^{min})$ for $|\eta(B_c^-)| <$ 2.5 for various p_T^{min} bins at $\sqrt{s}$=14 TeV.*

In chapter 6, results from [93] were presented (fig. 6.10). The cross section shown is much lower than the predictions derived here. Several causes for this discrepancy can be identified. First, in [93], only the B_c ground-state state is considered. When higher excited states are included, the total $b \to B_c$ quark fragmentation probability becomes a factor 5 larger, as shown in table 6.1. Secondly, in [93] evolution effects are explicitly not taken into account to facilitate a comparison with the tree-level $\mathcal{O}(\alpha_s^4)$ calculation. As already mentioned, the induced gluon fragmentation arising from the evolution equations, has to be taken into account in order to derive the total B_c cross section including full phase space. Thus the large $gg \to gg$ cross section and subsequent gluon fragmentation has not been accounted for in [93].

7.4 B_c events in ATLAS

A prediction for the number of B_c^- mesons at LHC was given in the previous section. Obviously, the meson can only be observed by reconstructing exclusive decay channels. To illustrate an analysis using ATLAS data, the channel $B_c \to J/\psi(l^+l^-)l\nu_l$, with which the B_c at the Tevatron was discovered, is chosen. This channel provides a very clear displaced tri-lepton decay vertex. Because a J/ψ is required, the currently foreseen B physics trigger menus for inclusive J/ψ selection are adopted. Trigger criteria and efficiencies are discussed in section 7.4.1. Possible backgrounds to the $B_c \to J/\psi(l^+l^-)l\nu_l$ channel are discussed in section 7.4.2. Analysis results are presented in sections 7.4.3 and 7.4.4.

7.4.1 Trigger criteria and trigger efficiencies

For a B-physics event, it is assumed that the LVL1 trigger requires a muon with $p_T > 6$ GeV and $|\eta| < 2.5$. The cut on the p_T reduces the contribution from $c \to \mu$ and decays in flight. The muon trigger system covers the range $|\eta|$ <2.5 over the full azimuth [34]. The efficiency of the LVL1 trigger for identifying the trigger muon is $\sim$ 79 % for the full pseudo-rapidity range [34].

As discussed in chapter 2, the first step in the LVL2 B-physics trigger algorithm consists of confirmation of the LVL1 muon. For this step, track segments in the Inner Detector are combined with tracks candidates in the muon detector obtained by the μfast algorithm [45]. The resulting efficiency as a function of p_T is shown in fig. 7.16. This distribution is parametrised and used in the analysis.

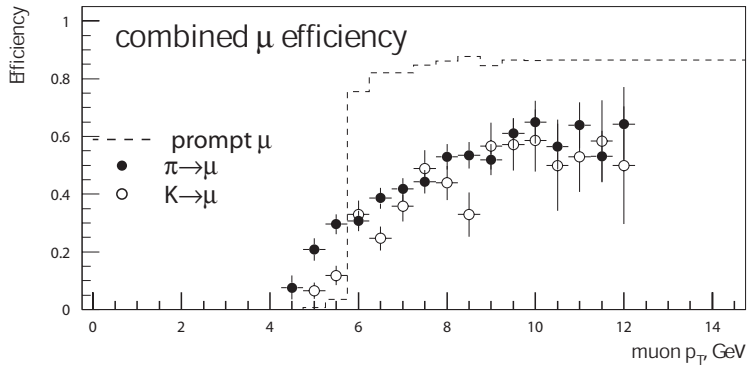

Figure 7.16: *The efficiency as a function of p_T for a muon passing the LVL1 selection, reconstructed by the μfast muon algorithm and subsequent track association from the SCT or Pixel detector, for $|\eta| < 2.5$.*

In the next step, tracks are reconstructed at LVL2. In contrast to the CDF experiment, ATLAS will be able to reconstruct low momentum electrons ($p_T \sim 1$ GeV). The electron reconstruction efficiency has been studied in detail for the channel $B_d \to J/\psi(e^+e^-)K_s$ [47] and is given as a function of p_T in fig. 7.17. The efficiency used is denoted by "TRT+Si+e-id", i.e. the track reconstruction is seeded by the TRT, then SCT and Pixel information is used. Finally, electron identification is performed using transition radiation information from the TRT. Pixel-seeded track reconstruction may be pursued, however, TRT-seeded electron reconstruction gives the best performance [47].
A second (non-trigger) muon in the event can be identified at LVL2 in the muon chambers and/or in the last compartments of the hadron calorimeter [121]. The muon search at LVL2 will be restricted to a limited volume of these detectors, within RoIs defined by the inner detector following a full track scan in the TRT. All tracks reconstructed in the Inner Detector with $p_T > 2.9$ GeV will be extrapolated to the calorimeters and/or muon detector, thus achieving 97 % efficiency for 3 GeV muons. Using selected $\mu^+\mu^-$ and e^+e^- pairs, a crude J/ψ selection may already be performed at LVL2 (see table 2.3) using loose mass constraints, however, it is chosen here to perform the J/ψ selection at the Event Filter stage where a J/ψ is reconstructed using both vertex and (more stringent) mass constraints. For

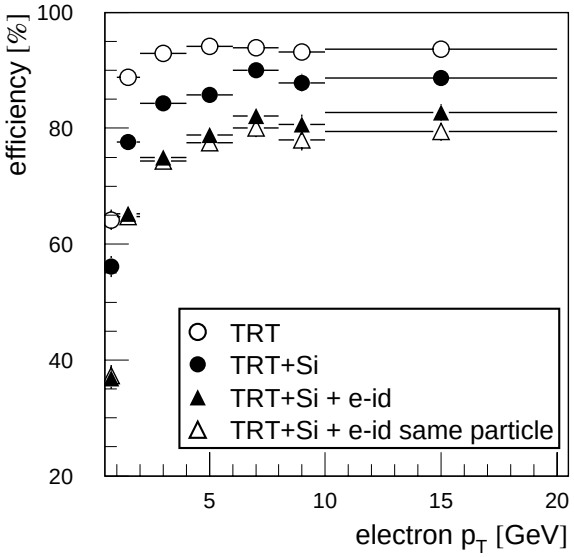

Figure 7.17: *The efficiency as a function of p_T for a TRT seeded reconstruction of electrons tracks for $|\eta| < 2.5$.*

the Event Filter, the mass window is $2.62 < M(J/\psi) < 3.34$. A transverse decay length of $L_{xy} > 220\ \mu m$ is demanded and the fit should satisfy $\chi^2/N_{d.o.f.} < 8.0$.

In summary, the following trigger criteria are applied :

- At LVL1, a μ with $p_T > 6$ GeV and $|\eta|$ <2.5, must always be present.
- At LVL2, at least one reconstructed additional muon track with $p_T > 3$ GeV or two reconstructed electron tracks with $p_T > 1$ GeV, all within $|\eta|$ <2.5 are required. J/ψ selection at LVL2 is omitted here.
- At the Event Filter, J/ψ candidates are selected with $2.62 < M(J/\psi) < 3.34$, $L_{xy}(J/\psi) > 220\ \mu m$ and $\chi^2/N_{d.o.f.}$ <8.0.

After the Event Filter, a sample remains that includes J/ψ candidates and additional leptons. In the analysis which follows two data sets are studied; one that is defined before and one that is defined after the Event Filter selection. Both samples allow for a detailed study on event selection efficiencies.

7.4.2 B_c and non-B_c contributions to the data sample

Major Standard Model sources of leptons in hadronic collisions are weak production and decay of intermediate vector bosons and QCD heavy flavour production. The former has a much smaller cross section than the latter, especially when no stringent isolation cuts on the leptons are imposed. For the QCD processes, open charm production gives the largest

integrated lepton rate. However, the transverse momentum spectrum of these leptons is significantly softer than those from bottom and top decays. Compared to bottom production, the inclusive top quark cross section is $\sim \mathcal{O}(10^5)$ smaller than $\sigma(pp \to bX)$.

The B_c event selection discussed here, requires a J/ψ candidate already at trigger (Event Filter) level. Main sources for J/ψ's are direct charmonium production (including cascade decays) and the decays of B mesons. Charmonium production in the decay of $b\bar{b}$ bound states is negligible, since the production cross section of bottomonium is relatively small. Prompt J/ψ, including those from cascade decays of excited states, can easily be removed from the data sample by imposing lifetime constraints, as advocated in the Event Filter selection. This will be demonstrated in the following section.
Both the reconstruction of the J/ψ and the tri-lepton invariant mass in the decay $B_c \to J/\psi lX$ suffer from accidental association with leptons from decays in flight in the same hemisphere. The CDF collaboration found that, in addition to a small background due to punch-through in their calorimeter (~ 2.5 %), roughly 25 % of their B_c sample suffers from the decay of pions and kaons. In the following study a crude upper limit on this background is estimated by allowing all π's and K's to decay within 2 m from the primary vertex. No decay-in-flight rejection algorithm has been applied to the Inner Detector tracks.
In summary, the following data samples have been generated :

- Two B_c "signal" samples: one with and one without contributions from decays in flight. For the determination of the inclusive b quark cross section the "baseline" option was chosen (see section 7.1). The samples include production and cascade decays of all possible excited B_c mesons.

- A "light" B meson ($B^{\pm}$, B^0, B_s) sample. Again the "baseline" option was used for the b quark production. Decays in flight are included as well.

- A "prompt" J/ψ sample generated with ARIADNE, properly normalised to the CDF data and extrapolated to pp collisions at $\sqrt{s}$=14 TeV. Decays in flight of pions and kaons is included. There is a large theoretical uncertainty in the extrapolation of the cross section for prompt J/ψ production. However, this background can easily be removed as will be demonstrated in the next section.

All samples are subject to the fast ATLAS simulation package ATHENA-ATLFAST [122]. In this simplified detector simulation, four-momenta of particles are taken and smeared according to the detector response obtained from full detector simulation. In the Inner Detector, four momenta of the charged particles are taken to form helix tracks in the magnetic field of the Inner Detector. Track smearing includes both multiple scattering effects and the deterioration due to the intrinsic resolution of the Inner Detector subdetectors. A similar procedure is applied to obtain the calorimeter response (electrons, γ's, etc.) and to estimate the momentum of the muon in the muon-detector [123], [124].

7.4.3 Inclusive lepton spectra and J/ψ selection

The B-physics trigger relies on efficient selection of a muon with $p_T > 6$ GeV ($|\eta| < 2.5$). The single electron trigger becomes efficient at much higher threshold ($p_T^e > 20$ GeV, $|\eta| <$

2.5), since low momentum electrons suffer from more severe backgrounds than muons. This implies that the single electron trigger contribution to the B-physics sample is negligible. This can also be demonstrated by analysing the inclusive muon transverse momentum spectrum presented in fig. 7.18. The dominant contribution stems from weak decays of light B mesons and decays in flight of pions and kaons in the same sample (solid line). Since muon and electron decay branching ratios in the considered channels are comparable, except for contributions from π and K decays, raising the transverse momentum cut from 6 GeV to 20 GeV reduces the cross section by ~ 2 orders of magnitude. In the same plot the p_T spectrum for muons from prompt J/ψ's (this sample includes decays in flight as well) is depicted (dotted line). The "light B" background exceeds the B_c signal (dashed line) by ~ 3 orders of magnitude, reflecting the small $b \to B_c$ fragmentation probability. This B_c sample does *not* include contributions from π and K decays and serves as reference. Since the threshold on the first (trigger) muon is higher than for additional muon candidates in the event, a second threshold at 3 GeV appears in the distributions.

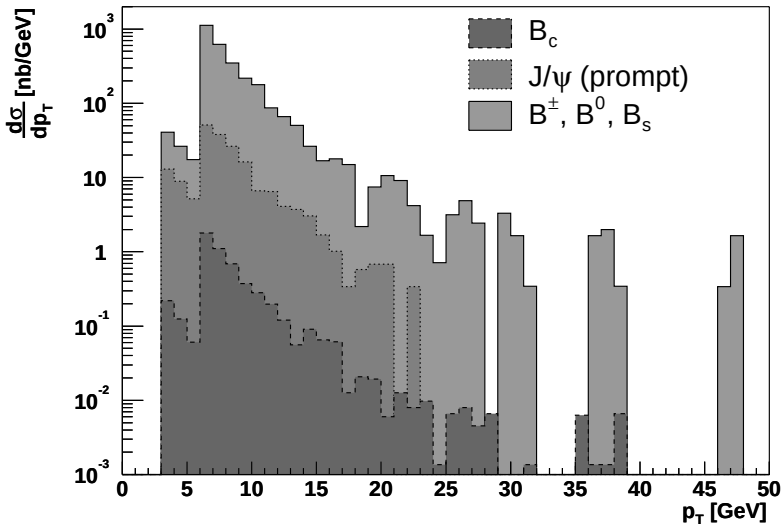

Figure 7.18: *Inclusive p_T spectrum of muons in the B_c reference sample, "light B" background and prompt J/ψ samples.*

The event sample will also be searched for electron candidates for which a much lower threshold applies ($p_T^e > 1$ GeV, $|\eta| < 2.5$), see fig 7.19. Demanding a trigger muon and additional electrons/positrons in prompt J/ψ events, reduces the sample significantly (dotted line); only a π or K decay will trigger the selection of electrons from J/ψ. The inclusive transverse momentum spectrum for electrons/positrons from decays of light B mesons (cascade decays including J/ψ are also contained) is given by the solid line. Finally, the inclusive p_T distribution of electrons/positrons in the B_c reference sample is derived (dashed line).
Next, a vertex finding algorithm similar to the one used in the Event Filter ($\chi^2/N_{d.o.f.} < 8.0$) is applied to reconstructed charged particle tracks in the Inner Detector volume. Electron-positron pairs and muons with opposite charge are selected that are associated with the same vertex. Their invariant mass is calculated, see fig. 7.20.

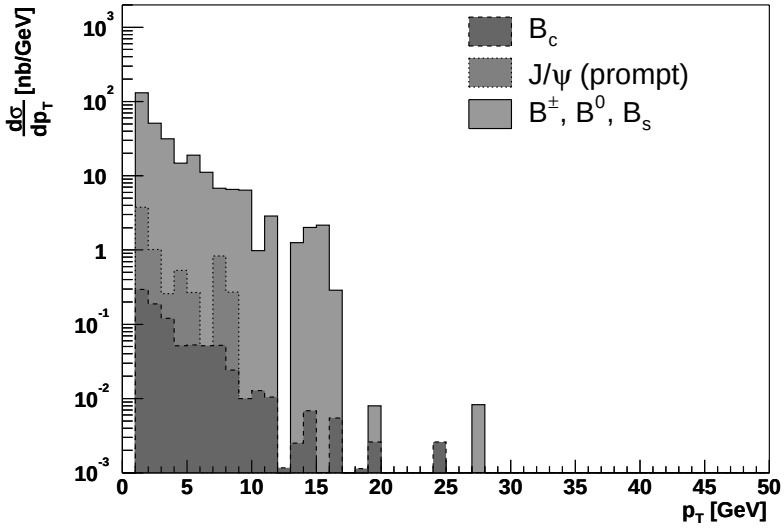

Figure 7.19: *Inclusive p_T spectrum of electrons in the B_c reference sample, "light B" background and prompt J/ψ samples.*

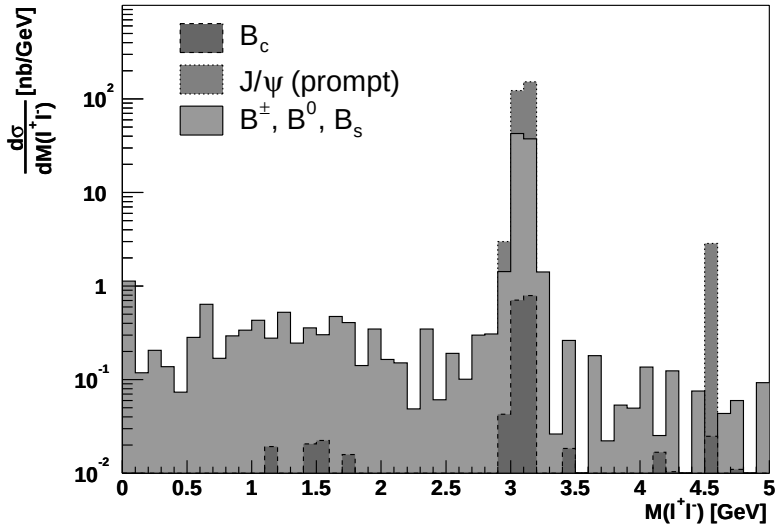

Figure 7.20: *Invariant mass distribution of e^+e^- and $\mu^+\mu^-$ pairs with a common reconstructed vertex with $\chi^2/N_{d.of.} < 8.0$*

Obviously, vertex association will reduce the muon background from decays in flight significantly. However, at the mass of the J/ψ (3.1 GeV), the signal (dashed line) is still overwhelmed by prompt J/ψ's (dotted line) and J/ψ's from light B meson decays (solid line).

Since the lifetime of the J/ψ is relatively small compared to the lifetime of the light B-mesons, the transverse decay length for prompt J/ψ's should be small. In fig 7.21 the transverse position of the J/ψ decay vertex with respect to the primary vertex is presented.

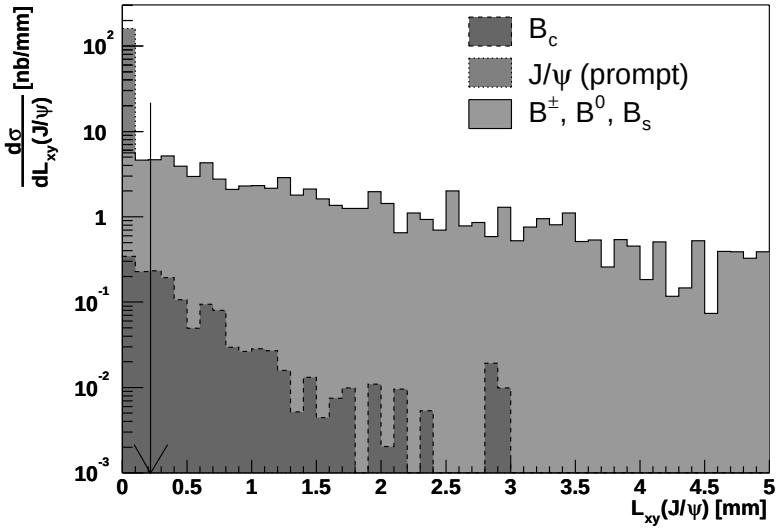

Figure 7.21: *Distribution of the transverse decay length L_{xy} for reconstructed J/ψ's. The J/ψ candidates are constrained to the Event Filter mass cut, the vertex fit must satisfy $\chi^2/N_{d.o.f.} < 8.0$. The transverse decay length imposed by the Event Filter cut (220 μm) is indicated by the arrow.*

Only those events are shown that have a J/ψ candidate with a mass in the range $2.62 < M(l^+l^-) < 3.34$ (the Event Filter mass cut). For prompt J/ψ's the production and decay vertices coincide within ~ 100 μm (dotted line). Since the lifetime of the B_c (~ 0.5 ps) is smaller than the lifetime of the light B mesons (~ 1.5 ps), the signal distribution (dashed line) drops more rapidly than that of the light B background (solid line). After full detector simulation, the proposed transverse decay length in the ATLAS Event Filter is $L_{xy}(J/\psi)$= 220 μm (arrow). Obviously, reducing this cut would enhance the signal over background as long as prompt J/ψ's can be effectively discriminated.
The J/ψ invariant mass distribution after the Event Filter cut is shown in fig. 7.22. Although the prompt J/ψ background has now completely been removed, the B_c signal (dashed line) is still significantly smaller than the contribution of J/ψ's from the decays of light B mesons (solid line). Further tightening of the cuts by applying offline criteria ($\chi^2/N_{d.o.f.} < 6.0$, $2.83 < M(J/\psi) < 3.26$ and $L_{xy}(J/\psi) > 250$ μm) does not drastically alter the signal (dashed line) over background (solid line) ratio (see fig. 7.23). The largest impact imposes the increased transverse decay length: a 3 % background reduction while 10 % of the B_c events will be removed.

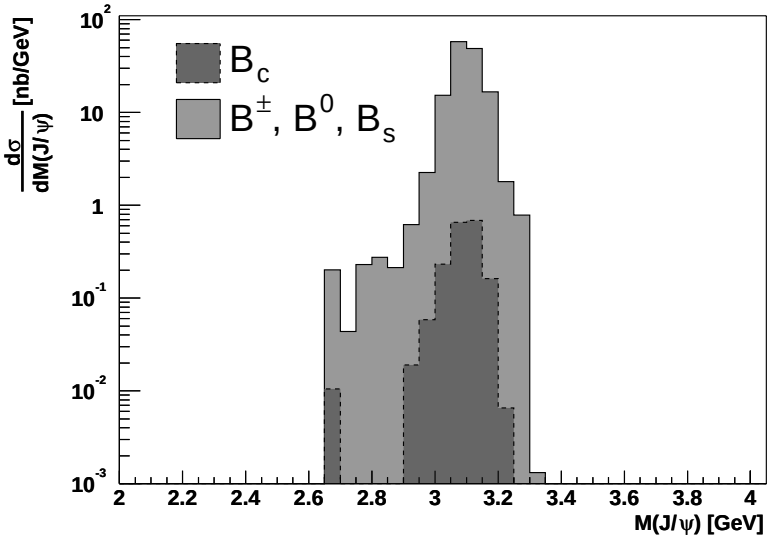

Figure 7.22: *Invariant mass distribution of J/ψ candidates after the Event Filter cut for the B_c reference sample and "light B" background. Prompt J/ψ's are completely removed from the sample by the transverse decay length cut.*

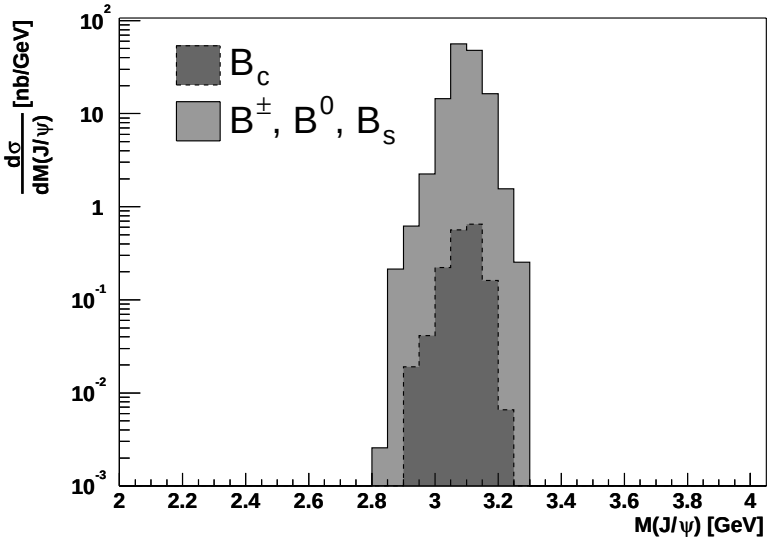

Figure 7.23: *Invariant mass distribution of J/ψ candidates after offline cuts are imposed.*

7.4.4 $B_c \to J/\psi l$ selection

In the $B_c \to J/\psi$ transition, the charm quark produced in the decay of the bottom quark combines with the spectator charm quark to bind into a charmonium state. The small invariant mass W in the decay $b \to cW$, will predominantly decay into light quarks (u,d,s) and leptons with small mass (e, μ). Due to the relatively short lifetime of the J/ψ, the latter decay modes will lead to a three-lepton vertex ($J/\psi \to l^+l^-$, $l^\pm$). Events with J/ψ candidates that pass the offline cuts can now be searched for additional charged leptons that can be associated with the J/ψ decay vertex ($\chi^2/N_{d.o.f.} < 8.0$).
The three lepton invariant mass distributions for background (solid line) and B_c reference signal events (dashed line) are presented in fig. 7.24. The low momentum neutrino will escape ATLAS undetected; the missing transverse energy resolution for low momentum neutrino's will be insufficient to properly reconstruct their energy and direction. The $J/\psi l$ invariant mass distribution is obtained by assuming $m_{B_c} = 6.27$ GeV. Restricting the invariant mass region as indicated by the arrows in fig. 7.24 leaves 85 % of the events in the reference sample unaffected. The integrated cross section corresponding to the mass window $4.0 < M(J/\psi + l) < 6.0$ yields ~ 13 pb.

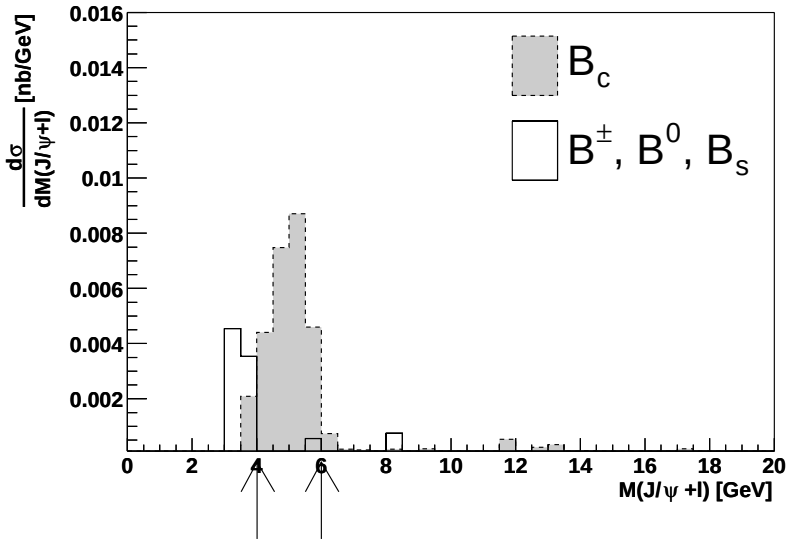

Figure 7.24: *Invariant $J/\psi + l^\pm$ mass distribution, where the J/ψ candidate passes offline mass and vertex cuts. The three lepton vertex fit satisfies $\chi^2/N_{d.o.f.} < 8.0$. The mass range associated with the B_c is limited to the region between the arrows.*

In the discussion of the transverse decay length distributions of fig. 7.21, it became apparent that the B_c signal sample is more strongly affected by a cut on the decay length than the light B meson sample. In fig. 7.25 the mass distribution similar to fig. 7.24 is presented for which the transverse decay length cut is less stringent: $L_{xy}(J/\psi l) > 60$ μm. Although ATLAS has a powerful central tracking system, the vertex reconstruction resolution needs further investigation when real data becomes available. The integrated cross section corresponding to the mass window $4.0 < M(J/\psi + l) < 6.0$ is enhanced to 19.2 pb

while the background is hardly affected, because only a very small number of events pass the tri-lepton vertex fit criteria.

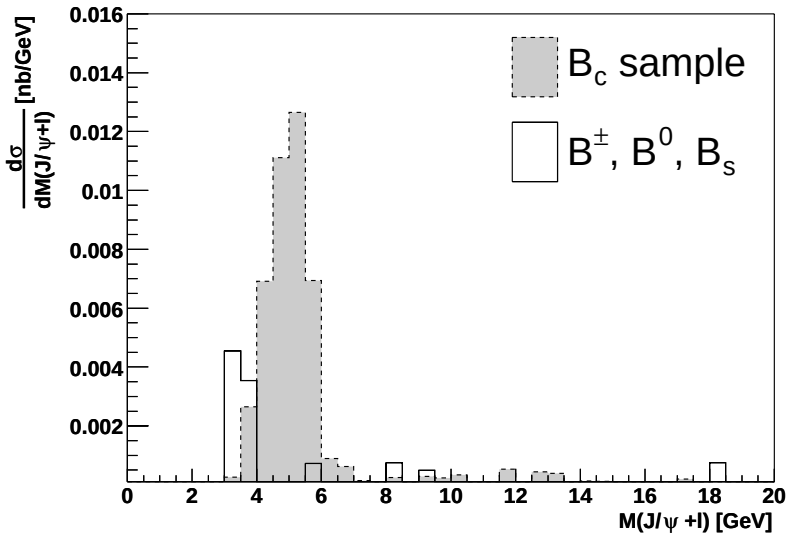

Figure 7.25: *Invariant $J/\psi + l^{\pm}$ mass distribution, where the J/ψ candidate passes the offline mass cuts and $L_{xy} > 60$ μm. The three-lepton vertex fit satisfies $\chi^2/N_{d.o.f.} < 8.0$. The reference signal and light B decay background is shown.*

Decays in flight in the B_c sample may obscure the vertex fitting procedure and may introduce an additional background. In fig. 7.26 the invariant mass distribution for the B_c reference sample (as depicted in fig. 7.25) is compared to the mass distribution for the B_c sample including decays in flight. The integrated cross section for $4.0 < M(J/\psi + l) < 6.0$ increases from 19.2 to 22.2 pb.

Table 7.5 summarises the selection and analysis procedure described in the previous sections. The number of reference events, B_c events including decays in flight (d.i.f.) and light B meson background events is calculated after Event Filter and subsequent analyses cuts after one year of operation at low luminosity ($\int \mathcal{L}dt = 10$ fb^{-1}.) The three lepton vertex requirement introduces the largest enhancement of the signal to background (S/B) ratio. With a relaxed cut on the transverse decay length of the $J/\psi + l^{\pm}$ system, on the order of 1.9×10^5 B_c events per year can be recorded by ATLAS. The background will be very small.

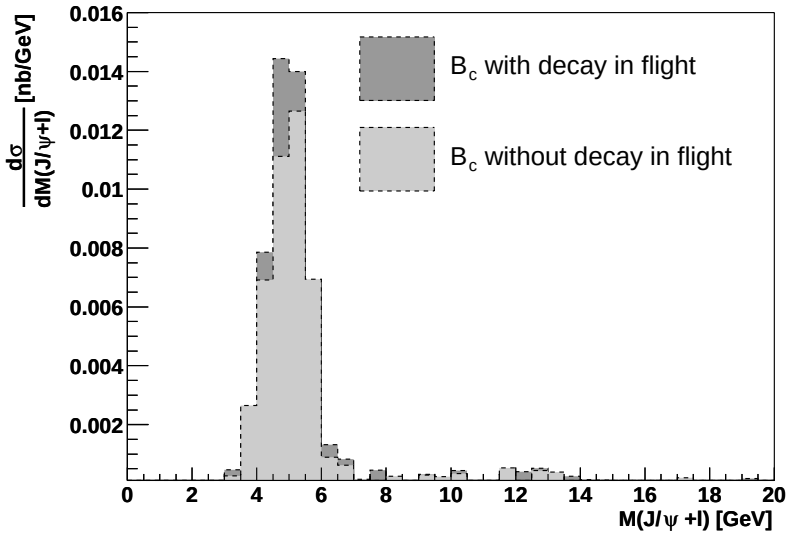

Figure 7.26: *Invariant mass distributions $M(J/\psi + l)$ using the same cuts that apply in fig. 7.25. The signal with and without decays in flight is shown.*

cut	S	S + d.i.f.	$B^{\pm}$, B^0, B_s	S/B	(S + d.i.f)/B
$2.62 < M(J/\psi) < 3.34$, $L_{xy}(J/\psi) > 220$ μm (J/ψ EF cut)	9.18×10^5	9.67×10^5	7.27×10^7	1.26×10^{-2}	1.33×10^{-2}
$2.83 < M(J/\psi) < 3.26$, $L_{xy}(J/\psi) > 250$ μm (J/ψ offline cut)	8.32×10^5	8.65×10^5	7.00×10^7	1.12×10^{-2}	1.23×10^{-3}
$4.0 < M(J/\psi + l) < 6.0$ $2.83 < M(J/\psi) < 3.26$, $L_{xy}(J/\psi) > 250$ μm	1.29×10^5	1.51×10^5	2.81×10^3	46.13	53.69
$4.0 < M(J/\psi + l) < 6.0$ $2.83 < M(J/\psi) < 3.26$, $L_{xy}(J/\psi + l) > 60$ μm	1.92×10^5	2.22×10^5	3.64×10^3	52.74	60.99

Table 7.5: *Number of events in the signal (with and without decays in flight) and background samples (with decays in flight), after various cuts. The number of events is based on an integrated luminosity of 10 fb^{-1}.*

7.5 Discussion

Although the probability for producing a bound state of a bottom and charm quark is very small (no B_c events were detected at LEP; the diagrams in fig. 6.6 are equally valid for e^+e^- colliders), production rates at hadron colliders are sizeable. The B_c has some very distinct decay modes of which the decay $B_c \rightarrow J/\psi l^{\pm}\nu_l$ with $J/\psi \rightarrow l^+l^-$ ($l = e, \mu$) has been investigated. The ATLAS trigger menus used in this thesis foresee the selection of the decay $J/\psi \rightarrow \mu^+\mu^-$ as well as the decay $J/\psi \rightarrow e^+e^-$. However, the latter trigger may turn out to be too time consuming in the present form: searching the full TRT for electron candidates. Currently, trigger menus are under study in which the search for lepton candidates is restricted to regions of interest. For the B_c process a dedicated trigger menu may be appropriate, since the event rate and background rates are small. Despite the fact that the missing energy in the decay $B_c \rightarrow J/\psi l^{\pm}\nu_l$ can not be measured precisely enough to contribute to the B_c invariant mass determination, reconstruction of the charged lepton tracks provides sufficient constraints to determine the B_c mass (CDF quotes an error of less than 10 % on the mass based on 20 B_c candidates). An even better mass determination may be obtained by studying the decay channel $B_c \rightarrow J/\psi\pi$ (branching ratio $\sim$ 0.9 %) with $J/\psi \rightarrow l^+l^-$ with $l = e, \mu$. The charged lepton and neutrino are replaced by a single charged particle, thus the secondary vertex with three charged tracks fully constrains the B_c system. Studies indicate that 93 % of the charged pions in ATLAS with $p_T > 1$ GeV and $|\eta| < 2.5$ can be reconstructed [47]. Full detector simulation is required (also to derive precise predictions on the resolution of the mass and lifetime measurement) to study this in detail and is beyond the scope of this thesis.

A number of events with small transverse momentum pass the trigger and reconstruction criteria (illustrated in fig. 7.27). Application of homogeneous and non-homogeneous evolution equations leads to different cross sections in the low momentum region. Careful analysis and optimisation of selection criteria may enhance the number of events in this region and discriminate between the two models.

The implementation of the model for the full fragmentation process for the B_c meson in the ARIADNE Monte Carlo program allows for more extensive studies in which details of the fragmentation procedure can be investigated. The model provides predictions for the relative B_c production rates in the processes $g \rightarrow B_c$ and $b \rightarrow B_c$. In both cases, an additional charm quark is involved, which may show up as a D^* associated with the B_c-jet. Measurement of the transverse and longitudinal momentum of the D^* with respect to the B_c-jet or B_c itself may reveal further insight in the fragmentation procedure. In case of the process $g \rightarrow B_c$ one may investigate whether both the D^* and an additional b quark end up in the same hemisphere and may be associated with the same jet.

Finally, the production rates predicted for the LHC, should enable the discovery of excited B_c states. Although association with the relatively soft photon in their decay will be far from trivial, it would be interesting to see whether the sample of fully reconstructed B_c events allows to perform B_c spectroscopy.

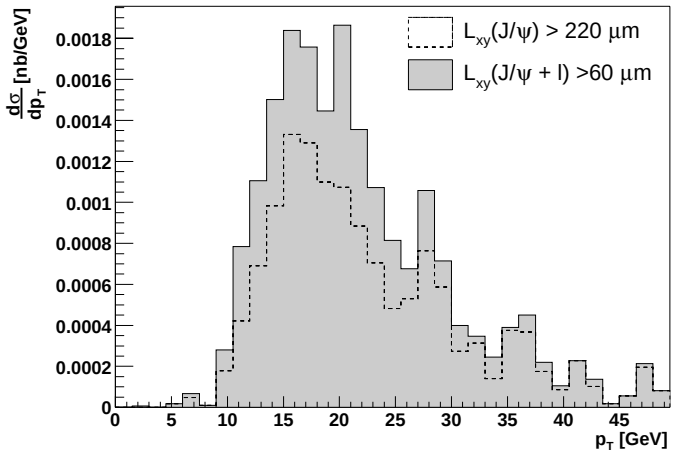

Figure 7.27: *$d\sigma/p_T$ of the decayed B_c^- in the mass window $4.0 < M(J/\psi + l^-) < 6.0$ GeV, with the Event Filter mass and vertex J/ψ cut, and with only the Event Filter mass J/ψ cut and $L_{xy}(J/\psi + l^-) > 60$ μm. (obtained without detector smearing and efficiency cuts).*

Appendix A

Module to MUR and MUR to ROBs maps

In this appendix the mappings of detector modules of the SCT and Pixel detectors on MURs (Minimum Units of Read-out) and of MURs on ROBs are specified.

A.1 Module to MUR maps

The module to MUR maps are shown in schematic overviews.

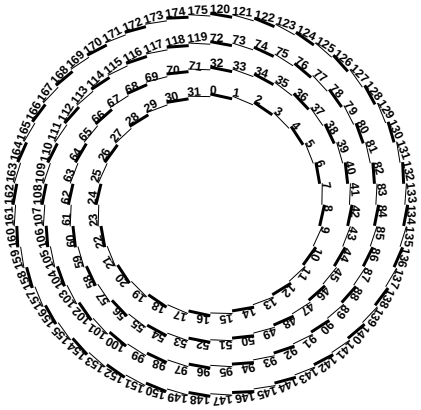

Figure A.1: *Map of SCT barrel modules to MURs. Shown are the four concentric SCT barrels. The view is perpendicular to the beam-axis, cutting the SCT barrel in half. One MUR here contains 6 SCT modules along the z direction.*

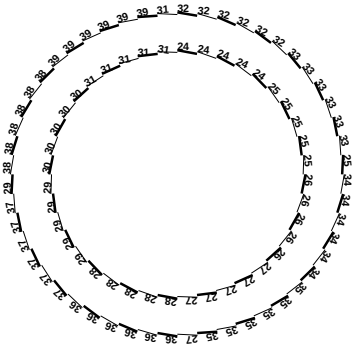

Module to MUR map of SCT endcap wheel 0.

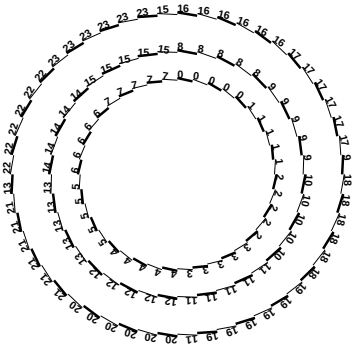

Module to MUR map of SCT endcap wheel 1.

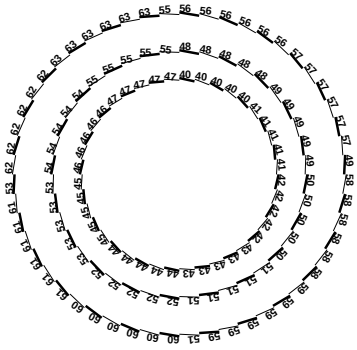

Module to MUR map of SCT endcap wheel 2.

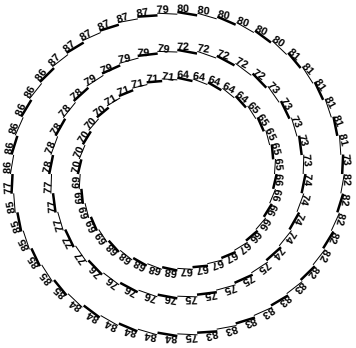

Module to MUR map of SCT endcap wheel 3.

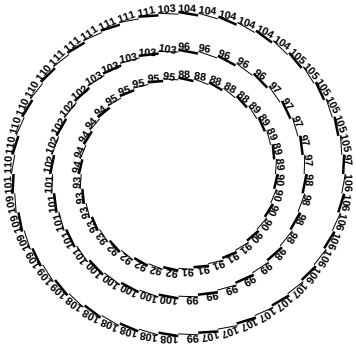

Module to MUR map of SCT endcap wheel 4.

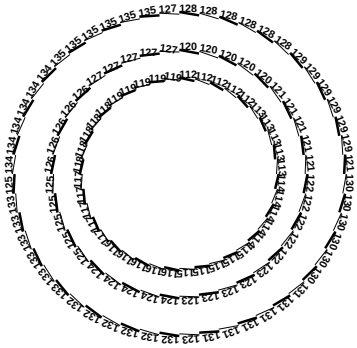

Module to MUR map of SCT endcap wheel 5.

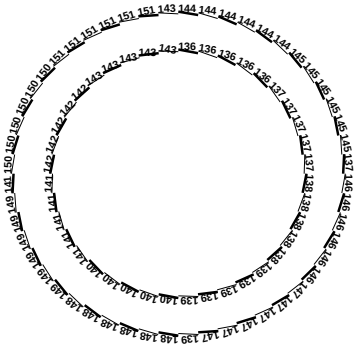

Module to MUR map of SCT endcap wheel 6.

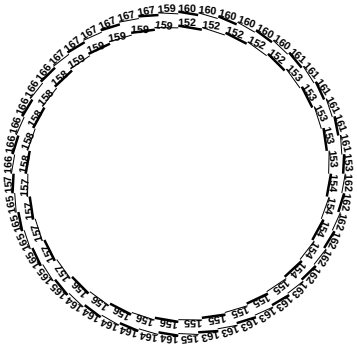

Module to MUR map of SCT endcap wheel 7.

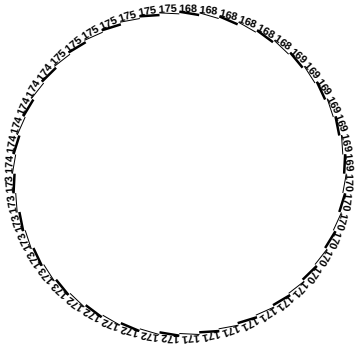

Module to MUR map of SCT endcap wheel 8.

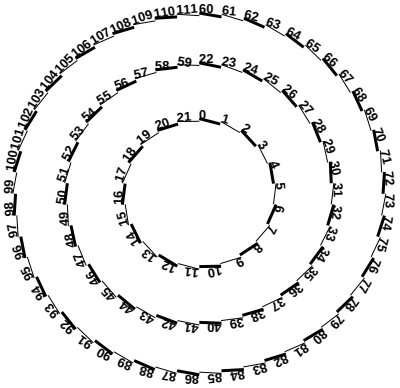

Fall 2001 geometry Pixel barrel module to MUR map.

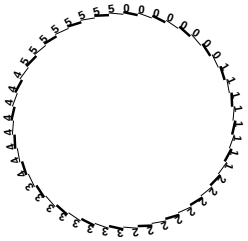

Module to MUR map of Pixel endcap wheel 0 (fall 2001 geometry).

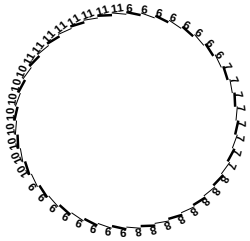

Module to MUR map of Pixel endcap wheel 1 (fall 2001 geometry).

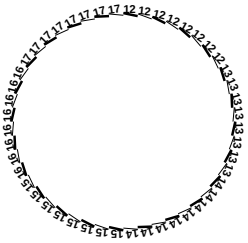

Module to MUR map of Pixel endcap wheel 2 (fall 2001 geometry).

A.2 MUR to ROB maps

The MUR to ROB maps are schematically shown below.

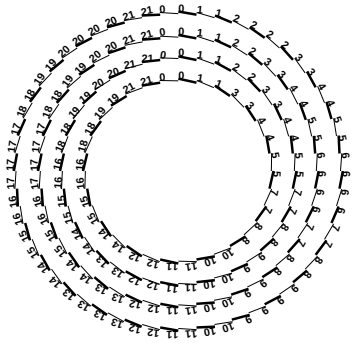

SCT barrel tower ROB mapping A (with adjacent pair constraint).

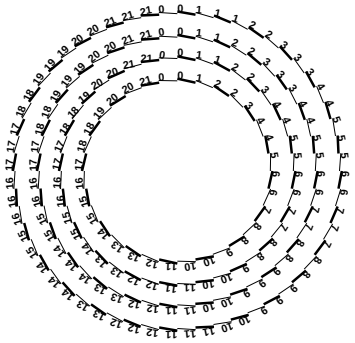

SCT barrel tower ROB mapping B (without adjacent pair constraint).

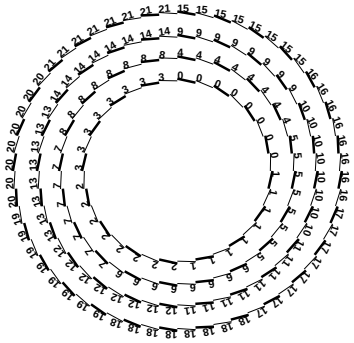

SCT barrel layer ROB mapping.

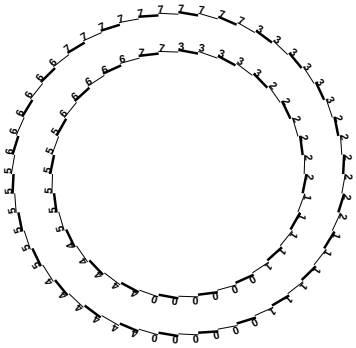

SCT endcap ROB tower mapping endcap wheel 0.

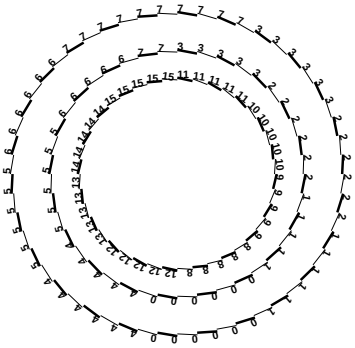

SCT endcap ROB tower mapping endcap wheel 1.

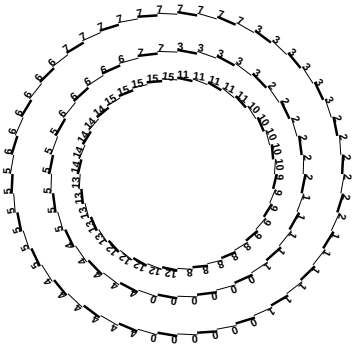

SCT endcap ROB tower mapping endcap wheel 2.

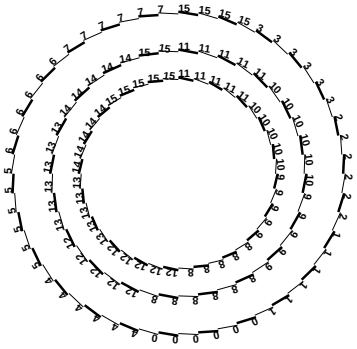

SCT endcap ROB tower mapping endcap wheel 3.

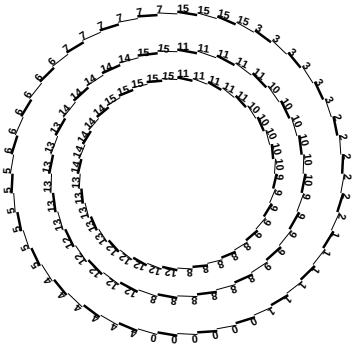

SCT endcap ROB tower mapping endcap wheel 4.

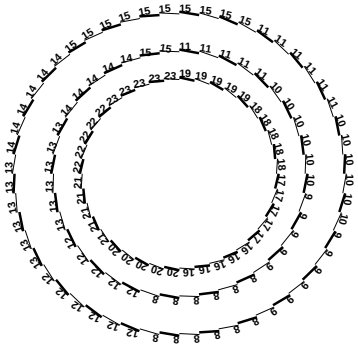

SCT endcap ROB tower mapping endcap wheel 5.

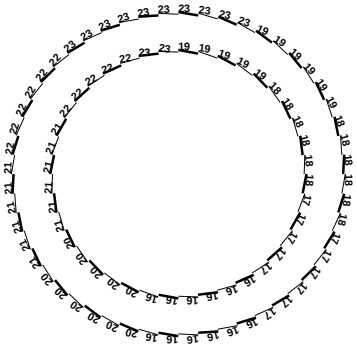

SCT endcap ROB tower mapping endcap wheel 6.

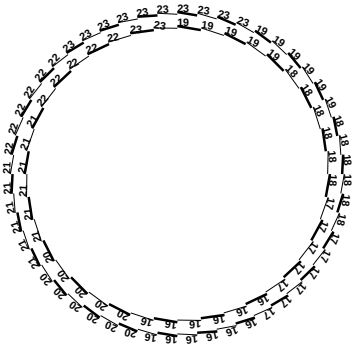

SCT endcap ROB tower mapping endcap wheel 7.

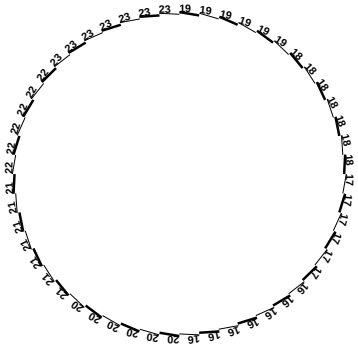

SCT endcap ROB tower mapping endcap wheel 8.

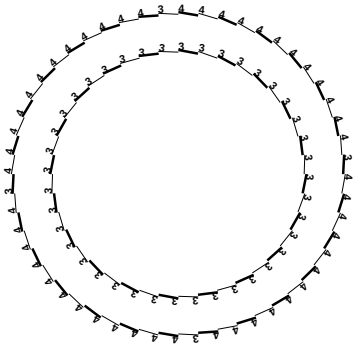

SCT endcap ROB layer mapping endcap wheel 0.

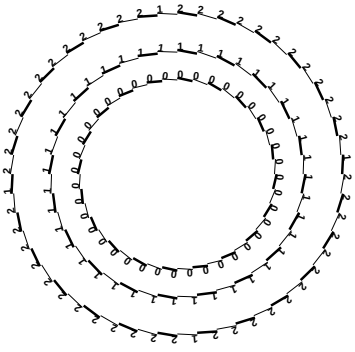

SCT endcap ROB layer mapping endcap wheel 1.

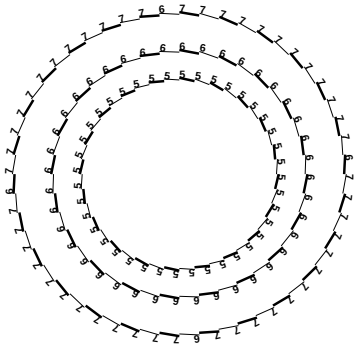

SCT endcap ROB layer mapping endcap wheel, the mapping of the endcaps wheels continues in an analogue fashion as for these three.

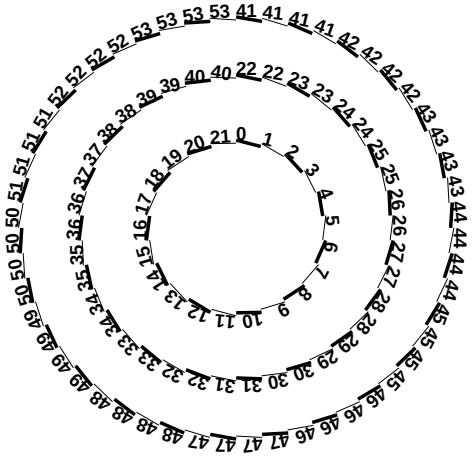

Pixel barrel ROB layer mapping.

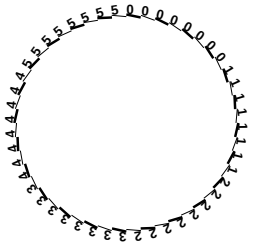

Pixel endcap ROB tower mapping wheel 0.

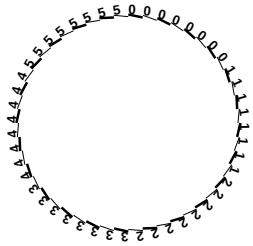

Pixel endcap ROB tower mapping wheel 1.

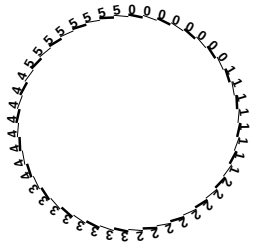

Pixel endcap ROB tower mapping wheel 2.

Appendix B

B_c Fragmentation functions

In this appendix, the fragmentation functions as implemented in ARIADNE are detailed. Note that the functions are given as a function of s and z, while the fragmentation functions given in chapter 6 have been integrated over s. The following definitions are used :

$$\begin{aligned} M &= m_c + m_b && \text{(B.1)} \\ r &= \frac{m_c}{m_b + m_c} && \text{(B.2)} \\ \bar{r} &= 1 - r = \frac{m_b}{m_b + m_c} && \text{(B.3)} \\ m &= \frac{m_c m_b}{m_c + m_b} && \text{(B.4)} \\ & && \text{(B.5)} \end{aligned}$$

where m_b and m_c are the mass of the b and c quark, respectively. The cut-off on s (energy squared) is implemented by the step function :

$$\theta_{step}(s,z) = \theta\left(s - \frac{M^2}{z} - \frac{m_c^2}{1-z}\right) \tag{B.6}$$

B.1 S-wave fragmentation functions

The fragmentation function for the ${}^1S_0$ B_c groundstate reads :

$$\begin{aligned} D_{\bar{b}\to B_c}(z,\mu_0) =& \frac{4(\alpha_s(\mu))^2|R(0)|^2}{27\pi m_c^3} \int ds \theta_{step}(s,z)\ P(s,z) \\ P(s,z) =& \frac{(1-z)(1+rz)^2 r M^2}{[1-(1-r)z]^2(s-m_b^2)^2} \\ & - \frac{[2(1-2r)-(3-4r+4r^2)z+(1-r)(1-2r)z^2]rM^4}{[1-(1-r)z](s-m_b^2)^3} \\ & - \frac{4r^2(1-r)M^6}{(s-m_b^2)^4} \end{aligned} \tag{B.7}$$

while the fragmentation function for the ${}^3S_1$ (or B_c^*) state is given by :

$$\begin{aligned} D_{\bar{b}\to B_c^*}(z,\mu_0) =& \frac{4(\alpha_s(\mu))^2|R(0)|^2}{27\pi m_c^3}\int ds\theta_{step}(s,z)\ P(s,z) \\ P(s,z) \ =& \frac{(1-z)(1+2rz+(2+r^2)z^2)rM^2}{[1-(1-r)z]^2(s-m_b^2)^2} \\ &- \frac{[2(1+2r)-(1+12r-4r^2)z-(1-r)(1+2r)z^2]rM^4}{[1-(1-r)z](s-m_b^2)^3} \\ &- \frac{12r^2(1-r)M^6}{(s-m_b^2)^4} \end{aligned} \tag{B.8}$$

B.2 P-wave fragmentation functions

The P-wave functions are given as a linear combination of a P-wave color singlet term and a S-wave color octet term :

$$D_{\bar{b}\to\bar{b}c(n^1P_1)}(z,\mu_0) = \frac{H_{1\bar{b}c}(n)}{m}D^{(1)}_{\bar{b}\to\bar{b}c({}^1P_1)}(z,\Lambda) + 3\frac{H'_{8\bar{b}c}(n)}{m}D^{(8)}_{\bar{b}\to\bar{b}c({}^1S_0)}(z) \tag{B.9}$$

$$D_{\bar{b}\to\bar{b}c(n^2P_J)}(z,\mu_0) = \frac{H_{1\bar{b}c}(n)}{m}D^{(1)}_{\bar{b}\to\bar{b}c({}^3P_J)}(z,\Lambda) + (2J+1)\frac{H'_{8\bar{b}c}(n)}{m}D^{(8)}_{\bar{b}\to\bar{b}c({}^3S_1)}(z) \tag{B.10}$$

where μ_0 and Λ are scales taken at the order of the heavy quark mass. The color singlet contribution to the ${}^1P_1$ state is given by:

$$D^{(1)}_{({}^1P_1)}(z,s) = \frac{32(\alpha_s(2m_c))^2}{81}\frac{r\bar{r}^3}{(1-\bar{r}z)^4}\sum_{n=0}^{3}\frac{f_nM^{8-2n}}{(s-\bar{r}^2M^2)^{5-n}} \tag{B.11}$$

with f_n defined by:

$$f_0 = 64r^2\bar{r}^3(1-\bar{r}z)^4, \tag{B.12}$$

$$f_1 = 8r\bar{r}(1-\bar{r}z)^3[3-2r-2r^2-2\bar{r}(2+4r-r^2)z+\bar{r}^2(1-2r)z^2], \tag{B.13}$$

$$\begin{aligned} f_2 =& -(1-\bar{r}z)^2[2(1-2r+4r^2)-(3-42r+64r^2-16r^3)z \\ &-2r\bar{r}(23-14r-4r^2)z^2+\bar{r}^2(1+12r)(1-2r)z^3], \end{aligned} \tag{B.14}$$

$$\begin{aligned} f_3 =& (1-z)[1-2(1-2r)z+(3-2r+2r^2)z^2-2\bar{r}(2+r-2r^2)z^3 \\ &+\bar{r}(2+r^2)z^4]. \end{aligned} \tag{B.15}$$

The color singlet contribution to the ${}^3P_J$ state reads:

$$D^{(1)}_{({}^3P_J)}(z,s) = \frac{32(\alpha_s(2m_c))^2}{243}\frac{r\bar{r}^3}{(1-\bar{r}z)^4}\sum_{n=0}^{3}\frac{f_n^{(J)}M^{8-2n}}{(s-\bar{r}^2M^2)^{5-n}} \tag{B.16}$$

with $f_n^{(J)}$:

$$
\begin{aligned}
f_0^{(0)} &= 64r^2\bar{r}^3(1-\bar{r}z)^4, && \text{(B.17)}\\
f_1^{(0)} &= 8r\bar{r}(1-\bar{r}z)^3[1-18r+14r^2-2\bar{r}^2(1-2r+7r^2)z+\bar{r}^2(1+2r)z^2], && \text{(B.18)}\\
f_2^{(0)} &= -(1-\bar{r}z)^2[2(1-4r)(1+6r-4r^2)-(5+14r-8r^2+80r^3-64r^4)z \\
&\quad +2\bar{r}(2+9r+18r^2-28r^3-16r^4)z^2-r^2(1+6r+16r^2-32r^3)z^3], && \text{(B.19)}\\
f_3^{(0)} &= (1-z)[1-4r-(1-4r)(1-2r)z-r\bar{r}(3-4r)z^2]^2, && \text{(B.20)}\\
f_0^{(1)} &= 192r^2\bar{r}^3(1-\bar{r}z)^4, && \text{(B.21)}\\
f_1^{(1)} &= 24r\bar{r}(1-\bar{r}z)^3[2(1-r-r^2)-\bar{r}(3+10r-2r^2)z+\bar{r}^2z^2], && \text{(B.22)}\\
f_2^{(1)} &= -6(1-\bar{r}z)^2[2(1+2r)-(5-2r+6r^2)z+2\bar{r}(2-3r-4r^2)z^2- \\
&\quad \bar{r}^2(1-2r+2r^2)z^3], && \text{(B.23)}\\
f_3^{(1)} &= 6(1-z)[1-2(1-2r)z+(1-4r)(1-2r)z^2+2r\bar{r}(1-2r)z^3+r^2\bar{r}^2z^4], && \text{(B.24)}\\
f_0^{(2)} &= 320r^2\bar{r}^3(1-\bar{r}z)^4, && \text{(B.25)}\\
f_1^{(2)} &= 8r\bar{r}(1-\bar{r}z)^3[2(4+13r)-(1+70r-26r^2)z-\bar{r}(7+8r)z^2], && \text{(B.26)}\\
f_2^{(2)} &= -4\bar{r}^2(1-\bar{r}z)^2[4(1+4r)-(7+12r-32r^2)z \\
&\quad +2(1+13r-26r^2+8r^3)z^2+(1-30r-5r^2+4r^3)z^3], && \text{(B.27)}\\
f_3^{(2)} &= 4\bar{r}^2(1-z)[2-4(1-2r)z+(5-8r+12r^2)z^2-2(1-2r)(3+2r^2)z^3 \\
&\quad +(3-12r+12r^2+2r^4)z^4]. && \text{(B.28)}
\end{aligned}
$$

The octet S-wave components that contribute to the total P-wave fragmentation function are given by:

$$D^{(8)}(z,s)=\frac{(\alpha_s(2m_c))^2}{81}\frac{r\bar{r}^3}{(1-\bar{r}z)^2}\sum_{n=0}^{2}\frac{g_nM^{6-2n}}{(s-\bar{r}^2M^2)^{4-n}} \qquad \text{(B.29)}$$

where g_n for the $^1S_0$ state reads :

$$
\begin{aligned}
g_{0(^1S_0)} &= -12r\bar{r}(1-\bar{r}z)^2, && \text{(B.30)}\\
g_{1(^1S_0)} &= -3(1-\bar{r}z)[2(1-2r)-(3-4r+4r^2)z+\bar{r}(1-2r)z^2], && \text{(B.31)}\\
g_{2(^1S_0)} &= 3(1-z)(1+rz)^2. && \text{(B.32)}
\end{aligned}
$$

Similarly, the g_n for the $^3S_1$ state reads :

$$
\begin{aligned}
g_{0(^3S_1)} &= -12r\bar{r}(1-\bar{r}z)^2, && \text{(B.33)}\\
g_{1(^3S_1)} &= -(1-\bar{r}z)[2(1+2r)-(1+12r-4r^2)z-\bar{r}(1+2r)z^2], && \text{(B.34)}\\
g_{2(^3S_1)} &= (1-z)[1+2rz+(2+r^2)z^2]. && \text{(B.35)}
\end{aligned}
$$

For a given principal quantum number n, the $^1P_1$ state and $^3P_1$ states mix to form physical states, $|1^{+'}>$ and $|1^+>$:

$$|1^{+'}> = \cos\theta|^1P_1> - \sin\theta|^3P_1> \quad \text{(B.36)}$$
$$|1^{+}> = \sin\theta|^1P_1> + \cos\theta|^3P_1> \quad \text{(B.37)}$$
$$\quad \text{(B.38)}$$

The fragmentation functions for a $\bar{b}$ to the physical states $|1^{+'}>$ and $|1^{+}>$ B_c states are then given by:

$$D^{(1)}_{\bar{b}\to\bar{b}c(1+')} = \cos^2\theta D^{(1)}_{\bar{b}\to\bar{b}c(^1P_1)}(z) + \sin^2\theta D^{(1)}_{\bar{b}\to\bar{b}c(^3P_1)}(z) - \sin\theta\cos\theta P^{(1)}_{mix}(z) \quad \text{(B.39)}$$
$$D^{(1)}_{\bar{b}\to\bar{b}c(1+)} = \sin^2\theta\ D^{(1)}_{\bar{b}\to\bar{b}c(^1P_1)}z) + \cos^2\theta D^{(1)}_{\bar{b}\to\bar{b}c(^3P_1)}z) + \sin\theta\cos\theta D^{(1)}_{mix}(z) \quad \text{(B.40)}$$
$$\quad \text{(B.41)}$$

The mixing term reads:

$$D^{(1)}_{mix}(z,s) = \frac{64\sqrt{2}(\alpha_s(2m_c))^2}{81}\frac{r\bar{r}^3}{(1-\bar{r}z)^3}\sum_{n=0}^{2}\frac{f^{mix}_n M^{6-2n}}{(s-\bar{r}^2M^2)^{4-n}} \quad \text{(B.42)}$$

where the f^{mix}_n are:

$$f^{mix}_0 = -8r\bar{r}(1-\bar{r}z)^3[2-3r-\bar{r}(1+r)z], \quad \text{(B.43)}$$
$$f^{mix}_1 = (1-\bar{r}z)[2(1+2r^2)-(5-24r+36r^2-8r^3)z+2\bar{r}(2-15r+10r^2-2r^3)z^2$$
$$-\bar{r}^2(1-8r-4r^2)z^3], \quad \text{(B.44)}$$
$$f^{mix}_2 = -(1-z)[1-(1-3r)z+r(2+r)z^2+\bar{r}r^2z^3]. \quad \text{(B.45)}$$

References

[1] K. Hagiwari et al. Phys. Rev. **D66**, 010001 (2002). `http://pdg.lbl.gov`.

[2] J.H. Christenson, J.W. Cronin, V.L. Fitch, R. Turlay. Phys. Rev. Lett. **13**, 138 (1964).

[3] B.Aubert et al. [BaBar Collaboration]. Phys. Rev. Lett. **87**, 091801 (2001).

[4] K. Abe et al. [Belle Collaboration]. Phys. Rev. Lett. **87**, 091802 (2001).

[5] K. Long, *QCD high energy (experiment)* . Talk given at the ICHEP 2002 conference in Amsterdam.

[6] ATLAS Collaboration, *Muon Spectrometer Technical Design Report*. CERN, 1997. CERN/LHCC 97-22.

[7] A. Martin, R. Roberts, W. Stirling, R. Thorne. Eur. Phys. J. **C23**, 73 (2002). (hep-ph/0110215).

[8] V.N. Gribov, L.N. Lipatov. Sov. J. Nucl. Phys. **15**, 438 (1972);
V.N. Gribov, L.N. Lipatov. Sov. J. Nucl. Phys. **15**, 675 (1972);
L.N. Lipatov. Sov. J. Nucl. Phys. **20**, 94 (1975);
G. Altarelli, G. Parisi. Nucl. Phys. **B126**, 298 (1977);
Yu L. Dokshitzer. Sov. Phys. JTEP **46**, 641 (1977).

[9] B. L. Combridge. Nucl. Phys. **B151**, 429 (1979).

[10] P. Nason, S. Dawson, R. Ellis. Nucl. Phys. **B327**, 49 (1989).

[11] B. Abbot et al. [DØ Collaboration]. Phys. Lett. **B487**, 264 (2000).

[12] S Abachi et al. [DØ Collaboration]. Phys. Rev. Lett. **74**, 3548 (1995).

[13] F. Abe et al. [CDF Collaboration]. Phys. Rev. **D58**, 072001 (1998).

[14] G. Altarelli, M.L. Mangano (ed.), *Proceedings of the workshop on Standard Model physics (and more) ath the LHC*. CERN, 2000. Yellow report CERN 2000-004.

[15] C. Peterson, D. Schlatter, I. Schmitt, P.M. Zerwas. Phys. Rev. **D27**, 105 (1983).

[16] A. Martin, R. Roberts, W. Stirling. Phys. Lett. **B387**, 419 (1996). (hep-ph/9606345).

[17] C. Albajar et al. [UA1 Collaboration]. Z. Phys. **C61**, 41 (1994).

[18] QCD chapter from ref. [14].

[19] S. Catani, M. Mangano, P. Nason, L. Trentadue. Nucl. Phys. **B478**, 273 (1996). (hep-ph/9604351).

[20] Section 5.4, "Small-x resummation" from ref. [14].

[21] D. Acosta et al. Phys. Rev. **D65**, 052005 (2002).

[22] P. Nason, M. Cacciari. Phys. Rev. Lett. **89**, 122003 (2002). (hep-ph/0204025).

[23] T. Sjöstrand, P. Eden, C. Friberg, L. Lönblad, G. Miu, S. Mrenna, E. Norrbin. Comp. Phys. Comm. **135**, 238 (2001). See also [61] and `http://www.thep.lu.se/~torbjorn/Pythia.html`.

[24] L. Lönnblad, *Ariadne 4*, August 2001. Version 4.12, original manual published in [125].

[25] Bottom production part, section 4, "A study of the $b\bar{b}$ production mechanism in PYTHIA" from ref. [14].

[26] H.L. Lai et al. Phys. Rev. **D51**, 4763 (1995). (hep-ph/9410404).

[27] *Proceedings of the International conference on HEP, October 2001.* 2001. (hep-ph/0110086).

[28] G.W. Bennet et al. [Muon g-2 Collaboration]. Phys. Rev. Lett. **89**, 101804 (2002). Erratum-ibid. 89 (2002) 129903.

[29] U. Amaldi, W. de Boer, H Fürstemann. Phys. Lett. **B260**, 447 (1991).

[30] E.L. Berger, B.W. Harris, D.E. Kaplan, Z. Sullivan, T.M.P. Tait, C.E.M.Wagner. Phys. Rev. Lett. **86**, 4231 (2001). (hep/ph-0012001).

[31] V. Savinov et al. [CLEO Collaboration]. Phys. Rev. **D63**, 051101 (2001).

[32] U. Nierste ,T. Plehn. Phys. Lett. **B493**, 104 (2000).

[33] P. Collier. `http://sl.web.cern.ch/SL/sli/Cycles.htm`, 2000.

[34] ATLAS Collaboration, *ATLAS Detector and Physics Performance Technical Design Report.* CERN, 1999. CERN/LHCC 99-15.

[35] ATLAS Collaboration, *ATLAS Inner Detector Technical Design Report.* CERN, 1997. CERN/LHCC 97-16.

[36] Stein Stapner, *"General ID issues", talk at ATLAS June 2002 Overview week.*

[37] A. Barr et al., *Beamtests of Prototype ATLAS SCT Modules at CERN H8 in June and August 2000* . Atlas Inner Detector note ATL-INDET-2002-005, 2002.

[38] ATLAS Collaboration, *Calorimeter Performance Technical Design Report*. CERN, 1997. CERN/LHCC 96-40.

[39] ATLAS Liquid Argon HEC Collaboration, *Performance of the ATLAS Hadronic End-Cap Calorimeter in Beam Tests* . Atlas Liquid Argon Detector Module note ATL-LARG-2001-019, 2001.

[40] Avioli, G. et al., *First results of the 2001 MDT chambers beam test* . Atlas Muon detector note ATL-MUON-2003-001, 2003.

[41] Herten, G, *Status of MDT and CSC production Status* . `http://hpfrs6.physik.uni-freiburg.de/~herten/atlas/muon/mdt/report/GH_mdt_021001.pdf`, September 2002.

[42] ATLAS Collaboration, *First-Level Trigger Technical Design Report*. CERN, 1998. ATLAS TDR-12.

[43] A. Di Mattia et al., *RPC trigger Robustness: Status Report* . Atlas TDAQ note ATL-DAQ-2002-015, 2003.

[44] ATLAS Collaboration, *ATLAS High-Level Triggers, DAQ and DCS, Technical Proposal*. CERN, 2000. CERN/LHCC 2000-17.

[45] A. Di Mattia, S. Falciano, C. Luci, A. Nisati, F. Petrucci, S. Robins, L. Zanello, *A muon trigger algorithm for Level-2 feature extraction* . Atlas TDAQ note ATL-DAQ-2000-036, 2000.

[46] J. Baines et al., *Resource estimates for the ATLAS B-physics trigger* . Atlas TDAQ communication ATL-COM-DAQ-2002-013, 2002.

[47] Baines, J. et al., *B-physics Event Selection for the ATLAS High Level Trigger* . Atlas TDAQ note ATL-DAQ-2000-031, 2000.

[48] J. Vermeulen et al., *A SHARC based ROB complex: design and measurement results* . Atlas TDAQ note ATL-DAQ-2000-021, 2000.

[49] *Analog devices, Inc*. `http://www.analog.com`.

[50] *Altera Corporation*. `http://www.altera.com`.

[51] P. Jansweijer, G. Kieft, J. Vermeulen, *A Compact Robin Using the SHarc* . `http://www.nikhef.nl/pub/experiments/atlas/daq/CRUSH-hw.pdf`.

[52] *Applied Micro Circuits Corporation*. `http://www.amcc.com`.

[53] *Silicon Software*. `http://www.silicon-software.de`.

[54] *SLIDAS, S-Link Infinite Data Source*. `http://hsi.web.cern.ch/HSI/s-link/devices/slidas/`.

[55] J. Vermeulen et al., *SHasHLINK documentation.* `http://www.nikhef.nl/pub/experiments/atlas/daq/crush.html` and `http://www.nikhef.nl/pub/experiments/atlas/daq/ShaSLINK.pdf`.

[56] J. Bystrycky, J. Vermeulen, *Paper modelling of the ATLAS LVL2 trigger system* . Atlas TDAQ communication ATL-COM-DAQ-2000-022, 2000.

[57] R. Cranfield, J. Vermeulen, *ROB Complex Master Working Document* . Atlas TDAQ communication ATL-COM-DAQ-033, 2000.

[58] J. Vermeulen, *Scenarios for a ROB system built with SHARC processors* . `http://www.nikhef.nl/pub/experiments/atlas/daq/CRUSH-hw.pdf`.

[59] R. Scholte, *Event Fragment Size Distributions for the Inner Detector* . Atlas TDAQ note ATL-DAQ-2003-015, 2003.

[60] *Dice reference manual.* `http://atlas.web.cern.ch/Atlas/GROUPS/SOFTWARE/DOCUMENTS/simulation.htm`.

[61] T. Sjöstrand, L. Lönblad, S. Mrenna, *Pythia 6.2, Physics and Manual*, August 2001. (hep-ph/0108264).

[62] M. Smizanska. `http://msmizans.home.cern.ch/msmizans/production/minbias.html`.

[63] Files taken from Tape Y00039.

[64] `http://www.cern.ch/Atlas/GROUPS/DAQTRIG/ATRIG/index.html`.

[65] *The ROOT Homepage.* `http://root.cern.ch`.

[66] M. Abolins and J.C. Vermeulen, *Draft version 0.99 of "Paper model results for the ATLAS Trigger/DAQ system"* . `http://www.nikhef.nl/pub/experiments/atlas/daq/papernote-2001.pdf`, 2001.

[67] J. Pater. Private communication.

[68] A. Dell'Acqua, D. Froidevaux et al., *1997 ATLAS Jet Production* . ATLAS Physics note ATL-PHYS-97-102, 1997.

[69] P.Clarke et al., *Detector and read-out specification, and buffer-RoI relations, for level-2 studies* . Atlas TDAQ note ATL-DAQ-99-014, 1999.

[70] A. Rozanov. Private communication.

[71] *Pixel Detector Technical Design Report.* CERN, 1998. CERN/LHCC 98-13.

[72] P. Lujan. Private communication.

[73] P. Dam, *A Study of ROD compression schemes for the TRT* . Atlas Inner Detector note ATL-INDET-2001-009, 1999.

[74] R. Scholte, R. Slopsema, B. van Eijk, N. Ellis, J. Vermeulen, *A LVL2 Zero Suppression Algorithm for TRT Data* . Atlas TDAQ note ATL-DAQ-2003-016, 2003.

[75] N. Ellis. Report to TRT electronics meeting, CERN, 30 November 1999.

[76] F. Luehring, *Description of the TRT Readout Scheme* . Atlas Inner Detector note ATL-INDET-2002-026, 2002.

[77] F. Abe et al. [CDF Collaboration]. Phys. Rev. **D58**, 112004 (1998). (hep-ex/9804014).

[78] E. Braaten, T.C. Yuan. Phys. Rev. Lett. **71**, 1673 (1993);
E. Braaten, K, Cheung, T.C. Yuan. Phys. Rev. **D48**, 4230 (1993).

[79] R. Barbieri, R Gatto, R. Remiddi. Phys. Lett. **B61**, 465 (1976).

[80] G. Bodwin, E. Braaten, G. Lepage. Phys. Rev. **D51**, 1125 (1995).

[81] E. Braaten, M. Doncheski, S. Fleming, M. Mangano. Phys. Lett. **B333**, 548 (1994). (hep-ph/9405407).

[82] B. van Eijk, R. Kinnunen. Z. Phys. **C41**, 489 (1988).

[83] E. Braaten, S. Fleming. Phys. Rev. Lett. **74**, 3327 (1995).

[84] P.Ernstron, L. Lönnblad. Z. Phys. **C75**, 51 (1997). (hep-ph/9606472).

[85] F. Abe et al. [CDF collaboration]. Phys. Rev. Lett. **79**, 572 (1997);
V. Papadimitriou, *Published in Proceedings from QCD and High Energy Interactions, XXXth Rencontres de Moriond, Les Arcs, France, March 19-26, 1995.* Fermilab-Conf-95/128-E, 1995;
[The CDF collaboration], *Contributed paper to the 27th International Conference on High Energy Physics, Glasgow, July 20-27, 1994.* Fermilab-Conf-94/136-E, 1994. (hep-ex/9412013).

[86] E. Braaten, K. Cheung, T.C. Yuan. Phys. Rev. **D48**, R5049 (1993).

[87] T.C. Yuan. Phys. Rev. **D50**, 5664 (1994).

[88] K.C. Cheung. Phys. Lett. **B472**, 408 (2000). (hep-ph/9908405).

[89] K.Cheung, T.C. Yuan. Phys. Rev. **D53**, 1232 (1996).

[90] K.C. Cheung, T.C. Yuan. Phys. Rev. **D53**, 3591 (1996).

[91] K. Cheung, T.C. Yuan. Phys. Lett. **B325**, 481 (1994).

[92] A.V. Berezhnoy et al. Phys. of Atomic Nuclei **60**, 1729 (1997). (hep-ph/9703341).

[93] K. Kolodziej, A. Leike,R. Rückl. Phys. Lett. **B355**, 337 (1995).

[94] E. Eichten, C. Quigg. Phys. Rev. **D49**, 5845 (1994). (hep-ph/9402210).

[95] S. Gershstein, V. Kiselev, A. Likhoded, A. Tkabladze. Phys. Rev. **D51**, 3613 (1995).

[96] D. Ebert, R Faustov, V. Galkin. Phys. Rev. **D67**, 014027 (2003).

[97] *Heavy Flavor Physics, Theoretical and experimental results in Heavy Quark Physics*, chapter Heavy Quark Theory. Scottish Universities Summer School in Physics and Institute of Physics Publishing, Bristol and Philadelphia, 2002. Proceedings of the Fifty-Fifth Scottish Universities Summer School in Physics, St. Andrews, 7 August - 23 August 2001.

[98] M. Beneke, G. Buchalla. Phys. Rev. **D53**, 4991 (1996).

[99] K. Anikeev et al., *B Physics at the Tevatron: Run II and Beyond*. FERMILAB-Pub-01/197, (hep-ph/0201071), 2002.

[100] V.V. Kiselev. Mod. Phys. Lett. **A10**, 1049 (1995).

[101] V.V. Kiselev, A.K. Likhoded, A.I. Onischenko. Nucl. Phys. **B569**, 473 (2000).

[102] P. Colangelo, F. De Fazio. Mod. Phys. Lett. **A14**, 2303 (1999). (hep-ph/9904363).

[103] C. Chang, D. Lü, G. Wang, H. Zong. Phys. Lett. **B434**, 358 (1998). (hep-ph/990447).

[104] C. Chang. Talk at XXXVIIth Rencontres de Moriond on QCD and High Energy Hadronic Interactions, 2002. (hep-ph/0205112).

[105] *At the Frontier of Particle Physics / Handbook of QCD'*, chapter QCD Sum Rules, a Modern Perspective. World Scientific, Singapore, 2001. (hep-ph/0010175).

[106] V.V. Kiselev, A. Tkabladze. Phys. Rev. **D48**, 5208 (1993).

[107] V.V. Kiselev, A.E. Kovalsky, A.K. Likhoded. Nucl. Phys. **B585**, 353 (2000).

[108] C.H. Chang, Y. Chen. Phys. Rev. **D49**, 3399 (1994).

[109] M.A. Ivanov, J.G. Korner, P. Santorelli. Phys. Rev. **D63**, 074010 (2001). (hep-ph/0007169).

[110] V.V. Kiselev. (hep-ph/9605451).

[111] J. Phys. **G28**, 595 (2002). (hep-ph/0110180).

[112] Y. Dai, D. Du. Eur. Phys. J. **C9**, 557 (1999). (hep-ph/9809386).

[113] R. Fleischer, D. Wyler. Phys. Rev. **D62**, 057503 (2000). (hep-ph/0004010).

[114] P. Ernström, L. Lönnblad, M. Vänttinen. Z. Phys. **C76**, 515 (1997). (hep-ph/9612408).

[115] L. Lönnblad. Private communication.

[116] R. Scholte. In preparation.

[117] H.L. Lai et al. Eur. Phys. J. **C12**, 375 (2000).

[118] G. Lim. Master's Thesis, University of Twente. In preparation (2003).

[119] C. Caso et al., *Particle data book*. Eur. Phys. J. **C3**, 1 (1998).

[120] F Abe et al. [CDF Collaboration]. Phys. Rev. **D57**, 5382 (1998).

[121] ATLAS Collaboration, *Trigger Performance Status Report*. CERN.

[122] *ATHENA-ATLFAST homepage*. `http://www.hep.ucl.ac.uk/atlas/atlfast`.

[123] E.J. Buis, R. Dankers, A. Reichold, S. Haywood, *Parameterisation of the Inner Detector Performance* . Atlas Inner Detector note ATL-INDET-97-195, 1997.

[124] E.J. Buis, R. Dankers, A. Reichold, S. Haywood, G.F. Tartarelli, N. Labanca, *Update of Inner Detector Performance Parameterisations* . Atlas Inner Detector note ATL-INDET-98-215, 1998.

[125] L. Lönnblad. Comp. Phys. Comm. **71**, 15 (1992).

Summary

The Large Hadron Collider (LHC) is currently being constructed at CERN, the European particle physics laboratory in Geneva, Switzerland. At the LHC, dense bunches of protons will collide every 25 ns at a centre-of-momentum energy of $\sqrt{s}$=14 TeV. Of the five experiments which will detect the products of the collisions, ATLAS will be the largest. Due to the high luminosity and the large proton-proton cross section, in combination with the low cross section for the processes to be studied, a trigger system is required to separate "interesting" physics from background processes. For ATLAS, a three stage trigger architecture is developed. This system uses data Read-Out Buffers, called ROBs, which hold the data from events accepted by the first level trigger (LVL1) and provide the event data on request, until a clear request has been received. A prototype ROB, called the "CRUSH", was developed at NIKHEF. In this thesis, the design and implementation of the CRUSH is discussed. The maximum input rate as a function of various parameters has been measured. The results have been fitted to yield simple parametrised equations which can be used for modelling purposes. The CRUSH shows good performance, both in a stand-alone test and in a ROB complex setup, and is able to store event fragments at the maximum LVL1 accept rate of $\sim$ 100 kHz.

To estimate the resources needed for the second level of the trigger system (LVL2), a "paper model" and a computer model of the LVL2 system are used. The paper model represents a static model, which uses average values of quantities such as event fragment sizes and algorithm processing times as input, whereas the computer model is a dynamic model and can use distributions of these quantities. With a detailed simulation of the appropriate detectors and electronics, distributions of event fragment sizes for Inner Detector ROBs, assuming operation of the LHC at low, intermediate and high luminosity, have been obtained. For the Pixel detector a new mapping of pixel modules to ROBs is introduced. The study shows that the distributions fall off very quickly, i.e. using average values in the calculation of LVL2 resources has irrelevant consequences for the accuracy with which the behaviour of the system is described.

One of the scenarios for the LVL2 B-physics trigger includes a full scan of the TRT detector, which implies that all channels are read out. Using a read-out scheme in which all TRT straws within one barrel or endcap segment are given a unique address header, this results in a large ($\mathcal{O}$(500 MByte/s)) data volume. To reduce this data volume, the implementation of a zero-suppression algorithm on a SHARC processor (as used in the CRUSH) and on an Intel platform was studied. An optimum data reduction of $\sim$ 30% can be achieved. The study shows that the algorithm takes about 1.9 ms on a SHARC processor, exceeding the average decision time for a LVL2 scan (0.2 ms). However, on an Intel platform the processing time is $\sim$ 0.04 ms, well within the specified limit.

Besides searching for the Higgs boson and possible "new physics" such as super-symmetry, ATLAS will also concentrate on B-physics. Apart from performing precise measurements which are related to CP violation in the B meson sector, ATLAS will measure the properties of B-mesons and baryons. This thesis focuses on the B_c meson, a bound state of a bottom and a charm quark. The production of the B_c meson is studied in the framework of Non-Relativistic Quantum-ChromoDynamics (NRQCD). Using this framework, so-called "fragmentation functions" can be derived. These functions give the probability of a b quark to fragment into a B_c meson. By means of evolution equations, gluon fragmentation into B_c mesons is also included. The derivation of the $b \to B_c$ fragmentation functions is reviewed. It is shown that similar fragmentation functions for $c \to \psi'$ correctly describe the measured prompt ψ' production cross section. From calculations on the mass spectrum of excited $b\bar{c}$ bound states it is manifest that states which have a mass below the threshold of production of a (light) B and D meson will decay, directly or indirectly, strongly or electromagnetically to the $b\bar{c}$ ground state. Therefore, all these excited states should be taken into account when predicting the total B_c production cross section. Fragmentation functions for these excited states are studied as well. Finally, theories that yield predictions for the inclusive lifetime, mass and branching ratio's of various $b\bar{c}$ states are discussed.

The fragmentation functions of the B_c states are implemented in ARIADNE, a Monte Carlo program that simulates the QCD cascade. Using PYTHIA for the hard interaction and the decays of excited $b\bar{c}$ states to the B_c ground state, an integrated B_c^- production cross section of 2.28 ± 1.14 nb ($p_T(B_c^-) > 6$ GeV) is predicted at Tevatron energies. By comparing the prediction with analytical results and measurements from CDF, it is shown that the implementation yields good agreement. Subsequently, it is predicted that the integrated B_c^- production cross section at LHC will be 66 ± 33 nb for $p_T(B_c^-) > 10$ GeV. Finally, the decay channel $B_c \to J/\psi(l^+l^-) + l + \nu_l$, $l = e, \mu$ is studied using a parameterised simulation of the ATLAS detector response. The displaced three-lepton decay vertex of this particular decay channel allows for a strong suppression of the background originating from prompt J/ψ (ψ') production as well as the decay of (light) B's to $J/\psi X$. The dominant background is formed by leptons, originating from decay-in-flight of pions and kaons, which are incorrectly associated to a (light) $B \to J/\psi X$ vertex. Using a cut on the transverse decay length of the $J/\psi(l^+l^-)+l$ system and an invariant mass constraint, $4.0 < M(J/\psi+l) < 6.0$, $\mathcal{O}(10^5)$ events remain assuming an integrated luminosity of 10 fb^{-1}. The study presented in this thesis, indicates that the background is very small, $S/B \sim$ 50-60. However, a study involving a full detector simulation should be carried out to investigate this in further detail.

Samenvatting

Bij CERN, het Europese deeltjes-fysica laboratorium in Genève, Zwitserland, wordt een nieuwe grote deeltjesversneller geconstrueerd, genaamd de "Large Hadron Collider" (LHC). De LHC zal elke 25 ns pakketjes met een grote hoeveelheid protonen met elkaar in botsing brengen bij een zwaartepuntenergie van $\sqrt{s}$=14 TeV. Van de vijf experimenten waarmee op verschillende botsingspunten in de ring van de LHC de producten van de botsingen zullen worden gedetecteerd, zal "ATLAS" de grootste zijn. Door de hoge luminositeit en de grote werkzame doorsnede van de proton-proton interacties, in combinatie met de kleine werkzame doorsnede van de processen die bestudeerd zullen worden, is een efficiënt trigger systeem noodzakelijk. Voor het ATLAS experiment is een trigger architectuur ontworpen opgebouwd uit 3 niveaus. Het trigger systeem maakt gebruik van zogeheten Read-Out Buffers of ROBs, die data van door het eerste trigger niveau geselecteerde gebeurtenissen opslaan en op verzoek doorgeven, totdat deze een signaal krijgen om de data te wissen. Een prototype van de ROB, de "CRUSH" genaamd, is ontwikkeld bij het NIKHEF. In dit proefschrift wordt het ontwerp en de implementatie van de CRUSH beschreven. Het aantal gebeurtenissen dat maximaal per seconde behandeld kan worden is gemeten als functie van verscheidene parameters. De resultaten zijn gefit aan eenvoudige geparametriseerde vergelijkingen die gebruikt kunnen worden in verschillende modellen. De CRUSH presteert naar behoren, zowel in een test waarin een enkele CRUSH uitgebreid is onderzocht als in een testomgeving waar meerdere ROBs aan elkaar gekoppeld zijn. De CRUSH is in staat om de maximale door het eerste trigger niveau per seconde geselecteerde hoeveelheid gebeurtenissen te verwerken ($\sim$ 100,000).

Om de aard, de snelheden en de aantallen van de componenten te bepalen die nodig zijn voor het systeem van het tweede trigger niveau, worden twee modellen van dit systeem gebruikt: een "paper" model en een computer model. Het "paper" model is een statisch model, dit wil zeggen dat gemiddelde waarden worden gebruikt voor grootheden als de grootte van data fragmenten en de executie tijd van een trigger algoritme. Het computer model daarentegen kan distributies van deze grootheden gebruiken. Distributies voor de grootte van data fragmenten voor ROBs van de "Inner Detector" zijn gegenereerd met behulp van een gedetailleerde simulatie van de desbetreffende detectoren en hun elektronica. De distributies zijn gegenereerd voor het functioneren van de LHC op lage, intermediaire en hoge luminositeit. Voor de Pixel detector is een nieuw schema geintroduceerd dat voorschrijft welke Pixel modules met welke Pixel ROBs verbonden zijn. Uit de studie blijkt dat de gegenereerde distributies snel afvallen voor grotere fragmenten, waaruit geconcludeerd kan worden dat gebruik van gemiddelde waarden in plaats van distributies toch tot een goede beschrijving van het gedrag van het systeem zal leiden.

Een van de scenario's voor de B-fysica selectie op het tweede trigger niveau voorziet in

de uitlezing van alle kanalen van de TRT detector. Als men vervolgens een uitlees-schema gebruikt waarin alle strootjes in een segment van het midden- of eindgedeelte van de TRT een uniek adres bezitten, resulteert een groot ($\mathcal{O}$(500 MByte/s)) data volume. Om dit volume te reduceren, is de implementatie van een "nul-onderdrukkings" algoritme op een SHARC processor (zoals gebruikt op de CRUSH) alsmede op een Intel systeem bestudeerd. Een optimale data reductie van ~ 30 % kan worden behaald. Uit de studie volgt bovendien dat de executie tijd van het algoritme op een SHARC processor ongeveer 1.9 ms bedraagt, een tijd die langer is dan de gemiddelde tijd die beschikbaar is (0.2 ms). Op een systeem met een moderne Intel processor daarentegen, neemt het uitvoeren van het algoritme slechts ~ 0.04 ms in beslag, ruim binnen de vastgestelde limiet.

Naast het zoeken naar het "Higgs" boson en mogelijke "nieuwe fysica" zoals supersymmetrie, zal met ATLAS ook B-fysica bestudeerd worden. De belangrijkste metingen zullen CP-schending in het verval van B-mesonen en B-baryonen betreffen, maar ook andere eigenschappen van deze deeltjes zullen worden bepaald. Dit proefschrift concentreert zich op het B_c meson, een gebonden toestand van een bottom en een charm quark. Het productie mechanisme van het B_c meson wordt bestudeerd aan de hand van Niet-Relativistische Quantum-ChromoDynamica. Gebruik makende van deze theorie kunnen zogeheten fragmentatie functies afgeleid worden. Deze functies specificeren de waarschijnlijkheid dat een b quark in een B_c meson fragmenteert. Met behulp van evolutie vergelijkingen kan ook de fragmentatie van gluonen naar B_c mesonen worden beschreven. De afleiding van de $b \to B_c$ fragmentatie functies wordt besproken. Vervolgens wordt gedemonstreerd dat soortgelijke fragmentatie functies voor $c \to \psi'$ de gemeten differentiële werkzame doorsnede voor directe ψ' productie correct beschrijven. Berekeningen betreffende het massa spectrum van aangeslagen $b\bar{c}$ toestanden laten zien dat alle toestanden die een massa hebben die beneden de productie drempel van een (licht) B en een D meson liggen, zullen vervallen naar de $b\bar{c}$ grondtoestand. Dit verval kan elektromagnetisch of sterk van aard zijn en kan zowel direct als indirect (via lager gelegen aangeslagen toestanden) plaatsvinden. Dit betekent dat al deze aangeslagen toestanden meegenomen moeten worden om een voorspelling te kunnen doen voor de totale werkzame doorsnede van de $b\bar{c}$ grond toestand. Fragmentatie functies voor de aangeslagen $b\bar{c}$ toestanden worden ook besproken in dit proefschrift. Tenslotte worden een aantal theorieën besproken die waarden afleiden voor de levensduur, de massa en de vervals-verhoudingen van de verschillende $b\bar{c}$ toestanden.

De fragmentatie functies voor het B_c meson zijn geïmplementeerd in ARIADNE, een computer programma dat gebaseerd is op Monte Carlo technieken. ARIADNE wordt gebruikt om de cascade van deeltjes die sterk wisselwerken, te simuleren. Door gebruik te maken van het programma PYTHIA, dat de harde interactie en het verval van de B_c deeltjes beschrijft, wordt een totale geïntegreerde werkzame doorsnede voor B_c^- productie van 2.28 ± 1.14 nb ($p_T(B_c^-) > 6$ GeV) voorspeld bij Tevatron energieën. Dit resultaat is in goede overeenstemming met eerdere analytische berekeningen en experimentele resultaten van CDF. Voor de LHC wordt een totale geïntegreerde werkzame doorsnede voor B_c^- van 66 ± 33 nb ($p_T(B_c^-)) > 10$ GeV) voorspeld. Tenslotte wordt het vervals-kanaal $B_c \to J/\psi(l^+l^-) + l + \nu_l$, $l = e, \mu$ bestudeerd met behulp van een geparametriseerde simulatie van de ATLAS detector respons. De trilepton vervals-vertex in dit specifieke verval is duidelijk te onderscheiden van het primaire interactiepunt en zorgt ervoor dat de achtergrond van directe J/ψ (ψ') productie alsmede het verval van (lichte) B-mesonen naar $J/\psi X$

sterk kan worden onderdrukt. De dominante achtergrond voor het trilepton signaal wordt gevormd door leptonen, geproduceerd in het verval van pionen en kaonen in hun vlucht, welke incorrect worden geassocieerd met een $B \rightarrow J/\psi X$ vertex. Door gebruik te maken van een snede op de vervalslengte gemeten in het transversale vlak van het $J/\psi(l^+l^-)l$ systeem, in combinatie met de eis dat de invariante massa van het $J/\psi + l$ systeem voldoet aan $4.0 < M(J/\psi + l) < 6.0$ GeV blijven er $\mathcal{O}(10^5)$ B_c gebeurtenissen over (waarbij een geïntegreerde luminositeit van 10 fb^{-1} is aangenomen). De studie geeft verder aan dat de achtergrond erg klein is, $S/B \sim$ 50-60. Een volledige detector simulatie is echter noodzakelijk om dit in meer detail te onderzoeken.

Dankwoord

Dit proefschrift heeft niet tot stand kunnen komen zonder de bijdrage, op wat voor wijze dan ook, van vele personen. Een aantal van deze mensen wil ik hier expliciet vermelden.

Allereerst wil ik mijn promotor Bob van Eijk bedanken. Zonder zijn inspirerende begeleiding en eindeloos geduld bij het beantwoorden van mijn vragen, zou ik nooit zover gekomen zijn. De vele discussies aangaande de fysica (en daarbuiten) zijn uiterst leerzaam en onderhoudend geweest. Terugkijkend op een periode van bijna 6 jaar (inclusief het afstuderen) heb ik onze samenwerking als zeer prettig ervaren. Bob, nogmaals mijn dank hiervoor. Mijn co-promotor Jos Vermeulen wil ik bedanken voor zijn dagelijkse begeleiding in allerlei opzichten, vooral in de eerste paar jaar van mijn aanstelling als promovendus. Het met grote precisie proef-lezen van de verschillende notes en later van de verschillende onderdelen van mijn proefschrift, hebben de hoeveelheid onvolkomenheden en foutjes aanzienlijk gereduceerd.

I would like to thank Nick Ellis for his contribution to the note on which chapter 5 of this thesis is based. I also would like to extend my gratitude to Leif Lönnblad, who provided me with a first rough modified version of his ARIADNE program which enabled me to implement the B_c production code. Futhermore, Leif was kind enough to answer my (naive) questions regarding the inner workings of ARIADNE.

Tijdens een deel van mijn promotie periode heb ik de eer gehad de kamer te delen met Ernst-Jan Buis. Ik wil hem bedanken voor de vele nuttige tips aangaande fortran, linux/Unix en scripting zaken, alsmede de tijden in menig café en restaurant zowel in Amsterdam als tijdens mijn korte verblijven op CERN.

Daarnaast hebben vele andere mede-promovendi en studenten op het NIKHEF ervoor gezorgd dat ik een zeer prettige tijd heb gehad aldaar. In het bijzonder wil ik Aart, Mieke, Bram, Martin, Marco, Marck, Rutger en Paul bedanken met wie ik op enigerlei wijze menige horeca-gelegenheid van binnen uitvoerig heb verkend. Ook wil ik de bewoners van de “Hall of Shame” bedanken voor de samenwerking (Gordon, Fabian) of voor het aanhoren van mijn klaagzangen dan wel om het maken van zo maar een praatje (Ytsen, Jeroen).

Naast collega’s van het NIKHEF wil ik ook uiteraard (oud) 9-2 bedanken, in het bijzonder Alex, Niels, Marc en Hendrick. De sessies oeverloos gezwets op ICQ/IRC zorgden voor de nodige ontspanning tijdens het werken aan en schrijven van het proefschrift. Bovendien vond ik Marc en Hendrick bereid om het paranimf-schap op zich te nemen, waarvoor nog-

maals mijn dank.

Tenslotte wil ik mijn moeder, Harriët, Harma en de rest van de familie bedanken voor hun steun gedurende de jaren van mijn promotie. Als laatste wil ik Annechien bedanken voor haar liefdevolle ondersteuning en begrip vooral gedurende de laatste paar maanden van het schrijven van het proefschrift. Ze heeft altijd voor me klaar gestaan met raad en daad. Chien, van harte bedankt, en van nu af aan wordt alles hopelijk wat minder hectisch.